Simultaneous Charging/Discharging of Phase Change Materials:

Characterization of Natural Convection Process

Mahmood Mastani Joybari

A Thesis

In the Department

of

Building, Civil and Environmental Engineering

Presented in Partial Fulfillment of the Requirements

For the Degree of

Doctor of Philosophy (Building Engineering) at

Concordia University

Montreal, Quebec, Canada

July 2017

CONCORDIA UNIVERSITY

SCHOOL OF GRADUATE STUDIES

This is to certify that thesis prepared

By: Mahmood Mastani Joybari

Entitled: Simultaneous Charging/Discharging of Phase Change Materials:

Characterization of Natural Convection Process

and submitted in partial fulfillment of the requirements for the degree of

DOCTOR OF PHILOSOPHY (Building Engineering)

complies with the regulations of the University and meets the accepted standards with respect to originality and quality.

Signed by the final examining committee:

_____ Chair
Dr. S. Bergler

_____ External Examiner
Dr. J. Srebric

_____ External to Program
Dr. A. Dolatabadi

_____ Examiner
Dr. H. Akbari

_____ Examiner
Dr. L. Wang

_____ Thesis Supervisor
Dr. F. Haghighat

Approved by

_____
Dr. F. Haghighat, Graduate Program Director

July 25, 2017   _____
Dr. A. Asif, Dean
Faculty of Engineering and Computer Science

Abstract

Simultaneous Charging/Discharging of Phase Change Materials: Characterization of Natural Convection Process

Mahmood Mastani Joybari, Ph.D.
Concordia University, 2017

In recent decades, latent heat storage in phase change materials (PCMs) received considerable attention. This is due to their high latent heat capacity, which is essentially required for managing and overcoming the temporal mismatch between energy supply and demand. Thus, at the time of energy availability at supply side, it is stored in PCMs so as to be extracted later on when it is needed. In order to provide continuous operation, there are some periods when a thermal storage has to be simultaneously charged and discharged. Most studies focused either on charging, discharging, or consecutive charging and discharging process, while limited work has been conducted for the case of simultaneous charging and discharging (SCD). The first objective of this dissertation is to develop a numerical model to analyze the heat transfer mechanism within a horizontal PCM storage under SCD. Since the possible heat transfer mechanisms within PCMs are conduction, convection or a combination of both, two models are used to identify the mechanism under SCD; i.e. the pure conduction (PC) model and combined conduction and natural convection (CCNC) model. The PC model is a hypothetical model, which neglects the natural convection during phase change process; however, the CCNC model is the real case one. Validation of the model results by comparison with experimental data shows an acceptable agreement both under melting and solidification. Therefore, the developed model can be used to numerically study the phase change process in PCMs.

Natural convection is the result of density changes, which create buoyancy forces within melted PCM and plays a significant role during melting. Currently, the most widely used method to account for natural convection is the effective thermal conductivity method. The method considers an artificial increase in thermal conductivity values to take into consideration the effect of natural convection by comparing the results with experimental data. Two major shortcomings of this method are that first, it is tedious

to obtain the proper value and second, the method does not provide information about the melting front location. In this dissertation, a novel simplified front tracking method is presented to replace the thermal conductivity method. The novel method is based on considering two separate melting fronts for the upper and lower halves of a horizontal thermal storage system. Therefore, two dimensionless correlations are developed to map the results of the simple PC model to that of the complicated CCNC model based on the presented logic. The method essentially creates a link between CCNC and PC models, which is also missing in the literature. Based on verification, the correlations can provide results within ±15% discrepancy.

Acknowledgement

First and foremost, I would like to express my deepest appreciation to my supervisor, Dr. Fariborz Haghighat, for his continuous guidance and support. I am grateful for the advice, criticism, encouragement and patience throughout my study.

I would like to extend my gratitude to the supervising committee members, Dr. Hashem Akbari, Dr. Ali Dolatabadi and Dr. Liangzhu Wang for their advice and support at every stage of the research.

I would like to acknowledge the contribution of Dr. Xiaolin Wang and Dr. Saeid Seddegh from University of Tasmania, Australia as well as Dr. Al-Abidi from Sana'a Community College, Yemen who provided the required experimental data for model validation.

I would like to thank the past and present members of Energy and Environment Research Group at Concordia University for their support and friendliness. I also would like to extend my appreciation to my dear friends including but not limited to Asefeh Salarinezhad, Rouzbeh Ghouchani, Nima Bayat-Makou, Rameh Mehrjoo and Fataneh Mobasheramini for their continuous support and friendship.

Last but not least, I wish to express my special appreciation and love to my beloved parents and my dear sister for their kindness and unconditional support. I hereby would like to dedicate this thesis to my family as a token of appreciation.

Contribution of Authors

Chapter	2, 3, 4
Title	Numerical investigation of a triplex tube heat exchanger with phase change material: Simultaneous charging and discharging
Authors	Mahmood Mastani Joybari, Fariborz Haghighat, Saeid Seddegh
Status	Published, Energy and Buildings
Description	Mahmood Mastani Joybari developed the model and conducted the numerical simulation. Dr. Fariborz Haghighat supervised the research and reviewed the contents of various drafts of the paper. Dr. Saeid Seddegh conducted the experiments and provided the required data for model validation.
Reference	M. M. Joybari, F. Haghighat, and S. Seddegh, "Numerical investigation of a triplex tube heat exchanger with phase change material: Simultaneous charging and discharging," *Energy and Buildings,* vol. 139, pp. 426–438, 2017.

Chapter	2, 5
Title	Heat transfer enhancement of phase change materials by fins under simultaneous charging and discharging
Authors	Mahmood Mastani Joybari, Fariborz Haghighat, Saeid Seddegh, Abduljalil Al-Abidi
Status	Revised version submitted, Energy Conversion and Management
Description	Mahmood Mastani Joybari conducted the numerical study and compiled the results as the paper. Dr. Fariborz Haghighat supervised the research and reviewed the drafts of the paper. Dr. Saeid Seddegh revised the paper. Dr. Al-Abidi provided the required data for model validation and commented on the paper.

Chapter	2, 6
Title	Natural convection characterization during melting of phase change materials: Development of a novel simplified front tracking method
Authors	Mahmood Mastani Joybari, Fariborz Haghighat, Saeid Seddegh
Status	Under review, Solar Energy
Description	The numerical simulations were conducted by Mahmood Mastani Joybari who also compiled the results as the paper. Dr. Fariborz Haghighat supervised the research and reviewed various drafts of the paper. Dr. Saeid Seddegh revised the paper and provided comments on the paper.

Chapter	Appendix A
Title	Heat and cold storage using phase change materials in domestic refrigeration systems: The state-of-the-art review
Authors	Mahmood Mastani Joybari, Fariborz Haghighat, Jeff Moffat, Paul Sra
Status	Published, Energy and Buildings
Description	Mahmood Mastani Joybari compiled the paper. Dr. Fariborz Haghighat revised various drafts of the paper. Jeff Moffat and Paul Sra provided some suggestions and comments.
Reference	M. M. Joybari, F. Haghighat, J. Moffat, and P. Sra, "Heat and cold storage using phase change materials in domestic refrigeration systems: The state-of-the-art review," *Energy and buildings,* vol. 106, pp. 111-124, 2015.

Chapter	Appendix B
Title	Exergy analysis of single effect absorption refrigeration systems: The heat exchange aspect
Authors	Mahmood Mastani Joybari, Fariborz Haghighat
Status	Published, Energy Conversion and Management
Description	Mahmood Mastani Joybari conducted the analyses and wrote the paper. Dr. Fariborz Haghighat supervised the research and reviewed various drafts of the paper.
Reference	M. M. Joybari and F. Haghighat, "Exergy analysis of single effect absorption refrigeration systems: The heat exchange aspect," *Energy Conversion and Management,* vol. 126, pp. 799-810, 2016.

Chapter	Appendix C
Title	Investigation of the effect of geometric and operating parameters on thermal behavior of vertical shell-and-tube latent heat energy storage systems
Authors	Saeid Seddegh, Mahmood Mastani Joybari, Xiaolin Wang, Fariborz Haghighat
Status	Revised version submitted, Energy
Description	Dr. Saeid Seddegh carried out the experimental investigation and wrote the paper. Mahmood Mastani Joybari conducted the numerical investigation and revised the paper. Dr. Xiaolin Wang and Dr. Fariborz Haghighat supervised and reviewed several drafts of the paper.

Chapter	Appendix D
Title	Experimental and numerical characterization of natural convection in a vertical shell-and-tube latent thermal energy storage system
Authors	Saeid Seddegh, Mahmood Mastani Joybari, Xiaolin Wang, Fariborz Haghighat
Status	Revised version submitted, Sustainable Cities and Society
Description	Dr. Saeid Seddegh carried out the experimental investigation and wrote the paper. Mahmood Mastani Joybari conducted the numerical investigation and revised the paper. Dr. Xiaolin Wang and Dr. Fariborz Haghighat supervised and reviewed several drafts of the paper.

Table of Contents

List of Figures

List of Tables

List of Symbols

English symbol	Description
a	Correlation constant
b	Correlation constant
c	Correlation constant
C	Mushy zone parameter (kg.m^{-3}.s^{-1})
C_p	Specific heat (J.kg^{-1}.K^{-1})
D	Diameter (m)
f	Friction factor (-)
Fo	Fourier number (-)
g	Gravity (m.s^{-2})
h	Sensible specific enthalpy (J.kg^{-1})
$\overline{h}$	Convective heat transfer coefficient (W.m^{-2}.K^{-1})
H	Total specific enthalpy (J.kg^{-1})
k	Thermal conductivity (W.m^{-1}.K^{-1})
m	Correlation exponent
n	Correlation exponent
Nu	Nusselt number (-)
p	Pressure (N.m^{-2})
Pr	Prandtl number (-)
r	Radius (m)

R	Shell-to-tube radius ratio
Ra	Rayleigh number (-)
Re	Reynolds number (-)
Ste	Stefan number (-)
t	Time (s or min)
T	Temperature (K or °C)
U	Dimensionless velocity (r-direction)
v	Velocity (m.s^{-1})
V	Dimensionless velocity (θ-direction)

Greek symbol	Description
α	Thermal diffusivity (m^2.s^{-1})
β	Thermal expansion coefficient (K^{-1})
δ	Small number to avoid division by zero, 0.001 (-)
γ	Liquid fraction (-)
ΔH	Latent specific enthalpy (J.kg^{-1})
ε	Heat exchanger effectiveness (-)
λ	Latent heat of fusion (J.kg^{-1})
μ	Dynamic viscosity (kg.m^{-1}.s^{-1})
ρ	Density (kg.m^{-3})
υ	Kinematic viscosity (m^2.s^{-1})
η_f	Fin effectiveness (-)

Subscript	Description
CCNC	Combined conduction and natural convection model
h	Hydraulic
i	Inner; initial; corresponding
l	Liquidus
m	Middle
o	Outer
PC	Pure conduction model
ref	Reference
s	Solidus
std	Steady

Superscript	Description
f	Final
L	Lower half
mod	Modified
U	Upper half
*	Dimensionless variable

Abbreviation	Description
CFD	Computational fluid dynamics

CHTF	Cold heat transfer fluid
CCNC	Combined conduction and natural convection
COP	Coefficient of performance
DHW	Domestic hot water
HHTF	Hot heat transfer fluid
HTF	Heat transfer fluid
NTU	Number of transfer units
PC	Pure conduction
PCM	Phase change material
SCD	Simultaneous charging and discharging
STHX	Shell and tube heat exchanger
TTHX	Triplex tube heat exchanger

Chapter 1: Introduction

1.1 Background

A large portion of buildings energy consumption is dedicated to the commercial sector. In 2011, the commercial sector accounted for about 13% of total energy consumption in Canada [1]. Furthermore, it is estimated that energy demand of this sector increases by about 0.7% each year reaching a total amount of 1650PJ by 2035. The commercial sector covers a vast class of buildings including office, governmental, institutional, warehouse, retail, utility, etc. In 2009, among about 83.6 thousands Canadian office buildings (excluding medical offices), about 88.6% were equipped with space cooling systems to provide thermal comfort during cooling season, which account for a huge amount of energy consumption [2].

A variety of air conditioning systems are available for indoor space cooling during hot season. Among these systems, vapor compression and absorption cooling systems (see Appendix B) are the most common ones. At the heat rejection side of these systems, normally, cooling towers are used to dissipate the generated heat to the ambient. A potential application for thermal energy storage is to replace cooling towers. PCMs have been used at heat rejection side of cooling systems for waste heat recovery or elimination of cooling towers. They extract and store waste heat from the hot heat transfer fluid (HHTF) flowing inside the heat rejection side of the cooling systems. This heat could be utilized for preheating of domestic hot water, which would be the cold heat transfer fluid (CHTF). Consequently, the storage can have three modes; (1) charging only; (2) discharging only; and (3) simultaneous charging and discharging (SCD). In other words, in order to provide continuous operation, there might be sometimes that a thermal storage needs to be simultaneously charged and discharged. There is a lack of extensive literature about the fundamentals of heat transfer under SCD within PCMs. Most of the earlier studies were either focused on a special geometrical design or developed oversimplified models.

The possible heat transfer mechanisms within PCMs are conduction, convection or a combination of both. Therefore, available studies in the literature are based on the considered heat transfer mechanism: the pure conduction (PC) model and the combined conduction and natural convection (CCNC) model. Early numerical modeling of the process considered only conduction as the dominant heat transfer mechanism during the melting and solidification processes. However, density changes create buoyancy forces resulting in natural convection, which greatly affect the process, particularly under melting. To account for the effect of natural convection under melting, some methods have been developed and the most well-known one is the effective thermal conductivity method. It is equivalent to an artificial increase in the thermal conductivity value of a PCM to account for the natural convection phenomenon. Despite its simplistic logic, (1) the implementation procedure is a tedious task; (2) the method requires plenty of experimental data; and (3) it cannot provide information about the melting front location since it is essentially a conduction model. Therefore, a systematic method which considers the effect of natural convection and provides front tracking is needed. The method should tackle the mentioned disadvantages and at the same time should be simple enough in logic to be able to replace the widely-used effective thermal conductivity method. In this study, horizontal latent heat thermal energy storage units are investigated since it has been reported that the phase transition in PCMs is faster in horizontal storages compared to vertical ones [3].

1.2 Objectives

The main objectives of this study are:

- Development of a model for investigation of heat transfer mechanism during simultaneous charging/discharging of PCMs in TTHXs
- Development of a novel front tracking method for STHXs based on geometrical analysis of the system

1.3 Thesis outline

Chapter 2 presents a critical literature review including the fundamentals of heat transfer models for PCMs. Chapter 3 contains the problem formulation and numerical model development. Model validation is also presented at the end of this chapter. Chapter 4 focuses on the fundamentals of heat transfer within a PCM under two SCD modes; i.e. internal-heating/external-cooling and internal-cooling/external-heating. The performance of the PC and CCNC models is also compared. Then, Chapter 5 discusses the heat transfer enhancement by integration of fins for the mode of internal-heating/external-cooling. The most suitable configurations for SCD, and non-SCD conditions are identified. Thereafter, Chapter 6 presents the development of the novel simplified front tracking method. The correlations are developed and the method is verified in this chapter. Finally, Chapter 7 summarizes the findings of this research and presents some recommendations for future studies.

Chapter 2: Literature review

2.1 Introduction

Thermal energy storage can generally be classified as sensible and latent heat storages. In recent decades, latent heat storage in phase change materials (PCMs) received considerable attention [4]. This is due to their high latent heat capacity, which is essentially required for managing and overcoming the temporal mismatch between energy supply and demand [5]. Therefore, this technology found several applications, e.g. mechanical ventilation systems [6], refrigeration systems [7] (see Appendix A), net zero energy buildings [8], hot water tanks [9], etc. In this chapter, a literature review is presented which is the base for the rest of the dissertation. Therefore, first, the common numerical methods to analyze PCMs are classified. Then, thermal conductivity enhancement methods for PCMs are presented. Thereafter, studies that investigated simultaneous charging and discharging are discussed. Finally, studies related to melt fraction and front tracking are presented.

2.2 Numerical analysis methods for PCMs

According to the literature, the numerical analysis of PCMs could be generally classified into two major categories based on the considered heat transfer mechanism: the pure conduction (PC) model, and the combined conduction and natural convection (CCNC) model. Early numerical modeling of the process considered only conduction as the dominant heat transfer mechanism during the melting and solidification processes [10]. This is equivalent to a circular (or cylindrical in 3D) PCM melting front shape around a tube [11, 12]. However, during the phase change process, the density changes create buoyancy forces resulting in natural convection in the melted PCM, which affects the heat transfer. The effect of natural convection on the phase change process has been reported [13, 14]. Nevertheless, some simple approaches such as the well-known ε-NTU approach for heat exchanger design ignore the effect of natural convection. Ignoring this effect resulted in the underestimation of effectiveness values during melting and

solidification processes [15]. Therefore, it is important to compare the results of the real process considering the effect of natural convection (combined phenomena) with those of the pure conduction assumption in order to understand the deviation of such an assumption.

2.3   Necessity of thermal conductivity enhancement in PCMs

The most noticeable shortcoming of PCMs is their low thermal conductivity. For organic and salt hydrate PCMs, typical thermal conductivity values are in the range of 0.15 ~ 0.3 W/mK and 0.4 ~ 0.7 W/mK, respectively [10]. This drawback results in high thermal resistance within PCMs during their operation, affecting their thermal response and efficiency [16]. Several solutions have been investigated in order to enhance the thermal conductivity of PCMs, which could be generally classified into the following major categories; introduction of high thermal conductivity additives/metal matrices, microencapsulation of PCMs, using multiple PCMs, increasing heat transfer surface area by utilization of extended surfaces (fins) or multiple tubes, etc. [17].

2.3.1   Methods of enhancement

Some studies focused on the thermal conductivity enhancement by dispersing additives with high thermal conductivity into PCMs; e.g. carbon nanotubes (CNTs) [18], graphene nanoplatelets (GNPs) [19, 20], etc. Although this method enhances the thermal conductivity, the viscosity of the PCM is negatively affected. For instance, samples with 1% (by weight) and 2% CNTs had dramatically higher viscosities; 1 and 2 orders of magnitude higher than the pure one, respectively [18]. This in turn interfered with natural convection where higher solid fractions undesirably resulted in higher suppression of natural convection during melting [19]. In addition, it was reported that instead of a single PCM, application of an array of PCMs (multiple PCMs) with phase change temperatures close to the HTF temperature profile could also enhance the heat transfer characteristics of a thermal storage [21]. However, availability of PCMs with desirable phase change temperatures and the economic justification of their application are the

main limitations of this approach. Finally, increasing the heat transfer surface area was also investigated including application of finned tubes, utilization of multi tube heat exchangers, etc. Advantages of fins include manufacturing and utilization simplicity as well as low cost [10]. Therefore, in this study, application of extended surfaces by fins is investigated.

2.3.2   Thermal conductivity enhancement by fins

In a cylindrical geometry, fins could be positioned radially or longitudinally. The main reasons to use radial fins are ease of design and manufacturing as well as low cost [16]. However, several experimental results indicated superior performance for longitudinal fins since they did not suppress the natural convection during melting and also helped the solidification process [22]. It is important to consider the fact that application of fins should not interfere with or prevent the natural convection during melting [23]. For instance, a configuration with four perpendicular short longitudinal fins was found to intensify natural convection [24]. The same study also reported that longer fins were more effective than shorter ones in terms of shortening the phase change process. Therefore, there is a conflict between heat transfer enhancement by fins and effectiveness of natural convection within PCMs. For instance, due to the utilization of longitudinal fins, the melted PCM motion was limited to the space left between fins and the shell wall [17]. An experimental study reported that at low Furrier numbers, the fin effectiveness was less than unity, which was attributed to the suppression of natural convection by fins [25]. In a recent study, an inflection point was reported during melting inside a longitudinally finned horizontal sleeve tube heat exchanger [24]. The point was attributed to the completion of melting at the upper half of the storage due to the buoyancy-induced motion. Beyond that point, conduction was found to replace natural convection to melt the rest of the PCM.

Longitudinal fin configurations were investigated in several horizontal shell and tube heat exchangers with PCM at the shell side. In a study, the configurations included four fins of straight and angled designs where the former included two vertical and two horizontal fins, while the latter was a rotation of the former by 45° [26]. It was found that

during melting under low HTF temperatures, the angled configuration presented superior performance, which was due to the higher natural convection by the increased heat transfer surface area at the lower half of the storage. Another study found that the key to enhancing heat transfer during melting by fins is to allocate fins to the lower half of a horizontal shell and tube system [24]. Given this, it was proposed that the optimum fin configuration is three fins over the tube located at the bottom of the system where one fin is vertically positioned at the bottom and the two others are located at an angle between 60° to 90° on its both sides.

2.4   Simultaneous charging and discharging of PCMs

The research in the area of phase change process of PCMs had a routine trend over the course of the past decades. This trend includes investigation of a PCM under a one-time charging or one-time discharging process or considering consecutive charging and discharging periods. Therefore, it is presumably assumed that the PCM is initially completely melted/solidified and then it undergoes solidification/melting. This ideal assumption ignores the fact that in real life applications, PCMs might go through SCD. In such scenarios, a PCM undergoes charging from one hand, while it simultaneously faces discharging from the other. Specifically, SCD can happen when dealing with unpredictable occupant behavior or intermittent consumption. For instance, in the case of solar thermal energy utilization for domestic hot water (DHW) heating, water consumption might occur at the same time when the thermal storage is being charged.

PCMs have been investigated in numerous studies under charging, discharging, or consecutive charging and discharging process; however, SCD of PCMs has been rarely studied. Liu et al. conducted experimental investigation into SCD of a heat pipe heat exchanger [27]. It was reported that the low PCM conductivity prevented efficient performance of the system. Murray and Groulx experimentally investigated consecutive charging/discharging [23] as well as simultaneous charging/discharging [28] of a cylindrical storage for DHW heating. The setup used in their studies consisted of a vertical cylindrical storage through which two finned parallel pipes were passed carrying heat transfer fluids (HTFs). The PCM was continuously charged by the hot HTF, while

the SCD was imposed intermittently to mimic a typical DHW usage. In such a scenario, the final steady state was reported to be the fully melted condition and independent from the initial PCM condition. Moreover, it was found that during SCD, low thermal conductivity of the solid PCM controlled the heat exchange process and the natural convection was not beneficial in this specific case. However, the shortcoming of this study is that the effect of natural convection could not be clearly justified from the discrete experimental temperature data from thermocouples. In a recent study, SCD of a PCM in a horizontal shell and tube heat exchanger (PCM at the shell side) was modeled and investigated experimentally [29]. An electric heater was mounted at the tube side, while air was blown over the shell side to cool down the system. The numerical analysis was greatly simplified assuming a symmetric 1D model solved by explicit finite difference approach for the temperature and liquid fraction.

Certain configurations have the capability of providing SCD; e.g. triplex tube heat exchangers (TTHXs). Basically, a TTHX is a concentric configuration of three tubes. For thermal storage applications, the middle tube is filled with a PCM while the inner and outer ones carry HTFs. Advantages of a TTHX over double pipe heat exchangers include its increased heat transfer surface area, possibility of low temperature heating/cooling of the PCM, and faster melting/solidification process [30]. Besides, it has the following characteristics, which make it suitable for several applications including solar DHW preheating:

- High storage density,
- High heat transfer area,
- Separate flow paths for the heat transfer fluid and potable water, satisfying sanitary requirements,
- Possibility of SCD of a PCM, and
- High natural convection so as to reduce heat transfer resistance of the solid PCM zone.

Table 2.1 shows a summary of the studies with a PCM in TTHXs.

Table 2.1: Summery of the studies with PCM in triplex tube heat exchanger

Ref.	Study Type		Objective	PCM	Process	
	Num.	Exp.			Melting	Solidification
[31]	✓	✓	DHW heating by air source heat pump	Paraffin 56#	✓	✓
[32]	✓	✓	Waste heat recovery	n-Hexacosane	✓	✓
[30]	✓	✓	Energy supply and demand mismatch	RT82		✓
[13]	✓	✓	Energy supply and demand mismatch	RT82	✓	
[17]	✓	✓	Energy supply and demand mismatch	RT82	✓	
[33]	✓	✓	Energy supply and demand mismatch	RT82	✓	
[34]		✓	Energy supply and demand mismatch	RT82	✓	✓
[35]		✓	Liquid desiccant air conditioning	RT82	✓	

Long and Zhu developed an air-source heat pump system coupled with thermal energy storage for DHW heating [31]. They investigated the heat transfer in the TTHX by considering the PC model during the phase change. COP enhancement was reported as a result of PCM integration to the heat pump cycle. Based on the same assumptions, Jian-You investigated the performance of a TTHX as a tool for waste heat recovery as well as peak load shaving [32]. These studies indicated that TTHXs have the potential to store heat of condensation. In a recent series of studies, Al-Abidi et al. investigated a TTHX either for heat or cold energy storage (i.e. non-SCD condition) with/without fins using a 2D heat transfer model [13, 17, 30, 33-35]. Their results indicated that the more the number of fins, the shorter was the phase change process. Similar results were reported for longer fins. However, the effect of fin thickness was found to be insignificant. It should be noted that despite the capability of TTHXs to provide SCD, the heat transfer enhancement by integration of fins in such systems has not been investigated under SCD.

2.5   Heat exchanger design tools

Basically, the design tools for heat exchangers could be classified in two major categories. The first category includes all the simplified methods including the well-known approaches of effectiveness-number of transfer units (ε-NTU) and logarithmic mean temperature difference (LMTD). These approaches normally oversimplify the process in PCMs and ignore some major phenomena such as natural convection. On the other hand, detailed CFD simulation of the process also leads to a design tool, which requires long computational time, is greatly complicated, and might be limited to the investigated case. However, between these two scenarios, some "enhanced tools" can also be developed, which are almost as simple as the first category but provide acceptable results comparable to CFD case.

2.5.1   Accounting for natural convection

To account for the buoyancy effect during the melting process, effective thermal conductivity was introduced in order to have better accuracy in the ε-NTU method. Comparing the results of ε-NTU method (1D) and CFD (3D), with experimental data it was found that 1D ε-NTU could be utilized for PCM heat exchanger design instead of the complicated time-consuming CFD if the natural convection is accurately accounted by the effective thermal conductivity [15]. Nevertheless, the main disadvantages of effective thermal conductivity are: (1) experimental data should be available *a priori* to evaluate the effective thermal conductivity; (2) derivation of effective thermal conductivity is a tedious task since several candidate thermal conductivity values should be examined to find the one that has similar heat transfer rate as that of the experimental process; (3) a constant value cannot be designated to the effective thermal conductivity of a fluid with varying temperature [36]; and (4) despite all the complexity, it cannot provide information about the melting front location since it is essentially a conduction model.

2.5.2 Melting front tracking

During the phase change process, knowing the location of melting front is greatly important since it shows what portion of the storage has gone through the phase change (also known as liquid fraction). However, this knowledge has been proven to be hard to obtain, in particular experimentally. Calculation of liquid fraction from experimental data was formerly conducted by interruption of the process at various stages to remove the remaining solid part [37]. However, in recent years, utilization of transparent tubes for direct visual observation [26] or digital high resolution photography [16], which might include image processing [38], replaced the old technique. Due to such complexities, it is preferred to obtain liquid fraction values from numerical analysis.

In early numerical studies, front tracking was also a great challenge. The problem was the complexity of simultaneously solving the conventional energy equation for solid and liquid domains together with the energy balance at the melting front (i.e. a moving-boundary problem). However, introduction of enthalpy method significantly improved numerical studies by replacing the simultaneous solving with a single enthalpy-based energy equation for the whole domain [39]. Nevertheless, melting front tracking by enthalpy method is a two-step process, where first the enthalpy values are calculated and then the location of the melting front is determined from the respective temperature values [40]. Furthermore, as of today, the numerical analysis is still complicated and computationally intense and requires expertise to develop in-house codes or familiarity with available commercial software.

Therefore, several studies developed correlations to characterize the phase change process within PCMs. Table 2.2 hierarchically summarizes some of these studies covering both solidification and melting processes. According to this table, most of the earlier studies focused on the phase change time by developing correlations for Fourier number (Fo), whereas liquid fraction (γ) correlations received attention more recently. Besides, absence of Rayleigh number (Ra) in many of these correlations shows that the effect of natural convection was neglected. Overall, despite separate correlation developments for natural convection as well as pure conduction model, to the best of the author's knowledge, no study has focused on a correlation between these two models.

Table 2.2: A summary of developed correlations for melting of PCMs

Ref.	Study type	Orientation	Storage type(s)	Correlation	Comment
[41]	Analytical		Cylindrical Spherical	$Fo = a + \dfrac{b}{Ste}$	Valid for solidification process; thus, natural convection was absent.
[42]	Analytical		Slab Cylindrical Spherical	$Fo = a + \dfrac{b}{Ste}$	Valid for both melting and solidification.
[43]	Experimental	Horizontal Vertical	Cylindrical	$Fo = a + \dfrac{b}{Ste}$	Valid for both melting and solidification. The author reported the effect of natural convection on the phase change process but did not include it in the correlation.
[44]	Experimental	Horizontal Vertical	Cylindrical	$Fo = a + \dfrac{b}{Ste}$	Valid for both melting and solidification. The author reported the effect of natural convection on the phase change process but did not include it in the correlation.
[45]	Numerical	Horizontal	Cylindrical	$Y = a(X)^2 + b(X) + c$	Valid for melting. Developed correlations for complete melting time and melt volume where X represents either Rayleigh (Ra) or Stefan (Ste) number.
[46]	Experimental Numerical	Vertical	Shell and tube	$\gamma = (FoSte)^a \, Ra_D^b \, \exp\!\left(\dfrac{c}{Ra_H}\right)$	Valid for melting. Based on four vertical shell and tube heat exchangers having different tube diameters.
[47]	Experimental	Vertical	Shell and tube	$Fo = a + b\,\mathrm{Re} + cSte$	Valid for melting.
[20]	Experimental	Vertical	Cylindrical	$\gamma = aFoSte^b Ra^c$	Valid for melting. Used the same correlation for a pure PCM as well as different weight percentages of graphene nanoplatelets (GNPs) in the PCM.

Chapter 3: Problem formulation and numerical model development

3.1 Introduction

The main limitation of CFD simulations is the available computational power and time as well as expertise. Accounting for natural convection during the phase change process can be computationally intense. Therefore, in this dissertation, a cross-sectional area of a heat exchanger (i.e. a 2D geometry) is studied to understand the heat transfer mechanism and the impact of natural convection. In this chapter, the governing equations are presented and the numerical approach is validated with experimental data.

3.2 Governing equations

In this section, the modeling procedure and its assumptions as well as the considered initial and boundary conditions are presented.

3.2.1 Assumptions

According to the physics of the problem as well as the common assumptions used in the literature, the following assumptions were made for the PCM phase change modeling:

- The flow of the liquid PCM was considered as laminar, incompressible Newtonian fluid flow,
- Viscous dissipation was neglected since large velocity gradients were not present in the study,
- No-slip boundary condition was present,
- At the boundaries heat transfer occurred with the corresponding HTF (Dirichlet boundary condition),
- Liquid fraction variation was assumed to be linear with temperature,
- The void created during solidification was neglected, and

- Phase-wise constant thermophysical properties was assumed for the PCM except for the density, which was evaluated based on Boussinesq approximation to account for the buoyancy forces.

3.2.2 Modeling

Consider a triplex tube heat exchanger as shown in Figure 3.1 where the inner and outer tubes carry hot and cold heat transfer fluids, respectively. Since the problem was symmetric (line of symmetry was $\theta = 0$), half of the annulus was modeled to save computational time.
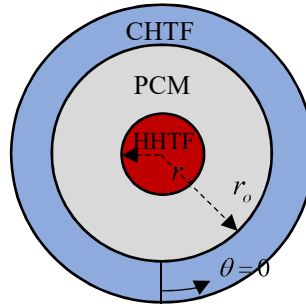
Figure 3.1: Schematic representation of the triplex tube heat exchanger

3.2.2.1 Continuity Equation

$$\frac{\partial \rho}{\partial t} + \frac{1}{r}\frac{\partial}{\partial r}(\rho r v_r) + \frac{1}{r}\frac{\partial}{\partial \theta}(\rho v_\theta) = 0$$

(3.1)

3.2.2.2 Momentum Balance

To develop momentum balance equations, Darcy's law was used to account for the flow of the mushy PCM due to the natural convection. The law appears as a source term in the momentum balance [48]:

$$S_i = \frac{C(1-\gamma)^2}{\gamma^3 + \delta} u_i$$

(3.2)

where γ is the liquid fraction of the melted PCM, which is presented later. To avoid division by zero, δ is added to the denominator with the value of 0.001 [39]. The mushy zone parameter C in Equation (3.2) is a measure that indicates the steepness of reaching zero velocity during solidification. For most modeling applications, values between 10^4 and 10^7 are recommended [49]; therefore, in this study, 10^5 kg.m^{-3}.s^{-1} was considered. The following equations were developed for the velocity components:

$$\frac{\partial(\rho v_r)}{\partial t} + \frac{1}{r}\frac{\partial(\rho r v_r v_r)}{\partial r} + \frac{1}{r}\frac{\partial(\rho v_r v_\theta)}{\partial \theta} =$$
$$-\frac{\partial p}{\partial r} + \mu\left[\frac{\partial}{\partial r}\left(\frac{1}{r}\frac{\partial}{\partial r}(r v_r)\right) + \frac{1}{r^2}\frac{\partial^2 v_r}{\partial \theta^2} - \frac{2}{r^2}\frac{\partial v_\theta}{\partial \theta}\right] + \rho g\cos\theta - \frac{C(1-\gamma)^2}{\gamma^3 + \varepsilon}v_r \qquad (3.3)$$

$$\frac{\partial(\rho v_\theta)}{\partial t} + \frac{1}{r}\frac{\partial(\rho r v_r v_\theta)}{\partial r} + \frac{1}{r}\frac{\partial(\rho v_\theta v_\theta)}{\partial \theta} =$$
$$-\frac{1}{r}\frac{\partial p}{\partial \theta} + \mu\left[\frac{\partial}{\partial r}\left(\frac{1}{r}\frac{\partial}{\partial r}(r v_\theta)\right) + \frac{1}{r^2}\frac{\partial^2 v_\theta}{\partial \theta^2} + \frac{2}{r^2}\frac{\partial v_r}{\partial \theta}\right] - \rho g\sin\theta - \frac{C(1-\gamma)^2}{\gamma^3 + \varepsilon}v_\theta \qquad (3.4)$$

Boussinesq approximation was introduced to account for the natural convection process in the melted PCM [33, 39]:

$$\rho = \rho_l\left[1 - \beta(T - T_l)\right] \qquad (3.5)$$

where β is the thermal expansion coefficient.

3.2.2.3 Energy Balance

Enthalpy method was adopted since it has been proven to prevent the difficulties of phase change front tracking of the normal energy balance equation [39]. Energy balance in terms of enthalpy variations is:

$$\frac{\partial(\rho h)}{\partial t} + \frac{1}{r}\frac{\partial(\rho r v_r h)}{\partial r} + \frac{1}{r}\frac{\partial(\rho v_\theta h)}{\partial \theta} = \frac{k}{C_p}\left[\frac{1}{r}\frac{\partial}{\partial r}\left(r\frac{\partial h}{\partial r}\right) + \frac{1}{r^2}\frac{\partial^2 h}{\partial \theta^2}\right] - S_h \tag{3.6}$$

where the source term (S_h) is:

$$S_h = \frac{\partial(\rho\Delta H)}{\partial t} + \frac{1}{r}\frac{\partial(\rho r v_r \Delta H)}{\partial r} + \frac{1}{r}\frac{\partial(\rho v_\theta \Delta H)}{\partial \theta} \tag{3.7}$$

In these equations, h and ΔH account for sensible and latent heat, respectively. Furthermore:

$$\Delta H = \gamma\lambda \tag{3.8}$$

where γ is the liquid fraction whose variation was assumed to be linear with temperature during the phase change process:

$$\gamma = \begin{cases} 0 & T < T_s \\ \dfrac{T - T_s}{T_l - T_s} & T_s < T < T_l \\ 1 & T > T_l \end{cases} \tag{3.9}$$

3.2.3 Initial and boundary conditions

According to the assumptions made earlier and Figure 3.1, the PCM under SCD was heated by the inner tube carrying hot heat transfer fluid (HHTF), while it was simultaneously cooled down by the cold heat transfer fluid (CHTF). Therefore, initial and boundary conditions for internal-heating/external-cooling mode were defined as:

$$t = 0 \longrightarrow T = T_0$$

$$r = r_i \longrightarrow \begin{cases} v_r = 0 \\ v_\theta = 0 \\ T = T_{HHTF} \end{cases}$$

$$r = r_o \longrightarrow \begin{cases} v_r = 0 \\ v_\theta = 0 \\ T = T_{CHTF} \end{cases} \tag{3.10}$$

$$\theta = 0, \pi \longrightarrow \begin{cases} \dfrac{\partial v_r}{\partial \theta} = 0 \\ v_\theta = 0 \\ \dfrac{\partial T}{\partial \theta} = 0 \end{cases}$$

while for the internal-heating/external-cooling only the HTF temperatures were swapped at the inner and outer boundaries.

3.3 Numerical approach

There is several commercial software available for numerical analysis of the melting/solidification process. However, according to a recent review [50], ANSYS Fluent is the most widely utilized software. Therefore, numerical study of the developed model was conducted using ANSYS Fluent v16.2. ANSYS Fluent uses the enthalpy-porosity approach in which the mushy zone is considered as a porous medium where the liquid fraction is its porosity.

A step-by-step approach was taken in ANSYS Workbench to simulate the process. First, the 2D symmetric half of the annulus was sketched using the DesignModeler environment. Then, ANSYS Meshing generated the mesh. Thereafter, the simulation was setup in ANSYS Fluent environment. To solve the equations, pressure-based solver was used since it is the only option in the software for solving melting/solidification processes [51]. Semi-implicit pressure-linked equation (SIMPLE) method was used for pressure-velocity coupling. For spatial discretization of the pressure and momentum, PRESTO (pressure staggering option) and QUICK schemes were adopted, respectively.

3.4 Model validation

In order to validate the model, the results were compared with the experimental data from two earlier studies. Model validation was carried out for melting and solidification processes, separately.

3.4.1 Melting process

Experimental data from an earlier study [33] was used for validation of the melting process. Validation was carried out by simulating the melting process of the paraffin RT82 (Rubitherm Technologies GmbH) with phase change temperature range of 77-85 °C. The experimental apparatus was a PCM-equipped horizontal triplex tube heat exchanger with internal and external fins to enhance the heat transfer through the PCM. The heat transfer fluid was water at 90 °C, which flowed inside the inner and outer tubes to charge the PCM. Figure 3.2 shows the comparison of numerical and experimental average temperatures. The numerical results followed the experimental ones but almost overestimated the average temperature. Nevertheless, there is an acceptable agreement with the experimental data, and the prediction made by the model. That means the developed model can be used to numerically study melting in the PCM-equipped TTHX system.
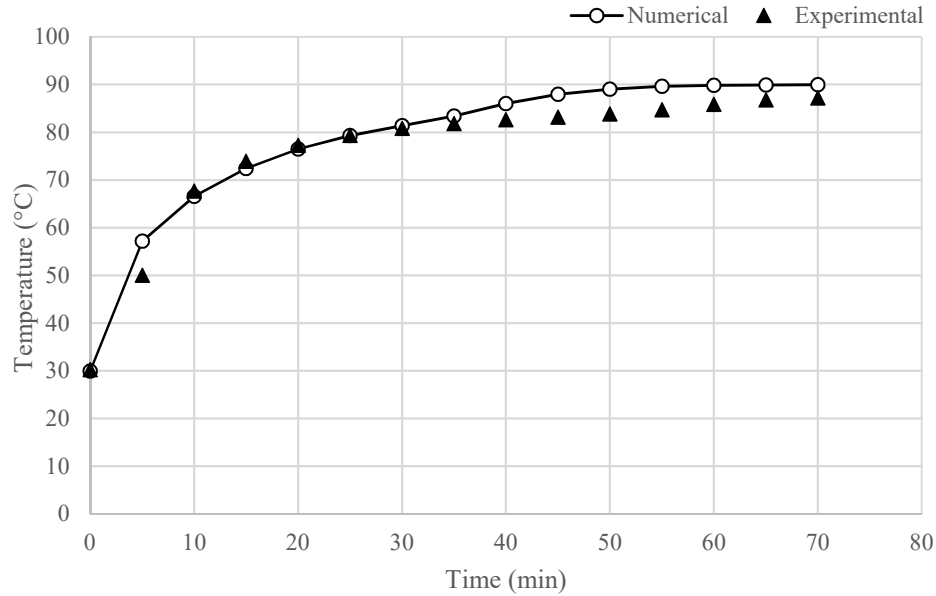
Figure 3.2: Comparison of the numerical and experimental average temperatures for melting

3.4.2 Solidification process

In order to validate the model for the solidification process, experimental data from a recent study [52] was utilized (see Appendix C). The process was simulated for the paraffin RT60 (Rubitherm technologies GmbH) whose phase change temperature range was 55-61 °C. The melted PCM was sitting at the shell side of a vertical shell-and-tube heat exchanger with water flowing as the HTF at 10 °C. In order to make sure that the model can predict temperature of points within the PCM, a specific point in the storage (T_8 for Cylinder D in [52]) was selected for comparison. Figure 3.3 shows the comparison between the experimental data and numerical results. According to the figure, there is an acceptable agreement between numerical results and experimental data. It should be noted that a source of deviation from the experimental data is the fact that the temperature recorded by any thermocouple is an indicator of a part of the PCM around it. Nevertheless, the numerical results are in a reasonable agreement with the experimental data and the model can be utilized to investigate SCD in TTHXs.
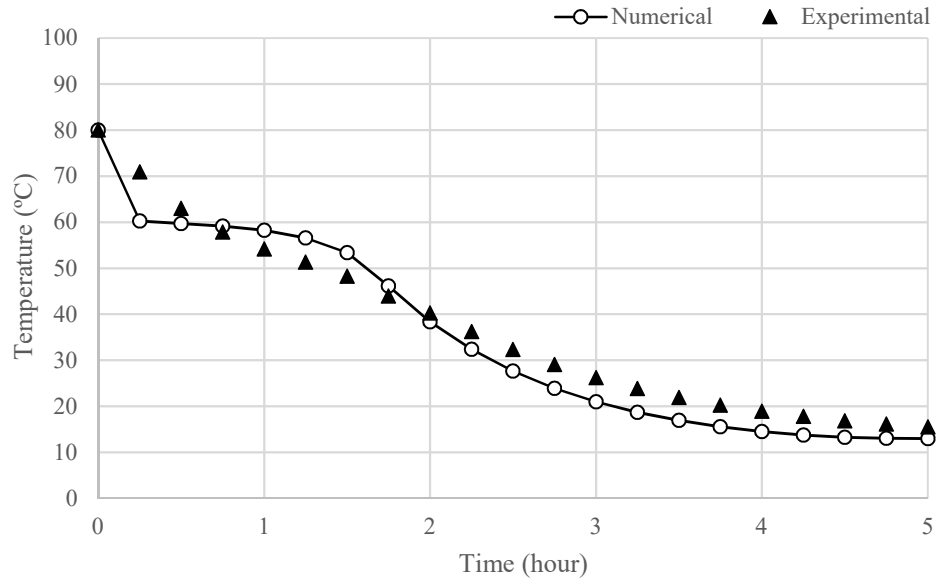
Figure 3.3: Comparison of the numerical and experimental temperatures for solidification

Chapter 4: Numerical investigation of heat transfer mechanism during SCD in a triplex tube heat exchanger

4.1 Introduction

According to Chapter 2, the main limitations of the literature include:

- In the investigated configurations with SCD, the solid PCM prevented heat transfer due to its higher thermal resistance. This could be tackled by means of a triplex tube heat exchanger due to the increased heat transfer area and more dominant natural convection,

- According to Table 2.1, the PCM was either charging or discharging and SCD in TTHXs has not been investigated so far,

- Many of the numerical studies considered some arbitrary radii for tubes in the investigated heat exchangers. However, commercial tubes follow sizing standards and as a result only specified tube radii are available in the market, and

- Detailed mathematical modeling and CFD simulation of the SCD process is a missing component in the literature.

In this chapter, simultaneous charging and discharging of latent heat thermal energy storage is numerically investigated in a triplex tube heat exchanger. The impact of natural convection in such a configuration is analyzed. Moreover, the effect of heat transfer mode is studied by comparing the results of internal-heating/external-cooling with those of internal-cooling/external-heating.

4.2 Materials and methods

In this section, the investigated TTHX dimensions, PCM properties, the initial and boundary conditions as well as analysis procedure are presented.

4.2.1 TTHX characteristics

The United States standard copper tube sizing approach was used in which "Type M" tubes are recommended for water heating purposes [53]. In the TTHX, the phase change material was surrounded in an annulus tube as shown in Figure 4.1. The heat exchanger had inner and middle tubes with nominal diameters of 2 in and 5 in, respectively. Therefore, the inner tube had a radius (r_i) of 25.51 mm and a thickness of 1.47 mm. The middle tube had a radius (r_o) of 62.32 mm with 2.77 mm of thickness.
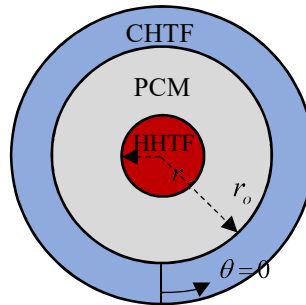
Figure 4.1: Schematic representation of the triplex tube heat exchanger

4.2.2 PCM thermophysical properties

A commercial PCM (RT31, Rubitherm Technologies GmbH) was considered for the investigation. Table 4.1 shows the thermophysical properties of the PCM, which filled the middle space in the TTHX as shown in Figure 4.1.

Table 4.1: Thermophysical properties of RT31 [54]

Property	Symbol	Value
Solidus temperature	T_s	300.15 K (27 °C)
Liquidus temperature	T_l	306.15 K (33 °C)
Solid density	ρ_s	880 kg/m^3
Liquid density	ρ_l	760 kg/m^3
Specific heat capacity	C_p	2,000 J/kg.K
Latent heat of fusion	λ	170,000 J/kg
Thermal conductivity	k	0.2 W/m.K
Thermal expansion coefficient	β	0.00076 1/K
Dynamic viscosity	μ	0.002508 kg/m.s

4.2.3 Initial and boundary conditions

According to the assumptions made earlier and Figure 4.1, the PCM was heated by the inner tube carrying hot heat transfer fluid (HHTF), while it was simultaneously cooled down by the cold heat transfer fluid (CHTF). Constant wall temperature values of 40 °C and 20 °C were assumed for the HHTF and CHTF, respectively. For internal-heating/external-cooling the HTF temperatures were swapped at inner and outer boundaries. The PCM was assumed to be initially fully melted or solidified depending on the case under investigation.

4.2.4 Analysis procedure

Prior to the analysis, grid size as well as time step size independency was checked for the numerical procedure. Three different grid resolutions of 2574, 4091 and 7930 cells were examined to check the independency on the liquid fraction. Also, three different time steps of 0.05 s, 0.1 s and 0.2 s were checked. Tables 4.2 and 4.3 show the liquid fraction for the three grid sizes and time steps. The liquid fraction values were

compared over 80 minutes of SCD. Since increasing the grid resolution from 4091 cells to 7930 cells did not significantly affect the liquid fraction, the former was selected to reduce the computational time. Therefore, a grid size of 4091 cells with a time step size of 0.1 s was selected for the simulation in order to achieve the momentum and energy equation convergence criteria of 10^{-3} and 10^{-5}, respectively.

Table 4.2: Grid size independency verification based on liquid fraction (time step size of 0.1 s)

Number of cells	300 s	600 s	1200 s	2400 s	4800 s
2,574	0.0238	0.0442	0.0918	0.1927	0.3632
4,091	0.0278	0.0540	0.1098	0.2283	0.3777
7,930	0.0312	0.0589	0.1153	0.2202	0.3854

Table 4.3: Time step size independency verification based on liquid fraction (4,091 cells)

Time step size	300 s	600 s	1200 s	2400 s	4800 s
0.05 s	0.0276	0.0537	0.1083	0.2228	0.3667
0.1 s	0.0278	0.0540	0.1098	0.2283	0.3777
0.2 s	0.0279	0.0542	0.1101	0.2302	0.3836

In this study, the primary focus is on the CCNC model during SCD. However, in order to clearly justify the effect of natural convection under SCD, the results for the individual heat transfer mode as well as SCD under the PC assumption are presented first. For the former case, the PCM was facing adiabatic condition on one side so as to observe how the heat source/sink individually affected the solid-liquid interface. Table 4.4 shows the considered cases. It should be noted that Cases 1 and 2 are common since they stand for an insulated shell and tube heat exchanger with PCM at the shell side. On the other hand, Cases 3 and 4 are not much practical and are only investigated to analyze the individual contribution of the heat source and heat sink, respectively.

Thereafter, the SCD results are presented for different heat transfer modes, i.e. internal-heating/external-cooling and internal-cooling/external-heating. Moreover, two different initial temperatures were assumed to analyze how natural convection affects the solid-liquid interface evolution. In other words, the effect of natural convection was examined for the cases, which were initially fully melted or fully solidified for different heat transfer modes (see Table 4.5). Figure 4.2 shows a graphic representation of the cases with their corresponding initial and boundary conditions.

Table 4.4: Investigated cases to separately analyze the effect of natural convection under individual heating/cooling

Case	Boundary condition	Initial condition
1	Internal-heating/external-adiabatic	Fully solidified
2	Internal-cooling/external-adiabatic	Fully melted
3	Internal-adiabatic/external-heating	Fully solidified
4	Internal-adiabatic/external-cooling	Fully melted

Table 4.5: Investigated cases for different heating/cooling modes and initial temperatures to analyze the effect of natural convection under SCD

Case	Boundary condition	Initial condition
5	Internal-heating/external-cooling	Fully solidified
6	Internal-heating/external-cooling	Fully melted
7	Internal-cooling/external-heating	Fully solidified
8	Internal-cooling/external-heating	Fully melted
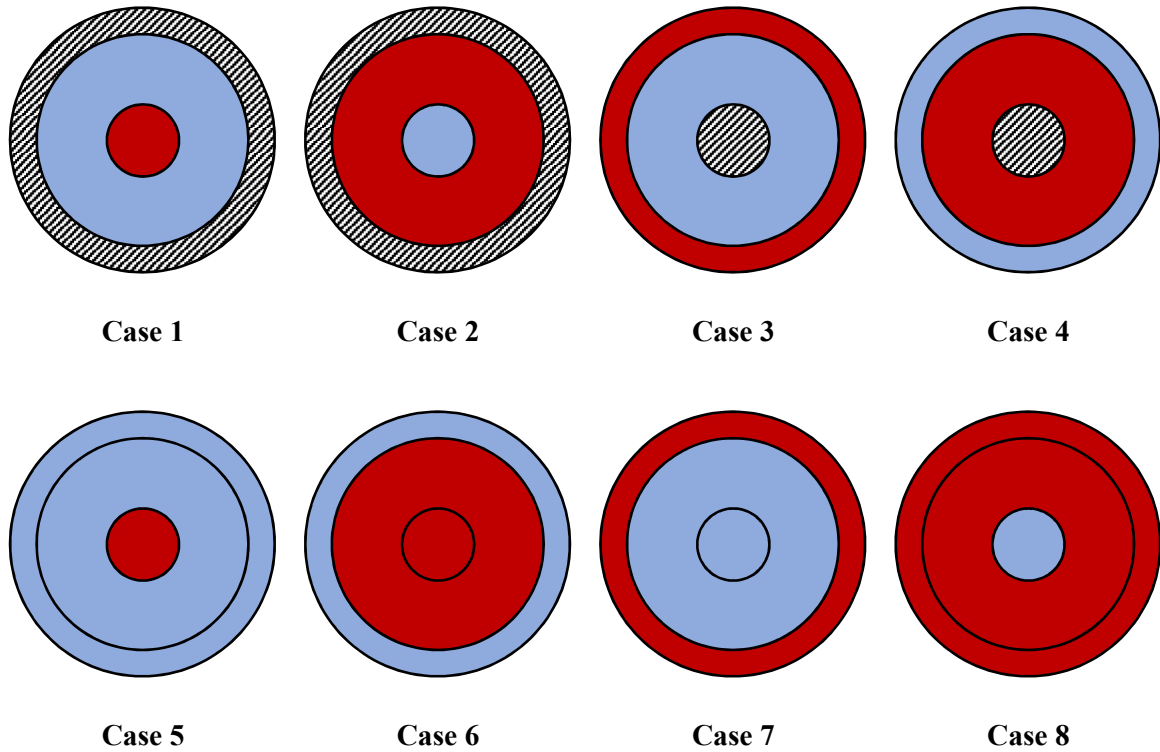
Figure 4.2: The investigated heat transfer modes and initial temperatures

4.3   Results and discussion

In this section, first, the effect of natural convection is analyzed for the heat sink and heat source separately, by imposing adiabatic boundary condition to the PCM (see Table 4.4). Thereafter, given the fact that many simplified models in the literature are based on the pure conduction assumption and ignore the effect of natural convection, SCD results are presented under the PC heat transfer mechanism. Thus, in order to understand the discrepancy of such an assumption with the reality, in this section, the four cases (see Table 4.5) are compared considering the PC model. Finally, the liquid fraction and temperature contours and heat transfer analysis of SCD are presented, using the CCNC model.

4.3.1 Separate analysis of natural convection

In order to better understand the effect of heat source/sink on the melting process, in this section, the results are categorized in two subsections of internal and external heat transfer, which is equivalent to the external and internal adiabatic boundary condition, respectively.

4.3.1.1 Internal heat transfer

Figure 4.3 presents the liquid fraction contours for the internal heat transfer mode. The contours on the left are for the case with internal heating of the initially fully solidified PCM (Case 1). According to the figure, after 5 minutes of melting, the melting front shape is almost circular. This is due to the fact that conduction is the dominant heat transfer mechanism at the early stages of melting. However, after a while, the melted PCM undergoes an upward motion due to the density change during the phase change process. This makes natural convection the dominant heat transfer mechanism. Clearly, natural convection greatly affected the upper half of the PCM due to the upward motion, while the lower half remained solidified. Therefore, once the upper half was completely melted (after about 90 minutes), the solid-liquid interface evolved much slower to the lower half of the PCM. Finally, it took a very long time to melt the remaining solid PCM.

The contours on the right-hand side (see Figure 4.3) show the solid-liquid interface evolution for the initially melted PCM under internal cooling. Unlike melting, the density of the PCM increases during solidification. Therefore, a weak downward cold PCM motion due to the natural convection during internal cooling affected the lower half of the PCM. Nevertheless, the circular melting front in the upper half of the PCM is evident and represents conduction as the dominant heat transfer mechanism. In fact, once the PCM is solidified, it cannot move anymore; hence, the heat transfer mechanism would remain pure conduction afterwards. Eventually, it would take a very long time to solidify the entire PCM domain due to the low thermal conductivity of the solid PCM that prevents heat transfer from the inner tube to the remaining liquid PCM. As confirmation to this, little solid-liquid interface evolution has been made after 60 minutes of internal cooling.
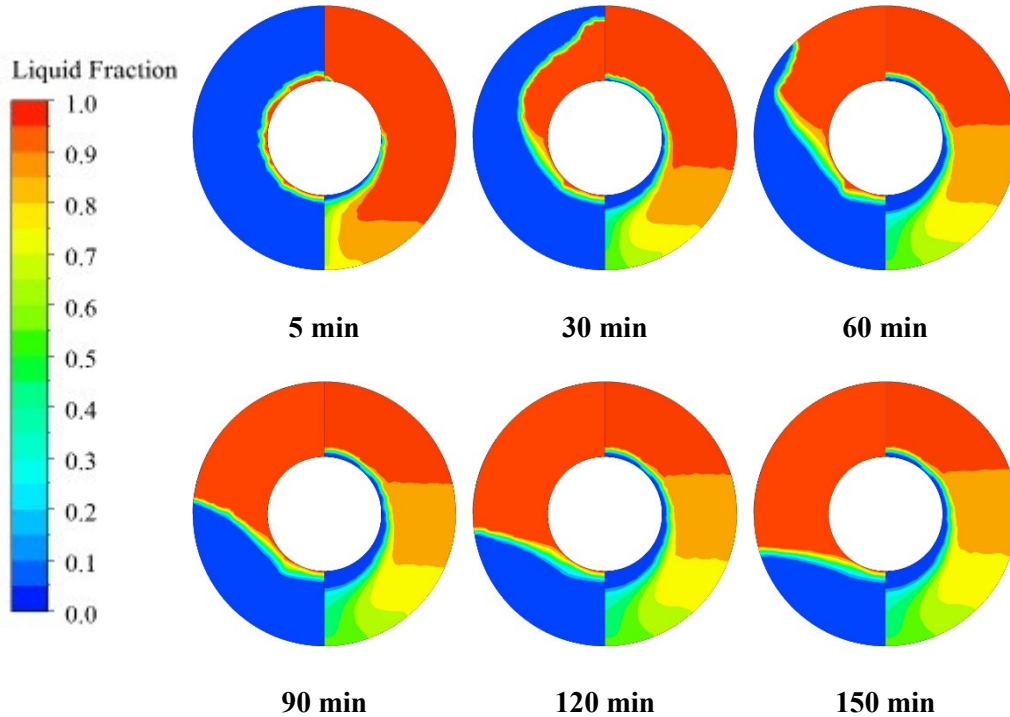
Figure 4.3: Liquid fraction contours for the externally adiabatic condition where each contour shows the initially solidified PCM under internal heating, Case 1 (left) and the initially melted PCM under internal cooling, Case 2 (right)

4.3.1.2　External heat transfer

Prior to the analysis, it is worth pointing out that it was expected the external heat transfer mode to have higher influence on the solid-liquid interface due to the higher heat transfer surface area. Left contours in Figure 4.4 show the melting front shape for the case of external heating of the initially solidified PCM (Case 3). As it is evident from the circular melting front, conduction was the dominant heat transfer mechanism at the early stages of the melting process. However, as the melting process continued, natural convection greatly affected the entire PCM domain. Again, the influence on the upper half was greater than the lower one due to the buoyancy-induced upward PCM motion. Surprisingly, the entire PCM domain was melted after 65 minutes, which shows the impact of natural convection. On the other hand, the initially melted PCM under external cooling (Case 4) underwent a completely different scenario (see right contours in Figure 4.4). At the very initial moments of the phase change process, conduction was the

28

dominant heat transfer mechanism. However, the downward solidifying PCM motion affected the PCM domain, especially the lower half. Thereafter, the conduction through the highly resistant solidified PCM close to the outer tube prevented further solid-liquid interface evolution. Therefore, similar to the case of internal cooling, it took a very long time to solidify the entire PCM domain under external cooling mode.
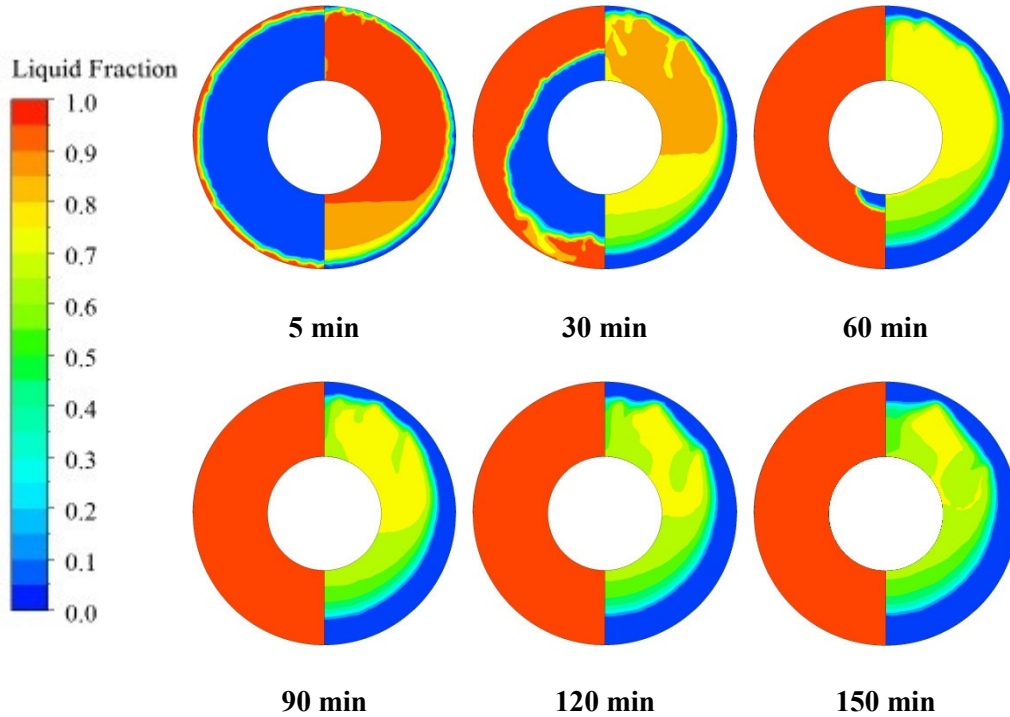
Figure 4.4: Liquid fraction contours for the internally adiabatic condition where each contour shows the initially solidified PCM under external heating, Case 3 (left) and the initially melted PCM under external cooling, Case 4 (right)

4.3.2   Pure conduction heat transfer mechanism

In the previous section, the impact of natural convection was illustrated during both melting and solidification processes. However, during the early stages of the phase change process and also inside the solid PCM, conduction is the main heat transfer mechanism. For a long period of time, it was believed that conduction was the dominant heat transfer mechanism during the phase change process. Therefore, there are some well-known modeling approaches, which ignore the effect of natural convection. In this

section, the results obtained for SCD are presented, intentionally neglecting the contribution of natural convection, i.e. the PC model.

Figures 4.5 and 4.6 show the solid-liquid interface evolution over time if conduction was the only heat transfer mechanism. Circular melting front shape is clearly observable in these contours. In left contours of Figure 4.5, the PCM was initially solidified and it was facing internal-heating/external-cooling (Case 5). Therefore, the interface departed from the inner tube growing towards the outer one. For the case of the initially melted PCM under internal-cooling/external-heating (Case 8) the melting front also behaves in the same manner (see the right contours). Comparing the contours on the right with those on the left in Figure 4.5, it is clear that assuming pure conduction during SCD results in no difference between these cases from the viewpoint of solid-liquid interface evolution. This is due to the fact that the thermal conductivity of PCM was almost constant during the phase change, resulting in identical thermal resistance for both cases.
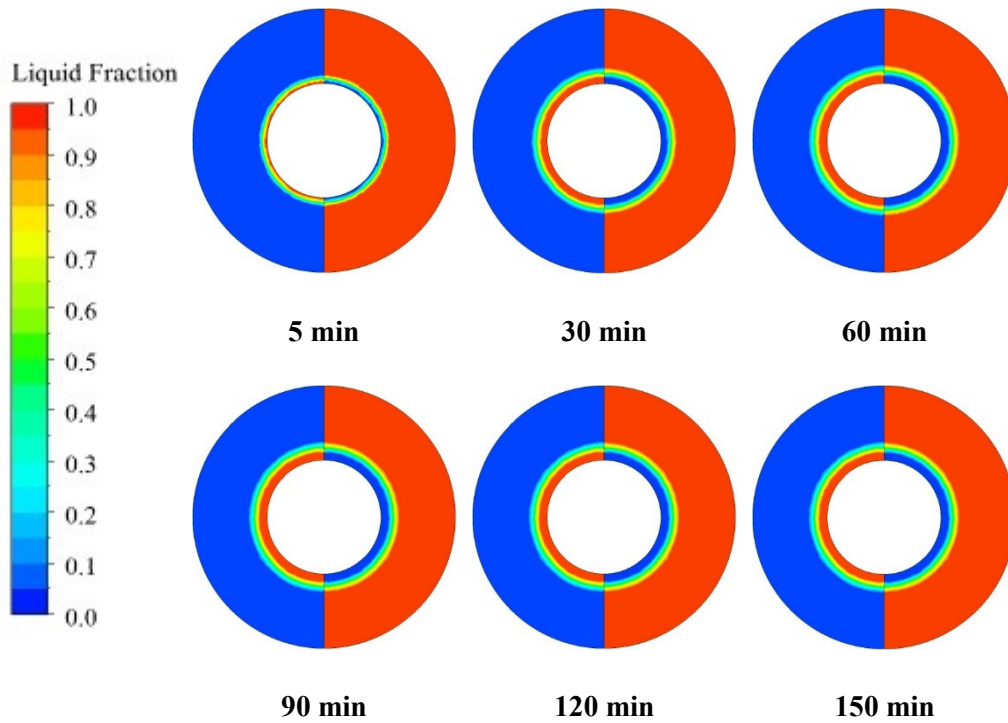
Figure 4.5: Liquid fraction contours where each contour shows the initially fully solidified PCM under internal-heating/external-cooling, Case 5 (left) and the initially fully melted PCM under internal-cooling/external-heating, Case 8 (right)

Figure 4.6 compares the liquid fraction contours of the initially melted PCM under internal-heating/external-cooling (Case 6) (on the left) with those of the initially solidified PCM under internal-cooling/external-heating (Case 7) (on the right). In such cases, the solid-liquid interface initiates from the outer tube and evolves towards the inner one. As before, due to the low thermal conductivity of the PCM, the circular melting front evolved slowly over time reaching a shape different from the one shown in Figure 4.5.
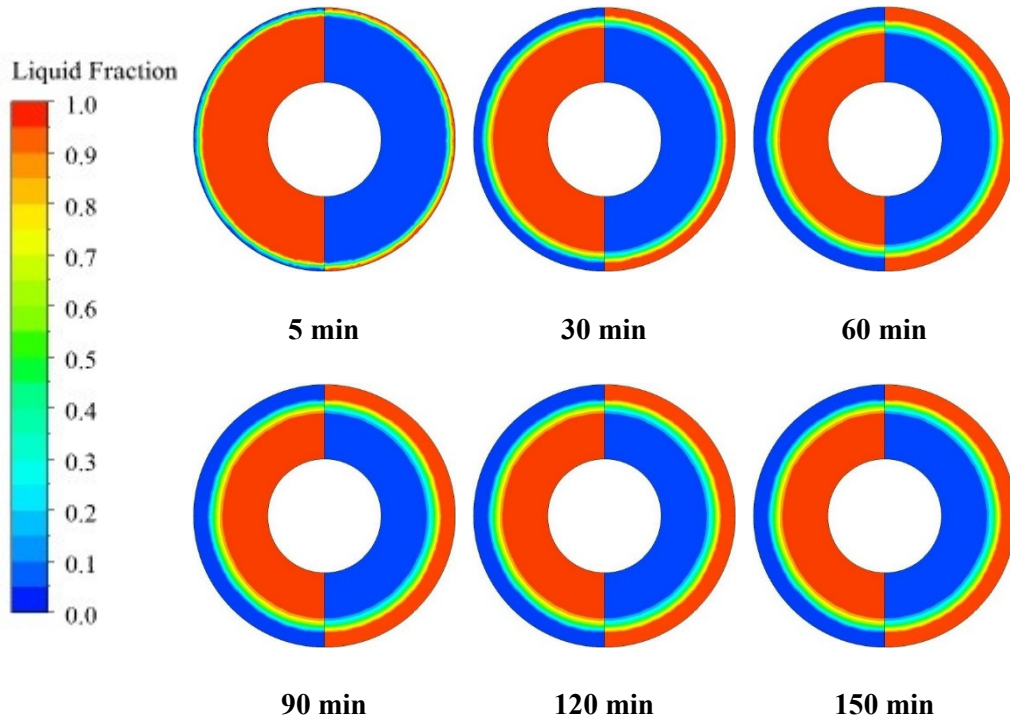
Figure 4.6: Liquid fraction contours where each contour shows the initially fully melted PCM under internal-heating/external-cooling, Case 6 (left) and the initially fully solidified PCM under internal-cooling/external-heating, Case 7 (right)

4.3.3 Solid-liquid interface evolution under SCD

In the case of SCD, a fully charged or fully solidified state would not be reached at the end of the process. Instead, a steady state is reached when neither the melting from the heat source nor the solidification from the heat sink can prevail. Therefore, the simulations were run until the steady state is reached, i.e. the moment when no changes would occur in the solid-liquid interface position. In this section, the liquid fraction and temperature contours are presented for the cases in Table 4.5.

4.3.3.1 Internal-heating/external-cooling

Figures 4.7 and 4.8 show the liquid fraction and temperature results for the internal-heating/external-cooling mode for the initially fully solidified (Case 5) and fully melted PCMs (Case 6), respectively. It is worth pointing out that these cases are similar to a combination of Cases 1 and 4 (see the left contours in Figure 4.3 and the right contours in

Figure 4.4). From Figure 4.7, it is clear that at the early stages of the phase change process, conduction was the dominant heat transfer mechanism resulting in a circular melting front shape. In addition, the bottom half of the PCM remained solid primarily due to the upward motion of the melted PCM and not as much by the cooling from the outer tube (see Figure 4.3, left contours). On the other hand, the upper half was affected by the melted PCM motion resulted by the heating from the inner tube. The melted PCM could desirably approach to the outer cold tube, enabling low resistance heat transfer through the thin solid PCM.
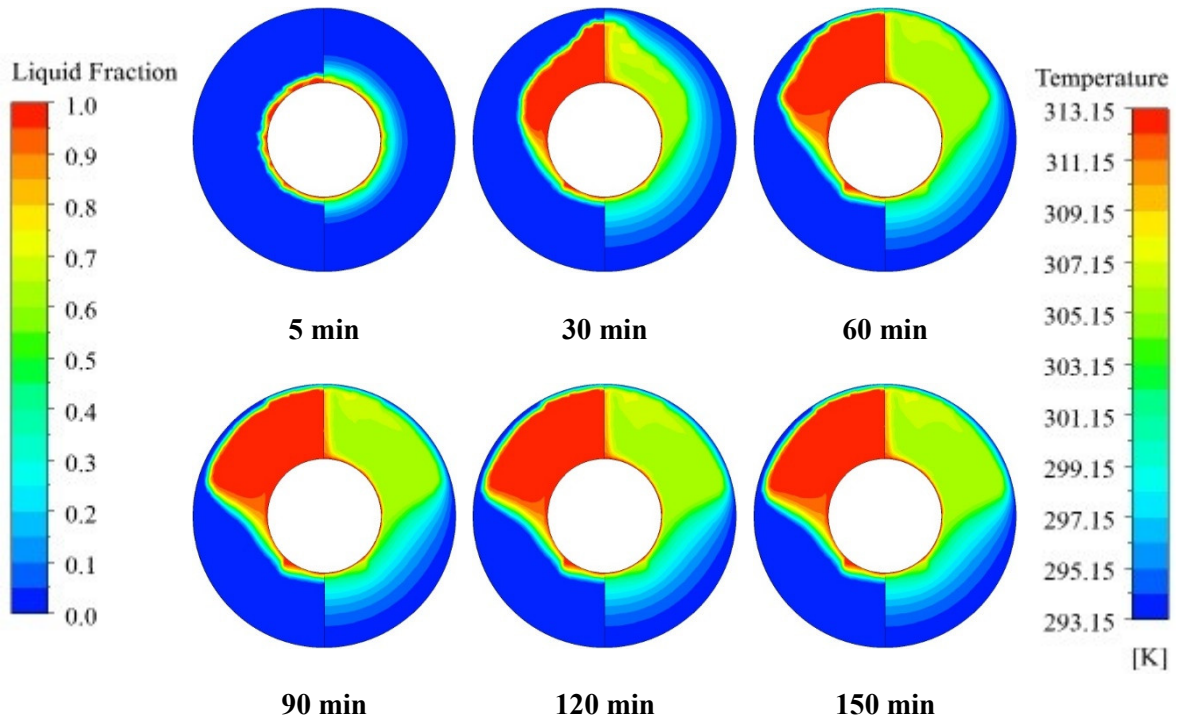
Figure 4.7: Liquid fraction (left) and temperature (right) contours for the initially fully solidified PCM inside the TTHX under internal-heating/external-cooling (Case 5)

In Figure 4.8, the melted PCM could touch the upper part of outer tube, which shows direct heat transfer between the melted PCM and the heat sink. In addition, in the lower half, cooling by the heat sink solidified the adjacent PCM but could not influence the melted PCM deeply, which could be attributed to the low thermal conductivity of the solidified PCM. Comparing the lower half of liquid fraction contours in Figure 4.8 with

those of the right contours in Figure 4.4 (Case 4), it is clear that the impact of melting by the heat source on the lower half of the PCM was almost negligible except for the PCM close to the inner tube. This could be attributed to the upward melted PCM motion, solely affecting the upper half. Interestingly, similar to Case 4, the solidification process continued to affect the lower half of the PCM very slowly over time, while the upper half reached a steady state melting front shape quickly. This shows how unrealistic it would be to neglect the effect of natural convection (see the left contours in Figure 4.6).
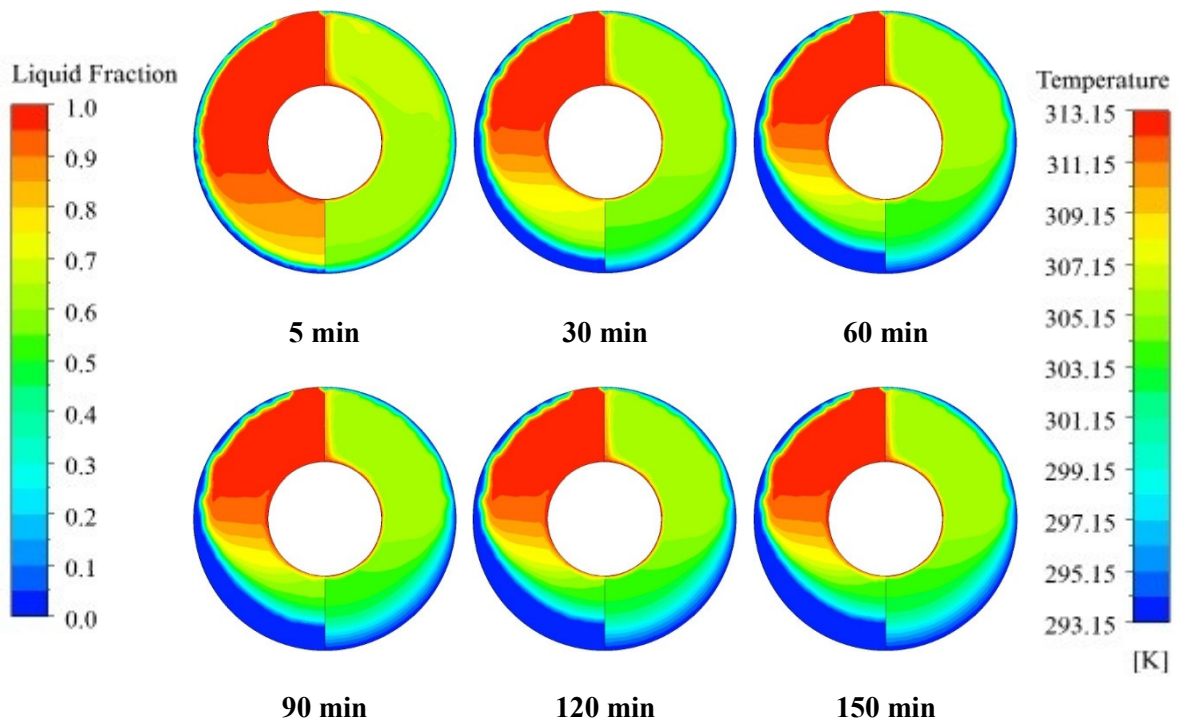
Figure 4.8: Liquid fraction (left) and temperature (right) contours for the initially fully melted PCM inside the TTHX under internal-heating/external-cooling (Case 6)

4.3.3.2   Internal-cooling/external-heating

The liquid fraction and temperature contours for the internal-cooling/external-heating mode for the initially fully solidified (Case 7) and fully melted (Case 8) PCMs are shown in Figures 4.9 and 4.10, respectively. It is worth pointing out that these cases are similar to a combination of Cases 2 and 3 (see the right contours in Figure 4.3 and the left contours in Figure 4.4). Figure 4.9 shows how the buoyancy-induced upward melted

PCM motion affected the entire domain and melted the solid PCM around the inner tube. However, comparing this figure with the left contours in Figure 4.4 one can see that the heat sink could maintain the adjacent PCM in its solid state, preventing it from being melted. Therefore, in such a scenario, the heat transfer from the melted PCM towards the heat sink occurs by conduction through the thin solid PCM layer. It is worth mentioning that even though a great portion of the PCM was melted, the temperature contours show a cold region on the lower half of the PCM. This should be expected from the right contours in Figure 4.3 displaying the downward motion of the high density cold PCM. This shows that the inner tube could only affect the lower half of the PCM sensibly.
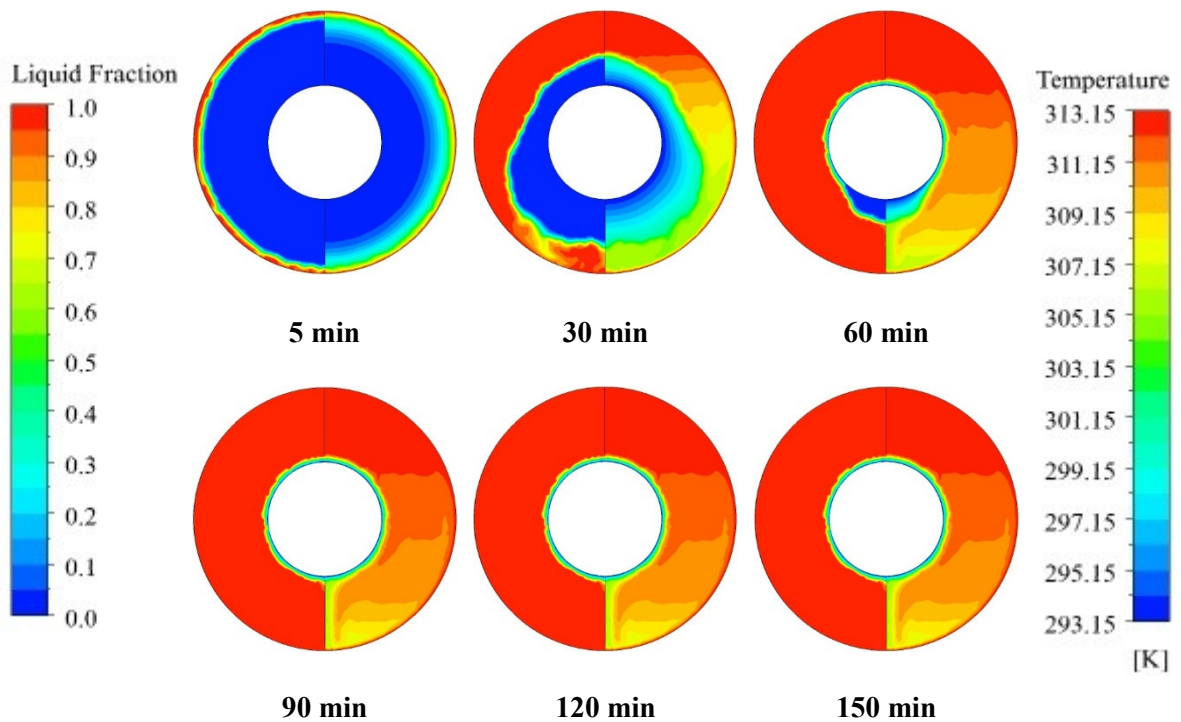
Figure 4.9: Liquid fraction (left) and temperature (right) contours for the initially fully solidified PCM inside the TTHX under internal-cooling/external-heating (Case 7)

Figure 4.10 shows the same heating mode for the initially fully melted PCM. In such a scenario, due to the continuous upward PCM motion, the heat sink could not even solidify the adjacent PCM layer close to the inner tube. In fact, the motion of the PCM prevented such solidification by sweeping the PCM off the inner tube before it become stationary. Therefore, for the upper half of the domain, direct heat transfer desirably occurred between the melted PCM and the heat sink. Instead, the lower half of the system

was affected more than Case 7 by the downward cold PCM motion. The direction of the PCM motion due to heating is clear in the liquid fraction contour and could be completely understood by comparing it to the right contours in Figure 4.3. From the view point of SCD, this scenario is greatly beneficial in providing instantaneous heating from the supply side to the demand side due to the low resistance heat transfer from the heat source to the heat sink.
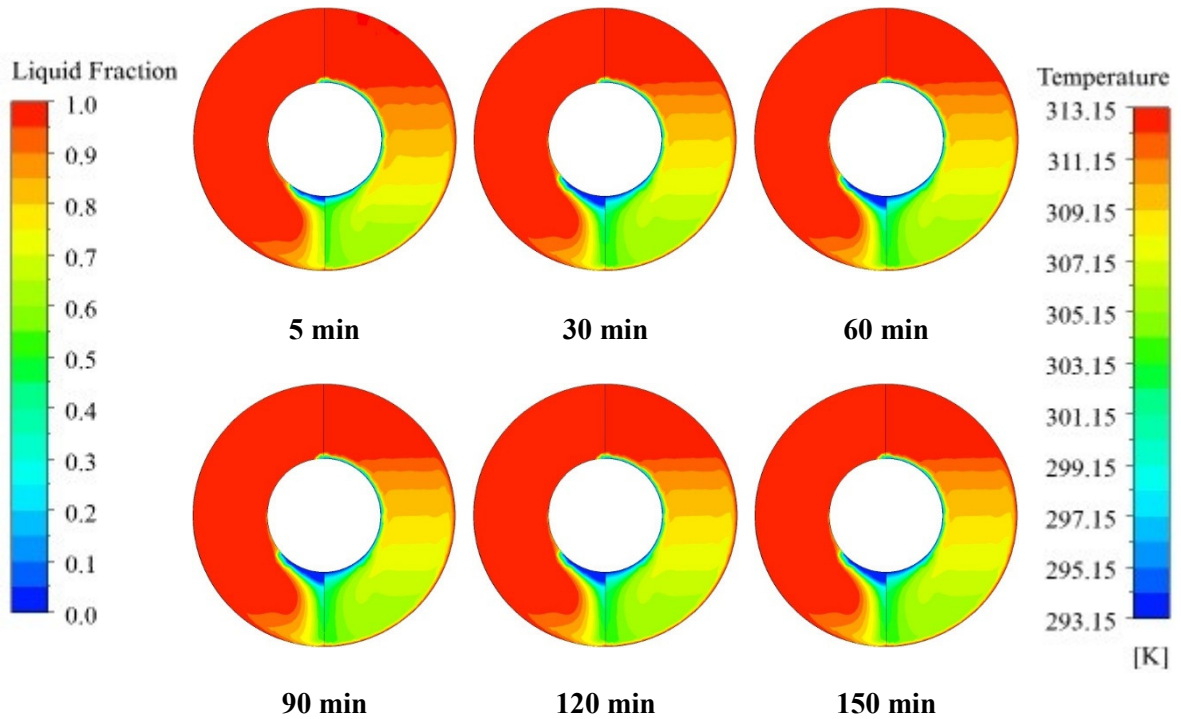
Figure 4.10: Liquid fraction (left) and temperature (right) contours for the initially fully melted PCM inside the TTHX under internal-cooling/external-heating (Case 8)

4.3.4   Heat transfer analysis

Figure 4.11 shows the liquid fraction variation over time for cases with adiabatic boundary condition. The solid and dotted lines show the solidification and melting processes, respectively. Comparing the slope of the lines, it is clear that generally melting process is faster than solidification. As mentioned, this is basically due to the slow heat transfer from the heat sink towards the PCM through a high resistance solid layer adjacent to the heat sink. In addition, the bold lines are for internal heat transfer, while

the regular lines are for external heat transfer. The figure demonstrates that regardless of the process, the external heat transfer occurs faster, which is due to the higher heat transfer area. These findings for adiabatic boundary condition are helpful for realizing the individual effect of the heat source/sink on the PCM during SCD.
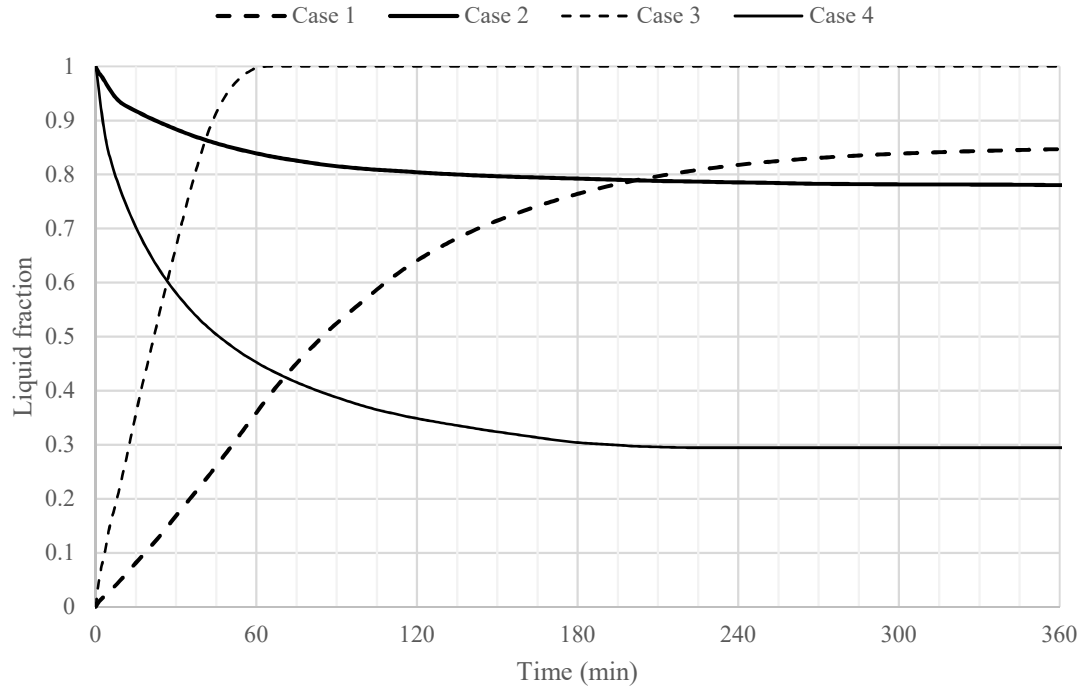
Figure 4.11: Liquid fraction variation versus time for cases with adiabatic boundary condition
(see Table 4.4)

Figure 4.12 shows the variation of liquid fraction for the cases under SCD. The black lines correspond to the CCNC model, while the gray lines are for the PC assumption. A very significant result from the figure is that the lengths l_1 and l_2 are identical. This means that under pure conduction assumption the magnitude of liquid fraction variation from the initial value to the steady one for the initially melted PCM under internal-cooling/external-heating (Case 8) is equal to the one for the initially solidified PCM under internal-heating/external-cooling (Case 5). Likewise, the same situation is correct for the lengths l_3 and l_4 for Cases 6 and 7. This is attributed to the identical thermal resistances ahead of heat transfer path through the PCM. However, the

melted PCM motion by buoyancy forces impacts the phase change process and the figure shows how the impact varies for different cases. A closer look to the figure reveals that the heat transfer enhancement by natural convection is greater for Cases 5 and 7, which are initially solidified PCMs under SCD. Numerically, a comparison between the steady liquid fraction and temperature values based on these models is shown in Table 4.6. It is shown that the simple pure conduction model could be applied to the initially melted PCMs under SCD with small error.
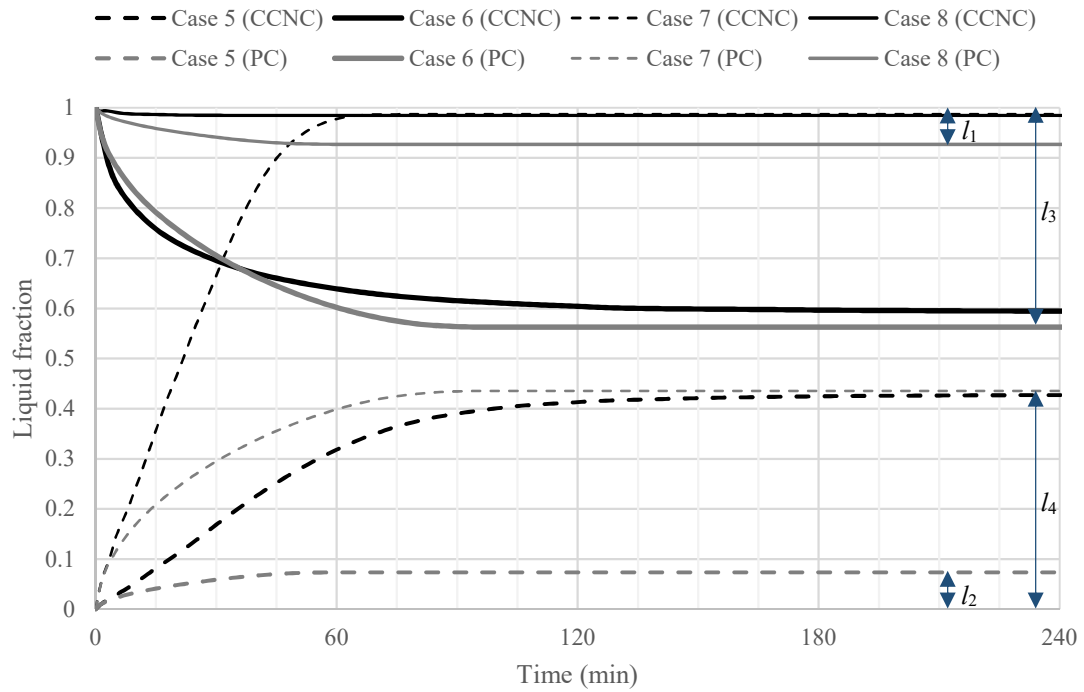
Figure 4.12: Liquid fraction variation versus time for cases under SCD assuming combined conduction and natural convection (CCNC, black lines) and pure conduction (PC, gray lines)

Table 4.6: Comparison between pure conduction model steady state results with those of combined conduction and natural convection

Model	Case 5		Case 6		Case 7		Case 8	
	T (°C)	γ	T (°C)	γ	T (°C)	γ	T (°C)	γ
CCNC model	300.56	0.4278	302.81	0.5925	311.28	0.9870	309.34	0.9847
PC model	296.33	0.0736	303.36	0.5628	302.93	0.4355	309.99	0.9271
Absolute error	**4.23**	**0.3542**	**0.55**	**0.0297**	**8.35**	**0.5515**	**0.65**	**0.0576**

4.4 Concluding remarks

This chapter presented the numerical investigation results for simultaneously charged and discharged PCM with different heat transfer modes and different initial conditions. Eight cases were compared showing the effect of natural convection on the phase change process. The most important findings are:

- For the case of internal-heating/external-cooling, the natural convection did not affect the lower half of the system; however, the upper half was affected by the upward melted PCM motion due to the buoyancy forces (natural convection). On the other hand, for the case of internal-cooling/external-heating, the buoyancy-induced upward PCM motion affected the entire domain.

- Depending on the initial condition of the PCM, different liquid fraction, temperature and solid-liquid interface locations were observed, which was totally different from the results obtained from the pure conduction model. This shows how unrealistic is such an assumption and to have accurate modeling of SCD, natural convection should be taken into account.

- Comparing the steady state temperature and liquid fraction results, it was found that the pure conduction model could be applied to the initially fully melted PCMs under SCD with small error, but for the initially solidified PCMs neglecting the natural convection would result in unacceptably high error.

Chapter 5: Heat transfer enhancement of PCMs by fins under SCD

5.1 Introduction

According to Chapter 2, the main limitations of the literature include:

- In the investigated configurations with SCD, the solid PCM prevented heat transfer due to its higher thermal resistance. This could be tackled by means of longitudinal fins inside a TTHX due to the increased heat transfer surface area and more dominant natural convection,

- According to Table 2.1, the PCM was either charging or discharging and SCD in TTHXs has not been investigated so far,

- Natural convection suppression occurred in several earlier studies with fins due to ignoring the mechanism of buoyancy-driven upward melted PCM motion, and

- Several finned configurations have been investigated with latent heat thermal energy storage in PCMs. Nevertheless, to the best of the author's knowledge, none of the studies focused on the SCD process.

In Chapter 4, a model was developed and validated with experimental data to study the heat transfer mechanism of the phase change process under SCD in a horizontal TTHX. It was found that for both initially melted and solidified PCMs under internal-heating/external-cooling, the upward melted PCM motion solely affected the upper half of the domain. On the other hand, the lower half remained solid with high thermal resistance, preventing effective heat transfer. Therefore, in this chapter, application of finned tubes is investigated to enhance the heat transfer inside a TTHX. First, three conventional fin configurations for non-SCD applications in TTHXs (from the literature) are studied to investigate their effectiveness under SCD. Thereafter, six configurations are developed, which are then analyzed for both SCD and non-SCD conditions. Finally, the effect of fin geometry including their number, length, and thickness are investigated under SCD.

5.2 Materials and methods

In this section, the investigated TTHX dimensions, PCM properties, and analysis procedure are presented.

5.2.1 TTHX characteristics

In this study, the United States standard copper tube sizing approach was used in which "Type M" tubes are recommended for water heating applications [53]. The heat exchanger (Figure 5.1) had inner, middle and outer tubes with nominal diameters of 2, 5 and 8 in, respectively. Table 5.1 shows the dimensions of the tubes in the investigated TTHX.
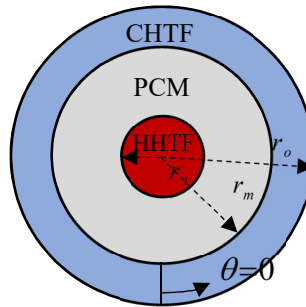
Figure 5.1: Schematic representation of the triplex tube heat exchanger

Table 5.1: Dimensions of the tubes in the TTHX [53]

Tube	Nominal diameter (in)	Inner radius (mm)	Thickness (mm)
Inner	2	25.51	1.47
Middle	5	62.32	2.77
Outer	8	98.89	4.32

5.2.2 PCM thermophysical properties

A commercial PCM (RT31, Rubitherm Technologies GmbH) was used in this study. Table 5.2 shows the thermophysical properties of the PCM, which filled the middle space in the TTHX as shown in Figure 5.1.

Table 5.2: Thermophysical properties of RT31 [54]

Property	Symbol	Value
Solidus temperature	T_s	300.15 K (27 °C)
Liquidus temperature	T_l	306.15 K (33 °C)
Solid density	ρ_s	880 kg/m^3
Liquid density	ρ_l	760 kg/m^3
Specific heat capacity	C_p	2,000 J/kg.K
Latent heat of fusion	λ	170,000 J/kg
Thermal conductivity	k	0.2 W/m.K
Thermal expansion coefficient	β	0.00076 1/K
Dynamic viscosity	μ	0.002508 kg/m.s

5.2.3 Analysis procedure

Table 5.3 shows the considered conventional fin configurations. Case 1 was the base case with no fins. Case 2 had two vertical external (over cold tube) and two horizontal internal (over hot tube) fins, while Cases 3 and 4 had 4 fins. It should be noted that the fin configuration of Case 4 was a rotation of that of Case 3 by 45°.

Table 5.3: Characteristics of conventional fin configurations

Case	No. of internal fins	No. of external fins	Fin length (mm)	Fin thickness (mm)
1	0	0	–	–
2	2	2	30	1
3	4	4	30	1
4	4	4	30	1

In order to reduce the natural convection suppression by fins in the horizontal thermal storage system, fins should be allocated on the lower and upper halves of the hot inner tube and cold outer tube, respectively. Based on this, six fin geometries have been developed as tabulated in Table 5.4. Since the outer tube has a larger heat transfer surface area compared to that of the inner one, initially internal fins were considered only (Cases 5-7). Then, Cases 8-10 were developed with fixed 3 internal fins of Case 7 but different external ones. Figure 5.2 shows schematic representations of all cases.

Table 5.4: Characteristics of the developed configurations

Case	No. of internal fins	No. of external fins	Fin length (mm)	Fin thickness (mm)
5	1	0	30	1
6	2	0	30	1
7	3	0	30	1
8	3	1	30	1
9	3	3	30	1
10	3	5	30	1
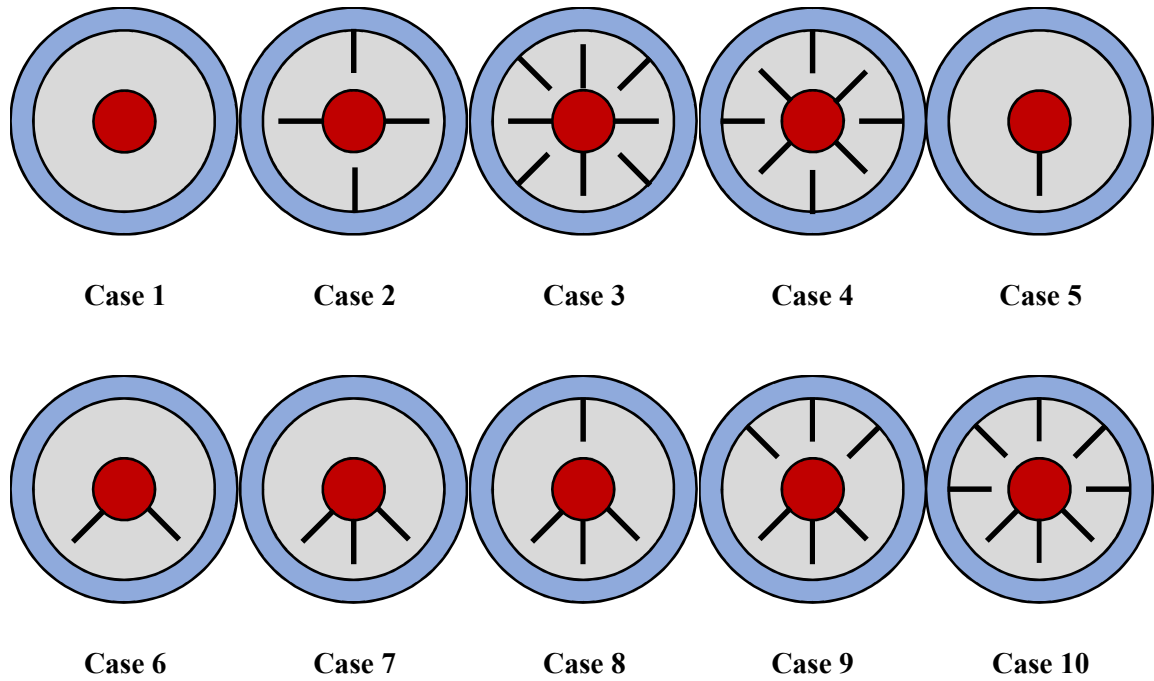
Figure 5.2: Schematic representation of the investigated cases

In order to conduct a comprehensive evaluation of both developed and conventional fin configurations, three different scenarios were investigated; (1) non-SCD with single side heat transfer, (2) non-SCD with both sides heat transfer and (3) SCD only. Figure 5.3 shows schematic representations of the scenarios, where the blue and red colors represent temperatures equal to the CHTF and HHTF, respectively. Furthermore, the dashed lines represent adiabatic boundary conditions.
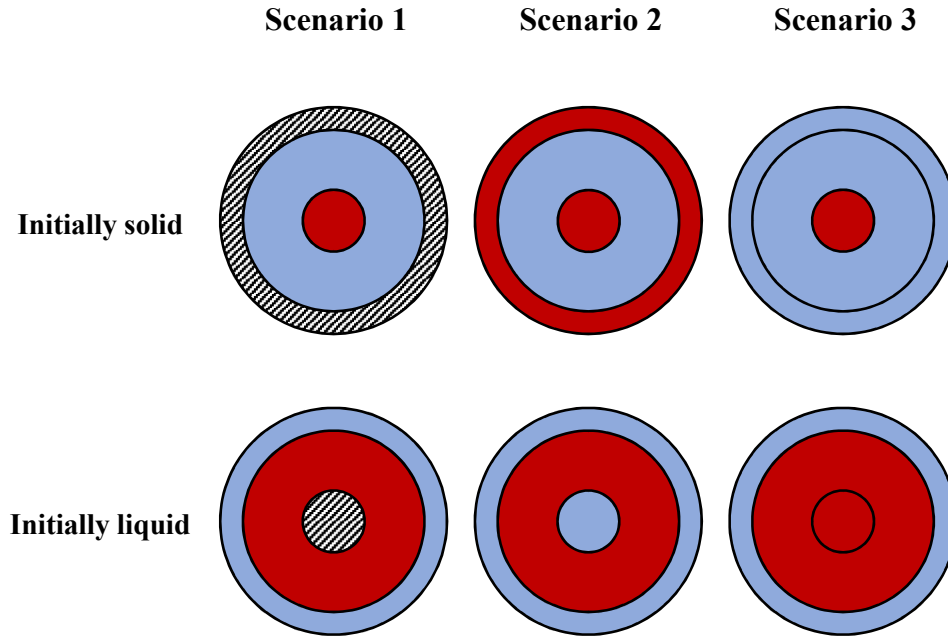
Figure 5.3: Schematic representation of the considered scenarios

In order to analyze the effect of fin length, four lengths of 10, 20, 30 and 33 mm were selected (see Table 5.5). As shown in the table, the effect of fin length was examined for Case 10 (highlighted by bright gray). Finally, the effect of fin thickness was examined for Case 14 (highlighted by dark gray) for thicknesses of 0.5, 1, 2 and 4 mm (see Table 5.6). The reason to select these cases was that they benefit from the maximum number of fins, both internal and external, simplifying the comparison among the cases with different lengths and thicknesses.

Table 5.5: Investigated cases to analyze the effect of fin length

Case	No. of internal fins	No. of external fins	Fin length (mm)	Fin thickness (mm)
11	3	5	10	1
12	3	5	20	1
13	3	5	30	1
14	3	5	33	1

Table 5.6: Investigated cases to analyze the effect of fin thickness

Case	No. of internal fins	No. of external fins	Fin length (mm)	Fin thickness (mm)
15	3	5	33	0.5
16	3	5	33	1
17	3	5	33	2
18	3	5	33	4

5.3 Results and discussion

Under SCD conditions, a fully melted or fully solidified state is not reached at the end of the phase change process. Instead, a steady state condition is reached when neither the melting from the heat source nor the solidification from the heat sink can prevail. Therefore, the simulations were run until the steady state condition was reached, i.e. the moment when changes would no longer occur in the solid-liquid interface position.

In this section, first, conventional fin geometries are analyzed under SCD for both initially solid and initially liquid PCM conditions. Thereafter, the developed fin geometries, which are compatible with natural convection, are also examined under SCD for the same initial conditions. Then, the performance of all configurations is investigated under non-SCD conditions. Finally, the proper geometrical fin design for each application (SCD or non-SCD) is identified.

5.3.1 Analysis of conventional fin configurations under SCD conditions

In earlier studies, the two fluids (HTFs) that flowed inside the inner and outer tubes of a TTHX had the same temperature and were used either to charge the storage or discharge it. Therefore, the PCM faced either heating or cooling from its both sides. However, as presented earlier, the PCM might undergo SCD conditions. In this section, the performance of conventional fin configurations is presented under SCD. According to Chapter 4, the final PCM condition under SCD was found to be different depending on

the initial PCM status, i.e. initially solid or liquid. Therefore, in this section, the results are presented for both cases.

5.3.1.1   Initially solid

Figure 5.4 shows the liquid fraction (left) and temperature (right) contours for such conditions. Since the PCM was initially solid, the heat transfer began by melting the solid PCM around the hot tube. The figure shows that the integration of fins enhanced the heat transfer within the solid PCM; however, the magnitude of impact was different. The more the number of fins, the higher was the amount of melted PCM after certain duration. Interestingly, comparing Cases 3 and 4 it was concluded that the angled inner fin configuration (Case 4) was greatly different from the non-angled one (Case 3). This was due to the presence of internal fins on the lower half of the system where natural convection was developed above the fins, which would otherwise remain solid for a long period of time during the phase change process (see Case 1). Besides, the angled configuration created a region at the lower half close to the inner tube where the PCM remained melted, enhancing the heat transfer to the solid PCM.

Case 1   Case 2   Case 3   Case 4

Liquid Fraction

1.0
0.9
0.8
0.7
0.6
0.5
0.4
0.3
0.2
0.1
0.0

Temperature

313.15
311.15
309.15
307.15
305.15
303.15
301.15
299.15
297.15
295.15
293.15

[K]

5 min

30 min

60 min
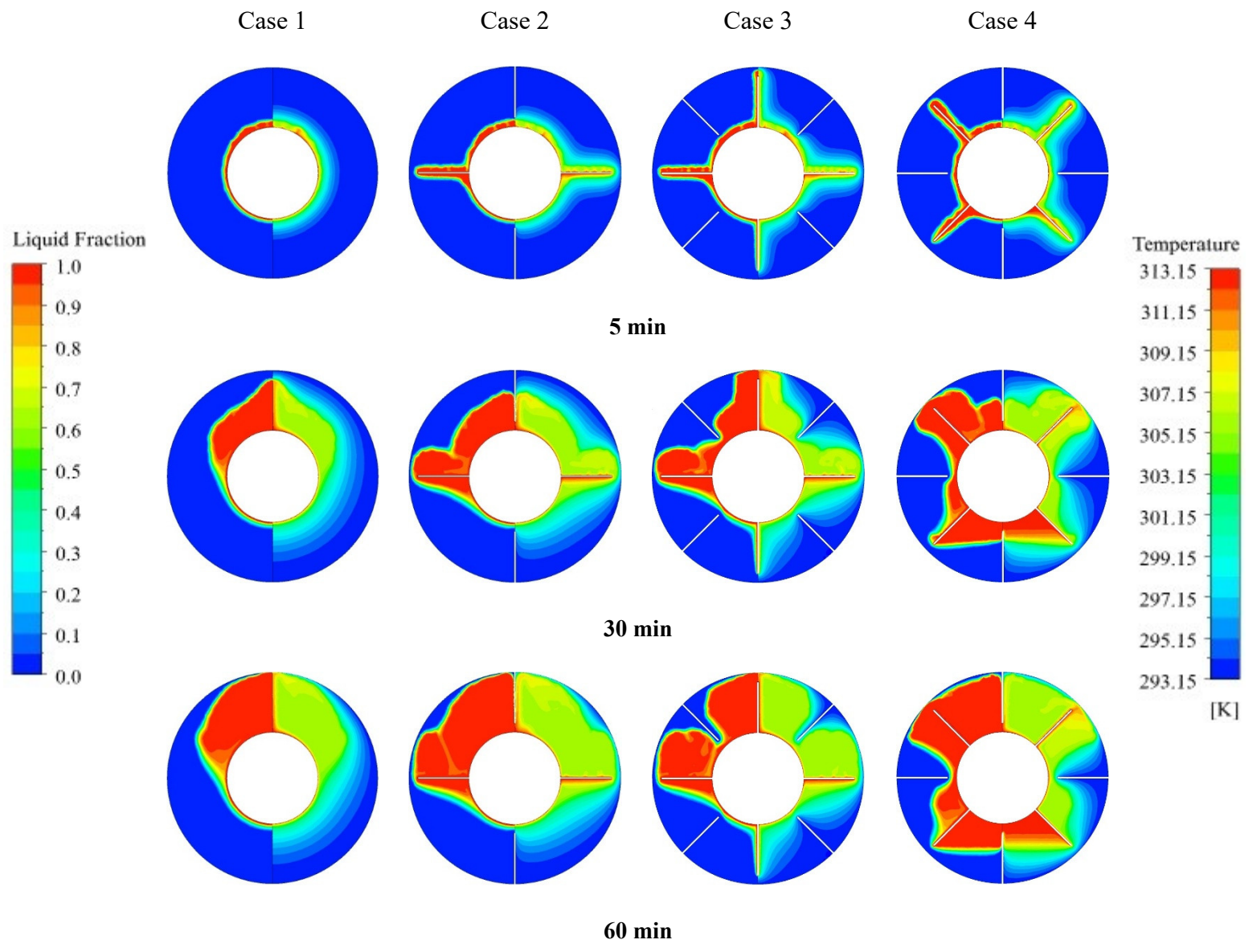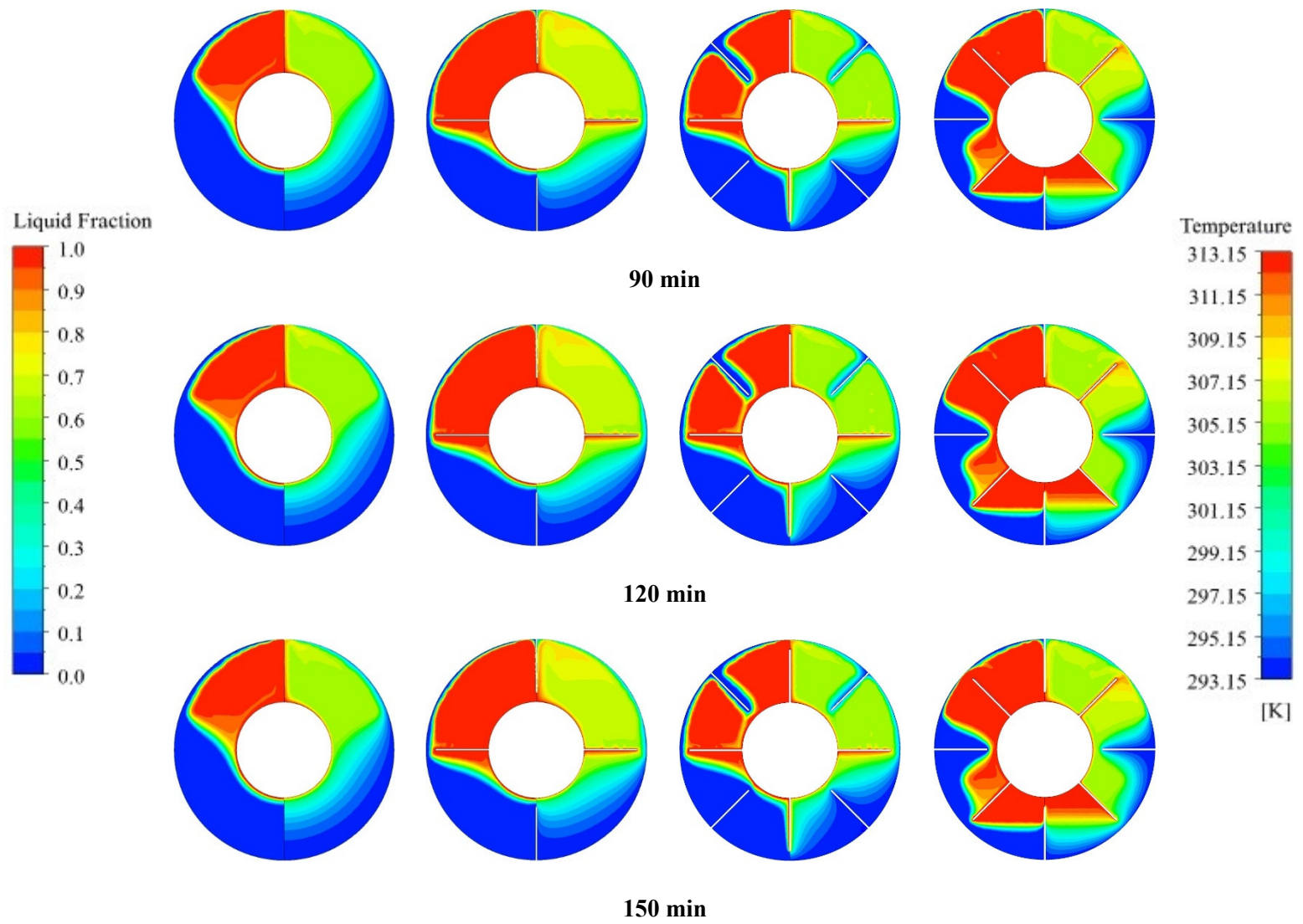
Figure 5.4: Liquid fraction (left) and temperature (right) contours for the conventional fin configurations with initially solid PCM under SCD

5.3.1.2　Initially liquid

Figure 5.5 shows the liquid fraction (left) and temperature (right) contours of Cases 1-4 for initially liquid PCM. As the PCM was already liquid at the beginning of the phase change process, the natural convection was established sooner than the cases with initially solid PCM. Over time, solid PCM was deposited on the cold external tube. However, due to the continuous buoyancy-driven hot liquid PCM motion at the upper half of the system, the solid deposition was greater on the lower half.
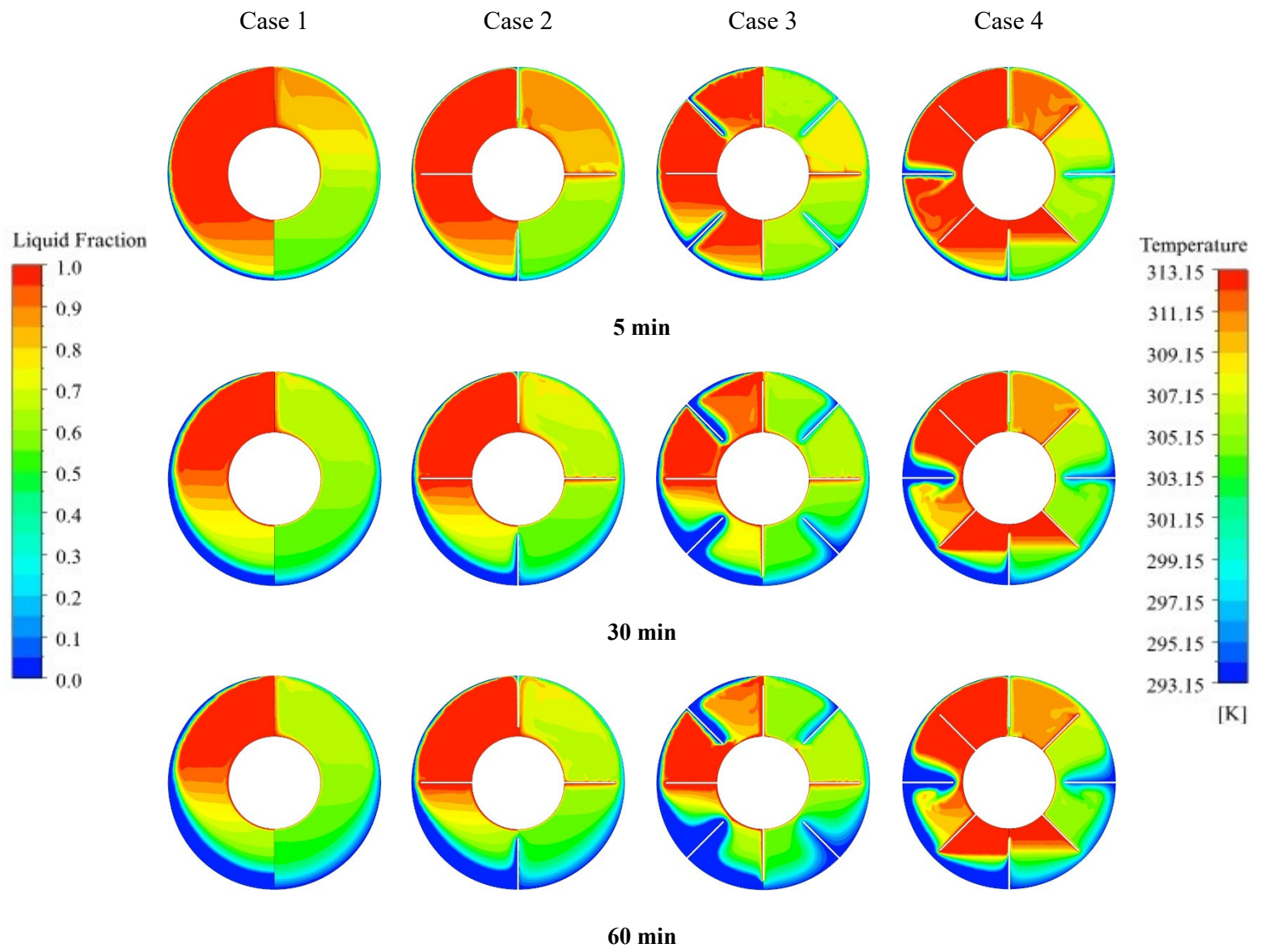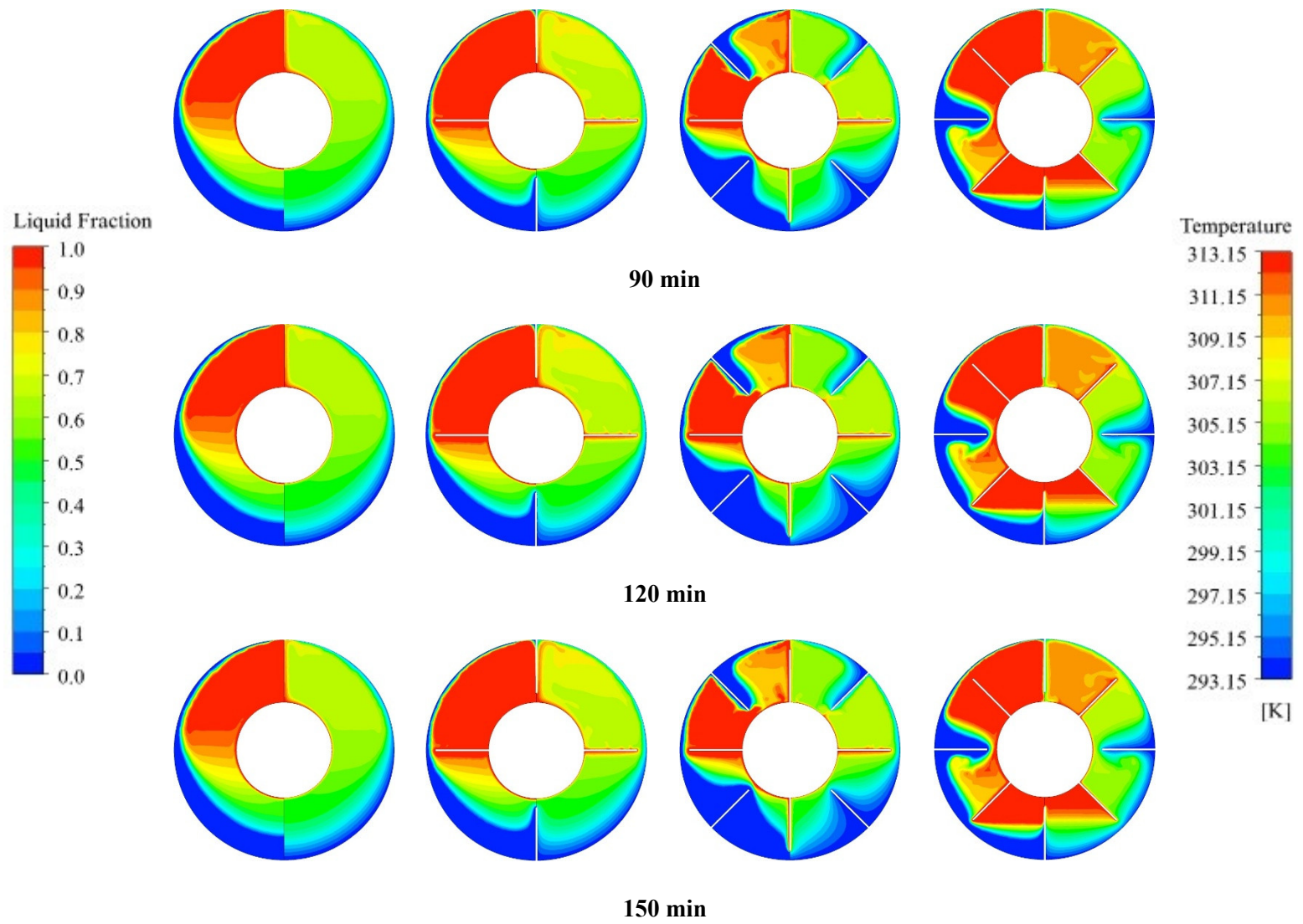
Figure 5.5: Liquid fraction (left) and temperature (right) contours for the conventional fin configurations with initially liquid PCM under SCD

5.3.1.3   Comparison

Comparing the contours in Figures 5.4 and 5.5 after 150 minutes of SCD, it was concluded that integration of fins enhanced the heat transfer. Moreover, for both initial conditions, the solid-liquid interfaces after 150 minutes were almost the same for Cases 3 and 4. However, in Chapter 4 (without fins) it was revealed that the final solid-liquid interface position depended on the initial PCM condition; i.e. solid or liquid (compare the contours for Case 1 in Figures 5.4 and 5.5). This difference was due to the fact that fins enhanced heat transfer, especially through the highly resistance solid PCM. For Case 1, which lacked this enhancement, the low thermal conductivity of the PCM prevented effective heat transfer between the heat source and heat sink.

Three key parameters should be considered to evaluate the performance of a thermal storage under SCD: (1) the steady state time (or stabilization time), which is the time required to achieve the steady state condition under SCD, (2) the steady liquid fraction value, which represents how much of the storage desirably remains charged at the steady conditions, and (3) the fin effectiveness (η_f), which is the ratio of the heat stored in the PCM with fins to that without fins. Figure 5.6 shows the liquid fraction variation of the cases for initially solid (left) and liquid (right) PCMs, respectively. Moreover, Table 5.7 shows the abovementioned key parameters for the conventional fin geometries under SCD. The steady state stability was assumed to be reached when the difference between two consecutive liquid fraction values was lower than 10^{-3}, which indicated the time beyond which negligible heat was stored within the PCM while heat continuously transferred through the storage from the heat source to the heat sink. The table shows that integration of more fins affected the final steady state liquid fraction in a way that there was no significant difference for the two initial conditions of solid and liquid. Moreover, Case 4 was the fastest one to reach the steady state for both initially solid and liquid PCMs. The rate of phase change could be identified by the slope of the curves in Figure 5.6 where Cases 2 and 4 had almost similar rates for initially solid PCM, whereas Case 3 followed by Case 4 had the highest rate for initially melted PCM. However, according to the table, Case 3 has an effectiveness value less than one, which means that addition of the fins undesirably resulted in less thermal energy storage in the PCM. In addition, Case 2 had the highest steady liquid fraction value among the cases.
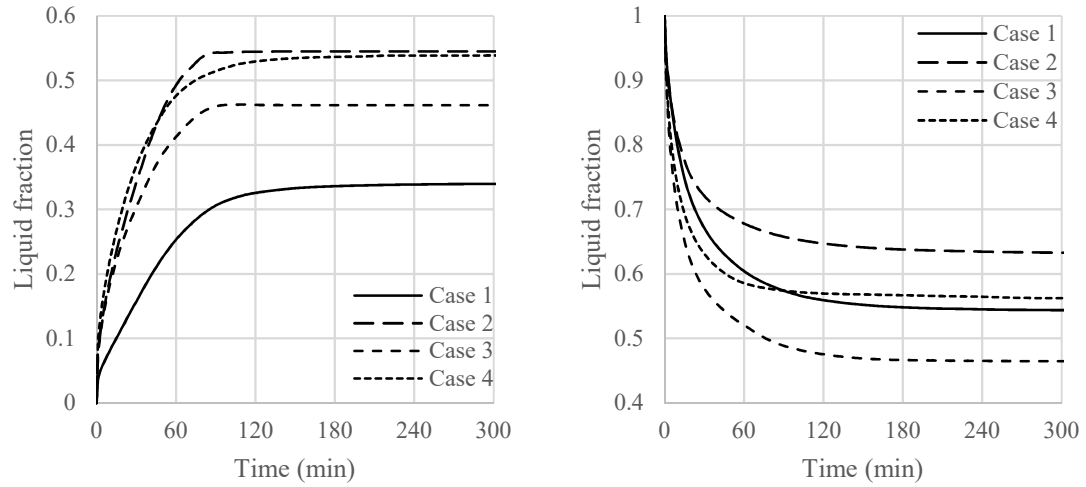
Figure 5.6: Liquid fraction variation of initially solid (left) and initially liquid (right) PCM with conventional fin configurations under SCD

Table 5.7: Steady state time and liquid fraction for the conventional fin configurations under SCD conditions

Case	Initially solid			Initially liquid		
	t_{std} (min)	γ_{std}	η_f	t_{std} (min)	γ_{std}	η_f
Case 1	94	0.3101	1.00	76	0.5855	1.00
Case 2	83	**0.5398**	**1.74**	58	**0.6792**	**1.16**
Case 3	84	0.4553	1.47	83	0.4940	0.84
Case 4	**79**	0.5051	1.63	**54**	0.5907	1.01

5.3.2   Analysis of developed configurations under SCD conditions

In the previous section, conventional fin configurations, which are normally used to charge and discharge PCMs consecutively, were investigated under SCD. In this section, the developed configurations, which are compatible with natural convection, are investigated.

5.3.2.1 Initially solid

Figure 5.7 shows the liquid fraction (left) as well as temperature (right) contours for Cases 5-10. Comparing Case 5 with Case 1 (in Figure 5.4), it was found that the addition of only one fin at the bottom of the internal tube enhanced the heat transfer to the lower half of the system. Instead of one vertical fin at the lower half (Case 5), Case 6 benefited from two fins with an angle of 45° from the gravity axis. According to the contours, not only the PCM above the fins was heated up by the natural convective motion, but also the PCM resting at the region between the two fins (at the lower half of the system) was melted, unlike Case 5. This shows that for the case of internal heating at least two angled fins at the lower half are required. Case 7 was basically a combination of Cases 5 and 6 where three fins were added to the internal tube. Compared to Case 6, the vertical fin in Case 7 obviously melted the PCM at further vertical positions close to the bottom of the system. This in turn eased the heat transfer to the external cold tube through a thinner solid layer. Overall, Case 7 was found to be the best option among the cases with internal fins. Therefore, the rest of the cases were developed on this basis. Case 8 was similar to Case 7 except that it had one vertical external fin at the top of the storage. As shown in the figure, the fin enabled heat transfer to the heat sink by 30 minutes (for Case 8). However, for Case 7 this type of heat transfer was achieved after 30 minutes. Therefore, the addition of this external fin resulted in faster response of the system under SCD. The same explanation applies to Cases 9 and 10 and they enabled more rapid response of the system. However, due to the addition of the fins, a continuous melted PCM motion was created at the right and left sides of the system, which confirmed continuous melting and solidification of the PCM at that region due to SCD.

Case 5 Case 6 Case 7 Case 8 Case 9 Case 10

5 min

30 min

60 min

56

90 min

120 min

150 min
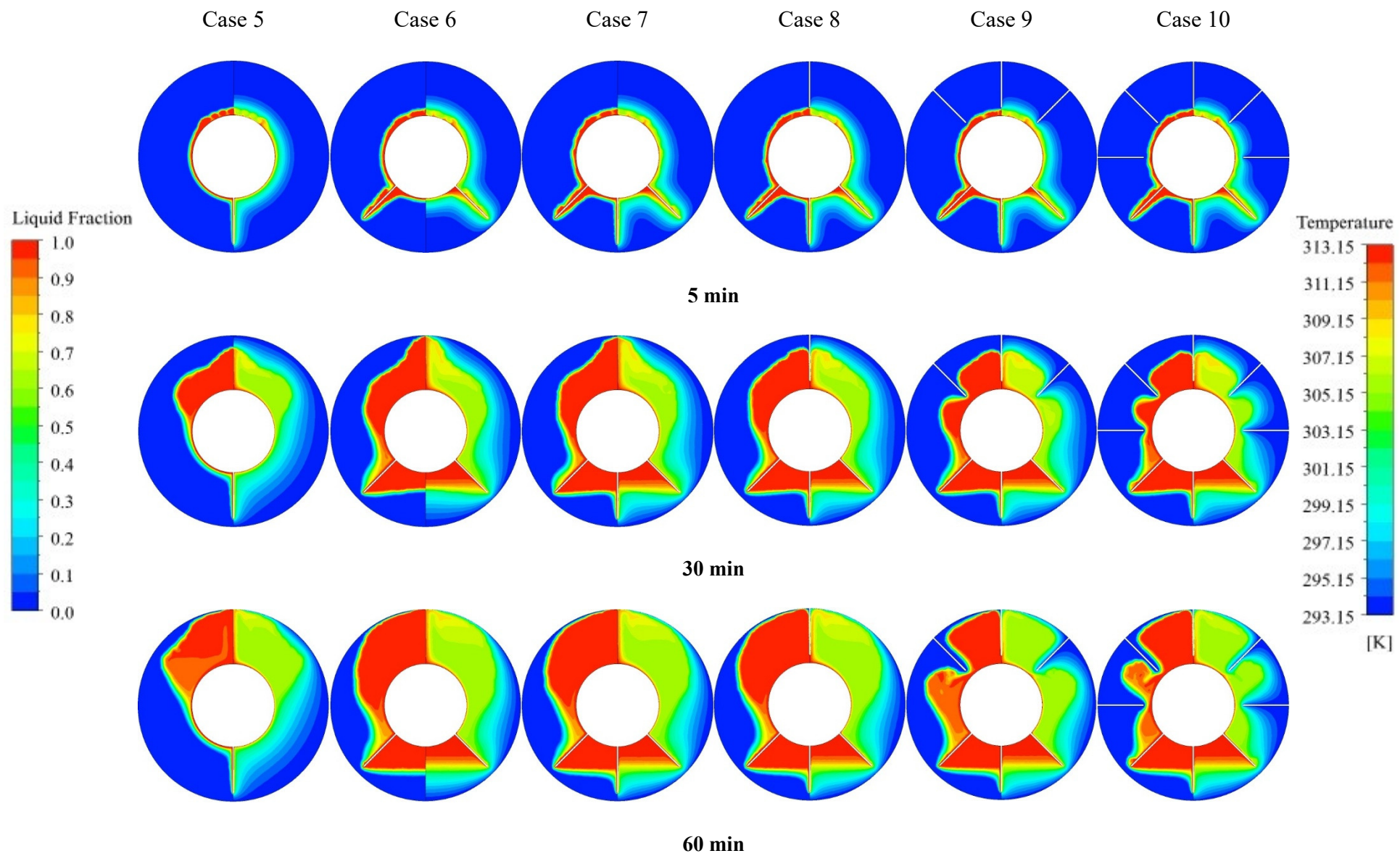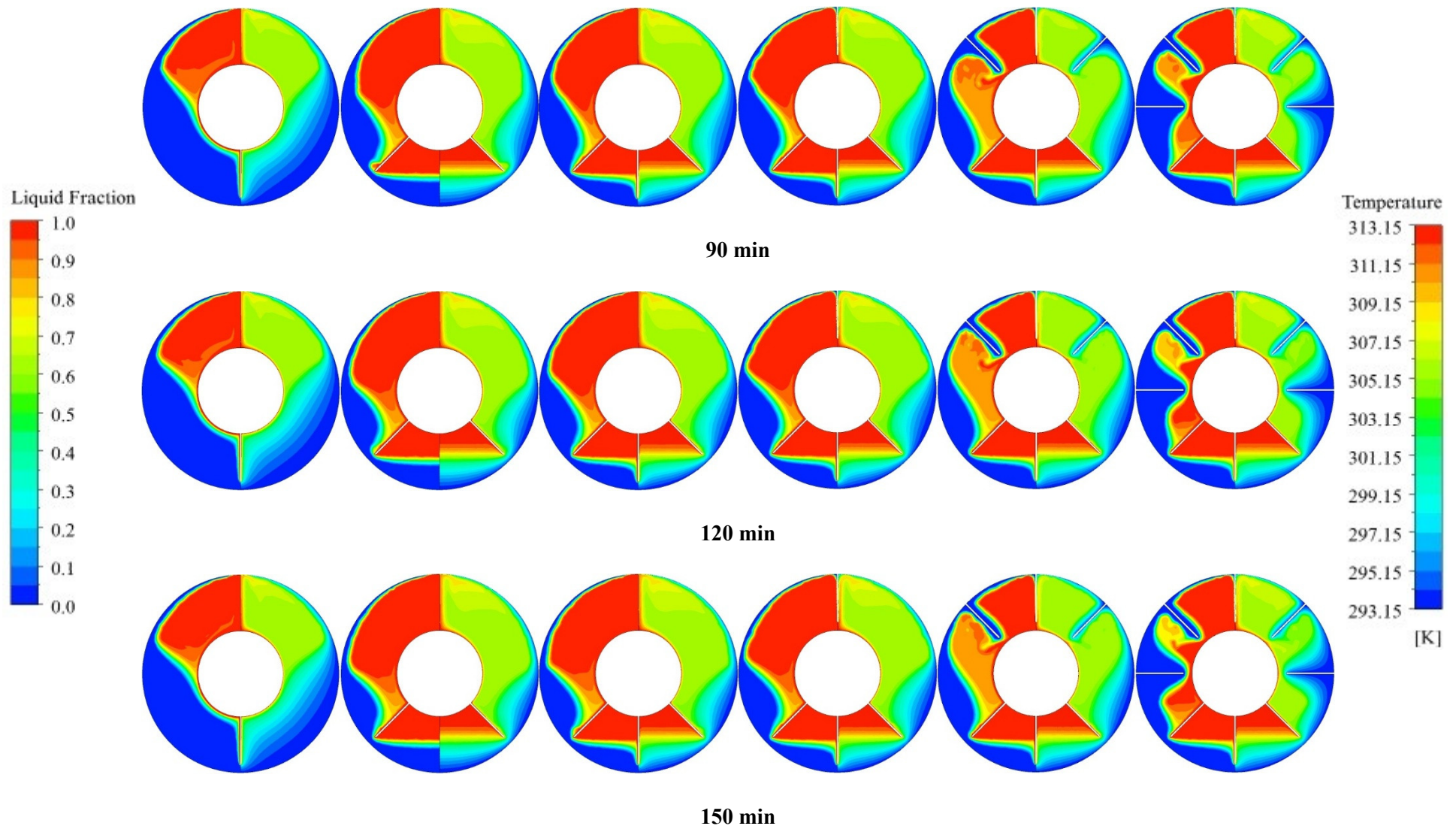
Figure 5.7: Liquid fraction (left) and temperature (right) contours for the developed fin configurations with initially solid PCM under SCD

5.3.2.2   Initially liquid

The liquid fraction and temperature contours of the initially liquid PCM under SCD are shown at left and right sides of Figure 5.8, respectively. According to the figure, a solid PCM layer was gradually deposited over the external wall. Comparing Case 5 with Case 1 (in Figure 5.5) it was found that the sole vertical internal fin kept the PCM melted at the lower half of the system. This together with the conduction through the highly resistant solid PCM resulted in easier heat transfer to the heat sink at the lower half of the system as compared to Case 1. In Case 6, a bigger portion of the system remained liquid after 150 minutes due to the utilization of two internal fins at the lower half. Nevertheless, comparing Cases 5 and 6 it was found that the solidified PCM layer located at the bottom of the storage was undesirably thicker for Case 6. Therefore, a vertical internal fin should be integrated and Case 7 showed superior performance to Cases 5 and 6. Addition of external fins in Cases 8-10 solidified more PCM at the upper half, which enabled continuous melting and solidification of the PCM at the sides due to SCD.

5 min

30 min

60 min

59
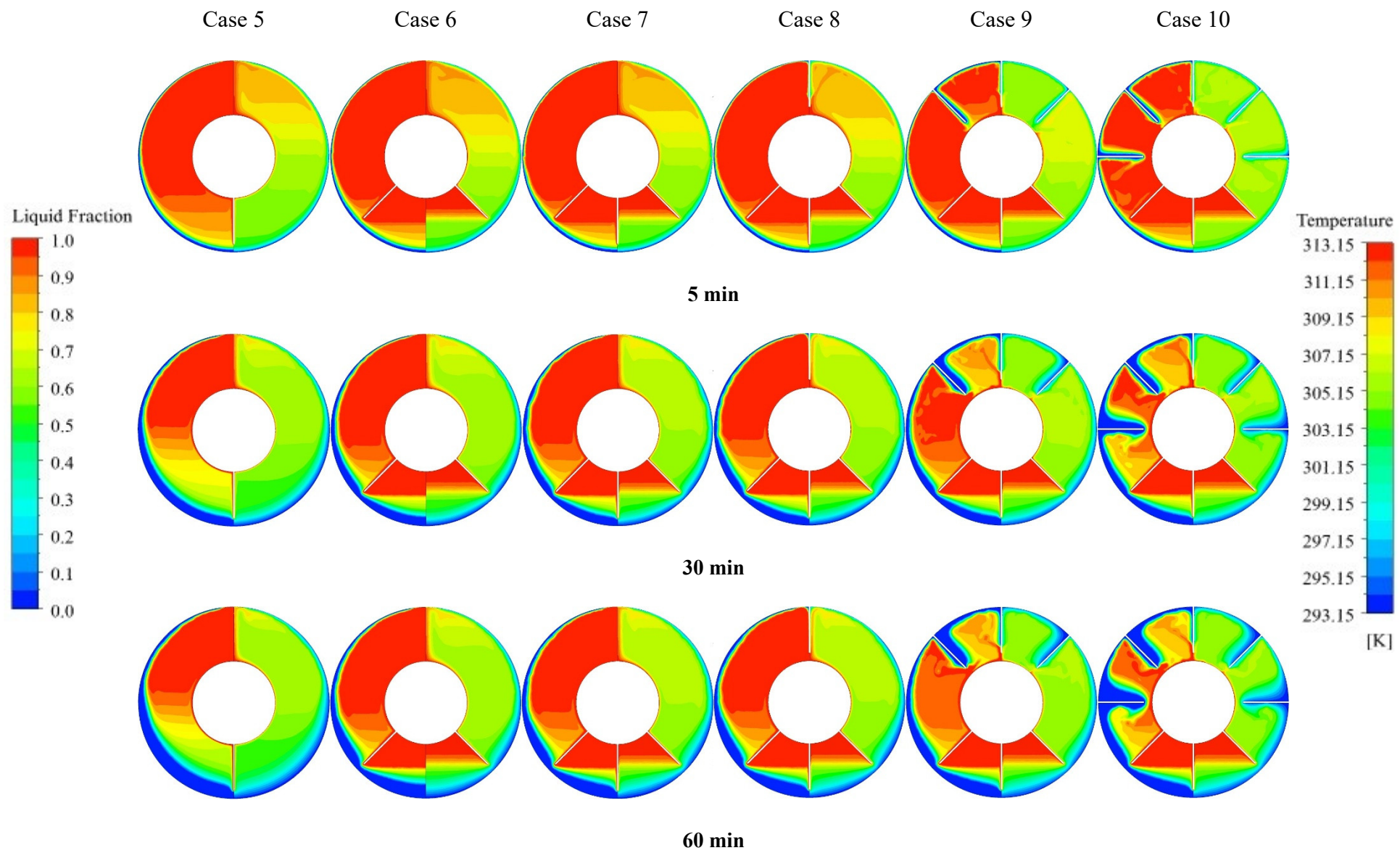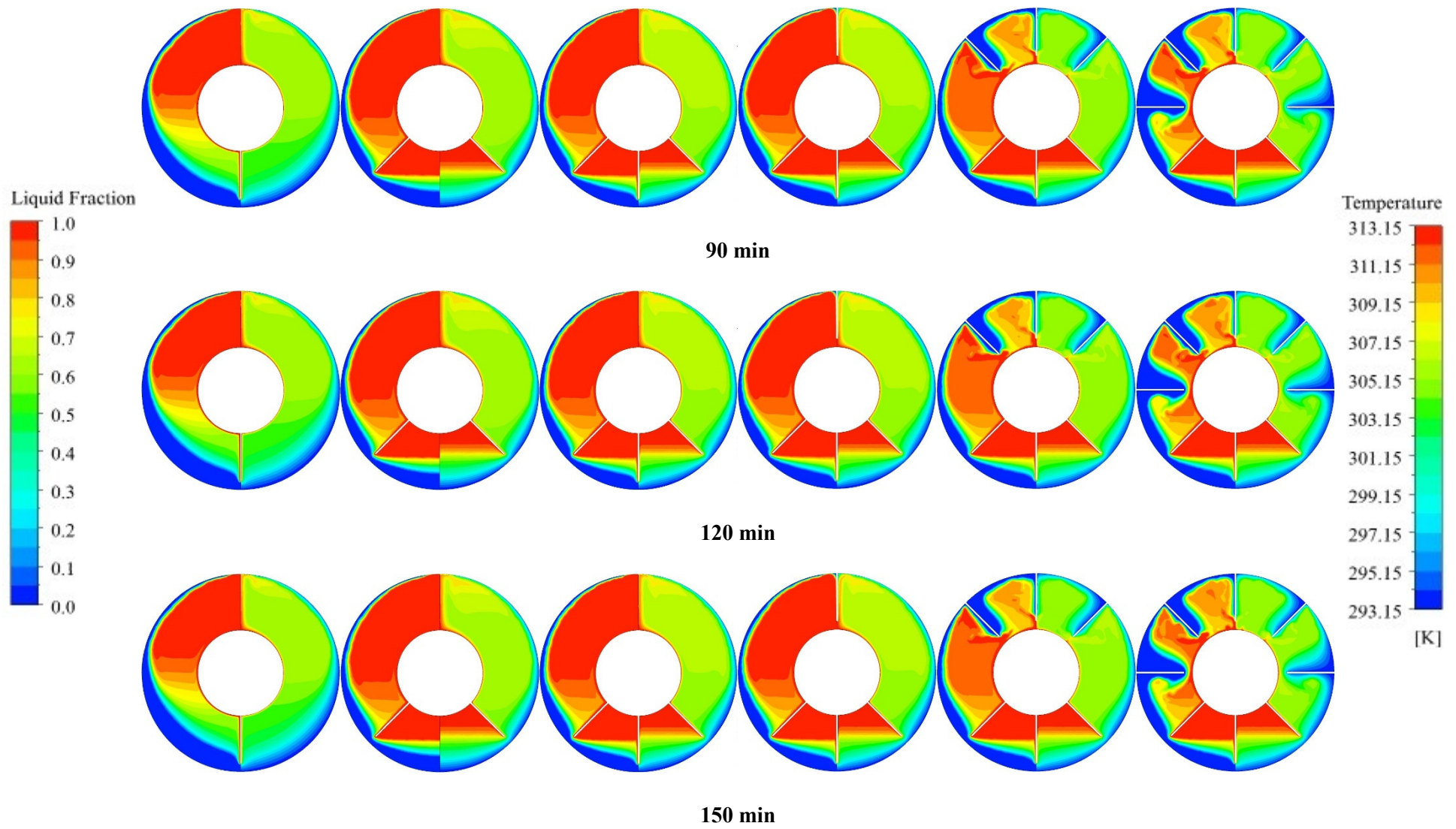
Figure 5.8: Liquid fraction (left) and temperature (right) contours for developed fin configurations with initially liquid PCM under SCD

5.3.2.3 Comparison

Table 5.8 shows the steady state liquid fraction values of the developed cases as well as the time required to achieve it. Comparing cases with internal fins only (Cases 5-7), it was found that Case 7 enabled the highest storage within an acceptable stabilization time compared to other cases. For the rest of the cases with external fins, although Case 8 had the highest steady liquid fraction, Case 10 had almost half an hour faster stabilization time for the initially solid PCM. This could be a requirement for some equipment where rapid response of the system is essential. In such cases, a compromise of the steady liquid fraction value as well as fin effectiveness might be the solution. It should be noted that the stabilization time for initially solid PCMs was longer than liquid ones. This was due to the initiation, domination, establishment and finally stabilization of natural convection. In other words, the melted PCM around the inner tube started to move upward as much as possible until the process was stabilized due to SCD. However, for initially liquid PCMs, since the natural convection was already established, it stabilized sooner under SCD.

Table 5.8: Steady state time and liquid fraction for the developed fin configurations under SCD conditions

Case	Initially solid			Initially liquid		
	t_{std} (min)	γ_{std}	η_f	t_{std} (min)	γ_{std}	η_f
Case 5	**92**	0.3147	1.00	69	0.6069	1.00
Case 6	120	0.5585	1.77	**43**	0.7089	1.17
Case 7	119	**0.5603**	**1.78**	46	**0.7164**	**1.18**
Case 8	114	**0.5388**	**1.71**	**46**	**0.7136**	**1.18**
Case 9	100	0.4713	1.50	54	0.6154	1.01
Case 10	**82**	0.3637	1.16	69	0.4552	0.75

5.3.3 Analysis of the configurations under non-SCD conditions

It is worth pointing out that it is not desirable to always run thermal storage systems under SCD since in such continuous SCD cases, the intermediate PCM could be

eliminated to enable direct heat transfer between the HTFs. Nevertheless, as mentioned earlier, there are some scenarios when such systems might be simultaneously charged and discharged. So far in this study, the heat transfer enhancement by fins under SCD process has been investigated. Since the developed fin configurations are consistent with natural convection, they could be beneficial for non-SCD conditions as well. In this section, their performance is investigated and compared with that of the conventional configurations.

5.3.3.1 One side heat transfer

For this scenario, the storage was facing either heating from the inner tube or cooling from the outer one under initially solid and liquid conditions, respectively. Therefore, one side heat transfer was investigated and the other tube was assumed to be insulated. Figures 5.9 and 5.10 show the liquid fraction contours of the conventional and developed fin geometries under either internal heating (left) or external cooling (right) conditions, respectively. As the figures show, for internal heating (left contours) the upward melted PCM motion greatly affected the upper half of the system for all cases. Therefore, allocating more fins to the lower half (e.g. Cases 6-10) enhanced the heat transfer and shortened the melting process. However, such allocation in Cases 6 and 7 was not helpful for the solidification process (see right contours). Integration of only one external fin in Case 8 greatly enhanced the heat transfer within the solid PCM. Overall, Cases 9 and 10 benefited from more external fins and had shorter solidification process.

Case 1 Case 2 Case 3 Case 4

5 min

30 min

60 min

Liquid Fraction
1.0
0.9
0.8
0.7
0.6
0.5
0.4
0.3
0.2
0.1
0.0
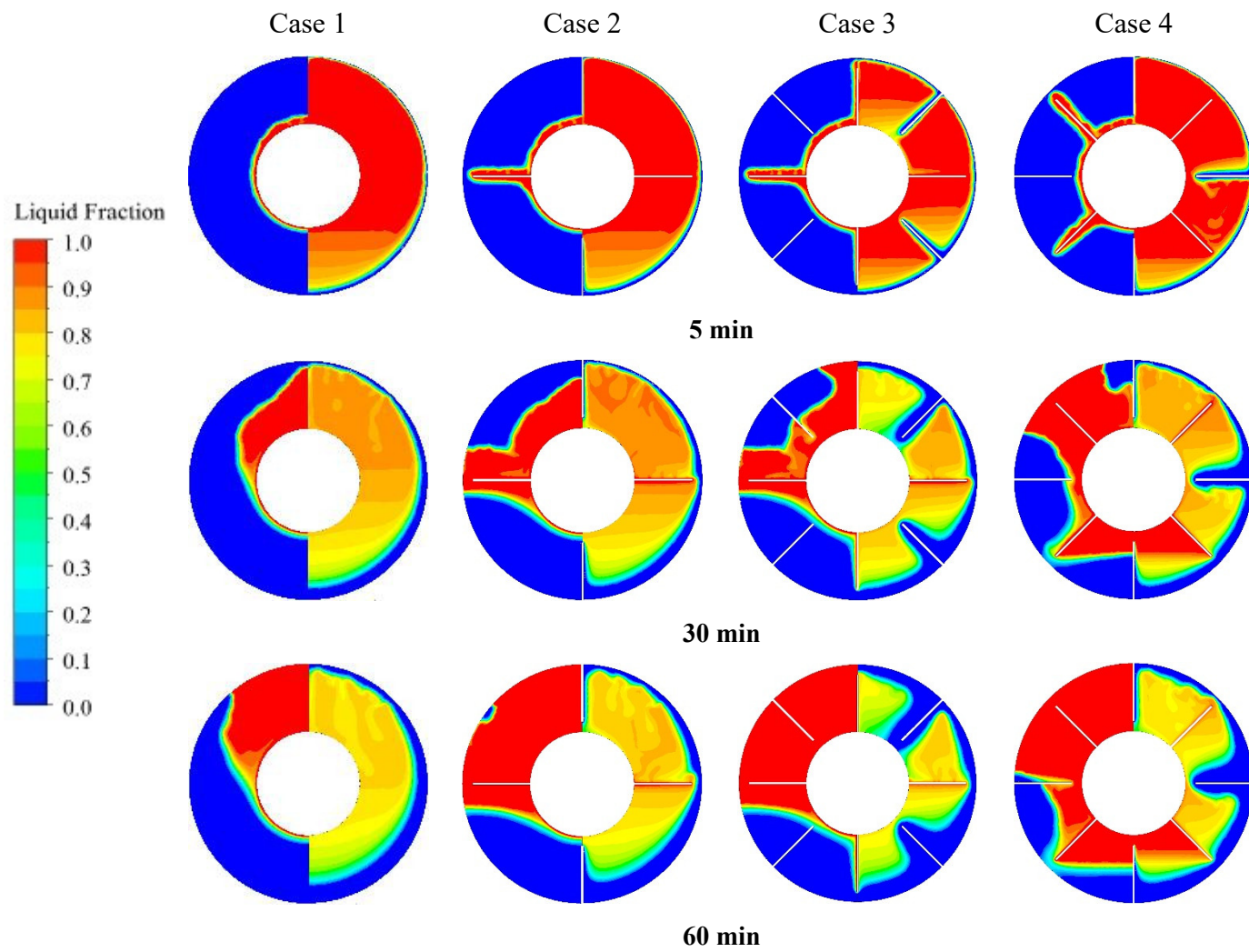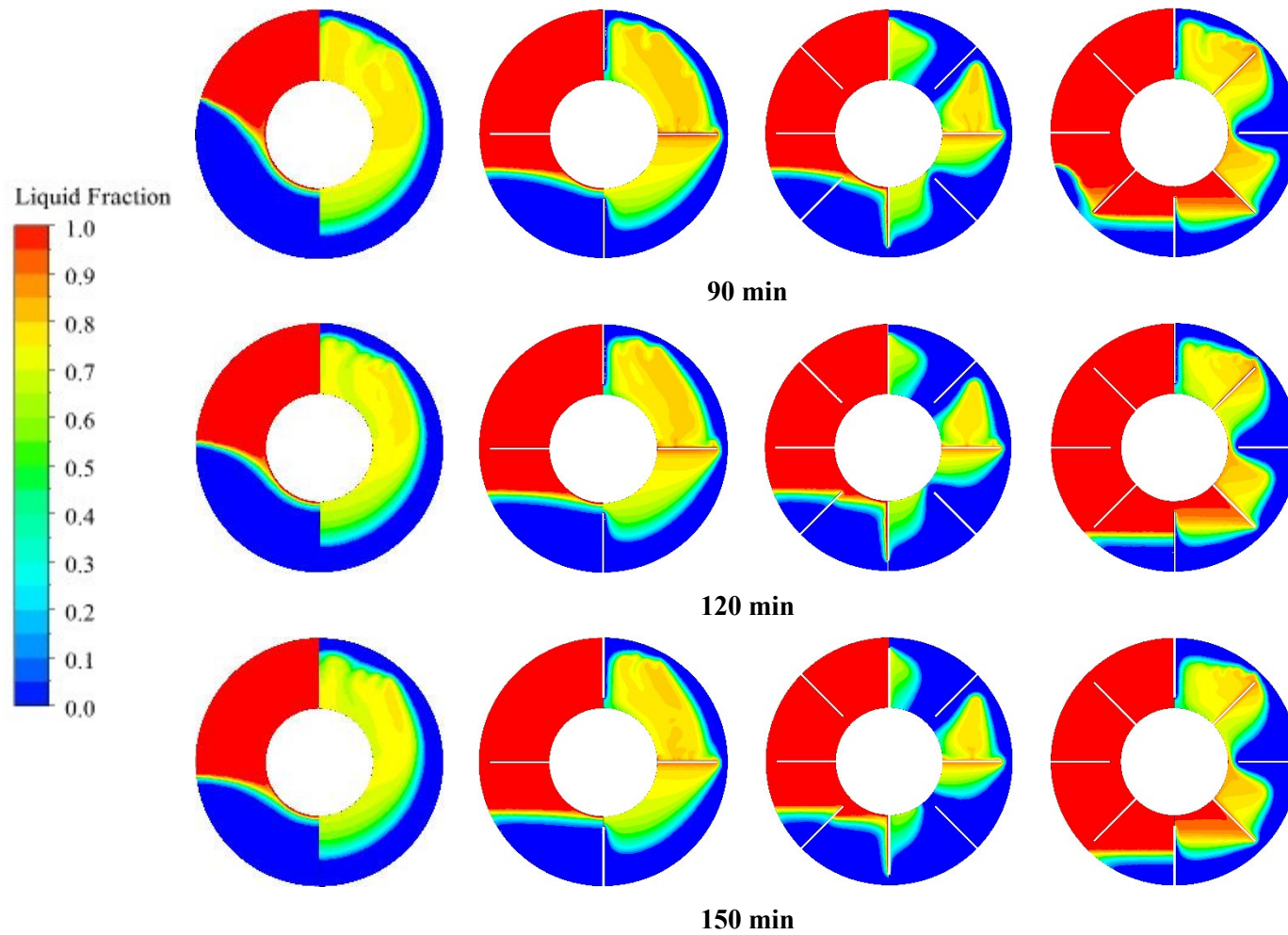
Figure 5.9: Liquid fraction contours for the conventional fin configurations under internal melting (left) or external solidification (right)

Liquid Fraction

5 min

30 min

60 min

90 min

120 min

150 min
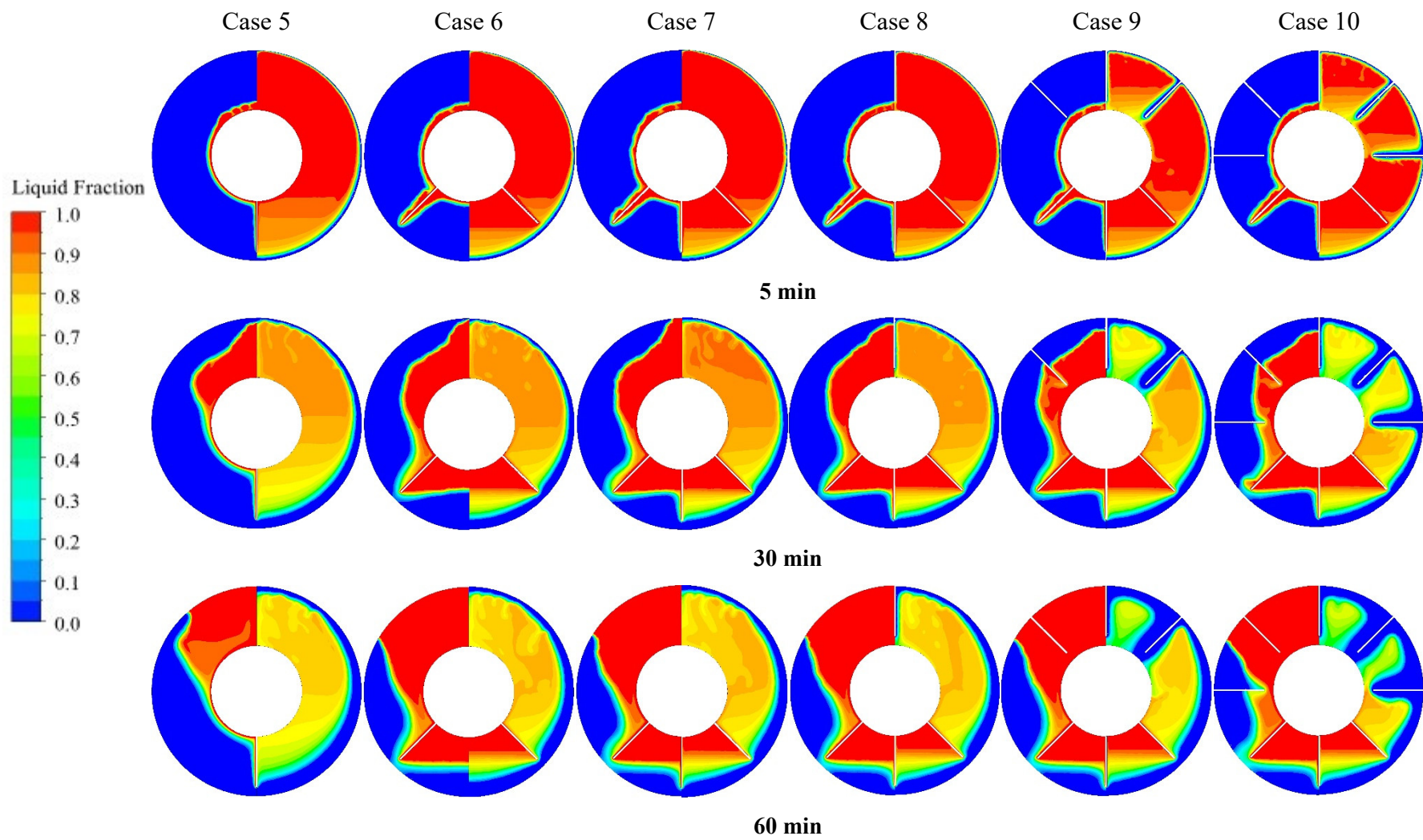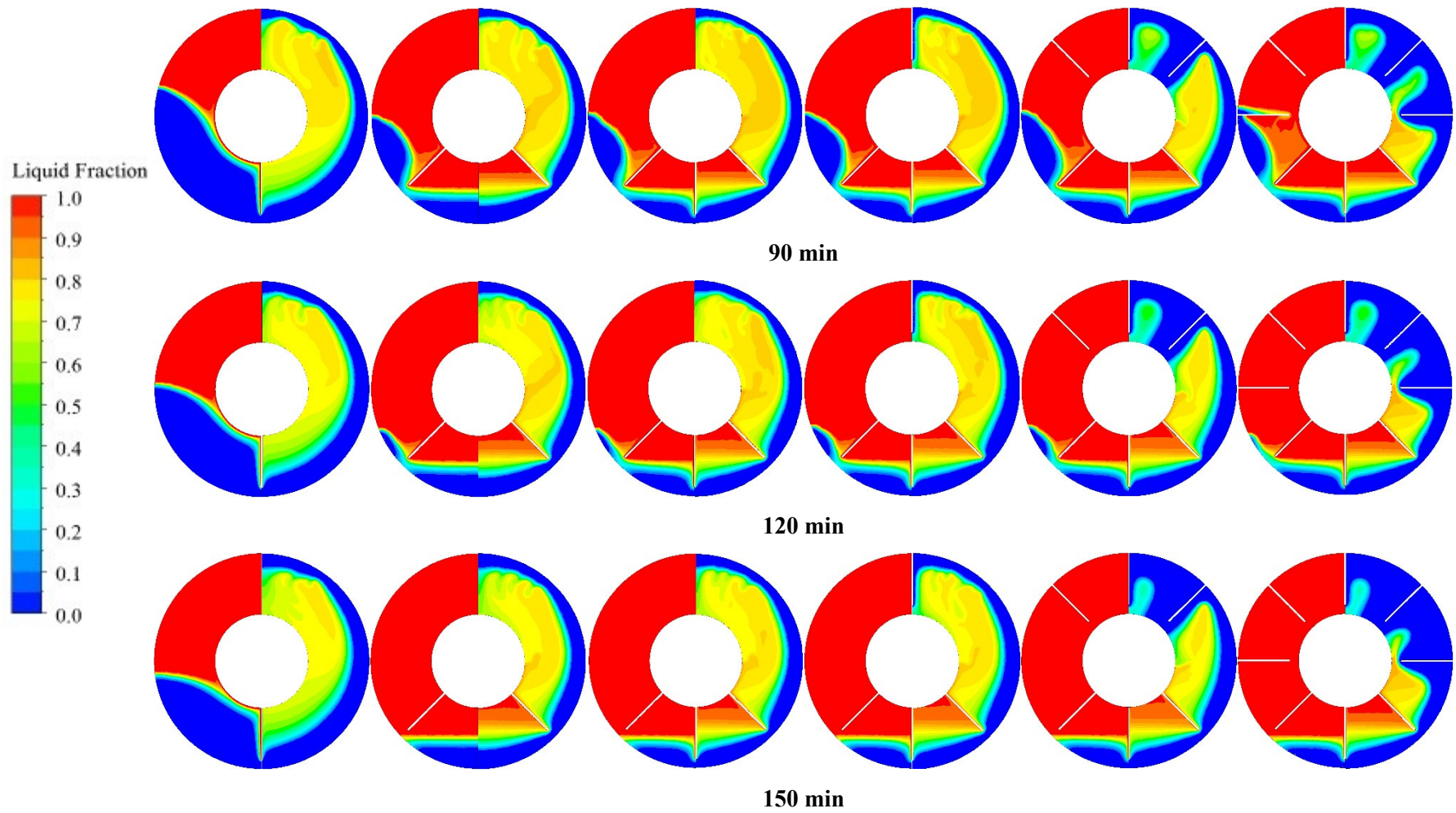
Figure 5.10: Liquid fraction contours for the developed fin configurations under internal melting (left) or external solidification (right)

5.3.3.2   Both sides heat transfer

Figure 5.11 shows the liquid fraction contours of the conventional cases under melting (left) and solidification (right) from both sides of the storage. The same contours for the developed fin configurations are shown in Figure 5.12. As the figures show, the melting process under both sides heat transfer was significantly shorter due to the higher heat transfer surface area (compared to one side heat transfer) together with the buoyancy-driven motion. Therefore, all cases achieved the fully melted condition within 90 minutes. On the other hand, although the heat transfer surface area attributed to shortening the solidification period, due to the lack of natural convection, solidification was longer than melting. Interestingly, addition of more fins created some liquid cells surrounded by solid PCM for Cases 3, 4, 9 and 10 after 60 minutes. This finding underscores the significance of fins to enhance solidification. These figures, similar to the figures for one side heat transfer (Figures 5.9 and 5.10), show how fast melting is compared to solidification thanks to the natural convection. This reveals that the challenge is to find a suitable geometry that accelerates solidification by enhancing the conductive heat transfer through the PCM.

Case 1   Case 2   Case 3   Case 4

5 min

30 min

60 min

Liquid Fraction

90 min

120 min

150 min
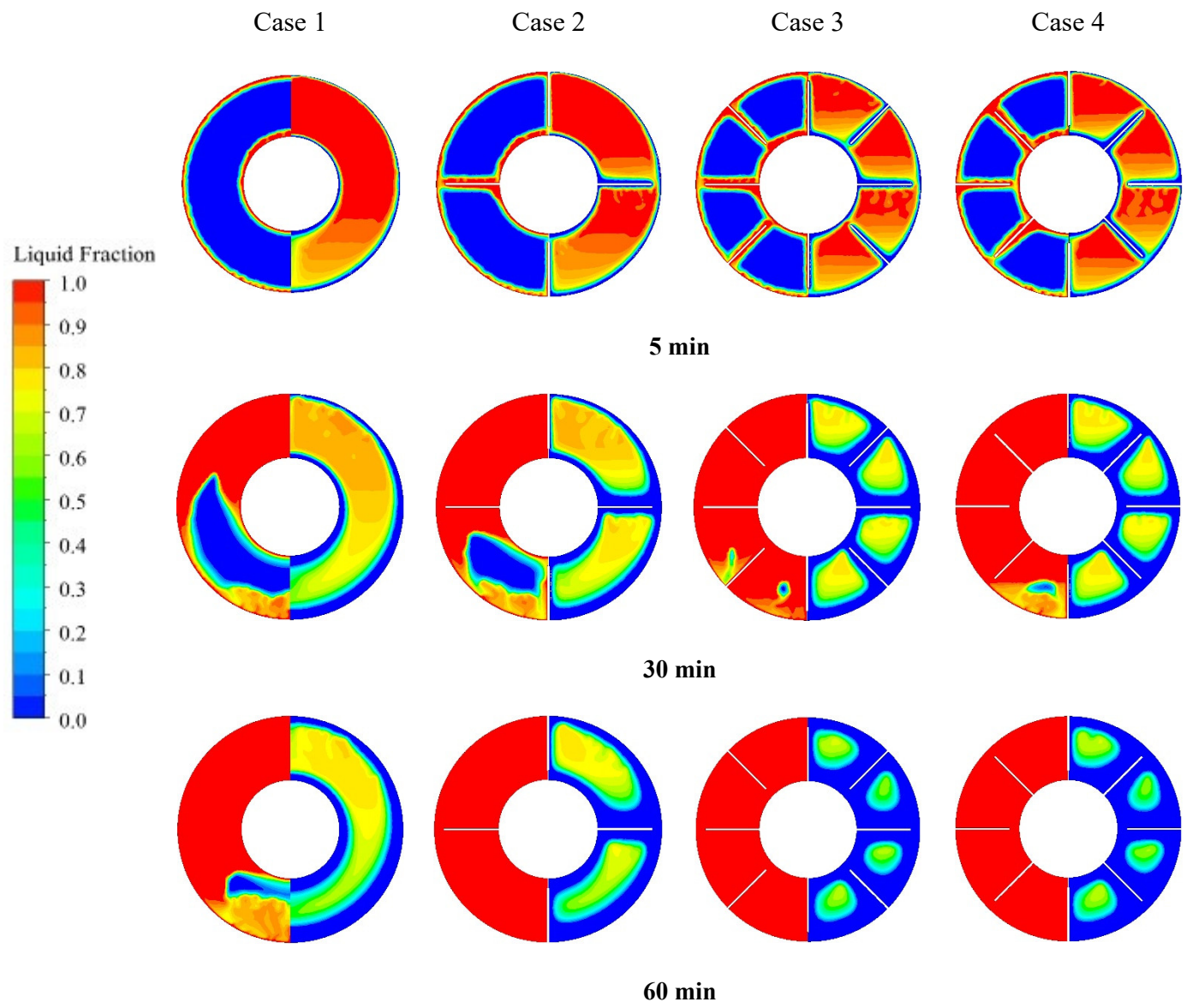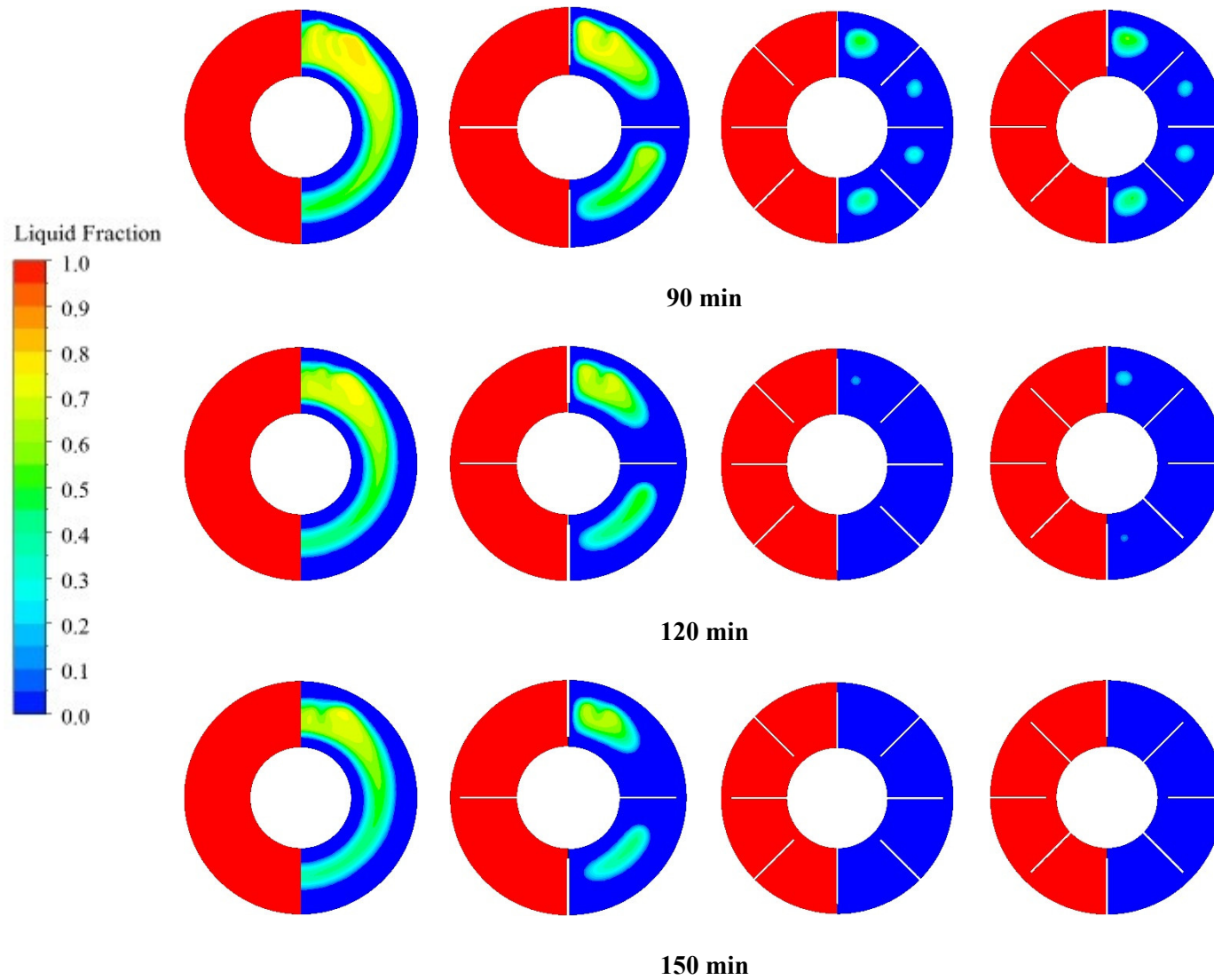
Figure 5.11: Liquid fraction contours for the conventional fin configurations under melting (left) or solidification (right) from both sides

Case 5 Case 6 Case 7 Case 8 Case 9 Case 10

5 min

Liquid Fraction

30 min

60 min

90 min

120 min

150 min
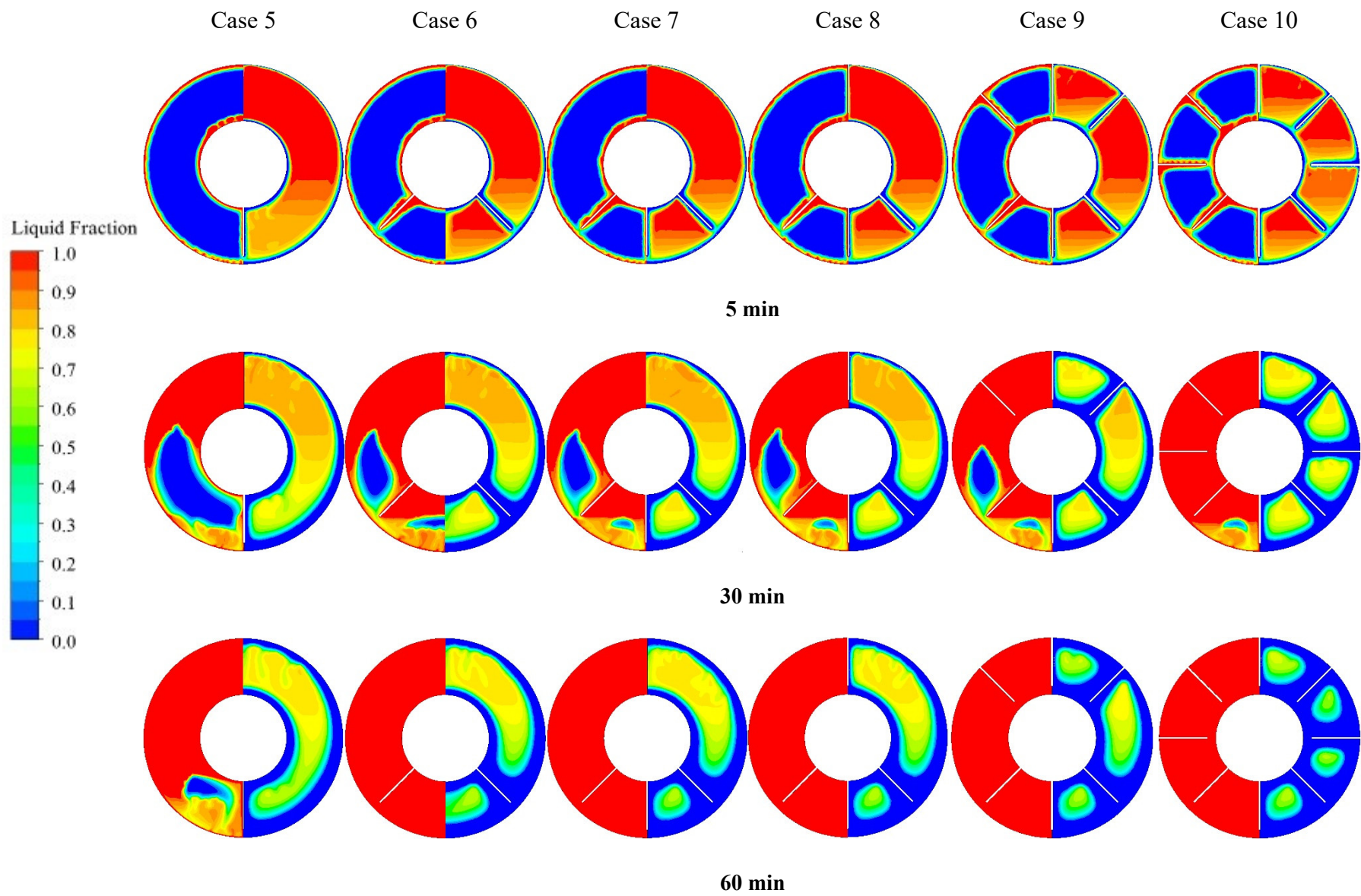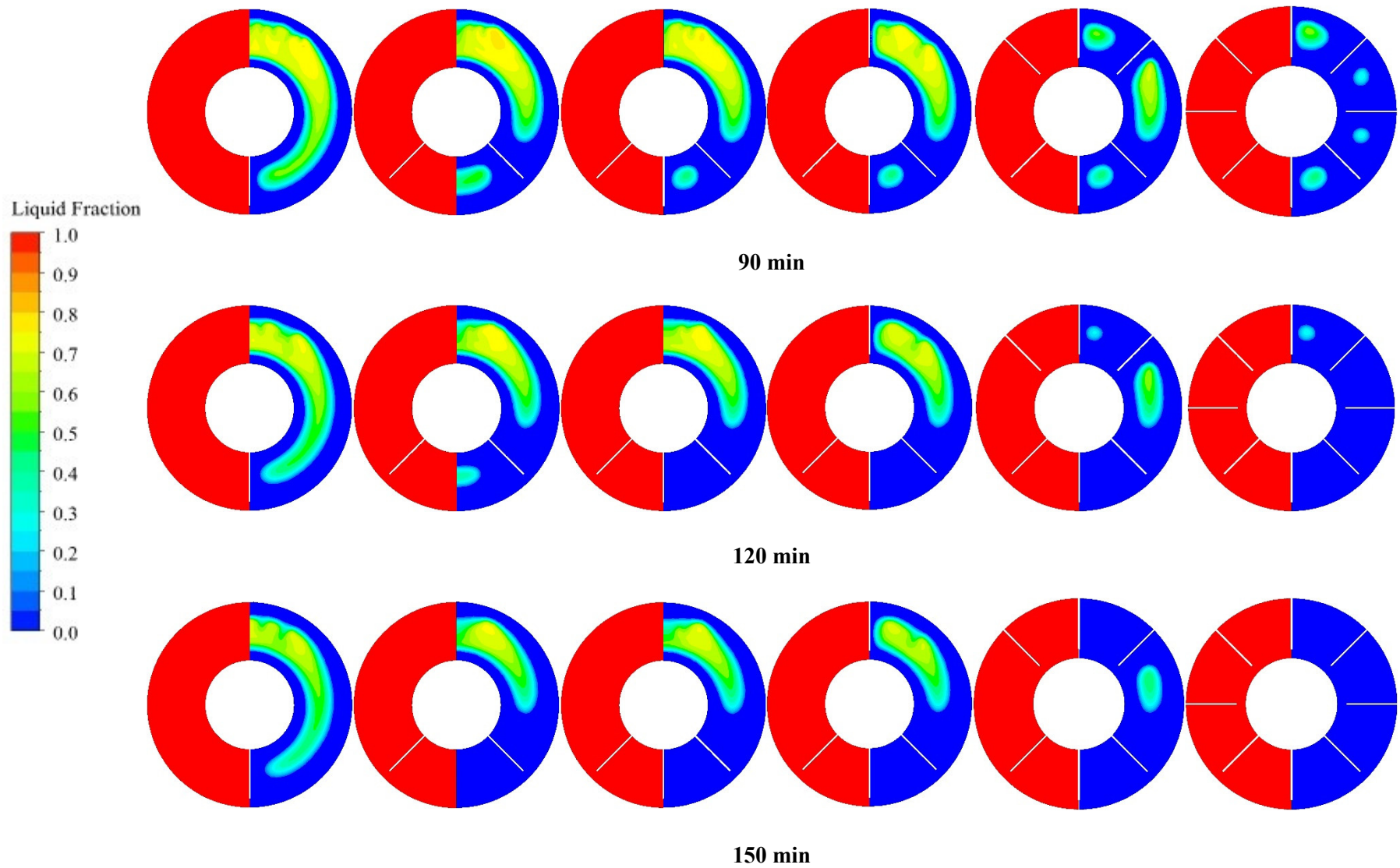
Figure 5.12: Liquid fraction contours for the developed fin configurations under melting (left) or solidification (right) from both sides

5.3.3.3　Comparison

Unlike SCD, the cases investigated in this section could achieve a fully solid or liquid condition at the end of the phase transition process. Therefore, the evaluation of the performance was based on the time required to reach such condition (see Table 5.9). It should be noted that the simulations were run for 14 hours (840 minutes) of the phase change process and if a fully melted or solidified state was not achieved, the final liquid fraction value was reported in parentheses. The reason is since renewable energy sources are inherently intermittent they are not normally available for long periods of time. For instance, maximum solar energy availability would not exceed 14 hours per day.

According to Table 5.9, the process was much longer for Case 1 compared to the others due to the low thermal conductivity of the PCM as well as lack of fins. Addition of conventional fins greatly improved the melting process, while for the solidification process the magnitude of impact was lower. Overall, due to the absence of natural convection, solidification was longer than melting. It is interesting to point out that the final liquid fraction value during solidification for Case 2 under one side heat transfer was higher than Case 1. This was due to the fact that the horizontal internal fins suppressed the downward cold PCM motion and hot PCM zones were created under the internal fins.

Table 5.9: Comparison of phase change time (only if accomplished by 14 hours) or final liquid fraction value (after 14 hours, shown in parentheses) for all cases under non-SCD conditions

	Phase change duration for non-SCD (min)			
Case	**One side**		**Both sides**	
	Melting	**Solidification**	**Melting**	**Solidification**
Case 1	> 840 (0.8504)	> 840 (0.2619)	75	> 840 (0.1039)
Case 2	> 840 (0.8617)	> 840 (0.3457)	58	269
Case 3	> 840 (0.8900)	> 840 (**0.1598**)	**34**	**122**
Case 4	**362**	> 840 (0.3017)	37	127
Case 5	> 840 (0.8841)	> 840 (**0.2833**)	75	569
Case 6	378	> 840 (0.2904)	49	407
Case 7	**332**	> 840 (0.3542)	**48**	**403**
Case 8	336	> 840 (0.3162)	48	375
Case 9	335	> 840 (0.2245)	46	195
Case 10	**327**	> 840 (**0.1726**)	**36**	**130**

5.3.4 Proper geometry selection for SCD and non-SCD conditions

In order to identify the best fin geometry for a specific application, all of the findings are compared in this section. The evaluation criteria differ based on the application of the storage; therefore, it is not possible to simply report one of the configurations as the best among others. In this section, the most suitable geometry for three specific scenarios, which TTHXs are capable of offering, are analyzed; (1) non-SCD with single side heat transfer, (2) non-SCD with both sides heat transfer and (3) SCD only.

5.3.4.1 Scenario 1: Non-SCD with one side heat transfer

The storage in this scenario faces either internal charging or external discharging. An example for this scenario is peak load shaving of an air conditioning with latent heat

thermal energy storage. In this case, a TTHX can be used with CHTF from the air conditioning system, which discharges the PCM during the night so as to be used later on to cool down the HHTF during daytime. The HHTF is then used inside a building for cooling applications. Keep in mind that, in such scenario, the HTFs have separate flow paths where the internal and external tubes are used for HHTF and CHTF, respectively. Therefore, the PCM is either internally charged or externally discharged.

According to Figure 5.13, Case 4 as well as Cases 6-10 achieved a fully melted condition within 14 hours of the phase change process, where the line shows the time required to achieve it. Although the times were close, Case 10 had a superior performance among others. For the solidification process, none of the configurations reached a fully solidified condition within 14 hours. Nevertheless, Cases 3 and 10 desirably had the lowest final liquid fraction value. In summary, Case 10 is recommended as the proper geometry for this scenario.
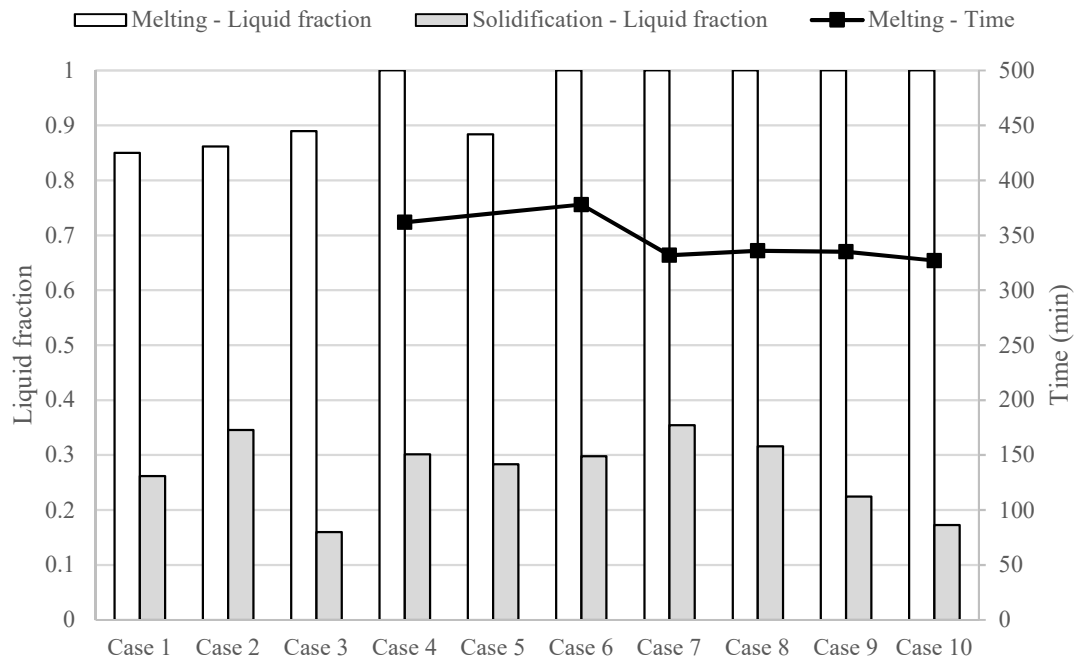
Figure 5.13: Phase change time (only if accomplished by 14 hours) or final liquid fraction value (after 14 hours) for the cases under non-SCD with one side heat transfer

5.3.4.2   Scenario 2: Non-SCD with both sides heat transfer

In this scenario, the storage faces either charging or discharging from its both sides. An example of this storage is the same as the one for one side heat transfer except that the HTFs do not have separate flow paths; therefore, both the internal and external tubes are used for heat transfer to/from the PCM, consecutively.

Figure 5.14 shows the time required to achieve complete phase change for the cases. It should be noted that Case 1 did not achieve complete solidification after 14 hours of heat transfer; hence; it is excluded from the figure. Interestingly, addition of only one vertical internal fin (Case 5) shortened the solidification time (compared to Case 1). Overall, melting process was shorter than solidification for both conventional and developed cases. Cases 3, 4 and 10 had almost similar performance but Case 3 was the best option to accomplish melting and solidification sooner than all other cases.
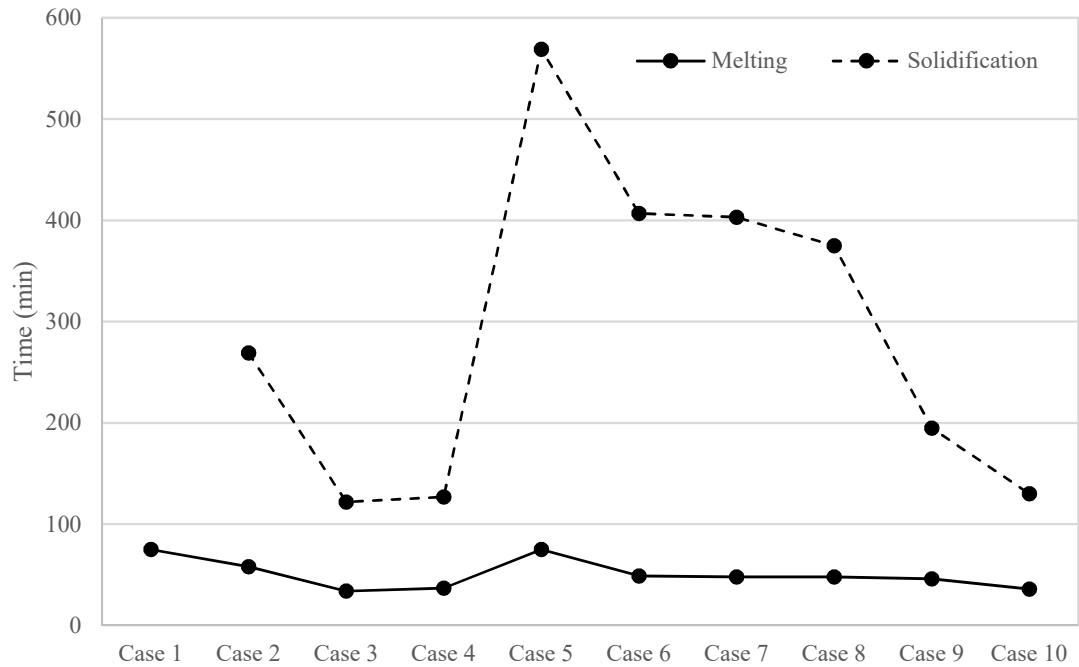
Figure 5.14: Phase change time for the cases under non-SCD with both sides heat transfer

5.3.4.3 Scenario 3: SCD only

Under SCD, the PCM faces internal charging, while it is simultaneously discharged externally. An example of this scenario is a thermal storage where heat is stored inside the PCM by an internal supply HHTF from a solar collector so as to be extracted simultaneously for SDHW (i.e. the CHTF) heating.

Figure 5.15 shows the steady state liquid fraction value and its corresponding required time for both initially solid and liquid storages. Overall, it is desirable to achieve a higher steady state liquid fraction value since in such condition the objective of the storage, which is storing higher amounts of heat, is met. Accordingly, for initially solid conditions, Cases 2, 4 and 10 had the shortest steady state time. However, Case 2 had a higher steady liquid fraction value. For initially liquid PCM, Cases 4 and 6-8 had the shortest stabilization time (i.e. reaching the steady state). However, Cases 7 and 8 had the highest steady liquid fraction value. As mentioned earlier, Case 8 enabled faster response of the system due to the integration of an external fin. Overall, the final decision should be made based on the requirements of the storage, where either the fast stabilization or higher liquid fraction value would prevail the other. Assuming the necessity of the highest steady liquid fraction value, Case 8 had the best performance for both initially solid and liquid conditions.
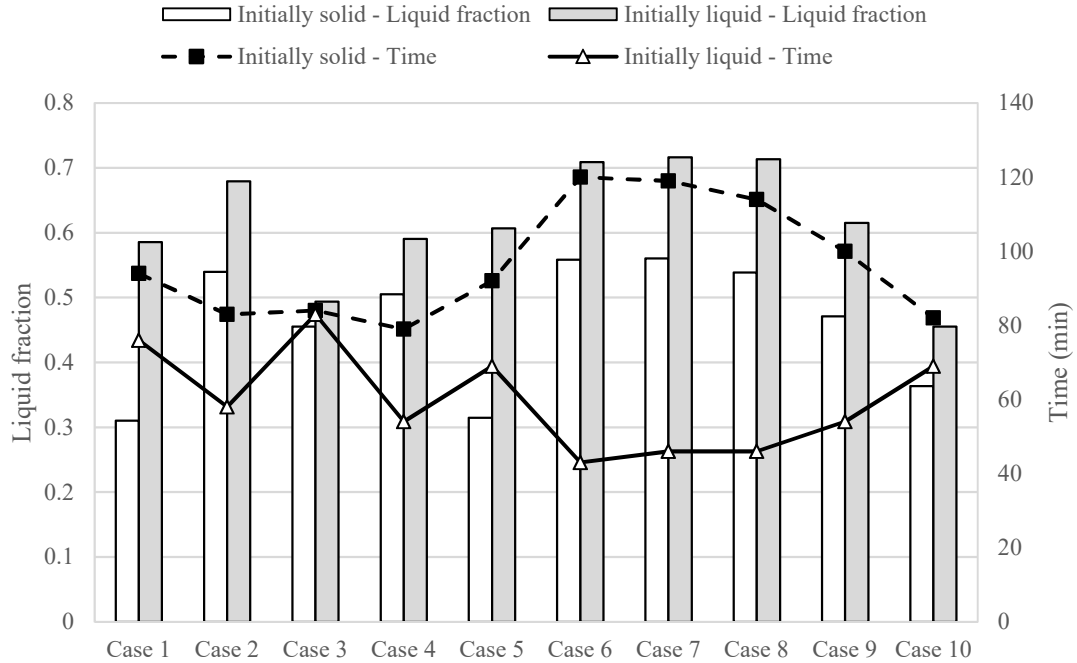
Figure 5.15: Steady state time and liquid fraction for the cases under SCD

5.4   Analysis of the effective parameters

In this section, the effect of fin numbers, length and thickness are investigated for the developed configurations under SCD conditions.

5.4.1   The effect of fin numbers

Figure 5.16 shows the liquid fraction variation for cases with internal (left) and external (right) fins for initially solid PCM. Since internal fins were attached to the hot tube whereas the cold ones were integrated to the cold tube, their effect on the phase change process was completely different. As the figure shows, addition of only one internal fin (Case 5) did not enhance the final liquid fraction value as much as other cases with at least two angled internal fins. On the other hand, the integration of external fins reduced the final liquid fraction value indicating higher extraction from the storage. Addition of only one external fin (Case 8) did not drop the final liquid fraction value as much as other cases. For initially liquid PCM, Figure 5.17 shows the liquid fraction variation of cases with internal (left) and external (right) fins. Case 5 had the lowest final

liquid fraction value among cases with internal fins. This was due to the fact that adding only one vertical fin was not effective enough to melt the PCM at the lower half of the system. Cases 6 and 7 had almost similar performance, which was because of adding at least two internal fins. For Cases 8-10, more external fins reduced the final liquid fraction values. The mechanism for the effect of fin numbers was explained in Section 5.3.2; thus, it is not repeated in this section.
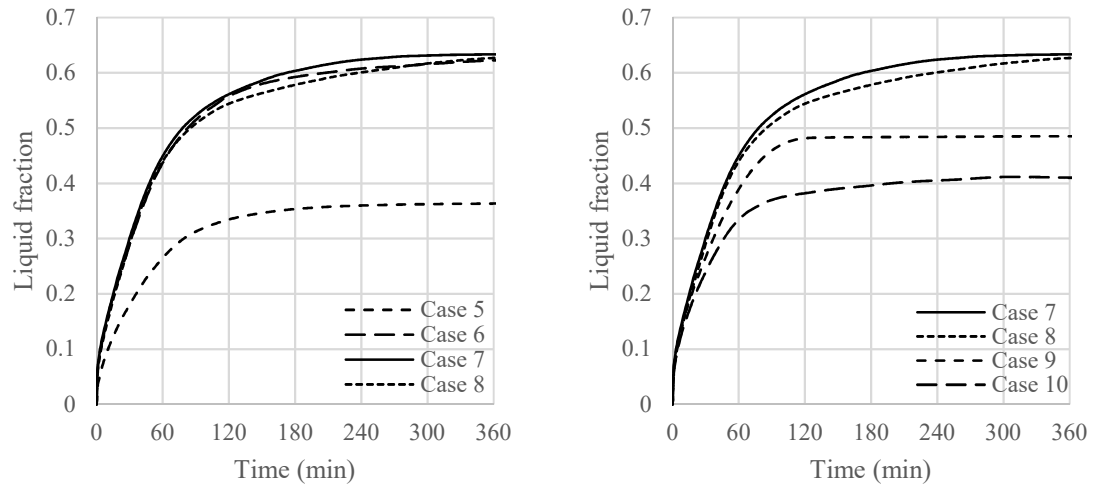
Figure 5.16: Temporal liquid fraction variation for cases with different internal (left) and external (right) fin number (see Table 4.4) for initially solid PCM
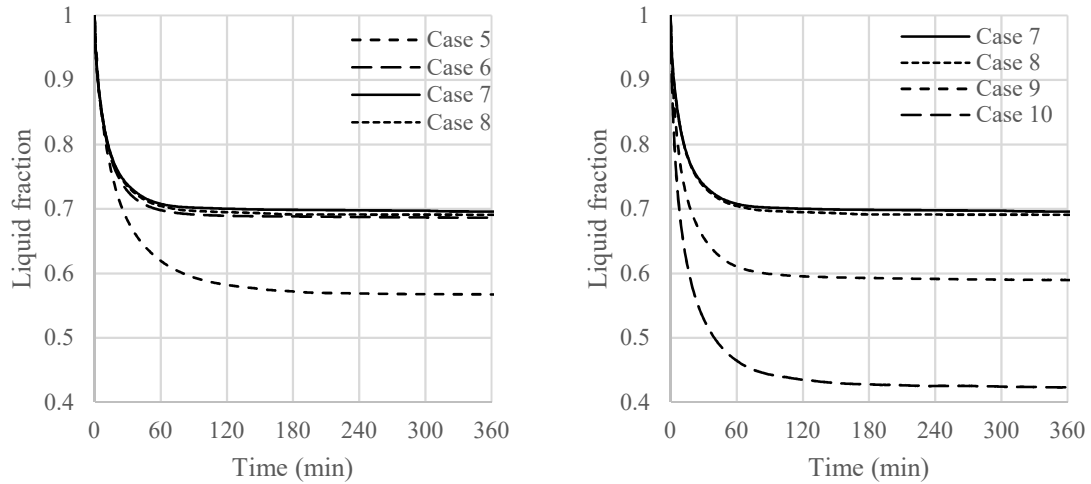
Figure 5.17: Temporal liquid fraction variation for cases with different internal (left) and external (right) fin number (see Table 4.4) for initially liquid PCM

5.4.2 The effect of fin length

The effect of fin length was investigated for the fin configuration of Case 10 (see Table 5.5). Figure 5.18 shows this effect for initially liquid (left) and solid (right) PCMs. In order to explain the effect of fin length under SCD, two key points should be considered. First, the impact of fin length on enhancement of conductive heat transfer from the corresponding surface to the PCM and second, the suppression of natural convection by adding longer fins. The overall outcome is dependent upon these opposite points. Case 11 had the shortest fin length (i.e. 10 mm) and the results showed that its steady liquid fraction value tended to be closer to the initial one. This means that for the initially solid PCM, its steady liquid fraction was the smallest compared to the rest of the cases, while it had the highest value under initially liquid conditions. Therefore, when the fin length was too short, the heat struggled to transfer within the PCM. Addition of another 10 mm to the fin length, Case 12 showed a better performance than Case 11. In addition to its enhanced steady liquid fraction value, the slope of the graphs revealed that the rate of heat transfer was also improved, especially for the initially liquid PCM. Regardless of the initial condition, elongating the fins for another 10 mm (Case 13) did not show a significant impact. This is a difference between SCD and non-SCD since earlier studies reported that under non-SCD conditions, longer fins shortened the phase

79

change process [24]. For the initially solid PCM, Case 13 showed a sudden raise in the liquid fraction value at about 120 minutes. This was due to the fact that enough melted PCM was formed to pass through the space left between the HHTF tube and the fins over the CHTF tube. For shorter fin lengths, the gap was wider; hence, the melted PCM was flowing more freely. Interestingly, Case 14 also lacked such a raise, which was due to the very small gap size, greatly limiting the motion of the melted PCM. Overall, the fins suppressed the natural convection over the CHTF tube for Cases 13 and 14.
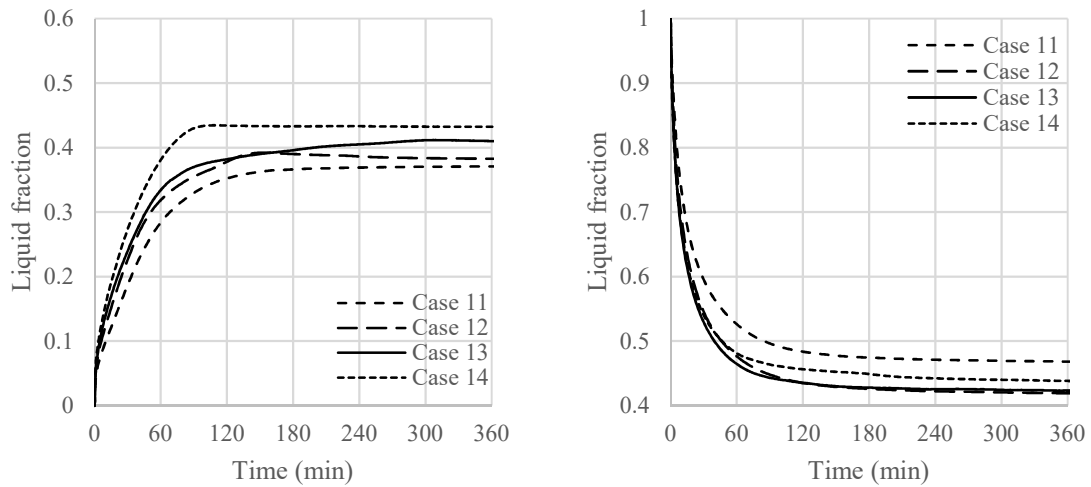
Figure 5.18: Temporal liquid fraction variation for cases with different fin length (see Table 5.5) for initially solid (left) and liquid (right) PCMs

5.4.3   The effect of fin thickness

Earlier studies reported that the effect of fin thickness on the heat transfer enhancement was negligible; however, its effect was only investigated under non-SCD conditions. Figure 5.19 shows the effect of fin thickness on the liquid fraction of initially solid (left) and liquid (right) PCMs under SCD. For the initially solid PCM (left), due to the simultaneous presence of conduction and natural convection, there was a very small difference between the cases. On the other hand, for the initially melted PCM (right), the lines could hardly be distinguished and almost coincided. Based on these results, it was concluded that regardless of heat transfer mechanism, the fin thickness had no significant effect on the heat transfer rate under SCD.
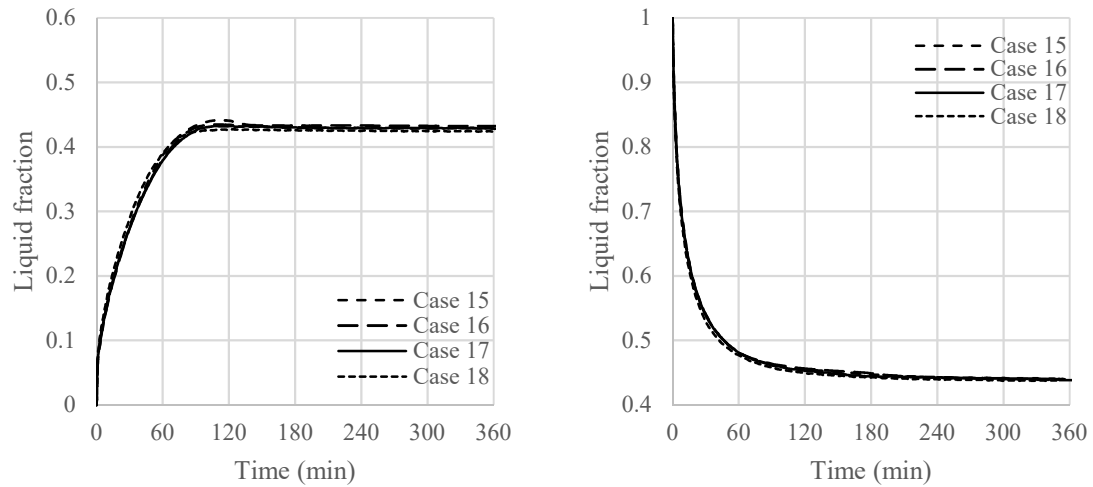
Figure 5.19: Temporal liquid fraction variation for cases with different fin thickness (see Table 5.6) for initially solid (left) and liquid (right) PCMs

5.5   Concluding remarks

This chapter presented the results of a numerical study, which investigated the effect of fin number, length, and thickness on the phase change process of a TTHX under SCD conditions. Moreover, some fin configurations were developed and compared with the conventional ones under both SCD and non-SCD conditions. The most important findings were:

- For systems with SCD applications, the recommended fin configuration includes one external and three internal fins. The internal fins should be located at the bottom of the system where one fin is vertically positioned at the bottom and two others are located at an angle of 45° on both sides of it. The external fin should be vertically located at the upper half of the system.

- For systems with non-SCD applications having both sides heat transfer, the recommended fin configuration includes four internal fins and four external fins. The internal fins should include two vertical and two horizontal fins, while the external fins should make an angle of 45° with internal ones.

- For systems with non-SCD applications having one side heat transfer, the recommended fin configuration includes five external fins (at 0°, 45°, 90°, 135° and

180°) at the upper half and three internal fins (at 225°, 270° and 315°) at the lower half of the system.

- Under SCD conditions, the effect of fin thickness was negligible. However, their number and length enhanced the heat transfer as long as the fins did not suppress the natural convection.

Chapter 6: Development of a novel simplified front tracking method

6.1 Introduction

According to Chapter 2, the main limitations of the literature include:

- CFD simulation of CCNC model is time consuming and might require intensive computational power,
- Despite its importance, the effect of natural convection has been neglected in many studies, and
- No earlier study developed a correlation between liquid fraction values of CCNC and PC models.

Therefore, the objective of this chapter is to develop an "enhanced tool"; a simplified front tracking method, which inherently considers the mechanism of natural convection.

6.2 Materials and methods

In this section, the properties of the investigated geometries and PCMs as well as the modeling approach are presented.

6.2.1 Setup characteristics

In this study, standardized tube sizes were considered for investigation. The US standard copper tube sizing approach was used in which "Type M" tubes are recommended for water heating purposes [53]. In the horizontal shell and tube heat exchanger (STHX), the PCM filled the shell side forming an annulus as shown in Figure 6.1. Three different geometries were used in this study to generate the required data. Table 6.1 shows the geometrical properties of the investigated STHXs. The shell diameter was fixed whereas tube diameter was altered.
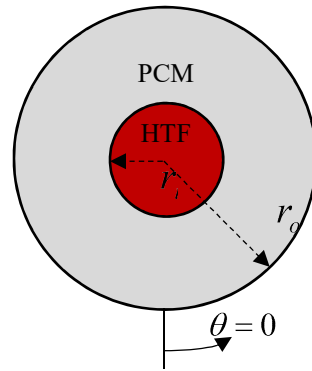
Figure 6.1: Schematic representation of the STHXs

Table 6.1: Geometrical properties of the STHXs [53]

| Geometry | Radius (mm) | | | | Shell-to-tube radius ratio |
| | Tube | | Shell | | |
	Inner	Outer	Inner	Outer	
Geometry 1	25.51	26.98	62.32	65.09	2.31
Geometry 2	37.86	39.69	62.32	65.09	1.57
Geometry 3	49.97	52.38	62.32	65.09	1.19

6.2.2 PCM thermophysical properties

Commercial paraffin-based PCMs (Rubitherm Technologies GmbH) were considered for the investigation. Table 6.2 shows the thermophysical properties of the PCMs, which filled the shell space in the STHXs as shown in Figure 6.1. It should be noted that the highlighted PCM (RT35HC) was not included in the model development phase so as to be used later for verification purposes.

Table 6.2: Thermophysical properties of the PCMs [55]

Property	Dimension	Symbol	RT31	RT35	RT35HC	RT44HC
Solidus temperature	K (°C)	T_s	300.15 (27)	302.15 (29)	307.15 (34)	314.15 (41)
Liquidus temperature	K (°C)	T_l	306.15 (33)	309.15 (36)	309.15 (36)	317.15 (44)
Solid density	kg/m^3	ρ_s	880	860	880	800
Liquid density	kg/m^3	ρ_l	760	770	770	700
Specific heat capacity	J/kg.K	C_p	2,000	2,000	2,000	2,000
Latent heat of fusion	J/kg	λ	170,000	160,000	240,000	250,000
Thermal conductivity	W/m.K	k	0.2	0.2	0.2	0.2
Thermal expansion coefficient	1/K	β	0.00076	0.00076	0.00076	0.00076
Dynamic viscosity	kg/m.s	μ	0.002508	0.002500	0.002700	0.003300

6.2.3 Analysis procedure

To conduct simulations, each PCM (see Table 6.2) was used inside each storage (see Table 6.1). Table 6.3 gives the combination of Stefan numbers and shell-to-tube radius ratios (R). It should be noted that the three cases designated by "Ver" indicate cases used for verification purpose. Since simulations were required both for PC and CCNC models, a total of 42 simulations were carried out.

Table 6.3: The investigated values of Stefan and shell-to-tube radius ratios

Case	*Ste*	*R*	Case	*Ste*	*R*	Case	*Ste*	*R*
Case 1	0.16	2.31	**Case 7**	0.25	2.31	**Case 13**	0.47	2.31
Case 2	0.16	1.57	**Case 8**	0.25	1.57	**Case 14**	0.47	1.57
Case 3	0.16	1.19	**Case 9**	0.25	1.19	**Case 15**	0.47	1.19
Case 4	0.24	2.31	**Case 10**	0.32	2.31	**Case 16**	0.50	2.31
Case 5	0.24	1.57	**Case 11**	0.32	1.57	**Case 17**	0.50	1.57
Case 6	0.24	1.19	**Case 12**	0.32	1.19	**Case 18**	0.50	1.19
Ver 1	0.17	2.31	**Ver 2**	0.17	1.57	**Ver 3**	0.33	1.19

6.3 Results and discussion

In this section, the results for the PC and CCNC models are briefly presented and compared. These results are then used in Section 6.4 to develop the novel method.

6.3.1 PC model

The PC model is based on the assumption that natural convection does not occur during melting and consequently conduction is the dominant heat transfer mechanism. Although this model is far from reality, it is a simple and fast model and could even be solved analytically under certain assumptions. Figure 6.2 shows the propagation of the melting front for RT31 if the PC model was valid. As it is clear in the contours, the melting front departs from the inner tube and propagates monotonically in all directions creating a circular melting front shape. For larger tube radii, due to the larger heat transfer surface area the melting under conduction occurs faster.
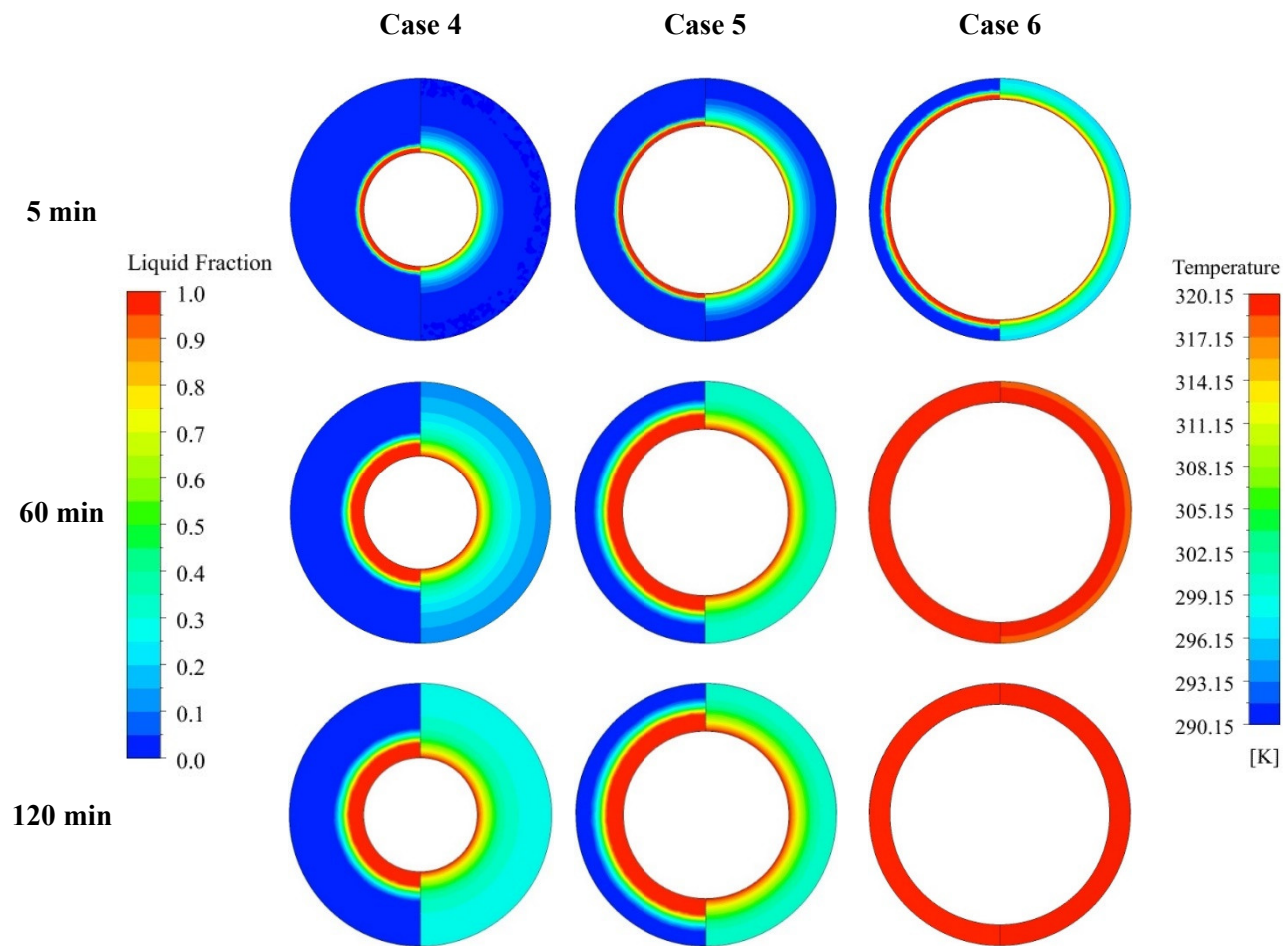
Figure 6.2: Liquid fraction (left) and temperature (right) contours of the PC model for Cases 4-6

6.3.2   CCNC model

As mentioned, the PC model is a hypothetical model, which assumes that conduction is the sole heat transfer mechanism during melting. However, in reality, density changes during melting create buoyancy forces resulting in natural convection. Figure 6.3 shows the propagation of melting front for RT31 using the CCNC model. As the contours show, the phenomenon is totally different from the results of the PC model (shown in Figure 6.2). Figure 6.3 shows that the upper half of the system is affected by the upward melted PCM motion, which enhances heat transfer and shortens the melting duration.
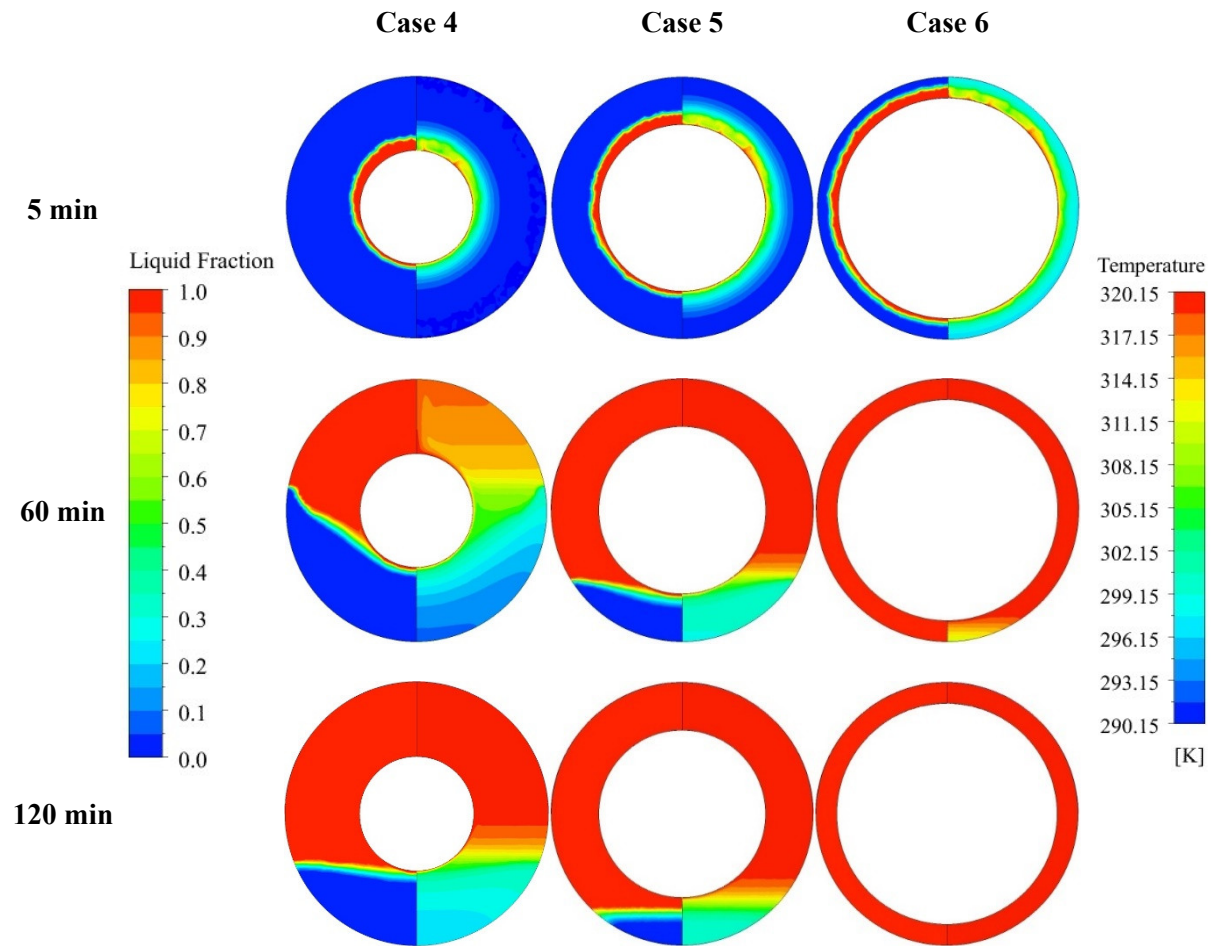
Figure 6.3: Liquid fraction (left) and temperature (right) contours of the CCNC model for Cases 4-6

6.3.3 Comparison

Comparing the PC and CCNC models, it is concluded that:

- Analysis setup for the PC model in the software (in this case ANSYS Fluent) is much faster than the CCNC model with less details,
- The running time for the PC model is much shorter than the CCNC model,
- Convergence criteria is much easily met for the energy equation of the PC model (due to the lack of continuity and momentum equations), and
- The PC model results could be obtained analytically (under certain simplifying assumptions). This can drastically reduce the required computational power and time.

Therefore, it is desirable to develop a simplified method, which (1) can provide the results of the CCNC model from PC model results and (2) can approximate the melting front location (outperforming the effective thermal conductivity method).

6.4 Front tracking method development

Earlier studies revealed that horizontal latent heat storages are suitable for partial melting [3]. However, detecting such condition requires sophisticated numerical analysis with the CCNC model. In this study, a novel front tracking method is presented which considers separate melting fronts for the upper and lower halves of a horizontal storage. Therefore, it would be easier to detect partial melting of the system. In this section, the simplified front tracking method is developed and its flowchart is presented. Thereafter, the method is verified with a PCM, which was not included in the development phase.

6.4.1 Method description

According to Table 2.2, Fourier number (*Fo*), also known as dimensionless time, is a common measure in earlier studies, and is defined as:

$$Fo = \frac{\alpha t}{D_i^2}$$
(6.1)

where α, t and D_i are thermal diffusivity, time and HTF tube diameter, respectively. In this study, however, the intent is to use the PC model liquid fraction as a measure of time to be able to link PC and CCNC models. Therefore, instead of time, the liquid fraction of the CCNC model would be a function of that of the PC model.

As presented in Section 6.3.1, when dealing with the PC model, the melting front departs from the HTF tube towards the outer shell forming a cylindrical shape (i.e. circular in 2D). This is due to the fact that gravity has no effect on the results of this model. Therefore, the upper and lower halves of the system have equal liquid fraction values, which is equal to that of the PC model:

$$\gamma_{PC} = \gamma_{PC}^{L} = \gamma_{PC}^{U}$$
(6.2)

However, in reality, buoyancy forces create an upward PCM motion affecting the upper half of the system. The logic behind the method is to assume that the difference between the results of the CCNC and PC models is due to the natural convection:

$$\gamma_{Conv} = \gamma_{CCNC} - \gamma_{PC}$$
(6.3)

6.4.1.1 Method logic

At the early stages of melting, conduction is the dominant heat transfer mechanism. As soon as enough PCM is melted, convection establishes, which later dominates the heat transfer. Based on this, the simplified method assumes that the lower half of the system remains the same as that of the PC model. This assumption is not far from reality, which has been reported in detail in our earlier study [3] (see Appendix D). Therefore, the lower half would have a semi-cylindrical front. On the other hand, the effect of natural convection is designated solely to the upper half of the system. Thus, the difference

between the CCNC and PC models is only attributed to the melting front propagation at the upper half, as long as the liquid fraction of the upper half is lower than unity. In other words, the upper and lower halves of the system would have two semi-cylindrical front shapes where the radius of the upper half's front is larger than that of the lower half (see Figure 6.4). A correlation (*f₁*) is developed to map the PC model liquid fraction to that of the upper half.
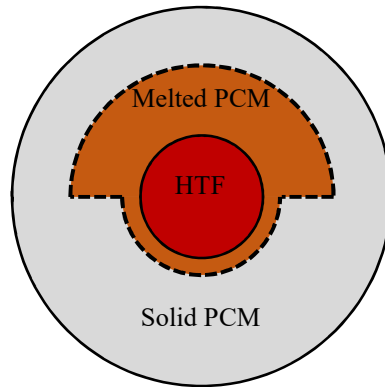
Figure 6.4: Schematic representation of two separate melting fronts for upper and lower halves

Once the upper half of the PCM is fully melted (i.e. when its liquid fraction reaches 1), the rest of the melting is attributed to the lower half, differing it from the PC model. The melting process continues until the maximum liquid fraction value is reached. In such conditions, another correlation (*f₂*) is developed to map the PC model liquid fraction to that of the lower half.

When there are two semi-cylindrical melting fronts for the upper and lower halves, the overall liquid fraction value would be the average of the two:

$$\gamma = \frac{\gamma^U + \gamma^L}{2}$$

(6.4)

Figure 6.5 shows the flowchart of the procedure used to develop the simplified method.
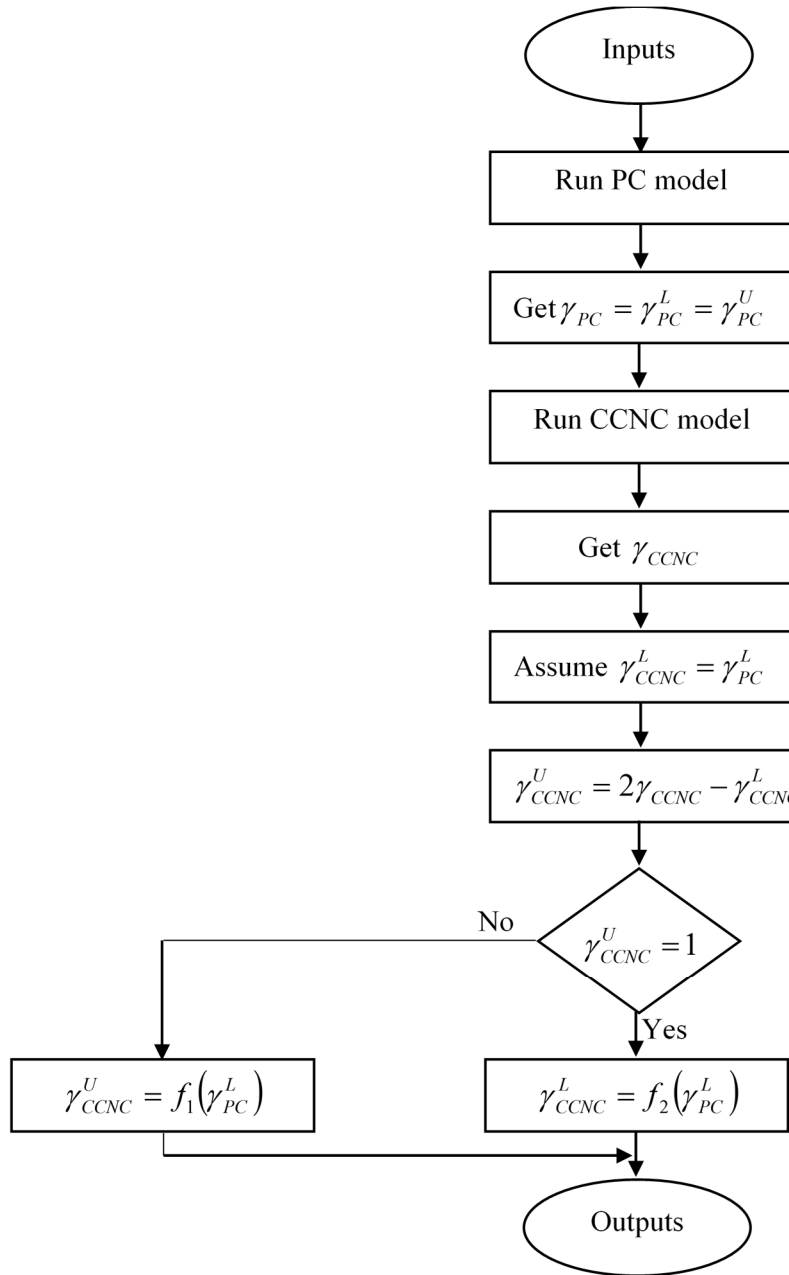
Figure 6.5: The procedure to develop the novel front tracking method

6.4.1.2 Logic verification

This section examines whether considering two different melting fronts for upper and lower halves of the system makes sense. To do so, two different upper half liquid fraction values of 0.5 and 1.0 were selected. Then, the corresponding CCNC and PC model results were verified to check how realistic such logic is. In Figure 6.6, each

93

contour shows the CCNC model results on the right, whereas the PC model results based on the novel front tracking method (for the upper and lower halves) are shown on the left. The figure shows how the real case melting front looks like when the assumed upper half values of 0.5 and 1.0 are achieved for Case 16 as an example. According to the contours, an acceptable visual agreement exists between the real cases and the upper half values of the front tracking method. Quantitatively, according to the simplified front tracking method results, the upper half liquid fraction values were 0.5 and 1.0 when the ones obtained from the CCNC model were 0.6009 and 0.9957, respectively. It should be noted that the deviation between the CCNC model and the novel method was found to decrease as more PCM melted due to the deceleration of natural convection. Therefore, the method can be useful for identifying partial melting of horizontal storages.
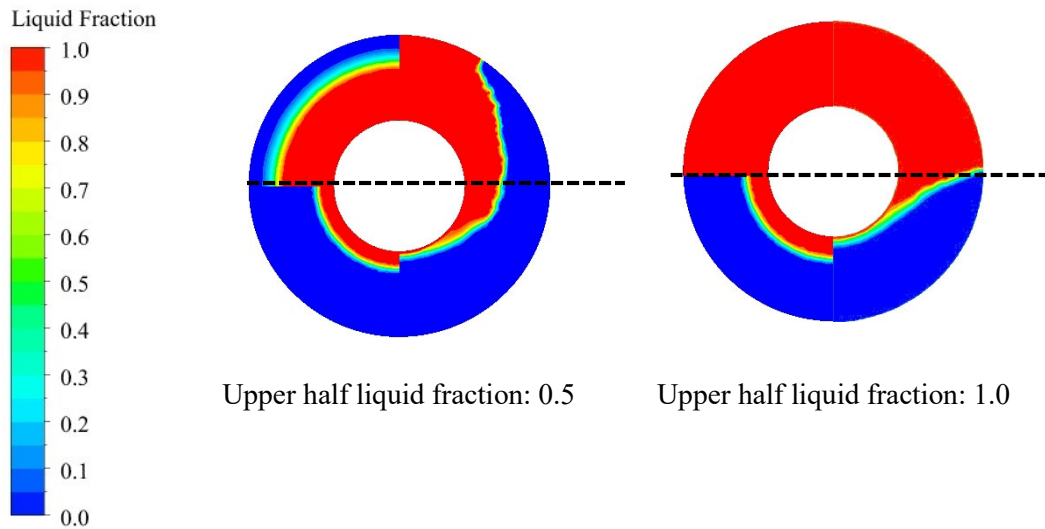
Figure 6.6: Logic verification where each contour shows the CCNC model (right) and the corresponding novel method results (left) for Case 16

6.4.2   Method flowchart

As mentioned in Section 6.4.1, the developed correlations are independent of time (i.e. Fourier number) and instead dependent on the liquid fraction of the PC model. Figure 6.7 shows the flowchart of the method for users. In order to generalize the flowcharts, the first decision symbol (i.e. the first diamond) compares the liquid and solid density values of the PCM. This is to make sure that the natural convection is designated

to the correct half of the system. For materials with lower liquid density (i.e. the current study) the buoyancy-induced motion is upward. However, for other materials such as water, the flow is downward.
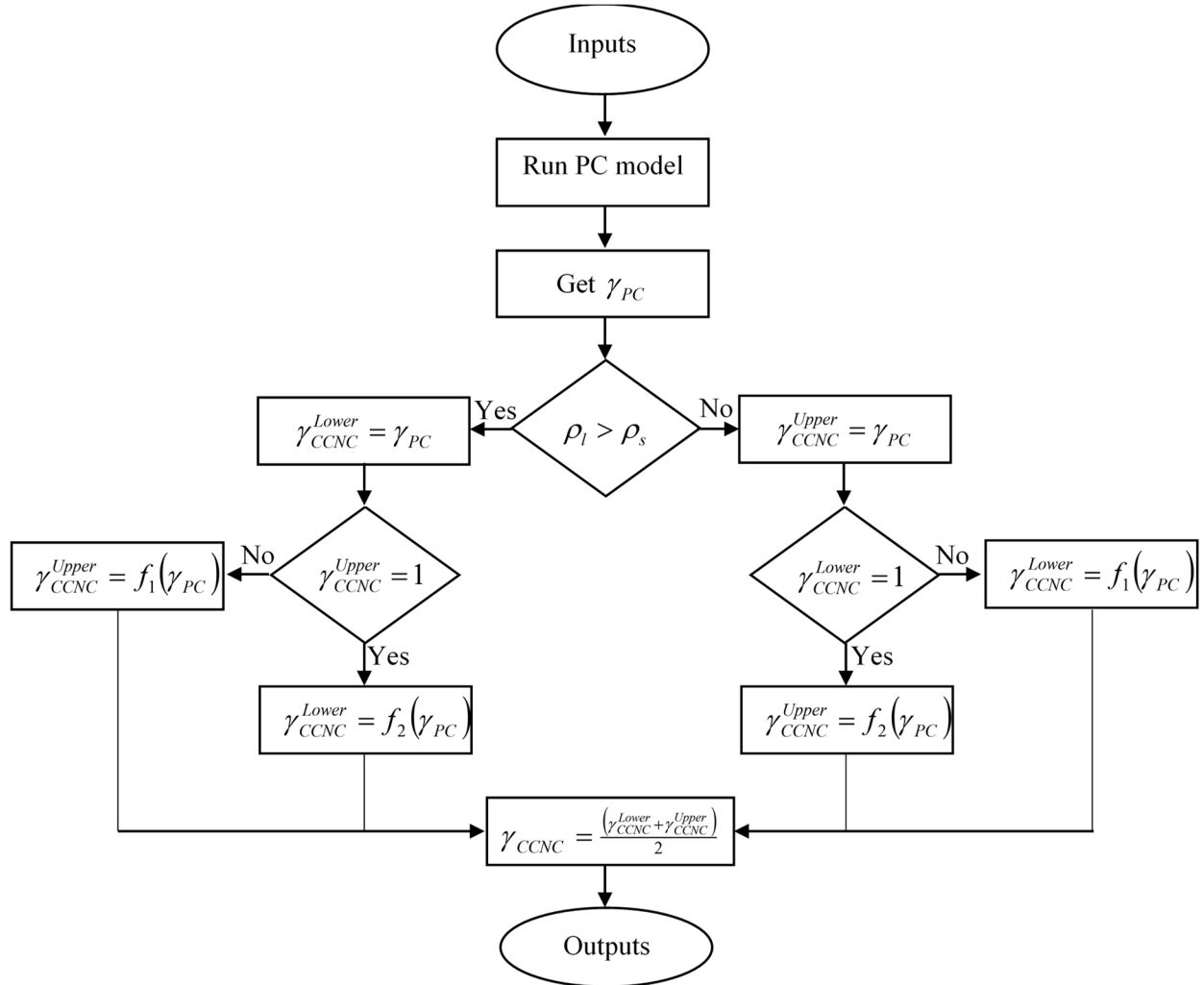
Figure 6.7: Flowchart of the novel front tracking method

6.4.3 Correlation development

In this section, the results for the upper and lower halves are presented, and based on them the respective correlations are developed.

6.4.3.1 Upper half correlation

Figure 6.8 shows the variation of upper half liquid fraction values versus those of the pure conduction model. Despite showing the results for different PCMs, the figure is dominated by three separate lines, each of which representing a geometry as presented in Table 6.1. Interestingly, the data for each geometry almost coincide, which confirms that the only effective parameter for the upper half liquid fraction versus that of the PC model is the geometrical properties of the system. In other words, the thermophysical properties of the PCMs have negligible effect. Therefore,

$$\gamma^U = c(R)^m (\gamma_{PC})^n \qquad (6.5)$$

where c, m and n are the three constants of the equation and R is the shell-to-tube radius ratio:

$$R = \frac{r_o}{r_i} \qquad (6.6)$$
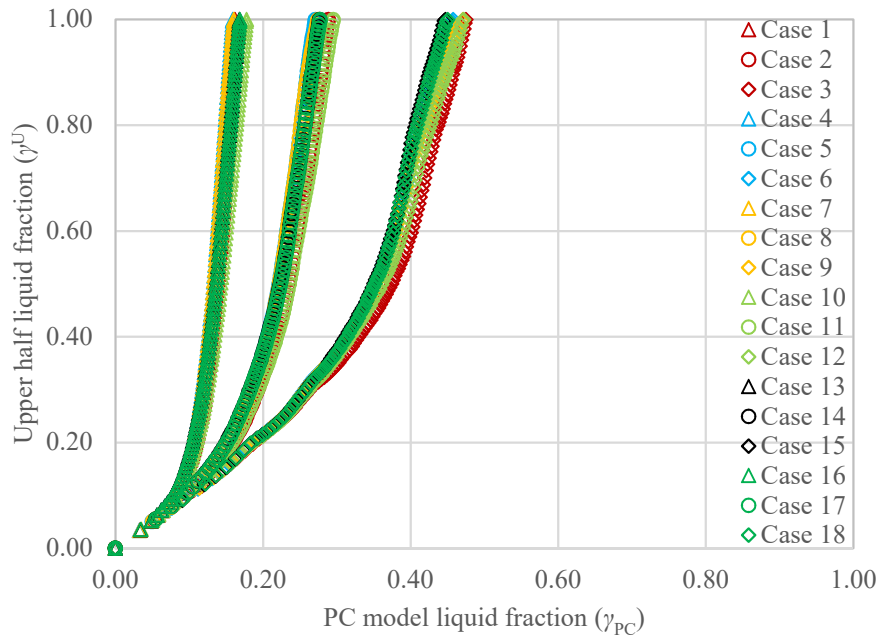
Figure 6.8: Variation of the upper half liquid fraction versus PC model liquid fraction

Regression results for all the cases are graphically shown in Figure 6.9 and the constants are tabulated in Table 6.4. The figure also shows that the majority of the data points (about 95%), lie within the range of ±15% discrepancy from the linear curve.
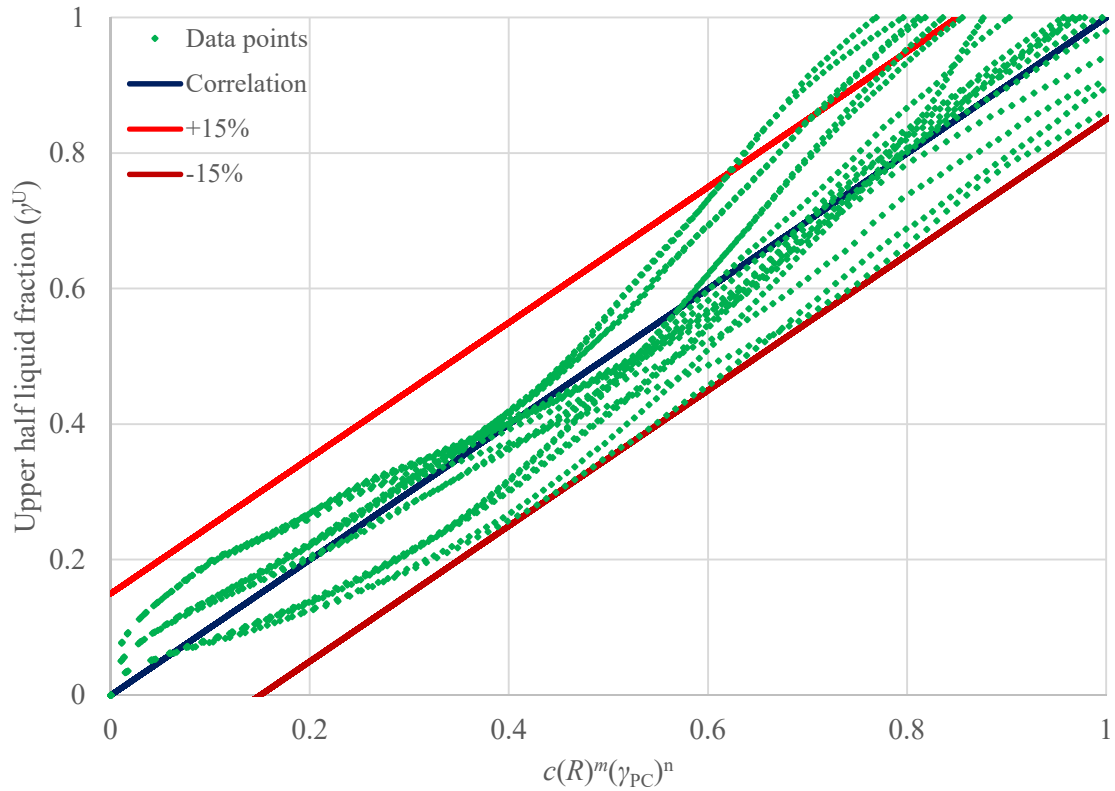
Figure 6.9: Variation of the upper half liquid fraction versus the developed correlation for all the cases

Table 6.4: Constants of Equation (6.5) for the upper half liquid fraction

c	*m*	*n*	*R²*	Range
3.981	3.747	2.553	0.9209	$R = 1.19 - 2.31$

6.4.3.2   Lower half correlation

Correlation development for the lower half is not as straightforward as the upper half. First of all, in order to use the same correlation format for the lower half, some modifications are required. The reason is graphically shown in Figure 6.10 for Case 17 as an example.
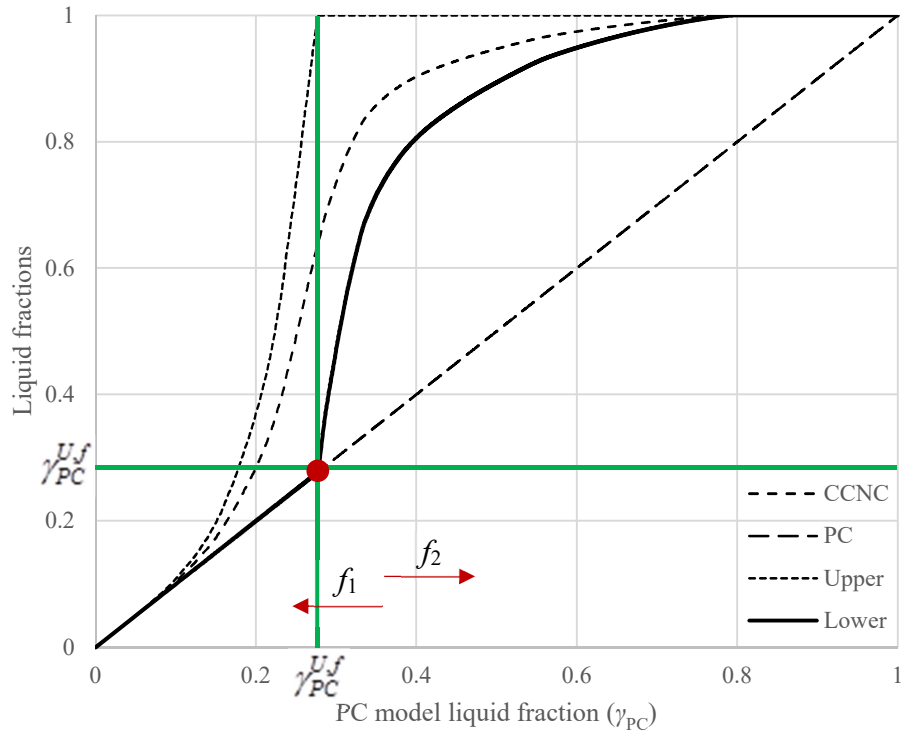
Figure 6.10: Liquid fraction variation for Case 17

According to Figure 6.10, since the lower half correlation (f_2) should initiate upon completion of melting in the upper half (shown by the vertical green line), its initial PC model liquid fraction value would be the last one of the upper half correlation (f_1). In other words, for each case, there is a different liquid fraction value of the PC model ($\gamma_{PC}^{U,f}$), upon which the upper half is completely melted, which is the starting point for the lower half correlation. To have consistency with the upper half, the coordinate of the origin should be transformed to that point (shown by a red dot). Consequently, for the horizontal and vertical axes, the values are modified so that the initial value for all the cases is zero, which would otherwise be different for each case, making the regression meaningless:

$$\gamma_{PC}^{mod} = \gamma_{PC} - \gamma_{PC}^{U,f}$$

(6.7)

$$\gamma^{L,mod} = \gamma^{L} - \gamma_{PC}^{U,f}$$

(6.8)

Another modification is related to the nature of conduction heat transfer. As the melting front propagates, the thermal resistance between the hot HTF tube and the melting front increases. Therefore, the heat transfer rate and consequently the rate of liquid fraction change decreases by time. Since this liquid fraction is used as the horizontal axis, whereas that of the lower half (which considers the effect of natural convection) is used as the vertical axis, after a certain period of time, the graph would become more and more vertical. The time when this happens (if any) depends on the thermophysical properties of the PCM, the geometrical properties of the thermal storage and the boundary conditions. To prevent complexity of the method and upon careful examination of the PC model data, it was found that prior to a certain time when the slope of PC model liquid fraction versus time is higher than 10^{-5}, a format close to that of the upper half could be utilized.

The variation of the modified lower half liquid fraction values versus the modified PC model results are shown in Figure 6.11. Again, three main separate lines exist in the figure per geometry; however, due to the vicinity of the data points they are barely distinguishable. Therefore, a similar format to that of the upper half is adopted:

$$\gamma^{L,mod} = c(R)^{m}\left(\gamma_{PC}^{mod}\right)^{n}$$

(6.9)
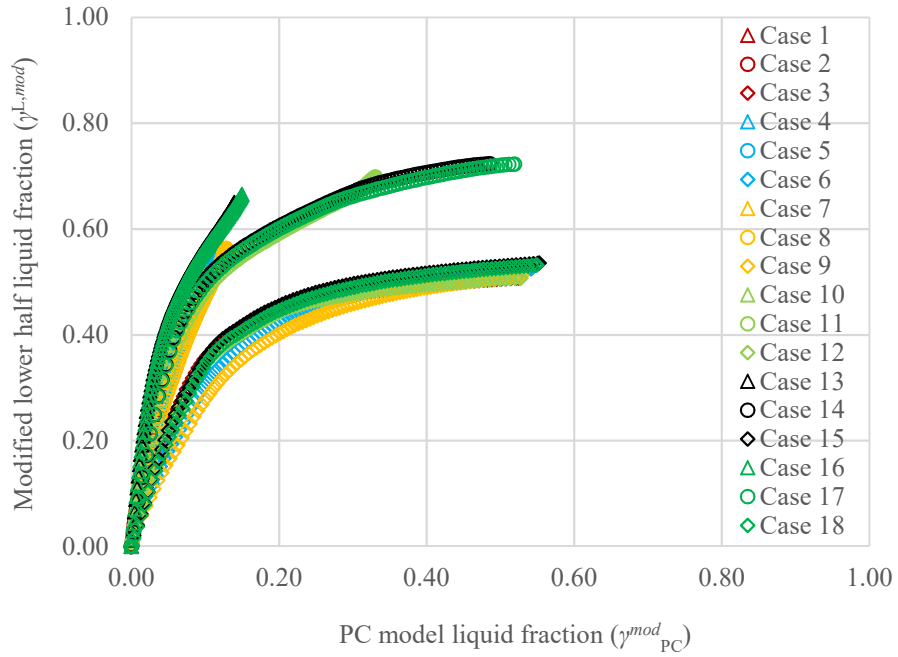
Figure 6.11: Variation of the modified lower half liquid fraction versus modified PC model liquid fraction

Figure 6.12 shows the regression results for all the cases and the obtained constants are shown in Table 6.5. The figure also shows that the majority of the data points (about 96%), lie within the range of ±10% discrepancy from the linear curve.
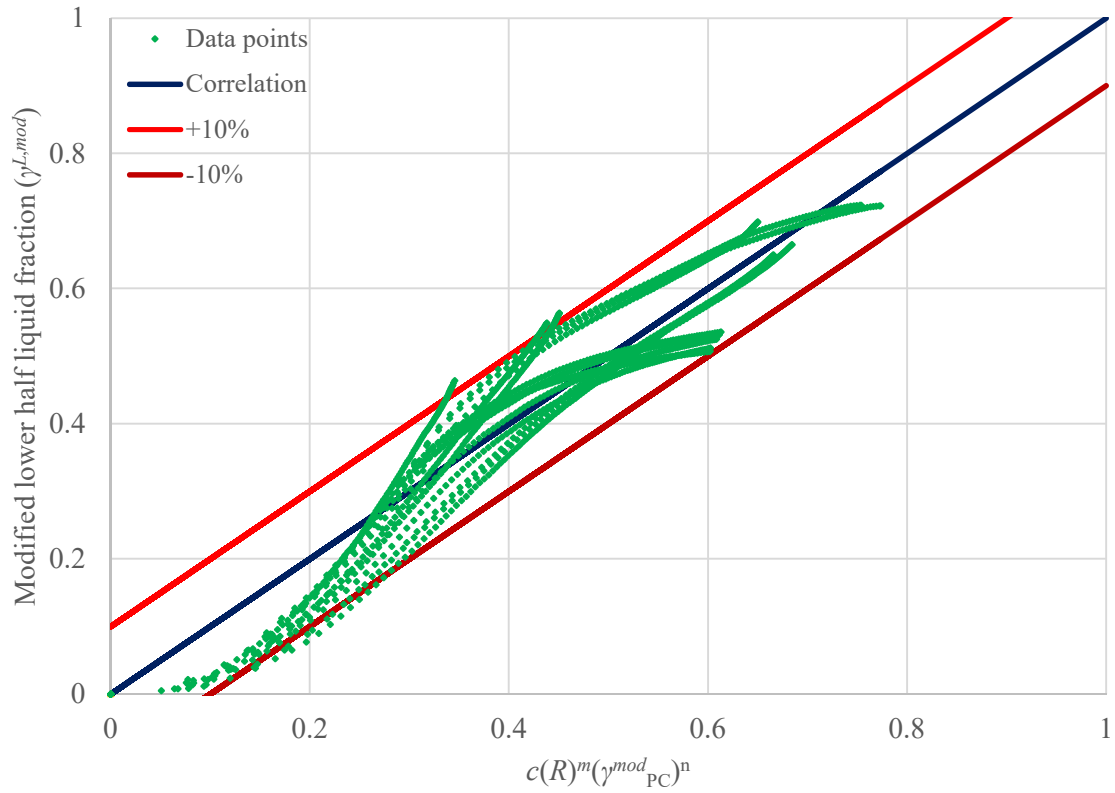
Figure 6.12: Variation of the modified lower half liquid fraction versus the developed correlation for all the cases

Table 6.5: Constants of Equation (6.9) for the modified lower half liquid fraction

c	m	n	R^2	Range
0.6558	0.9259	0.3857	0.8999	$R = 1.19 - 2.31$

6.4.4 Verification

Since the method was developed using the three PCMs presented in Table 6.2, its application should be verified by a new PCM. To examine the developed method, the correlations were used for a new PCM, RT35HC. Figure 6.13 shows the verification of the developed correlation for the upper half against the three verification cases (see Table 6.3). According to the figure, all data points lie within the range of ±15% discrepancy

from the linear curve (the correlation). The verification graph for the lower half is presented in Figure 6.14. Again, there is an acceptable agreement between the results from the correlation and the data points, which lie within the range of ±10% discrepancy.
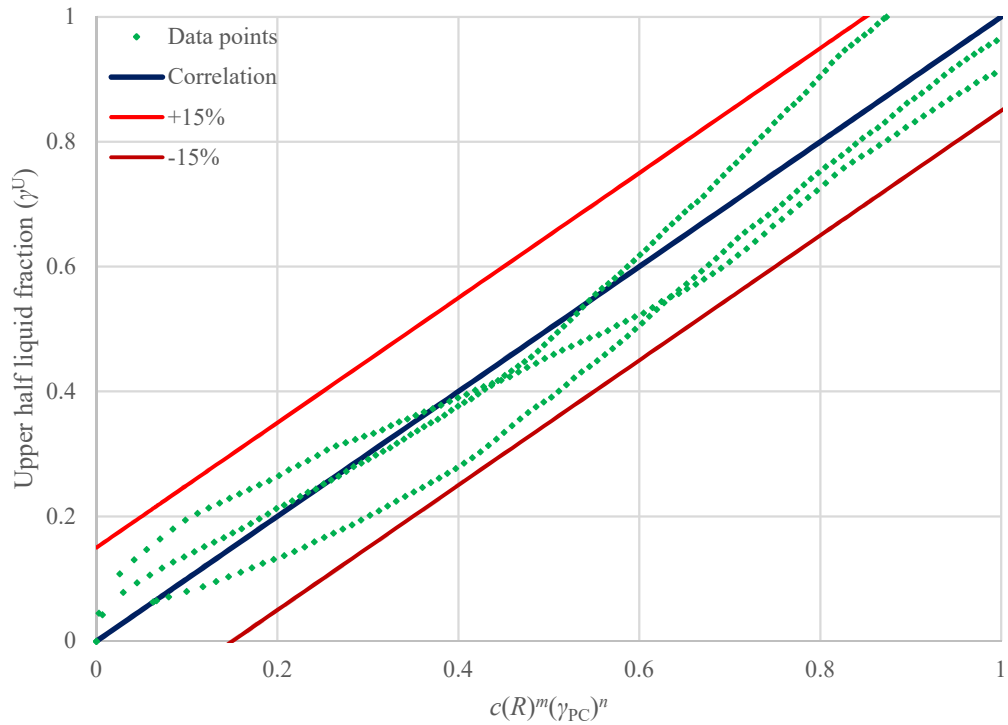
Figure 6.13: Verification of the developed correlation for the upper half liquid fraction
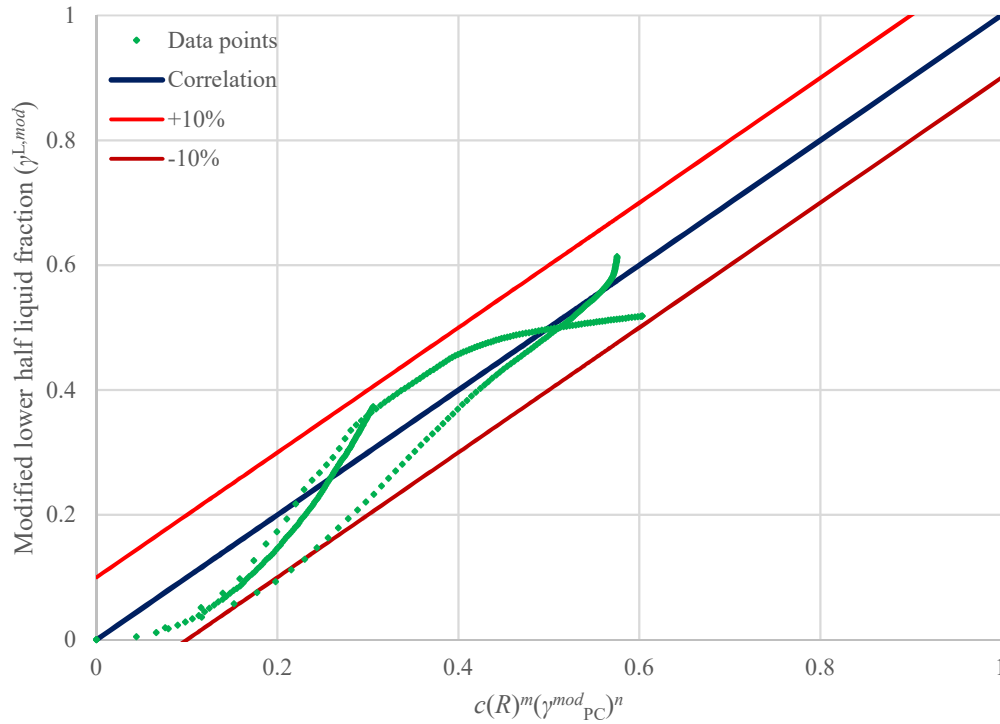
Figure 6.14: Verification of the developed correlation for the modified lower half liquid fraction

6.5   Concluding remarks

This chapter presented a simplified front tracking method, which considered the effect of natural convection during melting. Separate melting fronts were assumed for the upper and lower halves of the horizontal system and correlations were developed and verified. Interestingly, it was found that the thermophysical properties of the PCMs had negligible effect on the liquid fraction values of the upper and lower halves once they were correlated to the PC model liquid fractions instead of time (Fourier number). Therefore, the correlations were only functions of the shell-to-tube radius ratio and the PC model liquid fraction values. The main benefits of the novel front tracking method are:

- Compared to the effective thermal conductivity method, the presented method is not only simpler, but also provides information about the melting front location,
- The novel method provides identification of partial melting, which is greatly important for horizontal storages,

- The correlations are developed based on dimensionless parameters of shell-to-tube radius ratio as well as the liquid fraction of PC model (the latter is used instead of Fourier number),

- The location of the melting front is compatible with reality and can be more accurately tracked compared to the hypothetical PC model,

- Method users benefit from avoiding the complicated CCNC model and yet obtain acceptably accurate results (within maximum 15% discrepancy).

Chapter 7: Conclusions and recommendations for future work

7.1 Summary and conclusions

Thermal energy storage using phase change materials have found considerable attention in recent years. Therefore, understanding the heat transfer mechanism is greatly important, particularly, natural convection which was the focus of this study. In this dissertation, first, the heat transfer mechanism under SCD in a TTHX was investigated for both internal-heating/external-cooling and internal-cooling/external-heating. The conclusions of this investigation can be summarized as:

- For the case of internal-heating/external-cooling, natural convection did not affect the lower half of the system since it had almost similar temperature distribution; however, the upper half was greatly affected by the buoyancy forces and natural convection of the melted PCM. On the other hand, for the case of internal-cooling/external-heating, the buoyancy-induced upward PCM motion affected the entire domain.

- Depending on the initial condition of the PCM, different liquid fraction, temperature and solid-liquid interface locations were observed, which was totally different from the results obtained from the pure conduction model. This shows how unrealistic is such an assumption and to have accurate modeling of SCD, natural convection must be taken into account.

- Comparing the average temperature and liquid fraction results, it was found that the pure conduction model could be applied to the initially fully melted PCMs under SCD with small error, but for the initially solidified PCMs neglecting the natural convection would result in unacceptably high error.

Thereafter, since for internal-heating/external-cooling, the lower half of the system was not affected by the upward melted PCM motion (i.e. natural convection), different fin configurations were investigated to enhance the heat transfer to the lower half. It was found that:

- For systems with SCD applications, the recommended fin configuration includes one external and three internal fins. The internal fins should be located at the bottom of the system where one fin is vertically positioned at the bottom and two others are located at an angle of 45° on both sides of it. The external fin should be vertically located at the upper half of the system.

- For systems with non-SCD applications having both sides heat transfer, the recommended fin configuration includes four internal fins and four external fins. The internal fins should include two vertical and two horizontal fins, while the external fins should make an angle of 45° with internal ones.

- For systems with non-SCD applications having one side heat transfer, the recommended fin configuration includes five external fins (at 0°, 45°, 90°, 135° and 180°) at the upper half and three internal fins (at 225°, 270° and 315°) at the lower half of the system.

- Under SCD conditions, the effect of fin thickness was negligible. However, their number and length enhanced the heat transfer as long as the fins did not suppress the natural convection.

Finally, a simplified front tracking method was developed to consider the effect of natural convection in a STHX. The method should compete with thermal conductivity method. The main advantages of the method include:

- Compared to the effective thermal conductivity method, the presented method is not only simpler, but also provides information about the melting front location,

- The novel method provides identification of partial melting, which is greatly important for horizontal storages,

- The correlations are developed based on dimensionless parameters of shell-to-tube radius ratio as well as the liquid fraction of PC model (the latter is used instead of Fourier number),

- The location of the melting front is compatible with reality and can be more accurately tracked compared to the hypothetical PC model,

- Users benefit from avoiding the complicated CCNC model and yet obtain acceptably accurate results (within maximum 15% discrepancy).

7.2 Future work recommendations

According to the objectives, results and limitations of this dissertation, the main recommended future research works include:

- Since this study was focused on horizontal storages only, SCD in vertical storages needs to be investigated. Furthermore, development of a similar simplified front tracking method for vertical storages would be useful, if possible.

- This study investigated the heat transfer mechanism in a TTHX with a PCM under SCD. This needs to be extended to cover other types of storage and other types of PCM. Conducting a parametric study would be greatly useful in this regard.

- The numerical model was developed for a 2D cross-sectional area of a TTHX, forming a PCM annulus. Besides, since the problem was symmetric, half of the annulus was modeled to save computational time. Development of a comprehensive 3D model, which can also provide information about HTF side would be required.

- The simplified front tracking method should be extended to include simultaneous charging and discharging as well. This is challenging since unlike a STHX, in a TTHX, heat transfer occurs with two separate surfaces, simultaneously. Consequently, the propagation of melting front is controlled by the heat source as well as the heat sink.

References

[1] Canada's Energy Future 2013: Energy Supply and Demand Projection to 2035, in, National Energy Board, 2013.

[2] Survey of Commercial and Institutional Energy Use – Buildings 2009, in, Natural Resources Canada's Office of Energy Efficiency, Ottawa, Canada, 2012.

[3] S. Seddegh, X. Wang, A.D. Henderson, A comparative study of thermal behaviour of a horizontal and vertical shell-and-tube energy storage using phase change materials, Applied Thermal Engineering, 93 (2016) 348-358.

[4] D.N. Nkwetta, F. Haghighat, Thermal energy storage with phase change material—a state-of-the art review, Sustainable Cities and Society, 10 (2014) 87-100.

[5] P.A. Mirzaei, F. Haghighat, Modeling of phase change materials for applications in whole building simulation, Renewable and Sustainable Energy Reviews, 16 (7) (2012) 5355-5362.

[6] A. El-Sawi, F. Haghighat, H. Akbari, Assessing long-term performance of centralized thermal energy storage system, Applied Thermal Engineering, 62 (2) (2014) 313-321.

[7] M.M. Joybari, F. Haghighat, J. Moffat, P. Sra, Heat and cold storage using phase change materials in domestic refrigeration systems: The state-of-the-art review, Energy and Buildings, 106 (2015) 111-124.

[8] A. Bastani, F. Haghighat, Expanding Heisler chart to characterize heat transfer phenomena in a building envelope integrated with phase change materials, Energy and Buildings, 106 (2015) 164-174.

[9] A. Najafian, F. Haghighat, A. Moreau, Integration of PCM in domestic hot water tanks: Optimization for shifting peak demand, Energy and Buildings, 106 (2015) 59-64.

[10] S. Seddegh, X. Wang, A.D. Henderson, Numerical investigation of heat transfer mechanism in a vertical shell and tube latent heat energy storage system, Applied Thermal Engineering, 87 (2015) 698-706.

[11] N. Tay, M. Belusko, F. Bruno, An effectiveness-NTU technique for characterising tube-in-tank phase change thermal energy storage systems, Applied Energy, 91 (1) (2012) 309-319.

[12] M.M. Joybari, F. Haghighat, Natural convection modelling of melting in phase change materials: Development of a novel zonal effectiveness-NTU, in: 9th International Conference on Indoor Air Quality Ventilation and Energy Conservation In Buildings (IAQVEC 2016), Incheon Songdo, South Korea, 2016.

[13] A.A. Al-Abidi, S. Mat, K. Sopian, M. Sulaiman, A.T. Mohammad, Experimental Investigation of Melting in Triplex Tube Thermal Energy Storage, (2013).

[14] X. Sun, Q. Zhang, M.A. Medina, K.O. Lee, Experimental observations on the heat transfer enhancement caused by natural convection during melting of solid–liquid phase change materials (PCMs), Applied Energy, 162 (2016) 1453-1461.

[15] N. Tay, F. Bruno, M. Belusko, Experimental validation of a CFD and an ε-NTU model for a large tube-in-tank PCM system, International Journal of Heat and Mass Transfer, 55 (21) (2012) 5931-5940.

[16] J. Yang, L. Yang, C. Xu, X. Du, Experimental study on enhancement of thermal energy storage with phase-change material, Applied Energy, 169 (2016) 164-176.

[17] A.A. Al-Abidi, S. Mat, K. Sopian, M. Sulaiman, A.T. Mohammad, Internal and external fin heat transfer enhancement technique for latent heat thermal energy storage in triplex tube heat exchangers, Applied Thermal Engineering, 53 (1) (2013) 147-156.

[18] Y. Zeng, L.-W. Fan, Y.-Q. Xiao, Z.-T. Yu, K.-F. Cen, An experimental investigation of melting of nanoparticle-enhanced phase change materials (NePCMs) in a bottom-heated vertical cylindrical cavity, International Journal of Heat and Mass Transfer, 66 (2013) 111-117.

[19] D. Sun, S.R. Annapragada, S.V. Garimella, Experimental and numerical study of melting of particle-laden materials in a cylinder, International Journal of Heat and Mass Transfer, 52 (13) (2009) 2966-2978.

[20] L.-W. Fan, Z.-Q. Zhu, Y. Zeng, Q. Lu, Z.-T. Yu, Heat transfer during melting of graphene-based composite phase change materials heated from below, International Journal of Heat and Mass Transfer, 79 (2014) 94-104.

[21] T.K. Aldoss, M.M. Rahman, Comparison between the single-PCM and multi-PCM thermal energy storage design, Energy Conversion and Management, 83 (2014) 79-87.

[22] F. Agyenim, P. Eames, M. Smyth, A comparison of heat transfer enhancement in a medium temperature thermal energy storage heat exchanger using fins, Solar Energy, 83 (9) (2009) 1509-1520.

[23] R.E. Murray, D. Groulx, Experimental study of the phase change and energy characteristics inside a cylindrical latent heat energy storage system: Part 1 consecutive charging and discharging, Renewable Energy, 62 (2014) 571-581.

[24] P. Wang, H. Yao, Z. Lan, Z. Peng, Y. Huang, Y. Ding, Numerical investigation of PCM melting process in sleeve tube with internal fins, Energy Conversion and Management, 110 (2016) 428-435.

[25] U. Stritih, An experimental study of enhanced heat transfer in rectangular PCM thermal storage, International Journal of Heat and Mass Transfer, 47 (12) (2004) 2841-2847.

[26] C. Liu, D. Groulx, Experimental study of the phase change heat transfer inside a horizontal cylindrical latent heat energy storage system, International Journal of Thermal Sciences, 82 (2014) 100-110.

[27] Z. Liu, Z. Wang, C. Ma, An experimental study on the heat transfer characteristics of a heat pipe heat exchanger with latent heat storage. Part II: Simultaneous charging/discharging modes, Energy Conversion and Management, 47 (7) (2006) 967-991.

[28] R.E. Murray, D. Groulx, Experimental study of the phase change and energy characteristics inside a cylindrical latent heat energy storage system: Part 2 simultaneous charging and discharging, Renewable Energy, 63 (2014) 724-734.

[29] P. Omojaro, C. Breitkopf, Investigating and Modeling of Simultaneous Charging and Discharging of a PCM Heat Exchanger, Energy Procedia, 48 (2014) 413-422.

[30] A.A. Al-Abidi, S. Mat, K. Sopian, M. Sulaiman, A.T. Mohammad, Numerical study of PCM solidification in a triplex tube heat exchanger with internal and external fins, International Journal of Heat and Mass Transfer, 61 (2013) 684-695.

[31] J.-Y. Long, D.-S. Zhu, Numerical and experimental study on heat pump water heater with PCM for thermal storage, Energy and Buildings, 40 (4) (2008) 666-672.

[32] L. Jian-you, Numerical and experimental investigation for heat transfer in triplex concentric tube with phase change material for thermal energy storage, Solar Energy, 82 (11) (2008) 977-985.

[33] S. Mat, A.A. Al-Abidi, K. Sopian, M. Sulaiman, A.T. Mohammad, Enhance heat transfer for PCM melting in triplex tube with internal–external fins, Energy Conversion and Management, 74 (2013) 223-236.

[34] A.A. Al-Abidi, S. Mat, K. Sopian, M. Sulaiman, A.T. Mohammad, Experimental study of melting and solidification of PCM in a triplex tube heat exchanger with fins, Energy and Buildings, 68 (2014) 33-41.

[35] A.A. Al-Abidi, S. Mat, K. Sopian, M. Sulaiman, A.T. Mohammad, Experimental study of PCM melting in triplex tube thermal energy storage for liquid desiccant air conditioning system, Energy and Buildings, 60 (2013) 270-279.

[36] N. Amin, F. Bruno, M. Belusko, Effective thermal conductivity for melting in PCM encapsulated in a sphere, Applied Energy, 122 (2014) 280-287.

[37] E. Sparrow, J. Broadbent, Inward melting in a vertical tube which allows free expansion of the phase-change medium, ASME Journal of Heat Transfer, 104 (2) (1982) 309-315.

[38] B.J. Jones, D. Sun, S. Krishnan, S.V. Garimella, Experimental and numerical study of melting in a cylinder, International Journal of Heat and Mass Transfer, 49 (15) (2006) 2724-2738.

[39] V.R. Voller, C. Prakash, A fixed grid numerical modelling methodology for convection-diffusion mushy region phase-change problems, International Journal of Heat and Mass Transfer, 30 (8) (1987) 1709-1719.

[40] C.-Y. Li, S.V. Garimella, J.E. Simpson, Fixed-grid front-tracking algorithm for solidification problems, part I: Method and validation, Numerical Heat Transfer, Part B: Fundamentals, 43 (2) (2003) 117-141.

[41] D. Riley, F. Smith, G. Poots, The inward solidification of spheres and circular cylinders, International Journal of Heat and Mass Transfer, 17 (12) (1974) 1507-1516.

[42] A. Solomon, Melt time and heat flux for a simple PCM body, Solar Energy, 22 (3) (1979) 251-257.

[43] A. Hasan, Phase change material energy storage system employing palmitic acid, Solar Energy, 52 (2) (1994) 143-154.

[44] A. Hasan, Thermal energy storage system with stearic acid as phase change material, Energy Conversion and Management, 35 (10) (1994) 843-856.

[45] K.A. Ismail, E. Maria das Graças, Melting of PCM around a horizontal cylinder with constant surface temperature, International Journal of Thermal Sciences, 42 (12) (2003) 1145-1152.

[46] L. Katsman, V. Dubovsky, G. Ziskind, R. Letan, Experimental Investigation of Solid-Liquid Phase Change in Cylindrical Geometry, in: ASME/JSME 2007 Thermal Engineering Heat Transfer Summer Conference collocated with the ASME 2007 InterPACK Conference, American Society of Mechanical Engineers, 2007, pp. 239-244.

[47] R.M. K, B. Jyotirmay, Development of Correlation for Melting Time of Phase Change Material in Latent Heat Storage Unit, Energy Procedia, 75 (2015) 2125-2130.

[48] A.R. Darzi, M. Farhadi, K. Sedighi, Numerical study of melting inside concentric and eccentric horizontal annulus, Applied Mathematical Modelling, 36 (9) (2012) 4080-4086.

[49] ANSYS Fluent User's Guide, ANSYS Inc., Canonsburg, PA, USA, 2013.

[50] A.A. Al-abidi, S.B. Mat, K. Sopian, M. Sulaiman, A.T. Mohammed, CFD applications for latent heat thermal energy storage: a review, Renewable and sustainable energy reviews, 20 (2013) 353-363.

[51] ANSYS Fluent Theory Guide, ANSYS, Inc., Canonsburg, PA, USA, 2013.

[52] S. Seddegh, M.M. Joybari, X. Wang, F. Haghighat, Investigation of the effect of geometric and operating parameters on thermal behavior of vertical shell-and-tube latent heat energy storage systems, Under Review.

[53] The Copper Tube Handbook, Copper Development Association Inc., New York, NY, USA, 2011.

[54] RT31 Data sheet, in, Rubitherm Technologies GmbH, 2013.

[55] Rubitherm Technologies GmbH, in: Organic PCM, http://www.rubitherm.eu/en/index.php/productcategory/organische-pcm-rt/, Berlin, Germany, 2017.

[56] Energy Use Data Handbook, in, National Resources Canada, Ottawa, Canada, 2011.

[57] Statistics Canada, Canadian households in 2011: Type and growth, in, 2012.

[58] A. Marques, G. Davies, G. Maidment, J. Evans, I. Wood, Novel design and performance enhancement of domestic refrigerators with thermal storage, Applied Thermal Engineering, 63 (2) (2014) 511-519.

[59] W.-L. Cheng, B.-J. Mei, Y.-N. Liu, Y.-H. Huang, X.-D. Yuan, A novel household refrigerator with shape-stabilized PCM (Phase Change Material) heat storage condensers: An experimental investigation, Energy, 36 (10) (2011) 5797-5804.

[60] ASHRAE, Household Refrigerators and Freezers, 2010 ASHRAE Handbook: Refrigeration, American Society of Heating, Refrigerating Air-Conditioning Engineers, Atlanta, 2010.

[61] A.C. Marques, G.F. Davies, J.A. Evans, G.G. Maidment, I.D. Wood, Theoretical modelling and experimental investigation of a thermal energy storage refrigerator, Energy, 55 (0) (2013) 457-465.

[62] M.M. Joybari, M.S. Hatamipour, A. Rahimi, F.G. Modarres, Exergy analysis and optimization of R600a as a replacement of R134a in a domestic refrigerator system, International Journal of Refrigeration, 36 (4) (2013) 1233-1242.

[63] O. Ekren, S. Celik, B. Noble, R. Krauss, Performance evaluation of a variable speed DC compressor, International Journal of Refrigeration, 36 (3) (2013) 745-757.

[64] Y.C. Park, Transient analysis of a variable speed rotary compressor, Energy Conversion and Management, 51 (2) (2010) 277-287.

[65] C. Cuevas, J. Lebrun, Testing and modelling of a variable speed scroll compressor, Applied Thermal Engineering, 29 (2) (2009) 469-478.

[66] K. Liang, R. Stone, G. Davies, M. Dadd, P. Bailey, Modelling and measurement of a moving magnet linear compressor performance, Energy, 66 (2014) 487-495.

[67] H. Kim, C.-G. Roh, J.-K. Kim, J.-M. Shin, Y. Hwang, J.-K. Lee, An experimental and numerical study on dynamic characteristic of linear compressor in refrigeration system, International Journal of Refrigeration, 32 (7) (2009) 1536-1543.

[68] E. Hammond, J. Evans, Application of Vacuum Insulation Panels In the cold chain–Analysis of Viability, International Journal of Refrigeration, (2014).

[69] W.-H. Tao, C.-C. Chang, J.-Y. Lin, An Energy-Efficiency, Performance Study of, Vacuum Insulation Panels, Journal of Cellular Plastics, 36 (6) (2000) 441-450.

[70] M.I.H. Khan, H.M. Afroz, Effect of Phase Change Material on Performance of a Household Refrigerator, Asian Journal of Applied Sciences, 6 (2) (2013) 56-67.

[71] D.C. Onyejekwe, Cold storage using eutectic mixture of NaCl/H2O: An application to photovoltaic compressor vapour freezers, Solar & wind technology, 6 (1) (1989) 11-18.

[72] G. Cerri, A. Palmieri, E. Monticelli, D. Pezzoli, Identification of domestic refrigerator models including cool storage, in: International Congress of refrigeration, Washington DC, 2003.

[73] E. Maltini, G. Cortella, M. Stecchini, M. Del Torre, P. Pittia, M. Spaziani, G. Mansutti, Design and performances of a constant temperature compartment for domestic refrigerator, in: International Congress on Engineering and Food, Montpellier, 2004.

[74] K. Azzouz, D. Leducq, J. Guilpart, D. Gobin, Improving the energy efficiency of a vapor compression system using a phase change material, in: Second Conference on Phase Change Material and Slurry: Scientific Conference and Business Forum, 2005, pp. 15-17.

[75] F. Wang, G. Maidment, J. Missenden, R. Tozer, The novel use of phase change materials in refrigeration plant. Part 1: Experimental investigation, Applied Thermal Engineering, 27 (17) (2007) 2893-2901.

[76] F. Wang, G. Maidment, J. Missenden, R. Tozer, The novel use of phase change materials in refrigeration plant. Part 2: Dynamic simulation model for the combined system, Applied Thermal Engineering, 27 (17) (2007) 2902-2910.

[77] F. Wang, G. Maidment, J. Missenden, R. Tozer, The novel use of phase change materials in refrigeration plant. Part 3: PCM for control and energy savings, Applied Thermal Engineering, 27 (17) (2007) 2911-2918.

[78] K. Azzouz, D. Leducq, D. Gobin, Performance enhancement of a household refrigerator by addition of latent heat storage, International Journal of Refrigeration, 31 (5) (2008) 892-901.

[79] K. Azzouz, D. Leducq, D. Gobin, Enhancing the performance of household refrigerators with latent heat storage: an experimental investigation, international Journal of Refrigeration, 32 (7) (2009) 1634-1644.

[80] P. Subramaniam, C. Tulapurkar, R. Thiyagarajan, G. Thangamani, Phase change materials for domestic refrigerators to improve food quality and prolong compressor off time, in: International Refrigeration and Air Conditioning Conference at Purdue, 2010.

[81] B. Gin, M. Farid, P. Bansal, Effect of door opening and defrost cycle on a freezer with phase change panels, Energy Conversion and Management, 51 (12) (2010) 2698-2706.

[82] B. Gin, M.M. Farid, The use of PCM panels to improve storage condition of frozen food, Journal of Food Engineering, 100 (2) (2010) 372-376.

[83] B. Gin, M.M. Farid, P. Bansal, Modeling of phase change material implemented into cold storage application, HVAC&R Research, 17 (3) (2011) 257-267.

[84] M. Berdja, B. Abbad, M. Laidi, F. Yahi, M. Ouali, Numerical Simulation Of A Phase Change Material (PCM) In A Domestic Refrigerator Powered By Photovoltaic Energy, ICHMT Digital Library Online, (2012).

[85] E. Oró, L. Miró, M.M. Farid, L.F. Cabeza, Improving thermal performance of freezers using phase change materials, International Journal of Refrigeration, 35 (4) (2012) 984-991.

[86] E. Oró, L. Miró, M.M. Farid, L.F. Cabeza, Thermal analysis of a low temperature storage unit using phase change materials without refrigeration system, International Journal of Refrigeration, 35 (6) (2012) 1709-1714.

[87] M.K. Sharma, D. Buddhi, Temperature Variation and Energy Performance with or without PCM due to Introduction of Heat Loads, Journal of Alternate Energy Sources and Technologies, 3 (2) (2012) 19-38.

[88] W.-L. Cheng, X.-D. Yuan, Numerical analysis of a novel household refrigerator with shape-stabilized PCM (phase change material) heat storage condensers, Energy, 59 (2013) 265-276.

[89] M.I.H. Khan, H.M. Afroz, Experimental investigation of performance improvement if household refrigerator using phase change material, International Journal of Air-Conditioning and Refrigeration, 21 (04) (2013).

[90] E. Oró, A. de Gracia, L.F. Cabeza, Active phase change material package for thermal protection of ice cream containers, International Journal of Refrigeration, 36 (1) (2013) 102-109.

[91] J. Taneja, K. Lutz, D. Culler, Flexible loads in future energy networks, in: Proceedings of the fourth international conference on Future energy systems, ACM, Berkeley, California, USA, 2013, pp. 285-286.

[92] J. Taneja, K. Lutz, D. Culler, The impact of flexible loads in increasingly renewable grids, in: 2013 IEEE International Conference on Smart Grid Communications (SmartGridComm), IEEE, 2013, pp. 265-270.

[93] M.I.H. Khan, H.M. Afroz, Diminution of Temperature Fluctuation Inside the Cabin of a Household Refrigerator Using Phase Change Material, Recent advances in Mechanical Engineering (IJMECH), 3 (1) (2014) 43-52.

[94] M. Rahman, A. Hossain, S.K. Das, R. Adnan Hasan, Performance Improvement of a Domestic Refrigerator by using PCM (Phase Change Material), Global Journal of Researches In Engineering, 13 (10) (2014).

[95] M. Visek, C.M. Joppolo, L. Molinaroli, A. Olivani, Advanced sequential dual evaporator domestic refrigerator/freezer: System energy optimization, International Journal of Refrigeration, (2014).

[96] X.-D. Yuan, W.-L. Cheng, Multi-objective optimization of household refrigerator with novel heat-storage condensers by Genetic algorithm, Energy Conversion and Management, 84 (2014) 550-561.

[97] E. Oró, A. De Gracia, A. Castell, M. Farid, L. Cabeza, Review on phase change materials (PCMs) for cold thermal energy storage applications, Applied Energy, 99 (2012) 513-533.

[98] F. Wang, G. Maidment, J. Missenden, R. Tozer, A review of research concerning the use of PCMs in air conditioning and refrigeration engineering, Advances in Building Technology, 2 (2002) 1273-1280.

[99] A. Sharma, V. Tyagi, C. Chen, D. Buddhi, Review on thermal energy storage with phase change materials and applications, Renewable and Sustainable energy reviews, 13 (2) (2009) 318-345.

[100] G. Li, Y. Hwang, R. Radermacher, H.-H. Chun, Review of cold storage materials for subzero applications, Energy, 51 (2013) 1-17.

[101] H. Paksoy, S. Yilmaz, O. Gok, M.O. Yilmaz, M. Mazma, H. Evlia, Thermal Energy Storage for More Efficient Domestic Appliances, in: World Energy Congress, Montreal, Canada, 2010.

[102] A. Bastani, F. Haghighat, J. Kozinski, Designing building envelope with PCM wallboards: Design tool development, Renewable and Sustainable Energy Reviews, 31 (2014) 554-562.

[103] F. Agyenim, N. Hewitt, The development of a finned phase change material (PCM) storage system to take advantage of off-peak electricity tariff for improvement in cost of heat pump operation, Energy and Buildings, 42 (9) (2010) 1552-1560.

[104] P. Finn, C. Fitzpatrick, D. Connolly, M. Leahy, L. Relihan, Facilitation of renewable electricity using price based appliance control in Ireland's electricity market, Energy, 36 (5) (2011) 2952-2960.

[105] M.A. Zehir, M. Bagriyanik, Demand side management by controlling refrigerators and its effects on consumers, Energy Conversion and Management, 64 (2012) 238-244.

[106] H.S. Han, W.B. Jeong, M.S. Kim, S.Y. Lee, M.Y. Seo, Reduction of the refrigerant-induced noise from the evaporator-inlet pipe in a refrigerator, International Journal of Refrigeration, 33 (7) (2010) 1478-1488.

[107] S. Celik, E.C. Nsofor, Studies on the flow-induced noise at the evaporator of a refrigerating system, Applied Thermal Engineering, 31 (14) (2011) 2485-2493.

[108] D. Hartmann, C. Melo, Popping noise in household refrigerators: Fundamentals and practical solutions, Applied Thermal Engineering, 51 (1) (2013) 40-47.

[109] E. Oró, L. Miró, M.M. Farid, V. Martin, L.F. Cabeza, Energy management and CO2 mitigation using phase change materials (PCM) for thermal energy storage (TES) in cold storage and transport, International Journal of Refrigeration, 42 (0) (2014) 26-35.

[110] W.-L. Cheng, R.-M. Zhang, K. Xie, N. Liu, J. Wang, Heat conduction enhanced shape-stabilized paraffin/HDPE composite PCMs by graphite addition: preparation and thermal properties, Solar Energy Materials and Solar Cells, 94 (10) (2010) 1636-1642.

[111] S. Bendapudi, J.E. Braun, A review of literature on dynamic models of vapor compression equipment, 2002.

[112] B.D. Rasmussen, A. Jakobsen, Review of compressor models and performance characterizing variables, (2000).

[113] G.-l. Ding, Recent developments in simulation techniques for vapour-compression refrigeration systems, International Journal of Refrigeration, 30 (7) (2007) 1119-1133.

[114] A. Maia, R. Koury, L. Machado, Development of a control algorithm employing data generated by a white box mathematical model, Applied Thermal Engineering, 54 (1) (2013) 120-130.

[115] S. Porkhial, B. Khastoo, M. Saffar-Avval, Transient response of dry expansion evaporator in household refrigerators, Applied Thermal Engineering, 24 (10) (2004) 1465-1480.

[116] M. Ahmed, O. Meade, M.A. Medina, Reducing heat transfer across the insulated walls of refrigerated truck trailers by the application of phase change materials, Energy Conversion and Management, 51 (3) (2010) 383-392.

[117] EIA, Monthly Energy Review June 2015, in: United States Energy Information Administration (EIA), U.S. Department of Energy, Washington, DC, USA, 2015.

[118] EIA, Commercial Buildings Energy Consumption Survey (CBECS), in: United States Energy Information Administration (EIA), U.S. Department of Energy, Washington, DC, USA, 2012.

[119] EIA, Annual Energy Outlook 2014 With Projections To 2040, in: United States Energy Information Administration (EIA), U.S. Department of Energy, Washington, DC, USA, 2014.

[120] I. Dincer, M.A. Rosen, Exergy: energy, environment and sustainable development, Newnes, 2012.

[121] K.E. Herold, R. Radermacher, S.A. Klein, Absorption chillers and heat pumps, CRC press, 1996.

[122] H.C. Bayrakçi, A.E. Özgür, Energy and exergy analysis of vapor compression refrigeration system using pure hydrocarbon refrigerants, International Journal of Energy Research, 33 (12) (2009) 1070-1075.

[123] I. Dincer, Y.A. Cengel, Energy, entropy and exergy concepts and their roles in thermal engineering, Entropy, 3 (3) (2001) 116-149.

[124] I. Dincer, M.A. Rosen, Exergy Analysis of Heating, Refrigerating and Air Conditioning: Methods and Applications, Academic Press, 2015.

[125] I. Dincer, M.A. Rosen, Thermodynamic aspects of renewables and sustainable development, Renewable and Sustainable Energy Reviews, 9 (2) (2005) 169-189.

[126] M.A. Rosen, I. Dincer, M. Kanoglu, Role of exergy in increasing efficiency and sustainability and reducing environmental impact, Energy policy, 36 (1) (2008) 128-137.

[127] A. Şencan, K.A. Yakut, S.A. Kalogirou, Exergy analysis of lithium bromide/water absorption systems, Renewable Energy, 30 (5) (2005) 645-657.

[128] S.F. Lee, S. Sherif, Thermodynamic analysis of a lithium bromide/water absorption system for cooling and heating applications, International Journal of Energy Research, 25 (11) (2001) 1019-1031.

[129] J. Silveira, C. Tuna, Thermoeconomic analysis method for optimization of combined heat and power systems. Part I, Progress in energy and Combustion Science, 29 (6) (2003) 479-485.

[130] A. Tiwari, S. Dubey, G. Sandhu, M. Sodha, S. Anwar, Exergy analysis of integrated photovoltaic thermal solar water heater under constant flow rate and constant collection temperature modes, Applied Energy, 86 (12) (2009) 2592-2597.

[131] D. Wei, X. Lu, Z. Lu, J. Gu, Performance analysis and optimization of organic Rankine cycle (ORC) for waste heat recovery, Energy Conversion and Management, 48 (4) (2007) 1113-1119.

[132] T. Morosuk, G. Tsatsaronis, A new approach to the exergy analysis of absorption refrigeration machines, Energy, 33 (6) (2008) 890-907.

[133] O. Kaynakli, K. Saka, F. Kaynakli, Energy and exergy analysis of a double effect absorption refrigeration system based on different heat sources, Energy Conversion and Management, 106 (2015) 21-30.

[134] T. Gogoi, D. Konwar, Exergy analysis of a H 2 O–LiCl absorption refrigeration system with operating temperatures estimated through inverse analysis, Energy Conversion and Management, 110 (2016) 436-447.

[135] S. Kaushik, A. Arora, Energy and exergy analysis of single effect and series flow double effect water–lithium bromide absorption refrigeration systems, International Journal of Refrigeration, 32 (6) (2009) 1247-1258.

[136] O. Kaynakli, R. Yamankaradeniz, Thermodynamic analysis of absorption refrigeration system based on entropy, Current Science, 92 (4) (2007).

[137] M. Kilic, O. Kaynakli, Second law-based thermodynamic analysis of water-lithium bromide absorption refrigeration system, Energy, 32 (8) (2007) 1505-1512.

[138] M. Talbi, B. Agnew, Exergy analysis: an absorption refrigerator using lithium bromide and water as the working fluids, Applied Thermal Engineering, 20 (7) (2000) 619-630.

[139] M. Ishida, J. Ji, Graphical exergy study on single stage absorption heat transformer, Applied Thermal Engineering, 19 (11) (1999) 1191-1206.

[140] S. Aprhornratana, I. Eames, Thermodynamic analysis of absorption refrigeration cycles using the second law of thermodynamics method, International Journal of Refrigeration, 18 (4) (1995) 244-252.

[141] F. PanahiZadeh, N. Bozorgan, The energy and exergy analysis of single effect absorption chiller, International Journal of Advanced Design and Manufacturing Technology, 4 (4) (2011) 19-26.

[142] B.H. Gebreslassie, M. Medrano, D. Boer, Exergy analysis of multi-effect water–LiBr absorption systems: from half to triple effect, Renewable energy, 35 (8) (2010) 1773-1782.

[143] G. Gutiérrez-Urueta, A. Huicochea, P. Rodríguez-Aumente, W. Rivera, Energy and Exergy Analysis of Water-LiBr Absorption Systems with Adiabatic Absorbers for Heating and Cooling, Energy Procedia, 57 (2014) 2676-2685.

[144] T. Gogoi, K. Talukdar, Exergy based parametric analysis of a combined reheat regenerative thermal power plant and water–LiBr vapor absorption refrigeration system, Energy Conversion and Management, 83 (2014) 119-132.

[145] T. Avanessian, M. Ameri, Energy, exergy, and economic analysis of single and double effect LiBr–H 2 O absorption chillers, Energy and Buildings, 73 (2014) 26-36.

[146] S. Gong, K.G. Boulama, Parametric study of an absorption refrigeration machine using advanced exergy analysis, Energy, 76 (2014) 453-467.

[147] G. Gutiérrez-Urueta, A. Huicochea, P. Rodríguez-Aumente, W. Rivera, Energy and exergy analysis of an adiabatic water-LiBr absorption system, Journal of Renewable and Sustainable Energy, 6 (3) (2014) 033101.

[148] S. Gong, K.G. Boulama, Advanced exergy analysis of an absorption cooling machine: Effects of the difference between the condensation and absorption temperatures, International Journal of Refrigeration, 59 (2015) 224-234.

[149] K. Talukdar, T. Gogoi, Exergy analysis of a combined vapor power cycle and boiler flue gas driven double effect water–LiBr absorption refrigeration system, Energy Conversion and Management, 108 (2016) 468-477.

[150] R. Gomri, Second law comparison of single effect and double effect vapour absorption refrigeration systems, Energy Conversion and Management, 50 (5) (2009) 1279-1287.

[151] R. Gomri, Investigation of the potential of application of single effect and multiple effect absorption cooling systems, Energy Conversion and Management, 51 (8) (2010) 1629-1636.

[152] N. Bouaziz, D. Lounissi, Energy and exergy investigation of a novel double effect hybrid absorption refrigeration system for solar cooling, International Journal of Hydrogen Energy, 40 (39) (2015) 13849-13856.

[153] A. Hamed, S.A. Kaseb, A.S. Hanafi, Prediction of energetic and exergetic performance of double-effect absorption system, International Journal of Hydrogen Energy, 40 (44) (2015) 15320-15327.

[154] Y. Chen, W. Han, H. Jin, Analysis of an absorption/absorption–compression refrigeration system for heat sources with large temperature change, Energy Conversion and Management, 113 (2016) 153-164.

[155] G. Florides, S. Kalogirou, S. Tassou, L. Wrobel, Design and construction of a LiBr–water absorption machine, Energy Conversion and Management, 44 (15) (2003) 2483-2508.

[156] C. Gupta, C. Sharma, Entropy values of lithium bromide-water solution and their vapours, ASHRAE Transactions, 82 (Part 2) (1976) 35-46.

[157] E. Lemmon, M. McLinden, M. Huber, Reference fluid thermodynamic and transport properties (REFPROP), version 7.0, NIST standard reference database.

[158] L.G. Farshi, S. Mahmoudi, M. Rosen, M. Yari, M. Amidpour, Exergoeconomic analysis of double effect absorption refrigeration systems, Energy Conversion and Management, 65 (2013) 13-25.

[159] R. Misra, P. Sahoo, S. Sahoo, A. Gupta, Thermoeconomic optimization of a single effect water/LiBr vapour absorption refrigeration system, International Journal of Refrigeration, 26 (2) (2003) 158-169.

[160] S.F. Lee, S. Sherif, Second law analysis of various double-effect lithium bromide/water absorption chillers, ASHRAE Transactions, 107 (1) (2001) 664-673.

[161] F. Fornarelli, S. Camporeale, B. Fortunato, M. Torresi, P. Oresta, L. Magliocchetti, A. Miliozzi, G. Santo, CFD analysis of melting process in a shell-and-tube latent heat storage for concentrated solar power plants, Applied Energy, 164 (2016) 711-722.

[162] Y. Tao, V. Carey, Effects of PCM thermophysical properties on thermal storage performance of a shell-and-tube latent heat storage unit, Applied Energy, 179 (2016) 203-210.

[163] R. Jacob, M. Belusko, A.I. Fernández, L.F. Cabeza, W. Saman, F. Bruno, Embodied energy and cost of high temperature thermal energy storage systems for use with concentrated solar power plants, Applied Energy, 180 (2016) 586-597.

[164] D. Zhao, G. Tan, Numerical analysis of a shell-and-tube latent heat storage unit with fins for air-conditioning application, Applied Energy, 138 (2015) 381-392.

[165] S. Seddegh, X. Wang, A.D. Henderson, Z. Xing, Solar domestic hot water systems using latent heat energy storage medium: A review, Renewable and Sustainable Energy Reviews, 49 (2015) 517-533.

[166] F. Agyenim, N. Hewitt, P. Eames, M. Smyth, A review of materials, heat transfer and phase change problem formulation for latent heat thermal energy storage systems (LHTESS), Renewable and sustainable energy reviews, 14 (2) (2010) 615-628.

[167] Y. Cao, A. Faghri, Performance characteristics of a thermal energy storage module: a transient PCM/forced convection conjugate analysis, International Journal of Heat and Mass Transfer, 34 (1) (1991) 93-101.

[168] M. Lacroix, Numerical simulation of a shell-and-tube latent heat thermal energy storage unit, Solar energy, 50 (4) (1993) 357-367.

[169] M. Lacroix, Study of the heat transfer behavior of a latent heat thermal energy storage unit with a finned tube, International journal of heat and mass transfer, 36 (8) (1993) 2083-2092.

[170] C. Bellecci, M. Conti, Phase change thermal storage: transient behaviour analysis of a solar receiver/storage module using the enthalpy method, International Journal of Heat and Mass Transfer, 36 (8) (1993) 2157-2163.

[171] C. Bellecci, M. Conti, Latent heat thermal storage for solar dynamic power generation, Solar energy, 51 (3) (1993) 169-173.

[172] C. Bellecci, M. Conti, Transient behaviour analysis of a latent heat thermal storage module, International Journal of Heat and Mass Transfer, 36 (15) (1993) 3851-3857.

[173] M. Esen, A. Durmuş, A. Durmuş, Geometric design of solar-aided latent heat store depending on various parameters and phase change materials, Solar Energy, 62 (1) (1998) 19-28.

[174] K. Ismail, M. Goncalves, Thermal performance of a PCM storage unit, Energy Conversion and Management, 40 (2) (1999) 115-138.

[175] K. Ismail, C. Melo, Convection-based model for a PCM vertical storage unit, International Journal of Energy Research, 22 (14) (1998) 1249-1265.

[176] A. Trp, K. Lenic, B. Frankovic, Analysis of the influence of operating conditions and geometric parameters on heat transfer in water-paraffin shell-and-tube latent thermal energy storage unit, Applied Thermal Engineering, 26 (16) (2006) 1830-1839.

[177] A. Trp, An experimental and numerical investigation of heat transfer during technical grade paraffin melting and solidification in a shell-and-tube latent thermal energy storage unit, Solar Energy, 79 (6) (2005) 648-660.

[178] M. Rathod, J. Banerjee, Experimental investigations on latent heat storage unit using paraffin wax as phase change material, Experimental Heat Transfer, 27 (1) (2014) 40-55.

[179] M.K. Rathod, J. Banerjee, Thermal performance enhancement of shell and tube Latent Heat Storage Unit using longitudinal fins, Applied Thermal Engineering, 75 (2015) 1084-1092.

[180] Z.-X. Gong, A.S. Mujumdar, Finite-element analysis of cyclic heat transfer in a shell-and-tube latent heat energy storage exchanger, Applied Thermal Engineering, 17 (6) (1997) 583-591.

[181] Y. Tao, Y. He, Numerical study on thermal energy storage performance of phase change material under non-steady-state inlet boundary, Applied Energy, 88 (11) (2011) 4172-4179.

[182] Y.-B. Tao, M.-J. Li, Y.-L. He, W.-Q. Tao, Effects of parameters on performance of high temperature molten salt latent heat storage unit, Applied Thermal Engineering, 72 (1) (2014) 48-55.

[183] Y. Tao, Y. He, Z. Qu, Numerical study on performance of molten salt phase change thermal energy storage system with enhanced tubes, Solar Energy, 86 (5) (2012) 1155-1163.

[184] M. Avci, M.Y. Yazici, Experimental study of thermal energy storage characteristics of a paraffin in a horizontal tube-in-shell storage unit, Energy Conversion and Management, 73 (2013) 271-277.

[185] M. Hosseini, M. Rahimi, R. Bahrampoury, Experimental and computational evolution of a shell and tube heat exchanger as a PCM thermal storage system, International Communications in Heat and Mass Transfer, 50 (2014) 128-136.

[186] A. El-Sawi, F. Haghighat, H. Akbari, Centralized latent heat thermal energy storage system: model development and validation, Energy and Buildings, 65 (2013) 260-271.

[187] W.-W. Wang, K. Zhang, L.-B. Wang, Y.-L. He, Numerical study of the heat charging and discharging characteristics of a shell-and-tube phase change heat storage unit, Applied Thermal Engineering, 58 (1) (2013) 542-553.

[188] W.-W. Wang, L.-B. Wang, Y.-L. He, The energy efficiency ratio of heat storage in one shell-and-one tube phase change thermal energy storage unit, Applied Energy, 138 (2015) 169-182.

[189] S.S.M. Tehrani, R.A. Taylor, P. Saberi, G. Diarce, Design and feasibility of high temperature shell and tube latent heat thermal energy storage system for solar thermal power plants, Renewable Energy, 96 (2016) 120-136.

[190] B. Zalba, J.M. Marín, L.F. Cabeza, H. Mehling, Review on thermal energy storage with phase change: materials, heat transfer analysis and applications, Applied Thermal Engineering, 23 (3) (2003) 251-283.

[191] V. Kapsalis, D. Karamanis, Solar thermal energy storage and heat pumps with phase change materials, Applied Thermal Engineering, 99 (2016) 1212-1224.

[192] P.D. Silva, L. Goncalves, L. Pires, Transient behaviour of a latent-heat thermal-energy store: numerical and experimental studies, Applied Energy, 73 (1) (2002) 83-98.

[193] A. Sharma, L.D. Won, D. Buddhi, J.U. Park, Numerical heat transfer studies of the fatty acids for different heat exchanger materials on the performance of a latent heat storage system, Renewable Energy, 30 (14) (2005) 2179-2187.

[194] B. Zivkovic, I. Fujii, An analysis of isothermal phase change of phase change material within rectangular and cylindrical containers, Solar Energy, 70 (1) (2001) 51-61.

[195] N. Vyshak, G. Jilani, Numerical analysis of latent heat thermal energy storage system, Energy Conversion and Management, 48 (7) (2007) 2161-2168.

[196] E. Sparrow, S. Patankar, S. Ramadhyani, Analwsis of Melting in the Presence of Natural Confection in the Melt Region, (1977).

[197] D. Buddhi, N. Bansal, R. Sawhney, M. Sodha, Solar thermal storage systems using phase change materials, International journal of energy research, 12 (3) (1988) 547-555.

[198] M. Lacroix, T. Duong, Experimental improvements of heat transfer in a latent heat thermal energy storage unit with embedded heat sources, Energy Conversion and Management, 39 (8) (1998) 703-716.

[199] R. Velraj, R. Seeniraj, B. Hafner, C. Faber, K. Schwarzer, Heat transfer enhancement in a latent heat storage system, Solar Energy, 65 (3) (1999) 171-180.

[200] M.A. Hamdan, I. Al-Hinti, Analysis of heat transfer during the melting of a phase-change material, Applied Thermal Engineering, 24 (13) (2004) 1935-1944.

[201] L.-W. Fan, Z.-Q. Zhu, S.-L. Xiao, M.-J. Liu, H. Lu, Y. Zeng, Z.-T. Yu, K.-F. Cen, An experimental and numerical investigation of constrained melting heat transfer of a phase change material in a circumferentially finned spherical capsule for thermal energy storage, Applied Thermal Engineering, 100 (2016) 1063-1075.

[202] M.A. Ezan, M. Ozdogan, A. Erek, Experimental study on charging and discharging periods of water in a latent heat storage unit, International Journal of Thermal Sciences, 50 (11) (2011) 2205-2219.

[203] F. Agyenim, P. Eames, M. Smyth, Experimental study on the melting and solidification behaviour of a medium temperature phase change storage material (Erythritol) system augmented with fins to power a LiBr/H 2 O absorption cooling system, Renewable Energy, 36 (1) (2011) 108-117.

[204] M. Hosseini, A. Ranjbar, K. Sedighi, M. Rahimi, A combined experimental and computational study on the melting behavior of a medium temperature phase change

storage material inside shell and tube heat exchanger, International Communications in Heat and Mass Transfer, 39 (9) (2012) 1416-1424.

[205] F. Rösler, D. Brüggemann, Shell-and-tube type latent heat thermal energy storage: numerical analysis and comparison with experiments, Heat and Mass Transfer, 47 (8) (2011) 1027.

[206] M. Akgün, O. Aydın, K. Kaygusuz, Thermal energy storage performance of paraffin in a novel tube-in-shell system, Applied Thermal Engineering, 28 (5) (2008) 405-413.

[207] M. Akgün, O. Aydın, K. Kaygusuz, Experimental study on melting/solidification characteristics of a paraffin as PCM, Energy Conversion and Management, 48 (2) (2007) 669-678.

[208] M. Longeon, A. Soupart, J.-F. Fourmigué, A. Bruch, P. Marty, Experimental and numerical study of annular PCM storage in the presence of natural convection, Applied Energy, 112 (2013) 175-184.

[209] X. Xiao, P. Zhang, Numerical and experimental study of heat transfer characteristics of a shell-tube latent heat storage system: Part I–Charging process, Energy, 79 (2015) 337-350.

[210] X. Xiao, P. Zhang, Numerical and experimental study of heat transfer characteristics of a shell-tube latent heat storage system: Part II–Discharging process, Energy, 80 (2015) 177-189.

[211] Y. Wang, L. Wang, N. Xie, X. Lin, H. Chen, Experimental study on the melting and solidification behavior of erythritol in a vertical shell-and-tube latent heat thermal storage unit, International Journal of Heat and Mass Transfer, 99 (2016) 770-781.

[212] M.M. Joybari, F. Haghighat, S. Seddegh, Numerical investigation of a triplex tube heat exchanger with phase change material: Simultaneous charging and discharging, Energy and Buildings, 139 (2017) 426–438.

Appendix A: Application of PCMs in domestic refrigerators

A.1 Introduction

Nowadays, almost every household uses at least one refrigeration system for domestic food preservation or in the building's mechanical ventilation system to provide the required indoor thermal environment. Based on statistical data, in 2008, there were an average 1.27 and 0.54 refrigerators and freezers per household in Canada, respectively [56]. Besides, in 2011, there were a total number of 13,320,615 households in Canada [57]. This indicates a minimum of about 24 million household refrigerators and freezers are currently in use in Canada, which confirms that a huge amount of energy consumption is required for their operation. Thus, even small performance enhancement of these appliances brings huge amounts of energy saving. Generally, energy consumption of a refrigerator depends upon its components efficiency, ambient temperature, thermal load, door openings, set-point temperature in its compartment(s), and refrigerant type [58]. Hence, performance enhancement of refrigeration systems covers a vast research area since each part of the system has its own technical complexity. Therefore, it is not easy to classify all those efforts in few categories. Nevertheless, most of the ideas applied to refrigeration systems lie in three major categories: development of energy-efficient compressors, enhancement of thermal insulation, and enhancement of heat transfer from heat exchangers, i.e., condenser and evaporator [59].

The first category includes all the studies focused on compressor energy consumption and efficiency. In domestic refrigerators, the requirements for a suitable compressor are cost-effectiveness, low noise generation, high efficiency, high reliability and easy manufacturing process; thus, hermetically sealed reciprocating ON/OFF compressors are conventionally used [60]. The reason of significance is that more than 80% of the total energy consumption by a refrigerator is devoted to its compressor [61]. Furthermore, based on exergy analysis and using experimental data, it was found that the highest exergy destruction of a domestic refrigerator occurred in its compressor [62]. In

order to reduce exergy destruction in a compressor, its energy consumption should be reduced [63]. Thus, compressor modification is strongly recommended to enhance the performance of refrigerators. Some alternatives with lower energy consumption are available for conventional ON/OFF compressors, e.g. variable speed compressors and linear compressors. In variable speed compressors, motor speed continuously changes based on the load and driving efficiency [64]. Advantages of variable speed compressors include continuous control, lower noise generation, lower vibration, lower starting current, and better COP compared to the conventional ON/OFF systems [65]. However, still this technology is too expensive and is not cost-effective to be widely used in market [61]. Recently, linear compressors have received more attention for domestic refrigeration since they have significant advantages compared to the conventional reciprocating compressors. Elimination of crank mechanism and direct drive of piston by motor in linear compressors reduces frictional losses and enhances the performance of the system [66]. However, their application in refrigeration systems had some technical difficulties [67]. In summary, these promising alternatives raise some special difficulties preventing them from being widely and easily used. Therefore, cost-effective modification of systems with conventional compressors seems to be more desirable.

The second category is about enhancing thermal insulation of system walls. Polyurethane boards are conventionally used to insulate refrigerated compartments. Since the conductive heat transfer coefficient of polyurethane boards is almost high, even the optimum thickness has great heat loss. It is clear that the higher the thermal resistance of insulation in a refrigeration system, the longer the compartment remains cold. It is possible to further reduce heat loss from the walls of a refrigeration system by means of vacuum insulation panels (VIPs). VIP is highly resistant against the heat transfer, about 4 times more than a polyurethane board of equal thickness [68]. The core material of VIPs is encapsulated in a barrier which needs to be thin with low conductivity and low gas permeability [69]. These constraints as well as their reliability make them expensive, preventing their wide applications [61]. Therefore, more cost-effective methods of achieving high thermal insulation are required.

The last category includes the efforts for heat transfer enhancement of heat exchangers (condensers and evaporators) in refrigeration systems which can be further divided in four major groups [70]:

- Addition of a liquid-to-suction line heat exchanger (also known as superheating coil),
- Application of loop heat pipe evaporator,
- Application of micro-fins in condenser and evaporator, and
- Application of phase change materials.

It has been reported that the first two categories (compressor and insulation modification) are either costly or difficult to be applied. PCMs, on the other hand, have received considerable attention for heat transfer enhancement due to their inherent advantages. PCMs can be used in refrigerators for either heat or cold storage. The former requires integration of PCM to condenser side, while the latter is done by integration to evaporator or compartment. Since evaporator is the main source of cold in refrigerators, throughout this chapter, application of PCM at evaporator reflects all possible configuration for cold storage (including compartment).

Due to the high latent heat, integration of PCM at evaporator side of a refrigerator could prolong the compressor OFF time. This enables two new important options for refrigerators; to work off-peak and to maintain the compartment cold for longer periods of time even during power outages or blackouts, especially tight power supplies due to rolling blackouts.

Table A.1 shows some of the studies focusing on PCM application in domestic refrigeration systems. The main purpose of this chapter is to cover these studies including the investigations into heat and cold storage. This chapter not only reports the effect of PCM integration, but also tries to identify the effective parameters, which affect the performance of PCM. Therefore, the outcomes of both experimental and simulation work on this subject are reported and the potential for the application of PCMs is discussed.

Table A.1: Chronological tabulation of studies conducted using PCM in refrigeration system

No.	Reference	PCM type			Location			
		Water	Eutectic	Paraffin	Evaporator	Compartment	Condenser	Other[*]
1	Onyejekwe [71]		✓		✓			
2	Cerri et al. [72]		✓		✓			
3	Maltini et al. [73]		✓		✓			
4	Azzouz et al. [74]		✓		✓			
5	Wang et al. [75]		✓					✓
6	Wang et al. [76]		✓					✓
7	Wang et al. [77]		✓					✓
8	Azzouz et al. [78]		✓		✓			
9	Azzouz et al. [79]	✓	✓		✓			
10	Subramaniam et al. [80]				✓			
11	Gin et al. [81]		✓			✓		
12	Gin and Farid [82]		✓			✓		
13	Cheng et al. [59]			✓			✓	
14	Gin et al. [83]		✓			✓		
15	Berdja et al. [84]		✓		✓			
16	Oró et al. [85]		✓		✓	✓		
17	Oró et al. [86]		✓			✓		
18	Sharma and Buddahi [87]		✓			✓		
19	Cheng and Yuan [88]			✓			✓	
20	Khan and Afroz [70]	✓	✓		✓			
21	Khan and Afroz [89]	✓	✓		✓			
22	Oró et al. [90]		✓			✓		
23	Marques et al. [61]	✓	✓		✓			
24	Taneja et al. [91]		✓			✓		
25	Taneja et al. [92]		✓			✓		
26	Khan and Afroz [93]	✓	✓		✓			
27	Marques et al. [58]	✓			✓			
28	Rahman et al. [94]	✓			✓			
29	Visek et al. [95]	✓			✓			
30	Yuan and Cheng [96]			✓			✓	

[*] PCM was used between components (details in Table A.7)

A.2 PCM application at evaporator

In domestic refrigerators, the evaporator works based on either free or forced convective heat transfer. The former (also known as naturally-cooled evaporator) has low heat transfer rate and could result in temperature stratification inside the compartment, while the latter gives better temperature stability. However, its main drawbacks are higher energy consumption, the spread of odor, and the food weight loss due to high air circulation [73]. One approach to overcome these drawbacks is the application of thermal energy storage (i.e. PCMs). Several studies (see Table A.1) have focused on the performance analysis of refrigeration systems with PCM at evaporator. As a result of application of energy storage, the compressor needs to work for a longer period of time to charge the energy storage. Nevertheless, despite longer compressor ON time in each cycle to charge PCM, the global ON-time ratio decreases due to longer compressor OFF time. Main advantages of longer compressor OFF duration are lower overall energy consumption, better food quality, and preventing destructive effect of frequent compressor start/stop. Furthermore, PCM can be helpful in case of power outages or blackouts since it affects both product and air temperatures and their rate of increase during power loss [82]. In addition, more uniform compartment temperature can be achieved by PCM presence [80]. A detailed analysis of pros and cons of using PCM at evaporator will be presented in Section A.2.5.

Some studies reported that the direct contact of PCM with a naturally-cooled evaporator is more advantageous. The main reason is that it enhances heat transfer from the evaporator and also it can store excess cooling capacity of the system in the PCM [95]. Besides, this configuration results in higher evaporator temperature and pressure during phase change period of PCM [94]. Thus, refrigerant density is higher and, as a result, cooling capacity increases. Similar results were reported for cases where evaporator coils were immersed in PCM. In such cases, faster heat transfer is achieved which is due to the faster nature of conduction/convection in PCMs than natural convection of air. Therefore, due to the high thermal inertia of a PCM, the refrigerant pressure and temperature do not fall as much as the case with no PCM which in turn

gives higher refrigerant mass flow rate [70]. However, if the evaporator is immersed in a PCM with a phase change temperature higher than the compartment set-point temperature, a high thermal resistance is created around the evaporator which, in turn, brings more frequent compressor start/stop [84].

A summary of studies, which investigated effective parameters for PCM inclusion at evaporator side, is tabulated in Table A.2. Basically, all studies can be categorized based on analyzing parameters such as the phase change temperature, PCM thickness, its geometry and orientation, and also the effect of thermal load. In the following sections, the impact of each parameter is discussed and analyzed separately.

Table A.2: A summary of studies conducted using PCM at evaporator of refrigeration systems

No.	Ref.	Phase change temperature	PCM thickness	Thermal load							PCM shape and orientation
				Ambient temperature	Internal heater	Evaporation temperature	Power outage	Compartment load	Door opening	Defrost	
1	[74]	✓		✓							
2	[78]	✓	✓	✓					✓		
3	[79]		✓	✓	✓						
4	[84]	✓				✓					
5	[82]						✓				
6	[81]						✓		✓	✓	
7	[83]						✓				
8	[70]	✓	✓		✓	✓					
9	[93]	✓			✓						
10	[61]	✓									✓
11	[58]		✓	✓		✓					
12	[71]		✓	✓							✓
13	[85]					✓	✓	✓	✓		
14	[86]						✓	✓			
15	[90]						✓				
16	[87]						✓		✓		

A.2.1 Phase change temperature

Proper phase change temperature selection is of great importance in refrigeration systems since it directly affects not only the performance of the system but also the quality of the stored food. The main objective of domestic refrigeration systems is to preserve food; thus, phase change temperature should be compatible with this main objective. Keep in mind that selection of the phase change temperature is an important design parameter for proper functioning of PCM and, if applied inside the compartment, the melting point must fall within the thermostat temperature range of operation. In order to select the most beneficial melting/freezing point, it is worth noting the effect of unsuitably selected high or low phase change temperature. Obviously, high phase change temperature increases temperature in the compartment, decreasing stored food quality, while it increases COP of the system due to the lower power consumption [78]. Conversely, too low phase change temperature decreases the corresponding compartment temperature. This is more important for fresh food compartment since its temperature should never fall below zero (to prevent freezing and food quality loss). Therefore, an admissible phase change temperature range exists between these two high and low extremes. These effects are visually shown in Figure A.1 where the high and low limits are restricted to the thermostat temperature range. In addition, ambient temperature also affects compartment temperature; higher ambient temperature increases heat transfer through compartment walls which in turn increases compartment temperature [74]. Therefore, its effect should also be taken into account during selection of phase change temperature. This parameter is further discussed in Section A.2.3.

Low   **Phase change temperature**   **High**

- Lower compartment air temperature
- Better food quality

- Higher evaporation temperature
- Lower power consumption
- Higher COP
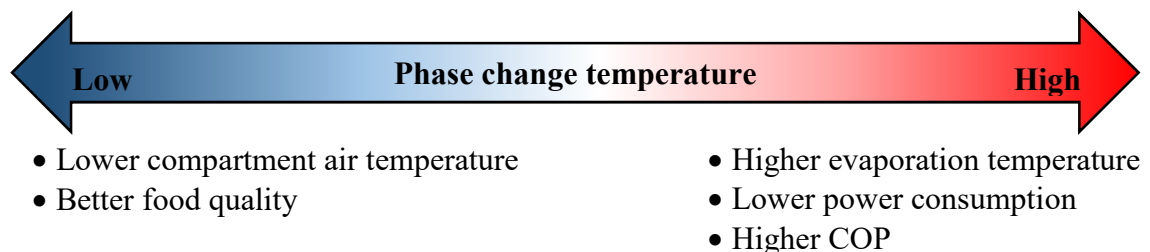
Figure A.1: Advantages of high/low phase change temperature on system performance

Using PCM around evaporator coils, it was found that enhancement of the system performance by PCM was higher if its melting point was not lower than the compartment set-point temperature [93]. This is due to the reduction of compressor start/stop frequency and higher system COP because of higher evaporation temperature during phase change. Otherwise, PCM does not perform well due to its low phase change temperature which prevents it from fully participating in the phase change process.

An important phenomenon that should be taken into account to find a proper phase change temperature is the supercooling effect [97]. Supercooling reduces system efficiency since it both prolongs phase change period, and reduces temperature difference between the PCM and evaporator [98]. Therefore, it reduces the heat transfer rate and prolongs the compressor ON time which consequently increases the energy consumption. Addition of nucleating agents can prevent the supercooling effect [99]. It should be noted that supercooling effect is also known as subcooling effect but the former is used in this chapter in order to make a clear distinction between this effect and refrigerant subcooling in condenser.

Proper phase change temperature should be selected by means of a material with suitable thermophysical properties. Water has received considerable attention due to its unique characteristics. This is mainly due to its availability, large latent heat value and sharp phase change point [58]. For subzero phase change temperatures, which is a requirement for frozen food compartment, water is not a good candidate due to its improper phase change temperature. Nevertheless, water-salt eutectic mixtures are normally used because of their high latent heat and desirable melting point [100]. It is interesting to point out that many studies which investigated water as PCM inside refrigerators also investigated eutectic mixtures, see Table 1. It was found that for the same application, the storage capacity of eutectic mixtures are lower than water which decreases OFF time period of the system [61]. Nevertheless, a eutectic PCM with phase change temperature (5°C) higher than water enhanced COP more than water due to the resulting higher evaporation temperature during phase change [70]. Table A.3 shows a list of some PCMs with suitable phase change temperature to be used in domestic refrigeration systems. According to the table, some organic PCMs are also available with

suitable thermophysical properties for domestic refrigeration applications; however, they have not been investigated yet. The main reason is their low latent heat capacity, low thermal conductivity and high price [97].

Table A.3: Thermophysical properties of some PCMs proposed/used in refrigeration systems

Material	Type	Composition (wt. %)	Melting point (°C)	Latent heat (kJ/kg)	Reference
$C_{14}H_{30}$	Organic	-	5.5	226	[93]
$Na_2SO_4/NaCl/KCl/H_2O$	Eutectic	31/13/16/40	4.0	234	[93]
$C_{13}H_{28}/C_{14}H_{30}$	Organic	20/80	2.6	212	[101]
$C_{13}H_{28}/C_{14}H_{30}$	Organic	40/60	0.7	148	[101]
H_2O	Water	-	0.0	333	[93]
$C_{13}H_{28}/C_{14}H_{30}$	Organic	60/40	-0.5	138	[101]
$C_{13}H_{28}/C_{14}H_{30}$	Organic	80/20	-1.5	110	[101]
$CuSO_4/H_2O$	Eutectic	11.9	-1.6	291	[100]
$FeSO_4/H_2O$	Eutectic	13	-1.8	287	[100]
Na_2CO_3/H_2O	Eutectic	5.9	-2.1	310	[100]
KNO_3/H_2O	Eutectic	9.7	-2.8	296	[100]
NaF/H_2O	Eutectic	3.9	-3.5	314	[100]
Na_2SO_4/H_2O	Eutectic	12.7	-3.6	285	[100]
$MgSO_4/H_2O$	Eutectic	19	-3.9	264	[100]
$NiSO_4/H_2O$	Eutectic	20.6	-4.2	259	[100]
$NaCl/H_2O$	Eutectic	90	-5.0	289	[70]
$KHCO_3/H_2O$	Eutectic	16.95	-5.4	269	[100]
$C_{12}H_{26}/C_{13}H_{28}$	Organic	20/80	-5.4	126	[101]
$Sr(NO_3)_2/H_2O$	Eutectic	24.5	-5.8	243	[100]
$ZnSO_4/H_2O$	Eutectic	27.2	-6.5	236	[100]
$BaCl_2/H_2O$	Eutectic	22.5	-7.8	246	[100]
$C_{12}H_{26}/C_{13}H_{28}$	Organic	40/60	-8.0	147	[101]
$C_{12}H_{26}/C_{13}H_{28}$	Organic	50/50	-9.1	145	[101]
$C_{12}H_{26}/C_{13}H_{28}$	Organic	60/40	-9.7	159	[101]
NaH_2PO_4/H_2O	Eutectic	23.4	-9.9	214	[100]
$MnSO_2/H_2O$	Eutectic	32.2	-10.5	213	[100]
KCl/H_2O	Eutectic	19.5	-10.7	283	[93]
$Na_2S_2O_3/H_2O$	Eutectic	30	-11.0	220	[100]
K_2HPO_4/H_2O	Eutectic	36.8	-13.5	198	[100]
NaH_4Cl/H_2O	Eutectic	19.5	-16.0	248	[100]
$Ca(NO_3)_2/H_2O$	Eutectic	35	-16.0	199	[100]
NH_4NO_3/H_2O	Eutectic	41.2	-17.4	186	[100]
$NaNO_3/H_2O$	Eutectic	36.9	-17.7	188	[100]
$(NH_4)_2SO_4/H_2O$	Eutectic	39.7	-18.5	188	[100]
$MgCl_2/H_2O$	Eutectic	25	-19.4	223	[100]
$NaCl/H_2O$	Eutectic	22.4	-21.2	222	[93]
KF/H_2O	Eutectic	21.5	-21.6	227	[100]

A.2.2 PCM thickness

After selection of a proper PCM with suitable thermophysial properties, the question is the amount of PCM to be used. Based on a very simple calculation, the minimum volume of PCM in order to meet required energy can be calculated [71]. If a compartment only contains PCM, the amount of energy (E) stored in PCM neglecting its sensible heat variations is:

$$E = \rho V \lambda$$

(A.1)

where ρ and λ are the density and the latent heat of fusion of PCM, respectively. The compartment inevitably has heat gain from the ambient as:

$$Q = (UA)_{cold} (T_{amb} - T_{cold})$$

(A.2)

where the indices *amb* and *cold* represent the ambient and cold compartment, respectively and *UA* is the overall thermal conductance. In order to marginally meet the required load, the amount of energy stored in the PCM should meet the amount of energy passing through compartment walls during compressor OFF time (t_{OFF}); thus, minimum volume for PCM is [71]:

$$V_{min} = \frac{t_{OFF} \left[(UA)_{cold} (T_{amb} - T_{cold}) \right]}{\rho \lambda}$$

(A.3)

Therefore, the amount of PCM should be more than what was calculated from Equation (A.3) to compensate for the heat gain through the walls during compressor OFF time. But PCM should not be thicker than a certain amount since otherwise not all the thickness has the chance to undergo phase change [79]. In such a case, PCM is partially melted/frozen which reduces its effectiveness. Besides, thicker PCM is more expensive and also requires longer compressor work for cold storage; thus, PCM thickness should be selected based on the load. As a confirmation to this, doubling PCM thickness (from 5 to 10mm), it was found that the system OFF period was extended only for about 3% [79]. The reason was due to the fact that only 6mm out of the 10mm thickness participated in

phase change during the compressor ON time. Similar results were reported where an approximate 40% volumetric increase in PCM size resulted in just 6% increase in the system COP [70]. However, whenever increasing the PCM thickness still kept all the PCM participating in phase change process, its effect was greatest on reducing the ON-time ratio as a consequence of longer compressor OFF time [78]. In other words, when the amount of PCM was increased, the system had to work longer in order to charge higher amounts of PCM; however, the ON-time ratio was reduced since the duration of compressor OFF period was much longer. Based on numerical modeling, it was reported that increasing PCM thickness from 2 to 5mm (2.5 times higher) prolonged both compressor ON and OFF periods for about 2.5 times longer (34min instead of 13min and 252min instead of 101min, respectively) [58]. Therefore, the compressor needs to work longer continuously to charge higher amounts of PCM. Since too long compressor ON time is not desirable, there is a limit to increase the amount of PCM. Thus, the total amount of PCM has an admissible range. It is important to point out that ON-time ratio of a refrigerator with PCM is predominantly determined by thermal load [79]. A framework for designing the optimum thickness of PCM has been developed [102]. In summary, Figure A.2 shows the advantages of each extreme.

Low — PCM thickness — High

- The whole PCM undergoes phase change
- Shorter compressor ON time
- Lower capital cost

- Longer compressor OFF time
- Higher COP
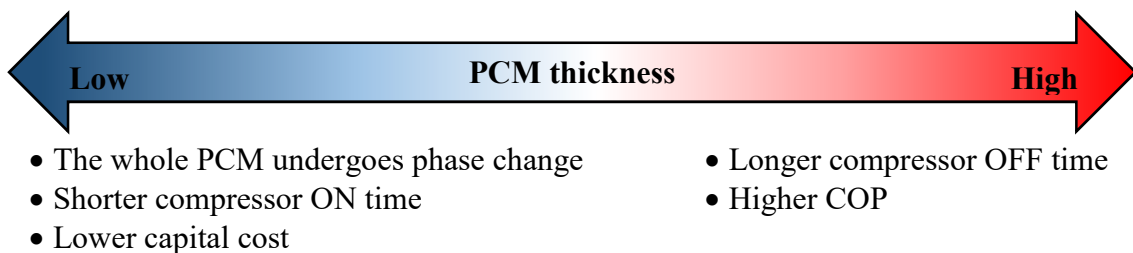
Figure A.2: Benefits of high/low PCM thickness on system performance

A.2.3 Thermal load

The impact of the influencing parameters on the system performance will be discussed in the following sections.

A.2.3.1 Ambient temperature

Ambient temperature affects both the performance of a refrigeration system and the usefulness of PCM. Generally, the higher the ambient temperature, the lower the COP of systems due to the higher compartment air temperature [74] and higher condensation temperature and pressure [70]. Earlier studies reported that by increasing the thermal load, system COP decreased even in presence of a PCM. The reason is that the increase in thermal load results in more partially melted PCM which in turn decreases the system COP [79]. High thermal load directly affects both charging and discharging duration of the PCM as it shortens melting time while it prolongs freezing time since the compressor has to both overcome the thermal load and charge the PCM [58]. In addition, very low ambient temperature also has a negative effect on the PCM performance. The reason is that when the refrigerator is working in a low thermal load, compartment temperature drops faster (due to the low heat gain through the walls) and reaches sooner to the set-point temperature; hence, the PCM does not have enough time to be fully solidified before compressor stops. Moreover, the temperature in fresh food compartment might drop below zero. It was found that a melting temperature of -3°C for PCM prevents subzero fresh food compartment temperature even for a low ambient temperature of 15°C [78].

In addition to purely considering the effect of ambient temperature, some studies investigated the effect of continuous thermal load by placing a heater inside the compartment. It was found that higher heat generation in a compartment shortens compressor OFF period and the system has to work longer in order to keep the refrigerated compartment cold; thus, COP decreases [79]. Besides, as mentioned earlier, high thermal load does not allow the PCM to be fully melted/frozen and the compartment temperature might go above the admissible limit since the PCM cannot meet the high energy requirement of the compartment [93]. Because of the abovementioned reasons, thermal load significantly affects the ON-time ratio of refrigeration systems. The type of PCM also affects the response of the system to the thermal load. Using PCM in a refrigerator, it was reported that when thermal load was low, eutectic PCM (with phase change temperature of -5°C) had shorter compressor ON time, while for higher loads, water was a better candidate [70]. This is due to the higher latent heat of water compared

to a eutectic mixture. Based on simulation results, by applying a sine wave change in evaporator outlet temperature (due to an imaginary thermal load), it was found that a PCM placed between the evaporator and compressor damped the temperature variation [77]. The reason is that a superheated gas (the refrigerant) is easily affected by evaporation temperature change, while a high capacity liquid (the PCM) resists against temperature fluctuations. Besides, PCM gave lower superheat at evaporator outlet; hence, it could provide more stable conditions. Disadvantages of high and low ambient temperatures are shown in Figure A.3.

Low   **Ambient temperature**   **High**

- Partially melted/frozen PCM
- Possibility of subzero fresh food compartment

- Partially melted/frozen PCM
- Higher compartment temperature
- Negative effect on food quality
- Lower COP
- Shorter compressor OFF period
- Longer compressor ON period
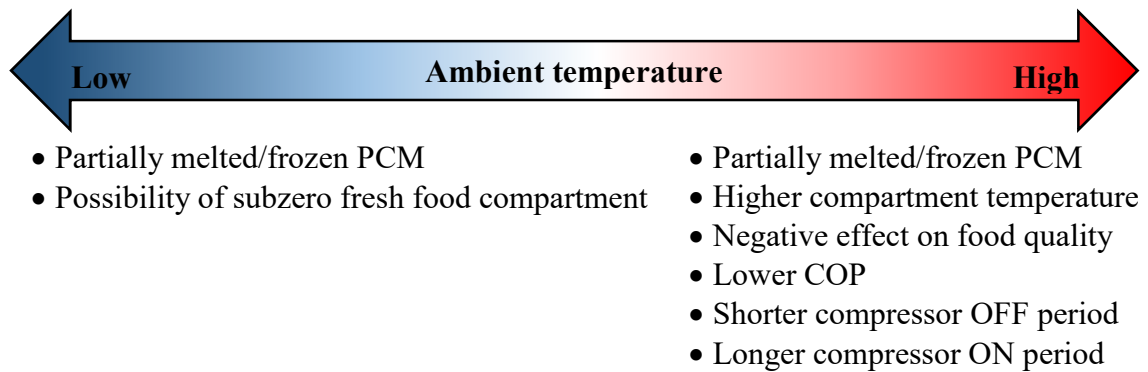
Figure A.3: Negative effects of high and low ambient temperatures on system performance

A.2.3.2 Evaporation temperature

PCM integration and evaporation temperature have mutual effects. Due to the high latent heat of a PCM giving it a high thermal capacity, it keeps evaporation temperature higher during phase change which is essentially controlled by its phase change temperature [78]. Besides, higher evaporation temperature means higher evaporation pressure as compared to a refrigerator without PCM [70] which results in higher COP. Lower evaporating temperature, on the other hand, requires longer PCM freezing time which is not only due to the heat transfer from PCM but also because of lower COP [58]. It is worth noting that compartment set-point temperature affects PCM performance. A refrigeration system needs to work longer for a lower set-point temperature in order to remove extra heat from the compartment which, in turn, means lower evaporation temperature. In such a case, PCM usefulness decreases since it cannot suitably minimize

temperature fluctuations in the corresponding compartment which is due to the temperature difference between the desirable set-point temperature and the PCM phase change temperature [85].

A.2.3.3 Door opening

When the door of a refrigeration system is opened, a sudden thermal load is introduced due to air exchange to compartment(s). Thus, the system has to work longer to remove the excessive heat and, as a result, its energy consumption increases. PCM can damp such a thermal load by adding to the thermal inertia of the compartment [78]. The only concern in such a case is whether the amount of energy consumption reduction due to the PCM dampening effect exceeds the amount of required energy consumption during its charging. The PCM effect was investigated considering automatic door opening for 1 minute with time intervals of every 40 minutes for a freezer loaded with M-packs [81]. The results indicated that energy consumption of the system was decreased by means of PCM by 6%. Nevertheless, its consumption was higher than the steady operation (no door opening) by 11%. This confirms the effectiveness of PCM as thermal energy storage. In order to further investigate the effect of PCM on the thermal load due to door opening, experiments were conducted with/without PCM for both loaded/unloaded freezer [85]. Since M-packs add to the thermal inertia of a compartment, the PCM performance for loaded freezer was less significant. Furthermore, the PCM showed promising performance when the set-point temperature of the compartment was close to its phase change temperature but for lower set-point temperatures it did not damp temperature significantly. This reconfirms the importance of proper selection of the PCM melting temperature. It is worth noting that the available heat transfer area of the PCM affects its performance due to the door opening. It was found that the larger the surface of the PCM panels, the lower the compartment temperature variation [87].

A.2.3.4 Defrost

Due to the moisture migration from the stored food products as well as from the air introduced by door openings, the compartment(s) air normally has high moisture content.

Therefore, the evaporator becomes frosted as the moisture deposits on the cold evaporator surface. In modern refrigerators, evaporators are defrosted by fitted electric resistance heaters, which switch ON automatically during compressor OFF period by a predefined pattern. The heat generated during defrost is another source of thermal load to the compartment(s). The effect of PCM on defrost of a freezer was investigated [81]. First, energy consumption of the base case system without PCM was compared to the one with PCM-equipped system (both without defrost) which showed a slight energy consumption difference. Comparing the same cases including a 30 min defrost showed that PCM could save 7% of energy consumption. It is worth noting that this energy saving was found with both lower peak air temperature inside the compartment and lower peak product temperature (about 3°C and 1°C, respectively). This potential comes from the high thermal inertia of the PCM which dampens temperature fluctuations. Even with a high latent heat capacity, PCM was fully melted after defrost due to the high power consumption of the heater (e.g. 250W). The effect of combined door opening and defrost for an unloaded compartment was also investigated. The results showed that PCM is more beneficial during defrost since it is the sole source of cold, while during door opening the compressor might be ON and its cooling power is much more than PCM (10 times higher in that specific case).

A.2.3.5 Power outage

In developing countries still the problem of power shortage or even outage exists which definitely affects the performance of refrigeration systems [85]. A conventional refrigeration system loses its driving force during power outage and cannot keep its compartment(s) cold for a long period of time due to the rapid heat gain through its walls. Therefore, food quality, energy consumption, and compressor durability are all affected by power outage. On the other hand, PCMs can store energy whenever the system is working and release it in case of power outage. It was reported that after two weeks with frequent power loss, PCM presented promising results during power outage to maintain food quality of ice cream and frozen meat against ice recrystallization and drip loss, respectively [82]. In another study, after 3 hours of power outage, compartment air

temperature was lower in an unloaded compartment with PCM compared with the loaded one without PCM [85]. Obviously, simultaneous presence of PCM and M-packs maintains compartment air temperature even lower due to the higher thermal storage. It should be noted that similar to defrost, PCM decreases the rate of temperature change for both air and products in case of power outage. Instead, once the power resumes, it requires longer compressor ON time in order to recharge PCM. Nevertheless, this has no negative effect on product temperature [81].

In order to quantify the usefulness of PCM during power outage, a factor called "period factor" was introduced [90]. Period factor is defined as the fraction of the period when a system is maintained colder than a certain temperature by PCM (period PCM) to the period when the same condition is held without PCM (period ref) as shown:

$$Period\ factor = \frac{Period\ PCM}{Period\ ref} \qquad (A.4)$$

The period factor greater than one means that PCM can help the system to remain cold longer. Based on experimental data, during power outage, period factor was higher than one confirming the absolute benefit of PCM [86]. Moreover, the lower the phase change temperature, the longer compartment temperature is maintained lower; however, as mentioned earlier, too low phase change temperature is not suitable and there has to be a compromise.

Therefore, PCMs can also act as an emergency backup in case of blackouts. The period that PCM can keep the corresponding compartment cold depends mainly upon its thermophysical properties, its thickness, and thermal load. Keep in mind that only cold storage in PCMs (evaporator side) is helpful for power outage and heat storage at the condenser side (will be explained in Section A.3) does not bring such an advantage.

A.2.4 PCM geometry and orientation

PCM should be placed in a container whose shape should be known *a priori*. The effect of container geometry was investigated based on thermal resistance comparison using identical volume and temperature difference for three different configurations [71]. It was found that parallelepiped configuration gives higher power exchange followed by

spherical and cylindrical ones. Obviously, the larger the surface area, the higher is the heat transfer. In addition, PCMs generally have low thermal conductivity and that is why normally PCM slabs are preferred. It should be noted hereby that the effect of PCM geometry is more significant under natural convection heat transfer mechanism. The same is correct for PCM orientation since it affects the temperature distribution along a naturally-cooled compartment. Using CFD, the effect of PCM orientation on the temperature distribution and air flow pattern in a naturally-cooled compartment was investigated [61]. It was found that a vertical orientation showed a circular airflow pattern in the compartment resulting in a stratified temperature distribution. On the other hand, a horizontal orientation resulted in a more uniform temperature distribution with lower average temperature in the compartment due to the different airflow pattern. But it was reported that a combinatory of these orientations resulted in a more uniform temperature with the bottom and top halves of the compartment mainly similar to the one for vertical and horizontal orientations, respectively. It should be pointed out that in the latter case, the amount of PCM was a combination of both cases, adding to thermal inertia of the compartment. Furthermore, it was reported that the same performance could be obtained by dividing the compartment into two parts and using two horizontal PCMs instead of one. Another study reported that the most optimal configuration and height for the PCM container are vertical and closest to the bottom of the compartment giving lower temperature and better energy storage than the horizontal one [71]. The reasons for contradictory conclusions are due to the differences in compartment height, phase change temperature and compartment set-point temperature. These results indicate the importance of proper selection of the PCM geometry and orientation for a naturally-cooled compartment.

A.2.5 Analysis of PCM at evaporator

Tables A.4 and A.5 summarize the advantages and disadvantages of PCM at evaporator, respectively. Besides, Table A.6 summarizes the results obtained for the use of PCM in refrigerators. To make the results comparable, ambient temperature, latent heat and melting point of the PCM, as well as its dimensions are given. Based on the

table, the inclusion of PCM prolongs the compressor OFF time and enhances the COP of the system. Based on this review, 2-74% enhancement of COP can be achieved by the application of PCM at evaporator. The amount of enhancement strongly depends on the ambient temperature, thermal load and PCM type.

Table A.4: Advantages of PCM at evaporator

Reference	Advantage	Comment
[70, 78, 79, 89, 94]	✓ Higher COP	• Better cooling performance of the system
[74, 78]	✓ Shorter compressor global ON-time ratio	• Less compressor work • Lower energy consumption • Lower noise generation
[78, 93]	✓ Longer compressor OFF time	• Lower overall energy consumption • Economic benefits • Helpfulness for the grid • Possibility of off-peak operation • Positive environmental impacts • Lower compressor ON/OFF frequency • Positive effect on compressor lifetime
[80-82, 85-87, 93-95]	✓ Slower compartment temperature changes	• Better food quality • Less compressor work • Potential of uniform temperature distribution
[77]	✓ More controlled temperature at compressor inlet	• Possibility of superheat minimization • Better system performance
[70, 78, 79, 89]	✓ More stable condition against thermal load variations	• Lower sensitivity against ambient temperature changes
[78, 79, 94]	✓ Higher refrigerant density at compressor inlet	• Higher refrigeration capacity
[81, 85, 86]	✓ Assistance in case of power outage	• Acting as an emergency backup • Keeping stored food cold for longer periods with no power supply • More useful during tight power supplies due to rolling blackouts
[81, 85]	✓ Helpfulness for damping defrost and door opening temperature increase	• Slower compartment temperature raise during defrost • Better food quality

Table A.5: Disadvantages of PCM at evaporator

Reference	Disadvantage	Comment
[95]	✓ Higher condensation temperature	• Negative effects on system performance • Higher heat transfer from condenser to compartment(s) • Requirement of condenser modification or utilization of condenser fan
[74, 78]	✓ Longer compressor ON time during a cycle	• More energy consumption in a cycle but overall energy consumption is lower (desirable) • Possibility of destructive effect on compressor due to long operation

Table A.6: Summary of the results obtained for the use of PCM in refrigerators

Ref.	Study type		PCM type	Melting Temperature (°C)	Dimensions of PCM (m³)	Compressor OFF time (h)	Ambient Temperature (°C)	Latent Heat (kJ/kg)	COP Without PCM	COP With PCM	% Enhancement
	Simulation	Experimental									
[72]	✓	✓	Eutectic	-3	-	-	-	-	0.83	0.98	18
[74]	✓		Eutectic	-6	0.03×0.5×0.5	10	20	280	1.09	1.9	74
[78]	✓	✓	Eutectic	-5	0.48m²×0.025	4.3	20	280	1.37	1.4	2
[79]		✓	Water	0	0.48m²×0.05	8.2	20	-	-	~2.2	-
			Water	0	0.48m²×0.01	8.76	20	-	-	-	-
			Water	0	0.48m²×0.005	9.2	15	-	-	~2.8	-
			Eutectic	-3	0.48m²×0.005	8.8	15	-	-	~2.6	-
[80]	✓		-	-	-	-	21	-	1.50	1.77	18
[70]		✓	Water	0	0.003m³	-	22.8-23.8	333	4.8	~5.8	21
			Eutectic	-5	0.003m³	-	22.8-23.8	289	4.8	~6.2	29
[58]	✓	✓	Water	0	0.005×0.45×0.46	4.8	20	-	-	-	-
			Water	0	0.005×0.45×0.46	4.0	25	-	-	-	-
			Water	0	0.005×0.45×0.46	2.9	30	-	-	-	-
[94]		✓	Water	0	-	-	30	-	5.5	9.04	64

PCM at the evaporator has a promising future since it helps the refrigeration system by cold storage (see Table A.4). Nevertheless, it was reported that PCM at the evaporator increases evaporation temperature (prevents evaporation temperature drop during phase change) which in turn increases compressor inlet temperature. Thus, the performance enhancement of a system equipped by PCM at evaporator side is somewhat limited by the high condensation temperature (see Table A.5). However, since compressor efficiency is more sensitive to evaporation temperature, generally, PCM at evaporator results in performance enhancement [78]. In a study, the requirement of more heat rejection from condenser was also identified and two remedies were proposed to overcome the issue; either using a fan or increasing heat transfer coefficient of a naturally-cooled condenser [95]. In the following sections, the potential applications of PCM at evaporator in domestic refrigeration is discussed.

A.2.5.1 System performance enhancement

As mentioned earlier, a PCM-equipped refrigerator has smaller ON-time ratio as well as higher COP. These two results are significantly important for performance enhancement of the system. Moreover, due to its high thermal inertia, the rate of temperature change in compartment is lower and better food quality is guaranteed by presence of PCM. This option not only helps the regular performance of the system, but also is greatly helpful for defrost. It is worth pointing out that domestic refrigerator manufacturers prefer to enhance the performance of their products by the lowest possible change in an existing manufacturing line and minimum additional costs. PCM involvement in refrigeration cycle seems to be a promising solution since it is cheaper as compared to the compressor or insulation change which in turn requires manufacturing line upgrading. Furthermore, another significant advantage of PCM over other available modifications such as compressor change or VIP is that it is even applicable to the existing refrigerators/freezers. This not only brings performance enhancement of the appliances, but also creates the required backup in case of power outage.

A.2.5.2 Helpfulness in case of power outages

As mentioned earlier, thermal storage by PCM at evaporator keeps compartment cold for longer periods of time. In case of a power outage, the thermal storage compensates the heat gain through the compartment walls. Moreover, PCM adds to the thermal capacity of the compartment, which is of great importance if the refrigerator door is opened during power outage. Since door opening during power outage introduces a sudden heat load resulting from hot ambient airflow into the compartment(s), an ordinary refrigerator, even with the highest possible insulation (i.e. VIP), cannot go back to a colder temperature after the air exchange. However, when PCM is used at evaporator it absorbs heat from compartment air, allowing lower air temperature. This is an important feature in case of rolling blackouts since the refrigerator can perform in such a scenario.

A.2.5.3 Reduction of peak hour consumption

Utility companies normally charge customers with different rates based on the consumption time since electricity generation costs more during grid peak hours. Therefore, shaving consumption from peak to off-peak hours is beneficial both for customers and utility companies [103]. A method, which has received considerable attention in recent years, is demand side management (DSM). DSM shifts the time of consumption from an undesirable time to a more desirable one [104]. It was found that about 38% of refrigerators have the potential to shift their demand to off-peak hours resulting in about 11% reduction in customers bill [105]. In refrigeration systems, PCM use at evaporator prolongs compressor OFF time. Thus, PCM can store cold during off-peak hours and release it to the compartment(s) during peak hours; hence, eliminating the compressor work. Potential cost savings of 30-54% was reported by applying PCM solely at evaporator [83]. Thus, a PCM-equipped refrigerator not only helps the grid and prevents environmental impacts of higher greenhouse gas emissions, but also gives economic advantages for customers as well.

Thermal storage in refrigeration systems can also help the penetration of renewable energy resources such as solar energy. Plenty of renewable energy is available during daytime and thermal storage can be useful for this case based on proper use of control

strategy. In an attempt to implement this idea, PCM was used in a domestic freezer-refrigerator whose control strategy was changed to adapt to grid supply availability in California [91, 92]. It was found that refrigeration systems could change their energy consumption pattern to have higher consistency with renewable source availability.

It is worth mentioning that due to the longer OFF period of refrigeration systems with PCM and lower energy consumption, PCM-equipped refrigerators can be a promising option to be used in net zero energy buildings (NZEBs). Their long OFF time can compensate for intermittency of renewable energy sources.

A.2.5.4   Reduction of refrigerator noise

It is clear that noise generation by domestic appliances is by no means desirable. Among the appliances, refrigerators are found more noisy since the noise from many other appliances have been diminished in recent years [106]. The refrigerator noise comes from its operation and refrigerant flow inside pipes [107]. A number of studies tried to modify the components of refrigeration system to make the equipment quieter, especially its compressor [108] and evaporator [106, 107]. It is clear that the more the appliance works, the more noise it generates. Thus, ON-time ratio of refrigeration systems has a crucial role in the noisiness of the appliance. As it was mentioned earlier, PCM use at evaporator prolongs OFF period of the compressor, reducing appliance's ON-time ratio and its consequent noise.

A.2.5.5   Reduction of overall costs

Phase change materials use in refrigeration systems is first added up to initial costs but since the operation of the system is affected, the overall costs will be lower over long-term application. Taking into account all the benefits of PCMs including prolonged compressor OFF time, reduction of customer bills, lower food quality loss, etc., all in all, bring economic advantages based on an initial investment in PCMs. As a confirmation to this, a cost and CO_2 mitigation analysis considering the benefit of cold storage in PCMs for the domestic sector in Europe showed that cost savings of 1082-4683 million euros

per year and huge CO_2 mitigation can be achieved; hence, evaporator PCM has a great implementation potential in the future [109].

A.3 PCM application at condenser

A condenser is a heat exchanger responsible for rejecting heat of compression from a refrigeration system to the environment. Three types of condensers are common in domestic refrigerators: naturally-cooled, forced-cooled, and hot-wall condensers. Naturally and forced-cooled condensers are those types that are cooled by means of free and forced convection heat transfer mechanisms, respectively. Hot-wall condensers are mounted on the inside surface of the refrigerator cabinet and are naturally-cooled by heat transfer through the wall. The more condenser heat removal from the refrigeration cycle is the better. The idea of using PCM at condenser is to achieve lower temperatures in condenser. Unlike wide investigation of PCM at the evaporator or inside compartment, its application at condenser did not receive much attention as shown in Table A.1. The reason might be some undesirable outcomes of such configuration.

Using PCM at condenser can extend condenser's heat rejection process to compressor OFF time so as to enhance condenser heat transfer and achieve lower condensation temperature [59]. In order to investigate this idea, a novel shape-stabilized phase change material (SSPCM) [110] was mounted around hot-wall condenser tubes [59]. Experimental results showed lower energy consumption for the new system (about 12% saving). Moreover, higher evaporator temperature, lower temperature fluctuation in the fresh and frozen food compartments, and higher COP were also reported. It should be noted that all these benefits were the results of a major deficiency in system performance (as a result of PCM inclusion) which was more frequent start/stop of compressor i.e. shortened period between two successive cycles. In other words, the compartment temperature fluctuation was prevented by more frequent compressor start/stop. This deficiency negatively affects compressor performance in long-term usage. Further on, the system was modeled to investigate the effect of ambient temperature, freezer set-point and phase change temperature [88]. It was found that when ambient temperature increased or freezer set-point decreased, COP decreased and energy consumption

increased. It was also reported that when the phase change temperature increased, the amount of energy consumption showed a minimum value at 49°C which was close to the phase change temperature of the SSPCM. This result confirms the importance of proper PCM melting point selection. Finally, the novel system was optimized based on cost and compared to a conventional system with hot-wall condenser [96]. The results indicated that the novel refrigerator could save 20-26% energy of that of the conventional one.

A series of experiments were conducted using different PCMs at different locations of a refrigeration plant as shown in Figure A.4. The PCMs were separately placed between the compressor and condenser (PCMA), between the condenser and expansion valve (PCMB), and between the evaporator and compressor (PCMC) [75]. Table A.7 shows each location has its own advantage and helps enhancing system COP. When located between compressor and condenser (PCMA), the PCM was acting as an extra condenser. In this case, COP was enhanced due to the lower temperature and pressure in condenser. For PCMB, lower phase change temperature resulted in higher COP [77]. The reason was due to the fact that the lower the phase change temperature, the higher the subcooling. Nevertheless, the heat rejection time is longer. Generally, higher ambient temperature deteriorates the COP but it was found that when PCMB was used, the magnitude of COP reduction was lower since the PCM created higher temperature difference between the refrigerant and the ambient during phase change. For the case when PCM was located between evaporator and compressor (PCMC), there were some advantages and at the same time some disadvantages. A lower superheat was observed which should have resulted in higher COP, but since the amount of pressure drop in suction line due to the PCM heat exchange was higher, it offset the COP enhancement. Nevertheless, PCMC had temperature-stabilizing effect. It should be noted that there was a major deficiency in their work; the amount of refrigerant was changed in each test, while it was reported that the performance of the system was sensitive to the amount of refrigerant. Therefore, this obviously prevents proper comparison of the results. Generally, PCMB resulted in the highest COP while PCMA and PCMC provided higher system stability. Further on, the system was also dynamically modeled [76].
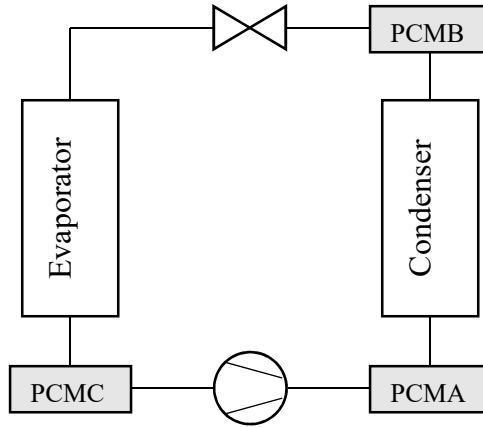
Figure A.4: Considered PCM locations in the refrigeration system investigated by Wang et al.

Table A.8 summarizes the advantages of the PCM placing at condenser side. However, there were some disadvantages which are given in Table A.9.

Table A.7: Advantages based on PCM location [75, 77]

Name	Location	Advantage	COP change
PCMA	Between compressor and condenser	Decreasing condenser pressure	6%
PCMB	Between condenser and expansion valve	Increasing subcooling	8%
PCMC	Between evaporator and compressor	Decreasing superheat	0%

Table A.8: Advantages of PCM use at condenser

Ref.	Advantage	Comment
[75, 77, 88]	✓ Higher COP	• Better cooling performance of the system
[59, 88]	✓ Shorter compressor global ON-time ratio	• Shorter compressor work in a cycle • Lower energy consumption • Lower overall noise generation
[59, 88]	✓ Lower energy consumption	• Economic benefits for users • Helpfulness for the grid • Positive environmental impacts
[59]	✓ Continuous heat rejection from condenser even during compressor OFF period	• Higher overall condenser heat transfer efficiency • Higher subcooling • Higher COP • Lower condensation temperature • Higher evaporation temperature
[59, 88]	✓ Smaller starting compressor power due to higher refrigerant	• Lower energy consumption • Longer compressor lifetime

Ref.	Advantage	Comment
	temperature in condenser	
[59]	✓ Faster stable condition of refrigeration system	• Better food quality • Shorter compressor work
[59, 75, 77]	✓ Lower condensation temperature and pressure	• Higher COP • Faster stable condition • Higher subcooling
[59, 88]	✓ Higher subcooling degree	• Higher cooling capacity
[59, 88]	✓ Lower heat gain from condenser to compartment during ON time	• Lower temperature change inside compartment • Better food quality • Shorter compressor work

Table A.9: Disadvantages of PCM use at condenser

Ref.	Disadvantage	Comment
[59]	✓ More frequent compressor ON/OFF	• Destructive effect on compressor lifetime • More frequent noise generation • Possibility of heat accumulation in PCM since it might not have enough time to reject the stored heat between compressor OFF and ON intervals
[59, 88]	✓ Higher heat gain from condenser to compartment during OFF time ✓ More refrigerant displacement losses	• Negative effect on food quality • More frequent compressor work • Compressor start/stop results in losses • The more frequent the compressor start/stop, the more the losses

In summary, lower condensation temperature for PCM-equipped condensers caused more frequent compressor start/stop. All the advantages of PCM at condenser are degraded by this major deficiency. Besides, higher evaporation temperature in such systems seems to be the result of the deficiency which prevented the temperature drop. This might be the most significant reason why such configurations have not received much attention. Nevertheless, proper heat storage in PCM at condenser can bring system stability by increasing subcooling and reducing condensation pressure [77] which requires further investigation.

Further research is needed to study the impact of PCM at the condenser since the earlier studies were limited to either a hot-wall condenser or a refrigeration plant: More comprehensive analysis and investigation into other systems is also needed.

A.4 Experimental protocols

Generally, there are a number of standard performance test procedures for refrigeration systems. However, for the cases with PCM inclusion, thermal analysis and energy consumption tests are the only two considered ones. For instance, ISO 15502 and EN 153 are two well-known standard energy consumption test procedures. In the existing literature, the purpose of conducting experiments were various but the most frequent ones were performance enhancement (including energy consumption reduction, COP enhancement, improving food quality, etc.) and also finding the best PCM design parameters. Therefore, the covered experimental procedures were different and involved both complying existing standard testing methods and/or case specifically developed methods. Nevertheless, all these procedures share some fundamental measurements:

- **Temperature measurement:** All of the studies covered this measurement; however, the numbers of measurements were different based on the requirements of the study. In the most comprehensive ones, temperature at compressor, condenser, evaporator, capillary tube, compartment, M-packs, PCM, etc. were measured. Measurements were carried out by means of thermocouples, thermistors, or RTDs.

- **Power consumption measurement:** In order to compare the energy consumption, change in the setup by means of PCM inclusion, its power consumption should be monitored. Therefore, several studies included this measurement in their investigation.

- **Pressure measurement:** PCM inclusion in the system affects the evaporation and condensation pressures. To monitor the magnitude of change, several studies included this measurement in their setup. Since evaporation and condensation processes are examples of a phase change process, the pressure change in these components is negligible (unless refrigerant superheating or subcooling takes place in the evaporator or condenser, respectively). Therefore, only two pressure transducers are normally sufficient for measurement in these components.

A.5   Modeling

Modeling of a refrigeration system consists of sub-models for each of its components. In this section, first a brief discussion is presented about the modeling schemes available for refrigerators and then modeling methods applied to simulate PCM-equipped systems are explained.

A.5.1   Modeling methods available for refrigeration systems

In order to model the whole refrigeration system, its major components should be modeled individually. These components consist of compressor, heat exchangers (condenser and evaporator), expansion device (normally capillary tube) and compartment(s).

Among the components of a refrigeration system, compressor modeling can be skipped by means of using manufacturer's data [111]. However, this makes the model limited to the validity range of the data and extrapolations are not guaranteed to give accurate results. On the other hand, modeling of a compressor basically depends on its thermodynamics and heat transfer mechanism. Generally, there are a wide variety of modeling methods available for compressors covering from black-box to white-box methods [112]. The former covers all the studies, which only consider input/output relations while ignoring phenomenological details of compressors. In contrast, the latter consists of several control volume models, which are too complicated to be used in the whole refrigeration system modeling. Between these two extremes, gray-box methods are used.

There are several approaches available for modeling of heat exchangers in domestic refrigerators; i.e. condenser and evaporator. Nevertheless, they can be generally classified in three major groups: global, zonal, and distributed modeling. Global or single-node modeling (also known as lumped parameter modeling) is the simplest modeling procedure, which considers the whole condenser as one lumped node. The major drawback of global modeling is its limited accuracy as well as its ineffectiveness for heat exchangers with refrigerant phase change [113]. In contrast, distributed or multi-node modeling considers several control volumes where parameters are lumped within. The

high accuracy of distributed modeling results in longer computational time. Between these two extremes, another modeling procedure is defined; zonal or nodal modeling, which is flexible with more desirable characteristics. This approach considers three zones of superheated, two-phase, and subcooled inside heat exchangers where parameters are considered as lumped. It should be noted that for the case of evaporators, no subcooled zone is considered. The accuracy as well as the computational time of this procedure lies between the two extremes, especially the accuracy is closer to the distributed modeling approach [113]. Table A.10 summarizes advantages and disadvantages of these approaches.

Table A.10: Comparison of advantages and disadvantages of modeling approaches for heat exchangers

Modeling	Advantages	Disadvantages	Ref.
Global	• The simplest method • Considers the heat exchanger as a single lumped node • Fastest computation	• Low accuracy • Elimination of spatial details • Becomes ineffective if phase change occurs	[76, 113, 114]
Zonal	• Acceptable computational time with accuracy closer to distributed modeling procedure • Performance lies between the two extremes of global and distributed modeling • Parameters are lumped in each zone	• Not suitable for applications with high accuracy • Possibility of failure during large transients in the system	[113, 114]
Distributed	• High accuracy • Providing subcooling effect for condensers and superheating effect for evaporators	• Long computational time • Some flow properties are not continuous between nodes • Iterative procedure is complicated	[76, 113-115]

The most commonly used expansion device in domestic refrigeration systems is capillary tube, a small tube connecting condenser outlet to evaporator inlet [60]. Capillary tube modeling basically depends upon its heat transfer mechanism; adiabatic or non-adiabatic. Obviously, whenever a capillary tube is covered by insulation, it is considered as adiabatic. Besides, since natural heat transfer to the environment is slow as compared

to fast refrigerant flow through capillary tube, it can be assumed as adiabatic as well [113].

Available modeling approaches for system components are tabulated in Table A.11. Besides, Table A.12 shows a summary of studies available in the open literature which are based on modeling the whole refrigeration system integrated with PCM for heat/cold storage where the first two used PCM at evaporator, while the rest applied it to condenser.

Table A.11: Modeling approaches available for components of the system

Compressor	Heat exchanger	Expansion device
• Manufacturer's data	• Global (lumped)	• Adiabatic (isenthalpic)
• Black-box	• Zonal	• Non-adiabatic (non-isenthalpic)
• Gray-box	• Distributed	
• White-box		

A.5.2 Modeling PCM at evaporator

Even though the two studies for the whole system modeling using PCM at evaporator used refrigerator as their test rig, the applied methodologies were different due to the setup differences. Cerri et al. [72] modeled the system based on a relatively simple method considering different time sets including transient, quasi-steady and OFF modes. Based on manipulating insulation resistance, 3-18% COP enhancement was reported. The major problem in their work seems to be the PCM surface area (not reported by the authors), which was not high enough to effectively meet the requirements of the system. Besides, since the controlling temperature for compressor start was evaporator temperature, PCM addition to the evaporator resulted in higher compartment temperature. Moreover, at the beginning of phase change (freezing) a temperature raise in evaporator was reported experimentally which was due to the supercooling effect of the PCM which was not considered in the modeling. Later, the effects of PCM phase change temperature and thickness, and ambient temperature on a PCM slab at the evaporator were

investigated by Azzouz et al. [78]. Modeling was developed for both compressor ON/OFF modes reflecting PCM charging/discharging. The difference between this study and the previous one is that the latter neglected the effect of transient phenomena. The results showed that experimental ON-time period was longer than the one predicted by simulation, which was due to the inexact estimation of heat losses through the walls of the compartment. The fact is that the lower the compartment temperature difference with ambient, the lower the rate of heat transfer. When the system reaches the final ON-time moments, the highest temperature difference is present which results in higher heat transfer through the compartment walls. In the study, since the rate of heat transfer through compartment walls during ON and OFF periods was not accurately modeled, such a discrepancy occurred. Besides, the rate of temperature change in the fully frozen PCM was assumed to be the same as the one for the evaporator. Even though this simplifying assumption prevented further complexity of the modeling approach; it is not an accurate assumption. The common limitation of these two studies was the application of single-node (lumped) modeling approach for heat exchangers.

To model heat transfer in PCM, the abovementioned studies used energy balance and had almost similar trends in this regard. Besides, the common assumption of small Stefan number was made. The limitation of these models lies in the fact that direct heat transfer from PCM to the compartment was not considered.

A.5.3   Modeling PCM at condenser

A comprehensive modeling approach was used to simulate the performance of a refrigeration plant equipped with a PCM heat exchanger where PCM was on the shell side at different locations (see Figure A.4) and refrigerant was flowing through the tube [76]. The reason for such a configuration was to maximize the heat transfer due to the fact that refrigerant flow in shell side (outside the tube) brings many difficulties. Heat transfer in the PCM was modeled assuming an equivalent conductivity to account for convection inside PCM and since a shell and tube heat exchanger was used, axial conduction through PCM was neglected as compared to the radial one. The results showed a deviation at early moments of operation basically due to the simplifying

assumptions made: The heat transfer coefficients were evaluated at steady state conditions [76]. The effectiveness of PCM locations against ambient temperature and load variations were investigated by simulation whose results were presented earlier in Section A.3.

The other two studies (3 and 4 in Table A.12) mounted PCM at the hot-wall condenser and were done using the same setup and PCM and similar methodology. The assumption for PCM modeling was considering heat conduction in a single solid phase [88, 96]. The reason was due to the fact that for the SSPCM used in their studies, not only convection was negligible, but also due to the presence of support material, it was possible to consider PCM as a single solid phase (as long as the temperature was below 110°C, which is always the case for domestic refrigerators). Therefore, three-dimensional heat conduction equations were used for the PCM. The model consisted of sub-models for all the components of the refrigeration system as well as for insulation and M-packs. Simulation results were in good agreement with the experimental ones confirming the validity of their assumption. The results indicated 19% enhancement in COP by PCM integration at the condenser side [88]. However, the constraints for the PCM (its type and modeling approach) as well as using PCM for a hot-wall condenser make their application limited.

It is worth pointing out that in contrast to these two latter studies (3 and 4 in Table A.12), no frequent compressor start/stop was reported by Wang et al. [76]. This seems to be due to the frequent heat transfer from the PCM-coated hot-wall condenser to compartments, a parameter that was absent in the set-up used by Wang et al. As mentioned earlier, hot-wall condensers are mounted on the inside surface of refrigerator cabinet and have a large heat transfer area which are prone to heat transfer to compartments. In a system with no PCM, compressor work removes the resulting heat transfer from hot-wall condenser to compartments and once it is turned OFF, no more heat transfer occurs (after a certain period) from condenser neither to the ambient nor to compartments. On the other hand, for a PCM-equipped hot-wall condenser due to the continuous heat rejection from condenser even during compressor OFF period, heat transfer occurs through compartment's wall that makes the compartment hotter and

inevitably the compressor has to work more frequently to remove the heat load. This heat transfer was taken into account in the modeling approach in the latter studies (3 and 4 in Table A.12), confirming the high heat transfer rate from condenser to compartments. Simulation results indicated about 7% decrease in total energy saving by PCM integration due to the heat leakage from the condenser to the compartment [88]. These results show that there is a need towards conducting more studies in order to clarify the usefulness of different PCMs at different types of condensers.

Table A.12: Summary of studies on modeling domestic refrigeration systems with PCM

No. Ref.	Simulation type	Setup	Refrigerant	Evaporator type	Condenser type	Heat exchanger	Capillary tube	Compartment	PCM model	Max. discrepancy
1 [72]	Dynamic	Refrigerator	-	Free	Free	Lumped	-	Lumped	Energy balance	N/A
2 [78]	Dynamic	Refrigerator	R600a	Free	Free	Lumped	Adiabatic	Lumped	Energy balance	5%
3 [88]	Dynamic	Refrigerator	R600a	Free	Hot-wall	Zonal	Adiabatic Nonadiabatic	Lumped	Conduction	3.5%
4 [96]	Dynamic	Refrigerator	R600a	Free	Hot-wall	Lumped	Adiabatic Nonadiabatic	Lumped	Conduction	N/A
5 [76]	Dynamic	Refrigeration plant	R22	Forced	Forced	Zonal	Adiabatic	Lumped	Energy balance	8%

A.6   Concluding remarks

A comprehensive review of PCM application in domestic refrigeration systems was carried and as shown in Table A.1 most of the studies investigated the effect of placing the energy storage on the evaporator side. The results were promising but still some modifications are required in order to find the most appropriate PCM for such application. Condenser PCMs, on the other hand, were not much successful due to their undesirable outcomes. In summary, the limitations of the studies are:

- Most of the conducted studies on PCM at condenser focused on a specific SSPCM; therefore, lack of comprehensive information exists for this configuration. Besides, the conducted studies are limited to either hot-wall condensers or application of PCM at condenser inlet or outlet. The former resulted in more frequent heat transfer through compartment walls and needs further investigation to clarify the usefulness of PCM at condenser.

- Comparing advantages and disadvantages of PCM integration at the evaporator side with those of the condenser side, there seems to be a mutual relation. Evaporator side PCM integration has some advantages which can cover disadvantages of condenser side PCM and vice versa. Therefore, it seems that simultaneous application of PCMs at condenser and evaporator could be more advantageous.

- PCM has not been used close to the insulation of refrigeration systems. Even though in such a case its objective would primarily be reduction of heat transfer through the wall, it can help keeping compartment cold for longer periods of time as it has been reported for refrigerated trucks [116].

- PCM use for cold storage requires cautions since otherwise it not only can degrade the performance of the system, but also can lower the food quality. This is more significant when the evaporator is immersed inside PCM.

- Despite the availability of modeling procedures for simulation of freezer-refrigerators, all modeling studies with PCM solely focused on refrigerators. Besides, modeling studies were also very limited both in number and types of PCMs used.

Appendix B: Exergy analysis of vapor absorption refrigeration systems

B.1 Introduction

A large portion of buildings energy consumption is dedicated to the commercial sector. In 2014, this sector accounted for about 19% of the total energy consumption in the United States [117]. The commercial sector covers a vast class of buildings including office, governmental, institutional, retail, utility, etc. In 2012, among about 5.6 million office buildings in the United States, about 80% were equipped with space cooling systems in order to provide the required thermal comfort during cooling season, which accounted for a huge amount of energy consumption [118]. However, the total energy consumption of this sector for space cooling is projected to decrease by about 0.2% per year reaching a total amount of 1750PJ by 2040 [119]. The projected goal is expected to be achieved despite the rapid growth in the commercial sector, which inevitably requires higher energy efficiency as well as identification and reduction of energy losses in cooling systems.

A variety of air conditioning systems are available for indoor space cooling during hot season. Among these systems, vapor compression and absorption cooling systems are the most common ones. The main difference between these two systems is that in vapor compression systems a compressor is used to increase the pressure of the refrigerant. However, in vapor absorption systems, the pressure change is carried out by means of an absorption/generation process. Nowadays, due to the advantages of absorption over vapor compression systems, absorption cooling is more favored. The advantages include low noise generation, less frequent maintenance requirements, high reliability, possibility of being driven by low-grade energy, better capacity management and control, etc. [120]. Besides, utilization of absorption cooling is in line with the current efforts to phase out environmentally unsafe refrigerants, which are normally used in vapor compression systems [62]. The generation process in absorption cooling can be carried out in several stages, which are known as "effects". The simplest configuration, single effect absorption, consists of a generator, absorber, condenser, evaporator, refrigeration

expansion valve, solution pump, solution expansion valve, and solution heat exchanger. Multi effect absorption systems have more generation stages with additional generators, condensers, solution expansion valves and solution heat exchangers [121]. In this study, a single effect absorption system is investigated.

The most commonly used measure to evaluate the efficiency of a refrigeration system is the energy efficiency in terms of coefficient of performance (COP) [122]. The first law of thermodynamics (energy analysis) is related to energy conservation, while the second law of thermodynamics (exergy analysis) takes entropy into account via irreversibilities and deals with the quality of energy [123]. Exergy is based on a combination of the first as well as the second law of thermodynamics; thus, it is a measure of the quantity and quality of energy. In systems without flow, exergy is defined as the maximum amount of work obtained from a process, which brings the system into equilibrium with its environment [124]. Consequently, unlike energy, exergy is dependent upon the properties of the system and its surrounding environment [120]. Exergy analysis is useful for improving the efficiency of energy-resource use, since it quantifies the locations, types and magnitudes of losses [125]. Therefore, minimizing exergy destruction of energy systems results in sustainable development [126].

Many studies analyzed the energetic and exergetic performance of different types of absorption systems. Table B.1 presents a summary of investigated single effect LiBr/H_2O absorption systems based on exergy analysis. The components are sorted from the highest exergy destruction to the lowest one. It shows that, generally, the absorber and generator had the highest exergy destruction, which was due to the heat of mixing [127]. Furthermore, Table B.2 shows a list of investigated parameters with exergetic analysis of single effect LiBr/H_2O absorption systems. It shows that the system components temperature (the first four rows) and HTF temperatures (the last three rows) were investigated in many studies. Earlier studies indicated that the higher heat source temperature resulted in higher COP, while the system exergetic efficiency decreased [127]. This was attributed to the higher exergy loss in the generator as a result of higher temperature difference with the ambient. Moreover, higher chilled water outlet temperature resulted in higher COP and lower exergetic efficiency [127, 128]. The reason

for the deteriorated exergetic performance is the higher capacity of cooling for colder chilled water temperature. The effect of HTF temperatures on the first law and second law efficiencies are depicted in Figures B.1 and B.2, respectively. They show that there is a conflict between the first and second law efficiencies for the suitable HTF temperature. This type of difference is further explained in this study.
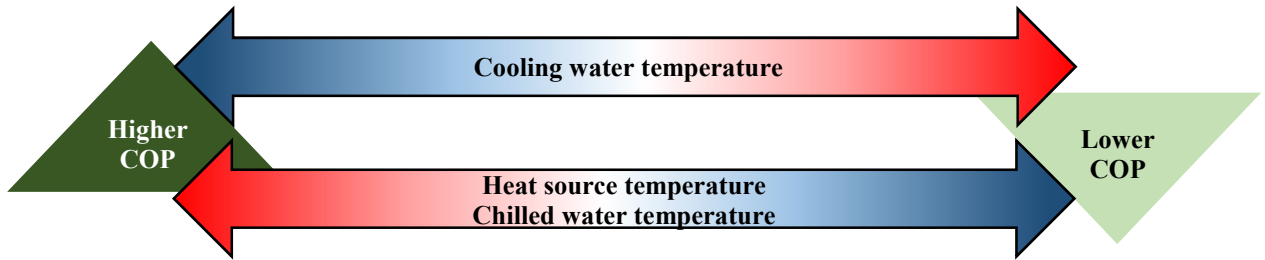
Figure B.1: The effect of HTF temperatures on the first law efficiency (COP)
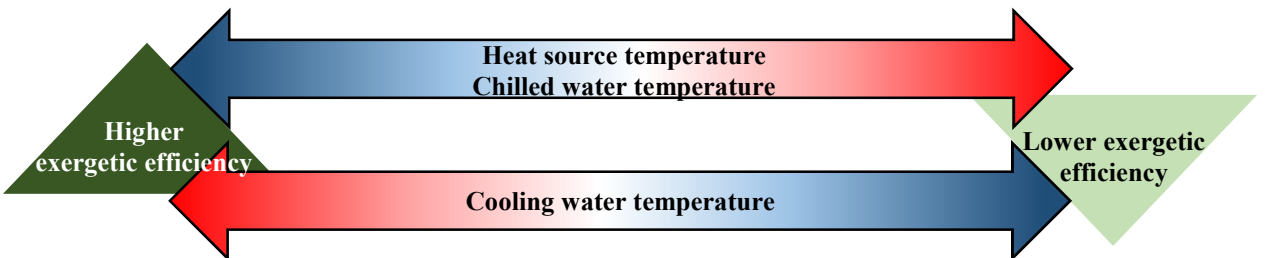
Figure B.2: The effect of HTF temperatures on the second law efficiency (exergetic efficiency)

In heat exchangers, HTF mass flow rate is an important design parameter. Advantages of higher HTF mass flow rate include higher convective heat transfer coefficient, which in turn brings better overall heat transfer. On the other hand, lower heat exchange rate, higher pressure drop and requirement of a bigger pump are the drawbacks. Therefore, the suitable HTF mass flow rate is the one that satisfies all the mentioned parameters. However, the effect of HTF mass flow rate variation on the exergetic performance of the system is also significant.

Different systems have been exergetically analyzed investigating the effect of mass flow rate; e.g. combined heat and power [129], solar PVT [130] and Rankine cycle [131]. For the absorption cooling, to the best of the author's knowledge, few studies focused on

HTF mass flow rate using exergy analysis. Morosuk and Tsatsaronis carried out a qualitative investigation under constant HTF temperatures [132]. It was concluded that, generally, increasing the heat source and absorber cooling water mass flow rate increases the exergy destruction. Kaynakli et al. only focused on the heat source and considered different temperature and mass flow rates [133]. It was reported that higher heat source HTF mass flow rate resulted in higher exergy destruction of the generators in a double effect absorption system. Recently, the effect of the refrigerant, solution and heat source steam mass flow rates in a LiCl/H_2O absorption refrigeration system was investigated [134].

According to Table B.2, the effect of HTF temperature on the exergy destruction rate has been extensively investigated. It is important to point out that in all of the earlier studies whether focused on the HTF temperature or component temperature, system COP was changed during the investigation, which was due to the changes in generation and/or evaporation heat transfer rates. On the other hand, the effect of HTF mass flow rate in every component and also its investigation with the HTF inlet temperature variation on the exergetic performance has not been addressed so far. Moreover, according to Table B.1, due to the effect of a number of parameters, a general statement cannot be made to rank the components based on their exergy destruction.

To address these issues, in this study, first the exergetic analysis of a base case single effect LiBr/H_2O absorption system is performed and the components are sorted out based on the impact on the system exergy destruction. Thereafter, the influence of HTF mass flow rate in the components on the exergy destruction is analyzed. Then, the effect of the cooling water, chilled water, and heat source inlet temperature on the exergetic performance of the corresponding component is evaluated while the system COP is kept constant. This means that the same amounts of heat were provided to/rejected from the system components but by means of different HTF inlet temperatures and mass flow rates, which in fact means different heat exchanger designs. In other words, earlier studies investigated the effect of HTF temperatures on the same system; thus, reported different COP values. However, in this study, different systems with identical COP are compared based on exergy analysis. Finally, the impact of HTF mass flow rate on

exergetic performance is compared for systems with equal COP values, which operate between the same heat source and chilled water temperatures as the base case system. The outcomes of this study can be used in the decision-making process for early design stages of absorption cooling systems to select an exergetically efficient design for the required heat exchangers based on the HTF mass flow rate and temperature. Besides, this study shows how the exergy analysis can distinguish among systems, which are considered to be identical from the energy analysis point of view. Since the focus of this study is on the heat exchange aspect only, the effect of abovementioned parameters is investigated assuming that supply systems and heat exchangers (whether economically feasible or not) are able to deliver such HTF mass flow rates for the given inlet temperatures.

Table B.1: Summary of studies with exergy analysis of single effect LiBr/H$_2$O absorption systems

[127]	[135]	[136]	[137]	[138]	[139]	[140]	[141]	[142]	[143]	[144]	[145]	[146]	[147]	[148]	[149]
A	A	G	G	A	G	G	G	A	A	G	G	G	A	G	G
G	C	A	A	G	A	E	A	G	G	A	A	A	SHX	A	A
SHX	E	E	E	E	E	A	C	E	SHX	E	E	E	C	E	C
C	G	SHX	SHX	SHX	C	C	E	C	C	C	C	C	G	C	E
E	SHX	C	C	C	SHX	SHX	SHX	SHX	E	SHX	SHX		E		SHX
REV		REV	RHX	REV		REV					REV				REV
		RHX	P	SEV		SEV					P				P
		P		P											

A: Absorber **E:** Evaporator **RHX:** Refrigeration heat exchanger   **SHX:** Solution heat exchanger   **P:** Pump

C: Condenser **G:** Generator **REV:** Refrigeration expansion valve **SEV:** Solution expansion valve

Table B.2: Summary of the investigated parameters in earlier studies

Reference	[127]	[128]	[133]	[135]	[136]	[137]	[139]	[140]	[141]	[142]	[143]	[144]	[145]	[146]	[147]	[148]	[149]	[150]	[151]	[152]	[153]	[154]
Generation temperature			✓	✓	✓	✓		✓			✓	✓	✓			✓	✓	✓	✓	✓	✓	✓
Evaporation temperature			✓	✓	✓	✓		✓			✓	✓	✓			✓		✓	✓		✓	
Condensation temperature			✓		✓	✓		✓			✓	✓				✓		✓	✓		✓	
Absorption temperature			✓	✓	✓	✓		✓			✓	✓				✓		✓	✓		✓	
Number of effects										✓				✓				✓	✓			
Solution heat exchanger effectiveness				✓				✓	✓													✓
Solution circulation ratio					✓		✓	✓	✓						✓							
Cooling water temperature		✓													✓		✓					
Chilled water temperature	✓	✓		✓					✓													
Heat source temperature	✓	✓	✓	✓					✓	✓					✓							✓

B.2 Materials and methods

In this section, the specifications of the absorption system and its auxiliary systems are introduced. Then, the modeling equations for energy and exergy analyses of each component, relative irreversibility and exergetic efficiency are presented.

B.2.1 Absorption system description

Şencan et al. [127] investigated a single effect LiBr/H_2O absorption system (see

Figure B.3). According to the figure, first the solution (LiBr/H_2O) is pumped to the solution heat exchanger (Flow 2) where heat transfer occurs between solutions from the generator outlet to the absorber outlet. Thereafter, the solution enters the generator (Flow 3) where the absorbent (LiBr) is endothermically desorbed from the refrigerant (H_2O). The hot pure refrigerant flows towards the condenser (Flow 7) where it is cooled down by heat transfer to the ambient. Throttling by means of an expansion device decreases refrigerant temperature and pressure (Flow 9) and prepares it to enter the evaporator where it extracts heat from the indoor environment, which should be cooled by the system. Finally, the heated refrigerant (Flow 10) enters the absorber to be exothermically mixed with LiBr again to form the solution; thus, the cycle is completed. The HTF in the system was H_2O as well. It should be noted that in this system both the condenser and absorber were cooled by a cooling tower [127]. Therefore, they have the same cooling water inlet temperature ($T_{13} = T_{15}$). Heat source inlet and chilled water inlet are marked by flows 11 and 17, respectively.
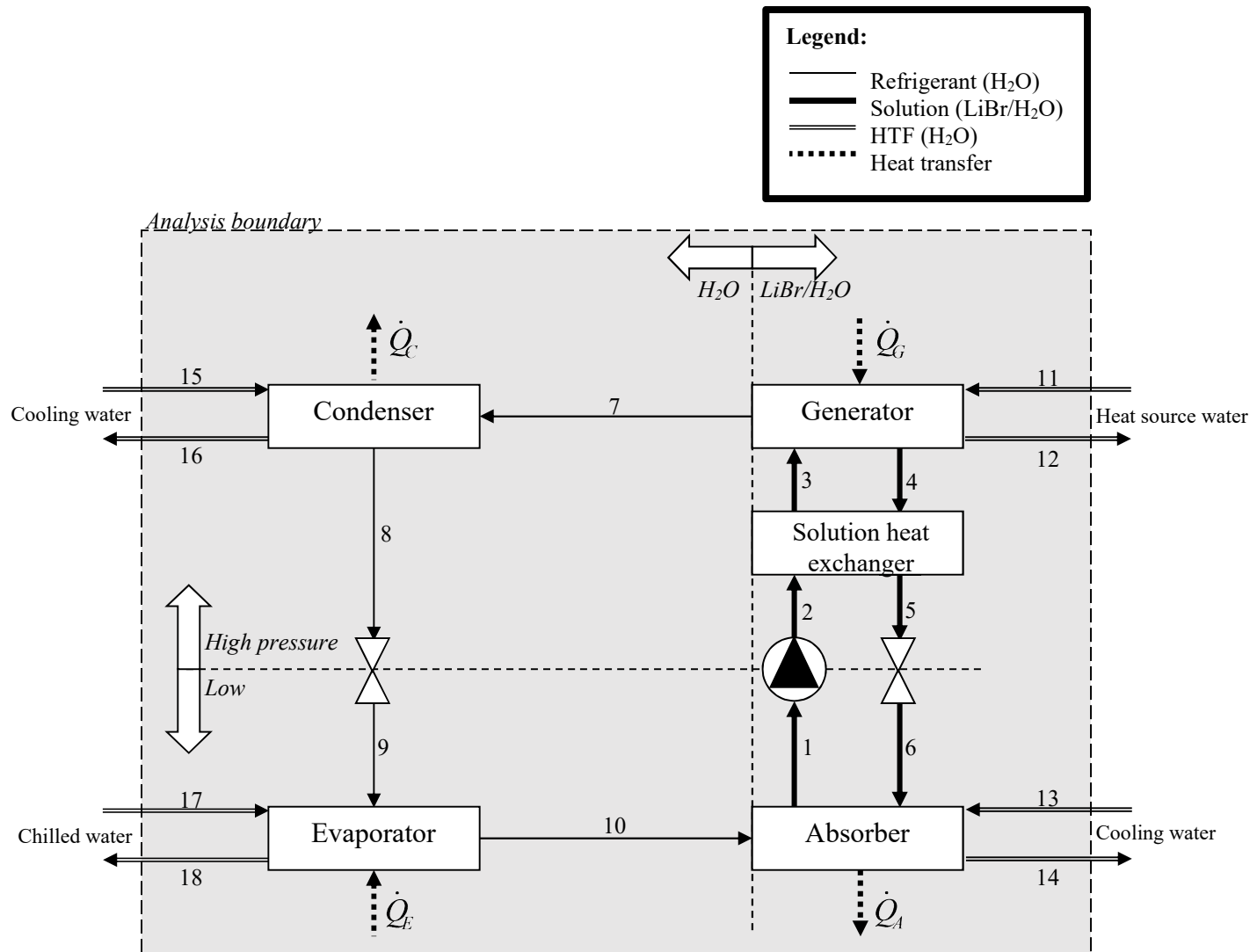
Figure B.3: Schematic representation of the case study absorption system

B.2.2 Analysis procedure

Table B.2 shows a summary of earlier studies on exergy analysis of absorption systems by investigating the effect of temperatures within the system (i.e. the generation, evaporation, condensation, and absorption temperatures), HTF temperatures supplied to the system (i.e. the heat source, chilled water, and cooling water temperatures), number of effects, effectiveness of the solution heat exchanger, etc. on their exergetic performance. However, in this study, the primary focus is on the effect of the HTF mass flow rate (Flows 11 through 18 in

Figure B.3) as well as the temperatures of the supplied heat source (Flow 11), cooling water (Flows 13 and 15), and chilled water (Flow 17) on the exergy destruction of the system components while delivering/absorbing a fixed amount of heat. In other words, in this study, unlike previous ones, the system COP is assumed to remain constant throughout the study and no change occurs inside the displayed analysis boundary in

Figure B.3 (the outermost dashed rectangle) except in Section B.3.6. To conduct the analysis, first the base case system presented in Section B.2.1 is analyzed based on energy and exergy analyses. Thereafter, the HTF mass flow rate and temperature of the supplied chilled/cooling water and heat source are altered to have the same values for the heat transfer rates at the generator ($\dot{Q}_G$), condenser ($\dot{Q}_C$), evaporator ($\dot{Q}_E$) and absorber ($\dot{Q}_A$) as the base case, ensuring constant system COP. These changes basically mean comparing different designs for the same heat load requirements. Exergy analysis is applied to investigate the effect of such external-to-system alterations on the performance of the system components. According to the abovementioned objectives, since the internal irreversibility of the absorbent/refrigerant solution is not changed, the exergy destruction is only investigated for the components with external heat transfer with HTFs: the generator, condenser, evaporator and absorber. Thereafter, in Section B.3.6, the analysis is extended to systems with slightly different heat transfer rates at the components. This step aims to generalize the analysis to systems with different heat transfer rates though with the same HTF inlet temperatures of chilled water and heat source as the base case. For instance, such cases occur in systems with the same HTF inlet temperatures yet with different generator and evaporator size (different HTF mass

flow rate). Table B.3 shows the considered range of the HTF mass flow rate, inlet temperatures, and heat transfer rates. Keep in mind that the analysis is conducted assuming that supply systems (whether economically feasible or not) are able to deliver such HTF mass flow rates for the given inlet temperatures.

Table B.3: The selected factors and the levels investigated in this study

	Condenser	Absorber	Evaporator	Generator
HTF mass flow rate (kg/s)	1.0 – 4.0	1.0 – 4.0	1.0 – 4.0	1.0 – 4.0
HTF inlet temperature (°C)	25 – 35	25 – 35	14 – 24	90 – 100
Heat transfer rate (kW)	–	–	6 – 14	21 – 29

As shown in

Figure B.3, the system can be primarily subdivided into two sections. The one on the left uses pure refrigerant (H_2O), and the one on the right uses a solution of the absorbent and refrigerant ($LiBr/H_2O$). Based on this, two different tools are applied to evaluate the enthalpy and entropy values at different points of the system. For the solution, the enthalpy and entropy values are evaluated based on the method presented in [155] and tables in [156], respectively. The pure refrigerant as well as HTF (H_2O) properties are evaluated using REFPROP software [157].

B.2.3   Energy and exergy analyses

The following assumptions are considered for the system analysis:

- Each component is treated as a control volume for energy and exergy balances,

- All processes are at the steady state conditions,

- Negligible potential, kinetic and chemical exergy changes,

- Heat transfer rates ($\dot{Q}$) are positive values,

- Negligible pump work input,

• Negligible pressure and frictional losses in the system,

• No heat transfer between the system and the surroundings other than that of the considered components (at the generator ($\dot{Q}_G$), condenser ($\dot{Q}_C$), evaporator ($\dot{Q}_E$) and absorber ($\dot{Q}_A$)),

• Condenser and evaporator outlet conditions are saturated liquid and saturated vapor, respectively, and

• The dead state is defined as water at 25°C and 1atm.

B.2.3.1 Energy analysis

According to the first law of thermodynamics and the considered assumptions, the energy balance for a component at steady state condition is expressed as:

$$\sum \dot{E}_{in} - \sum \dot{E}_{out} + \sum \dot{Q}_{in} - \sum \dot{Q}_{out} = 0$$

(B.1)

Therefore, for each component, the heat transfer rate is derived as shown in Table B.4.

Table B.4: Energy analysis of the components

Component	Heat transfer rate
Generator	$\dot{Q}_G = \dot{m}_{11}\left(h_{11} - h_{12}\right)$
Condenser	$\dot{Q}_C = \dot{m}_{15}\left(h_{16} - h_{15}\right)$
Evaporator	$\dot{Q}_E = \dot{m}_{17}\left(h_{17} - h_{18}\right)$
Absorber	$\dot{Q}_A = \dot{m}_{13}\left(h_{14} - h_{13}\right)$

The coefficient of performance for an absorption refrigeration system is calculated by dividing the heat gained by the evaporator to the heat delivered to the generator:

$$COP = \frac{\dot{Q}_E}{\dot{Q}_G}$$

(B.2)

B.2.3.2   Exergy analysis

In this study, the so-called F-P-L (fuel-product-loss) definition is adopted for exergy analysis. Based on the assumptions made earlier, exergy destruction rate of a component at a steady state process is expressed as [158]:

$$\dot{Ex}_D = \dot{Ex}_F - \dot{Ex}_P - \dot{Ex}_L$$

(B.3)

where $\dot{Ex}_D$ is the exergy destruction and $\dot{Ex}_F$, $\dot{Ex}_P$, and $\dot{Ex}_L$ are fuel, product and loss exergy rates, respectively. Basically, product exergy indicates the exergy of the desirable flow, while fuel exergy is defined as the exergy of the flow by which the product is generated. Besides, exergy loss is associated with the exergy flow to the environment without further use. Table B.5 shows the fuel, product and loss exergies for each component according to

Figure B.3.

Table B.5: Exergy analysis of the components based on the F-P-L definition

Component	Fuel	Product	Loss
Generator	$\dot{Ex}_{11} - \dot{Ex}_{12}$	$\dot{Ex}_{4} + \dot{Ex}_{7} - \dot{Ex}_{3}$	–
Condenser	$\dot{Ex}_{7} - \dot{Ex}_{8}$	–	$\dot{Ex}_{16} - \dot{Ex}_{15}$
Evaporator	$\dot{Ex}_{9} - \dot{Ex}_{10}$	$\dot{Ex}_{18} - \dot{Ex}_{17}$	–
Absorber	$\dot{Ex}_{6} + \dot{Ex}_{10} - \dot{Ex}_{1}$	–	$\dot{Ex}_{14} - \dot{Ex}_{13}$

Once the exergy destruction of each component is calculated separately, the total exergy destruction of the components is equal to the summation of all components:

$$\dot{Ex}_{D,T} = \sum_{i} \dot{Ex}_{D,i} = \dot{Ex}_{D,G} + \dot{Ex}_{D,C} + \dot{Ex}_{D,E} + \dot{Ex}_{D,A}$$

(B.4)

The relative irreversibility of a component is equal to the ratio of its exergy destruction to the total exergy destruction:

$$RI = \frac{\dot{Ex}_{D,i}}{\dot{Ex}_{D,T}}$$

(B.5)

Finally, the exergetic efficiency is defined as the ratio of the evaporator product exergy over the generator fuel exergy [159]:

$$\eta = \frac{\dot{Ex}_{18} - \dot{Ex}_{17}}{\dot{Ex}_{11} - \dot{Ex}_{12}}$$

(B.6)

B.3 Results and discussion

In this section, first, the exergy analysis of the base case system is carried out. Thereafter, the effect of HTF mass flow rate, cooling water temperature, chilled water temperature, heat source temperature, and heat transfer rate on the system exergy performance is assessed, separately.

B.3.1 Analysis of the base case system

Table B.6 shows the temperature and mass flow rate data for different points of the system. The values on the left side are adopted from Şencan et al. [127], while the values on the right are evaluated in this study based on the provided temperature data on the left. Energy analysis of the system gives the heat transfer rates at the heat exchangers (Table B.7). The amounts of the exergy destruction and relative irreversibility of each component are shown in Table B.8. Based on these results, the highest exergy destruction occurred in the absorber followed by the generator, condenser and evaporator. This shows that in order to enhance the performance of the system, the absorber should be the first option to be considered for the improvement. Moreover, Table B.9 shows the energetic and exergetic performance of the system based on the system COP and exergetic efficiency, respectively. It should be noted that since the values of heat transfer rate (Table B.7) are constant in this study (except for Section B.3.6), the system COP is also constant.

It is worth pointing out that there are some slight differences (maximum 5% error) between enthalpy and entropy values evaluated in this study and the ones reported by Şencan et al. [127] (see Table B.6). The reason is due to the application of different methodologies for the enthalpy and entropy calculations. Nevertheless, the energy analysis results are compared in Table B.7, which shows less than 1% error in the heat transfer rate calculations. This negligible error could be attributed to the numerical error due to rounding. However, it is not possible to compare the exergy analysis results of the two studies since they have different bases.

Table B.6: The available and calculated data for the absorption system

Point	T (°C)	Q (kg/kg)	X (% LiBr)	ṁ (kg/s)	h (kJ/kg)	s (kJ/kg.K)	h (kJ/kg)	s (kJ/kg.K)	Ex (kJ/kg)	h (%)	s (%)
		Adopted from Şencan et al. [127]					**This study**			**Error**	
0	25	Subcooled	0	0			104.92	0.3672	0		
1	40	–	57.59	0.5	104.34	0.31	103.85	0.2968	19.9008	-0.47	-4.26
2	40	–	57.59	0.5	104.34	0.31	103.85	0.2968	19.9008	-0.47	-4.26
3	67.6	–	57.59	0.5	159.03	0.46	158.99	0.4566	27.4326	-0.03	-0.74
4	80	–	58.15	0.495	185.53	0.52	185.71	0.5225	34.4853	0.10	0.48
5	52	–	58.15	0.495	130.31	0.36	130.19	0.3667	25.4169	-0.09	1.86
6	52	0	58.15	0.495	130.31	0.36	130.19	0.3667	25.4169	-0.09	1.86
7	80	Superheated	0	0.005	2643.68	8.53	2649.77	8.4848	124.5939	0.23	-0.53
8	40	0	0	0.005	167.57	0.57	167.53	0.5724	1.4399	-0.02	0.42
9	7	0.0556	0	0.005	167.57	0.57	167.53	0.5993	-6.5880	-0.02	5.14
10	7	1	0	0.005	2514.27	8.98	2513.70	8.9741	-156.9369	-0.02	-0.07
11	100	0	0	0.7	419.04	1.31	419.17	1.3072	34.0360	0.03	-0.21
12	91.5	Subcooled	0	0.7	383.15	1.21	383.37	1.2102	27.1517	0.06	0.02
13	27	Subcooled	0	0.75	113.24	0.40	113.28	0.3952	0.0281	0.04	-1.20
14	34.8	Subcooled	0	0.75	145.90	0.50	145.88	0.5024	0.6628	-0.01	0.48
15	27	Subcooled	0	0.75	113.24	0.40	113.28	0.3952	0.0281	0.04	-1.20
16	30.8	Subcooled	0	0.75	129.17	0.45	129.17	0.4477	0.2410	0.00	-0.51
17	16	Subcooled	0	0.45	67.19	0.24	67.27	0.2390	0.5733	0.12	-0.42
18	10	Subcooled	0	0.45	42.02	0.15	42.12	0.1511	1.6244	0.24	0.73

T: Temperature   **Q:** Refrigerant quality   **X:** LiBr mass fraction $\dot{m}$ **:** HTF mass flow rate

h: Specific enthalpy   **s:** Specific entropy   **Ex:** Specific exergy

Table B.7: Heat transfer rate at heat exchangers

Component	Symbol	Rate (kW)		Error (%)
		Şencan et al. [127]	This study	
Generator	$\dot{Q}_G$	25.12	25.05	-0.28
Condenser	$\dot{Q}_C$	11.95	11.91	-0.33
Absorber	$\dot{Q}_A$	24.50	24.45	-0.20
Evaporator	$\dot{Q}_E$	11.33	11.31	-0.18

Table B.8: Exergy destruction and relative irreversibility of components

	Absorber	Generator	Condenser	Evaporator	Total
Exergy destruction (kW)	1.3689	0.8297	0.4623	0.2787	2.9396
Relative irreversibility (%)	46.57	28.22	15.73	9.48	100.00

Table B.9: Energetic and exergetic performance of the system

COP	η
0.45	9.89

B.3.2 Effect of HTF mass flow rate

In this section, it is assumed that the heat transfer rate ($\dot{Q}$) values remain constant. In other words, for a given HTF inlet condition, mass flow rate variation requires the HTF outlet enthalpy to change, which in turn affects its outlet exergy. Thus, HTF mass flow rate variation affects exergy destruction of the corresponding component.

The HTF mass flow rate change from 1kg/s to 4kg/s affected the outlet exergy and exergy destruction rate of each component of the system as shown in Figures B.4 and B.5. Figure B.4 indicates that the effect of mass flow rate on the outlet exergy of the components was different. For the cooling water, the increase in the mass flow rate required the outlet enthalpy and entropy to decrease and become closer to the values of the dead state condition. Since whenever the enthalpy and entropy of a flow is close to the dead state, its specific exergy approaches zero, Ex_{14} and Ex_{16} had descending exergy

outlet trends. On the other hand, the increase of the chilled water mass flow rate resulted in higher enthalpy and entropy values; however, the values became closer to the dead state. Therefore, a similar trend to that of the cooling water occurred for Ex_{18}. Similar to the chilled water, the heat source outlet enthalpy and entropy increased by raising the HTF mass flow rate; nevertheless, the values shifted further away from the dead state ones and unlike other components resulted in increasing outlet exergy (Ex_{12}). Despite the complexity of Figure B.4, a very clear conclusion can be drawn if the outlet exergy rate of the flows is plotted. According to Figure B.6, the outlet exergy rate of the cooling water decreased as the HTF mass flow rate increased, while those of the chilled water and heat source increased. The reason is that the direction of heat transfer in the condenser and absorber is opposite to that of the generator and evaporator.

Figure B.5 shows that generally an increase in the HTF mass flow rate increased the rate of exergy destruction of the corresponding component. However, the magnitude of the impact was different for the different components. It is worth pointing out that each curve in the figure was generated while keeping the other parameters constant (one-at-a-time procedure).

According to Equation (6), the exergetic efficiency of a system is influenced by the generator fuel and evaporator product exergies. These parameters are changed by the variation of HTF mass flow rate of the heat source and chilled water while the COP remains constant. Figure B.7 shows that higher chilled water flow rate results in lower exergetic efficiency compared to that of the heat source. Therefore, lower heat source HTF mass flow rate is more favored.
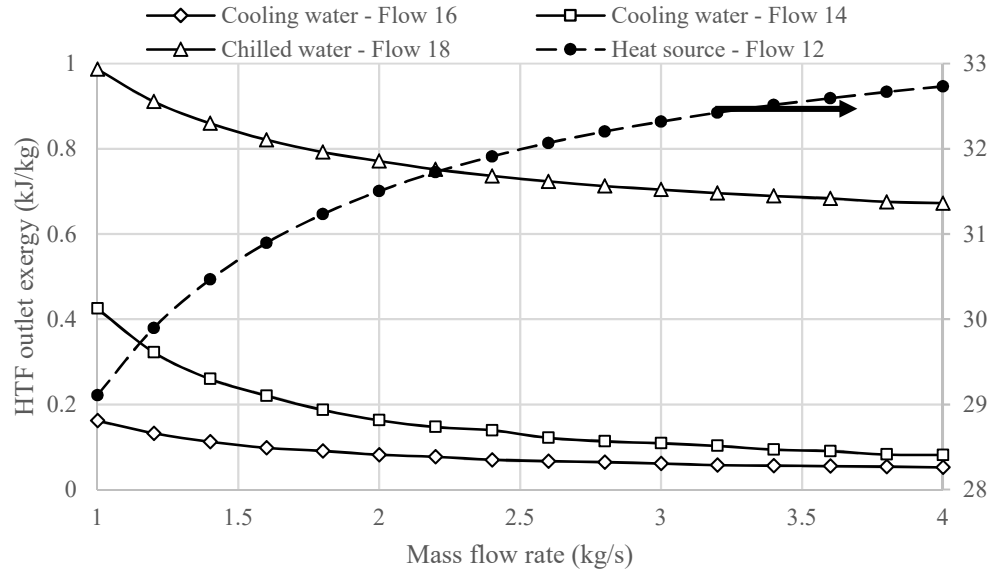
Figure B.4: HTF outlet specific exergy variation versus mass flow rate
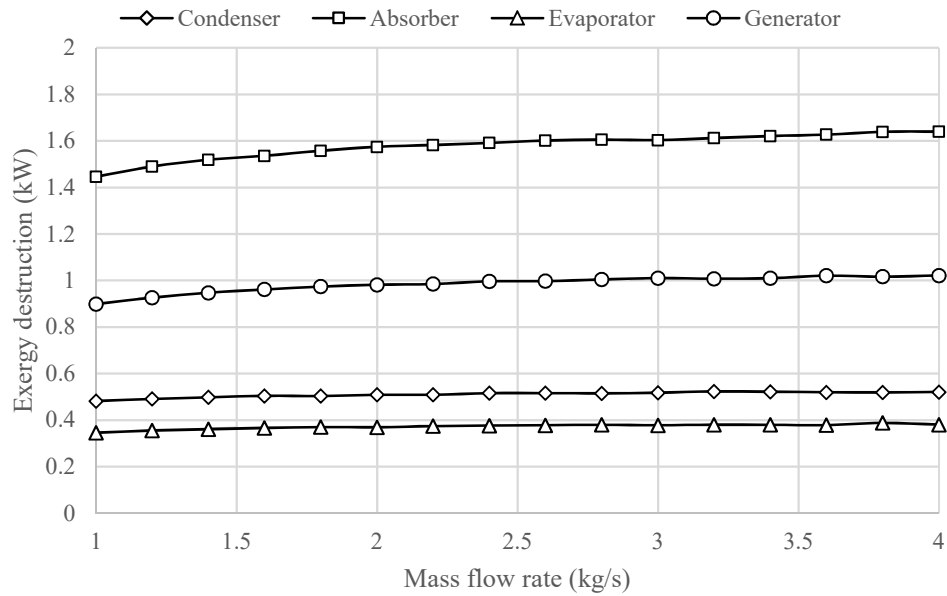
Figure B.5: Exergy destruction variation of the components versus HTF mass flow rate
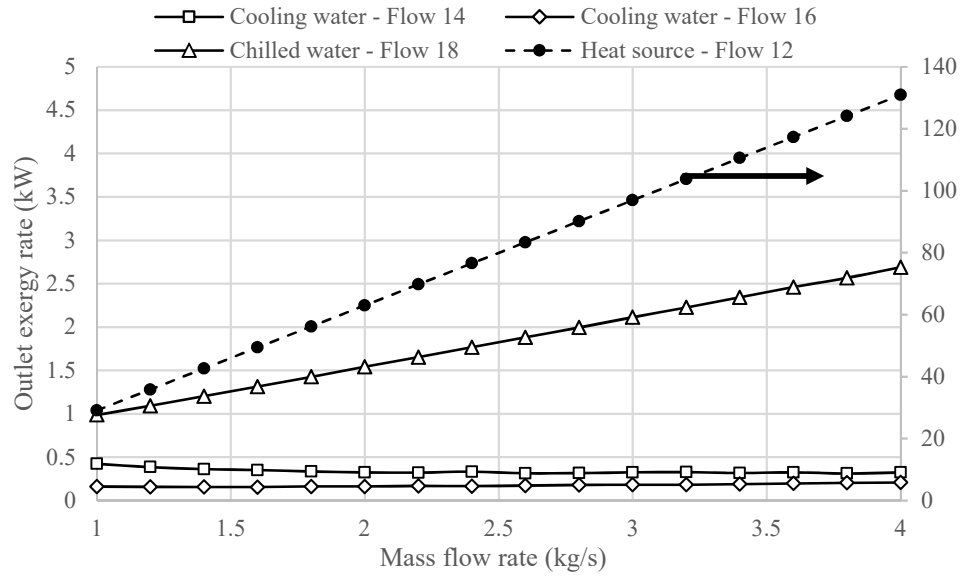
Figure B.6: HTF outlet exergy rate variation versus mass flow rate
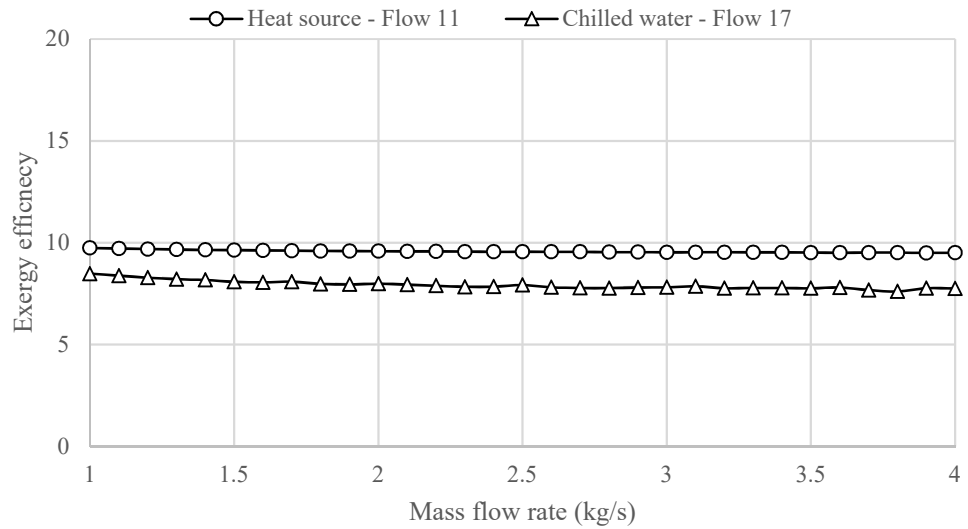
Figure B.7: Variation of exergetic efficiency (η) with the mass flow rate of heat source ($\dot{m}_{11}$) and chilled water ($\dot{m}_{17}$)

B.3.3   Effect of cooling water temperature

The absorber and condenser are the two components of a system where heat is rejected to the environment from the absorption system. The former dissipates the heat to condense the refrigerant, while the latter rejects the heat generated during an exothermic

mixing of the refrigerant with the absorbent. Since both the absorber and condenser were cooled by means of the same cooling tower, the change in the cooling water temperature and its mass flow rate affected the performance of both components, simultaneously. Figures B.8 and B.9 show the effect of these parameters. Generally, whenever the temperature of a flow is close to the dead state, its specific exergy gets close to zero. Therefore, in Figure B.8a, for the lower cooling water inlet temperatures, the HTF outlet exergy was closer to zero. This figure also shows that the higher HTF mass flow rate resulted in lower HTF specific exergy values at the absorber outlet. However, in exergy analysis, exergy destruction rate of a component is the measure, which reflects its performance, see Figure B.8b. This figure indicates that a lower HTF mass flow rate and a higher cooling water inlet temperature resulted in a lower exergy destruction. According to the results, for all HTF mass flow rates, the increase of cooling water inlet temperature reduced the absorber exergy destruction almost linearly by about 0.08kW/°C. These are due to the higher HTF outlet exergy values (as shown in Figure B.8a). Compared to the absorber, the impact of HTF mass flow rate change on the condenser HTF outlet exergy (Figure B.9a) and condenser exergy destruction (Figure B.9b) was lower (keeping the same graph scale, the figures were generated for the absorber). Nevertheless, increasing the cooling water inlet temperature, a condenser exergy destruction reduction of about 0.04kW/°C was calculated for all mass flow rates. The reason is the higher enthalpy and entropy changes due to the higher heat transfer rate of the absorber compared to the condenser (see Table B.7). However, the trends were the same for both heat exchangers.
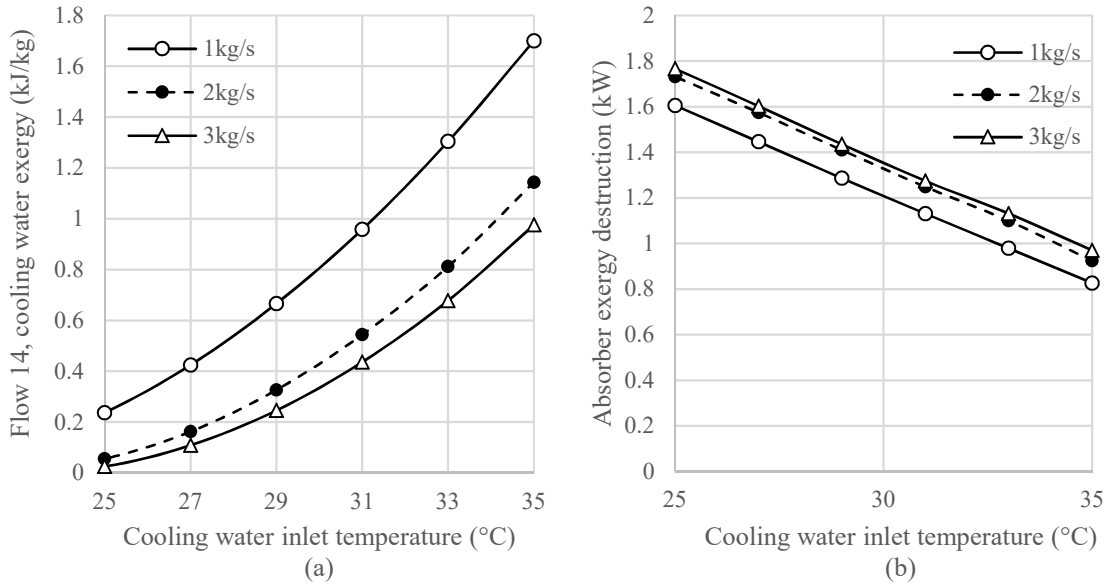
Figure B.8: Variation of (a) absorber HTF outlet exergy, Ex_{14} and (b) absorber exergy destruction versus cooling water inlet temperature (T_{13}) at different mass flow rates
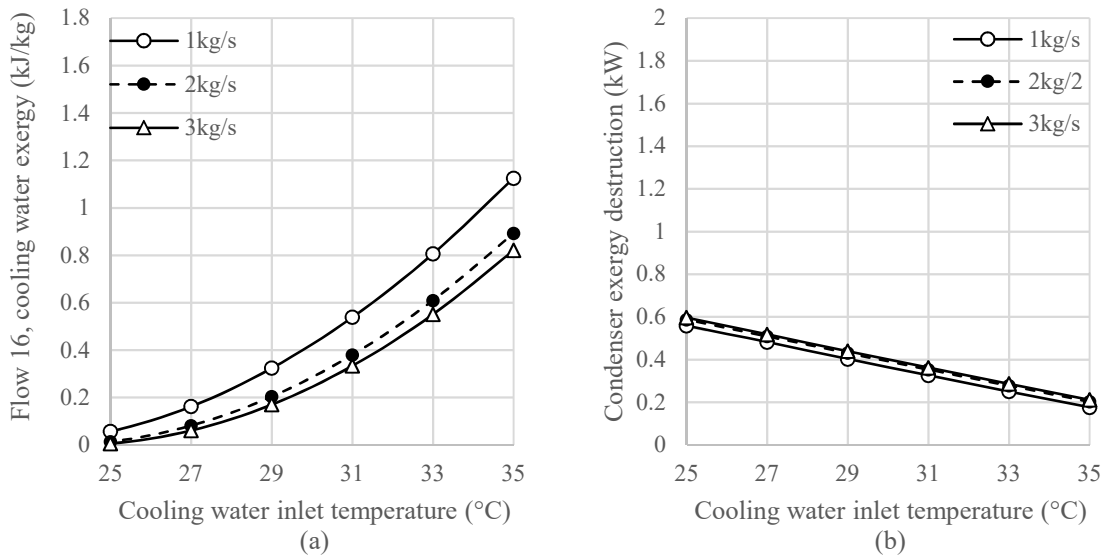
Figure B.9: Variation of (a) condenser HTF outlet exergy, Ex_{16} and (b) condenser exergy destruction versus cooling water inlet temperature (T_{15}) at different mass flow rates

As mentioned, a cooling tower rejected the heat from the absorber and condenser. Table B.8 shows that the absorber and condenser account for about 62% of the total exergy destruction of the system. This indicates that the cooling tower is among the

options responsible for more than half of the total exergy destruction. Therefore, cooling tower should be among the top priorities for system modification in order to improve its exergetic performance. Cooling water inlet temperature and its mass flow rate modification can be helpful in this regard. Figure B.10 presents their impact on the total exergy destruction of the system. According to the figure, the lower cooling water mass flow rate as well as the higher cooling water inlet temperature resulted in lower exergy destruction in the system. It should be noted that, the increase in the cooling water temperature is recommended as long as the cooling tower can meet the heat rejection requirements of the system.
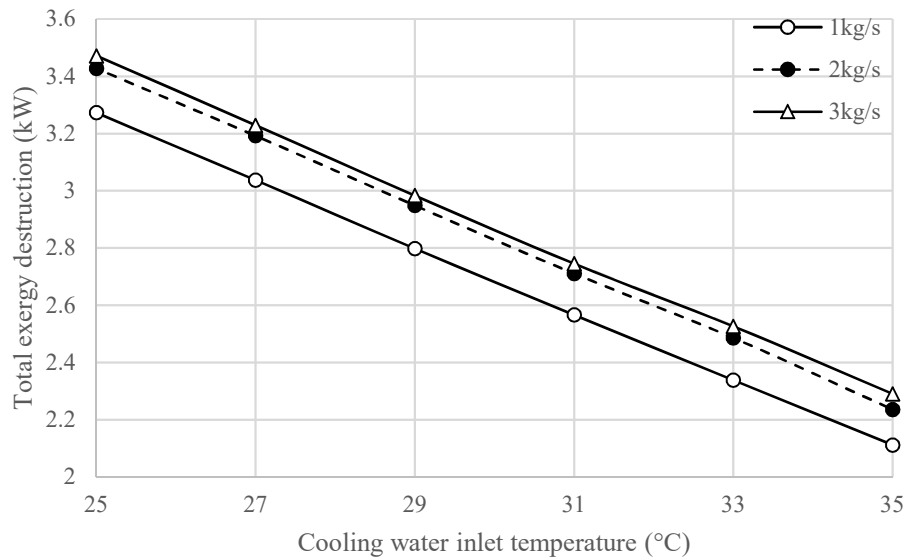
Figure B.10: Total exergy destruction variation versus cooling water inlet temperature ($T_{13} = T_{15}$) at different mass flow rates

B.3.4 Effect of chilled water temperature

Absorption cooling systems are utilized to provide chilled water for the cooling applications. The chilled water inlet temperature variation affected the evaporator HTF specific outlet exergy such that the inlet temperatures closer to the dead state resulted in lower specific exergy as shown in Figure B.11a. The effect of HTF mass flow rate was similar to those of the condenser and absorber. Besides, the lower chilled water inlet

temperature and mass flow rate resulted in lower evaporator exergy destruction rate (Figure B.11b), improving the exergetic efficiency of the system (Figure B.12). These are due to the higher evaporator outlet exergy values (see Figure B.11a). Numerically, the higher chilled water inlet temperature increased evaporator exergy destruction by about 0.04kW/°C regardless of the HTF mass flow rate value.

(a) (b)
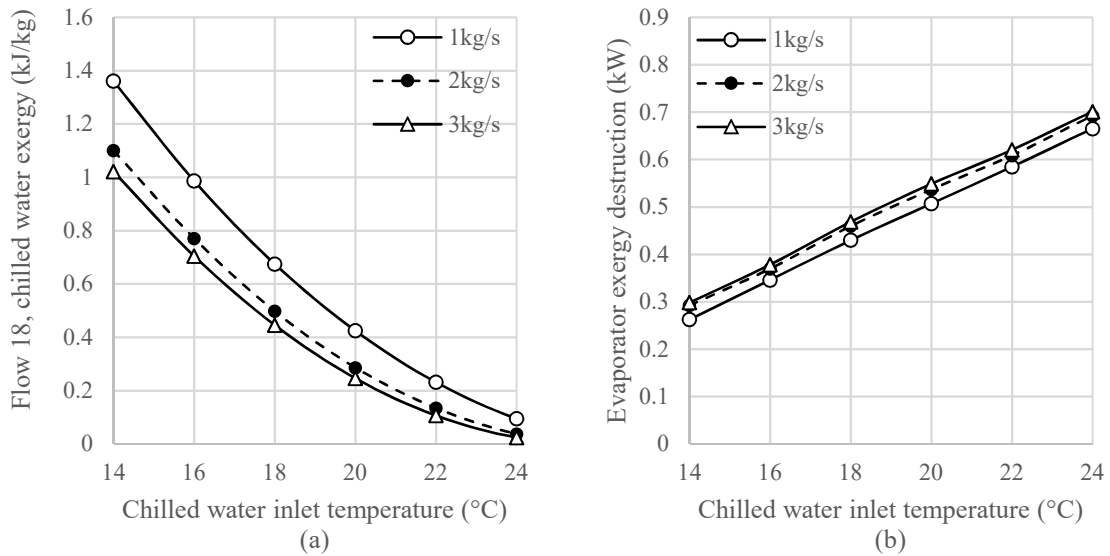
Figure B.11: Variation of (a) evaporator HTF outlet exergy, Ex_{18} and (b) evaporator exergy destruction versus chilled water inlet temperature (T_{17}) at different mass flow rates
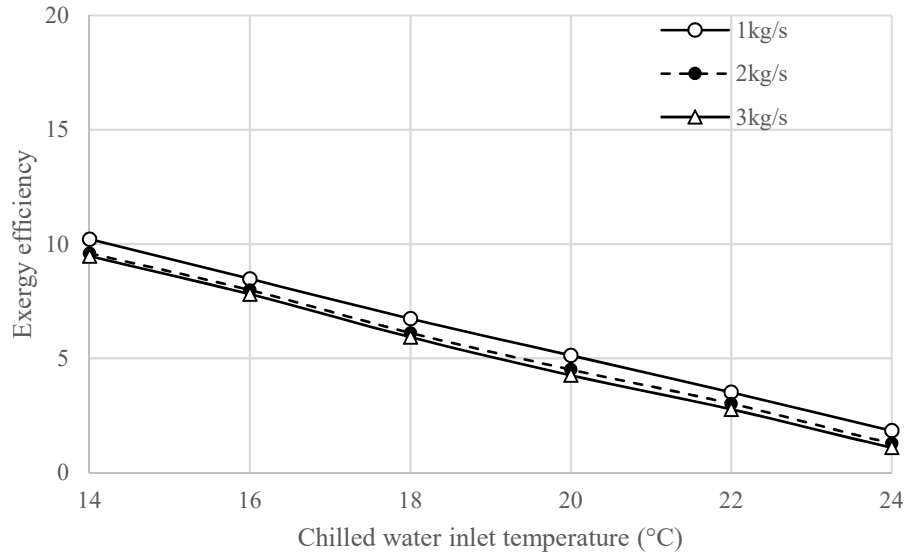
Figure B.12: Variation of exergetic efficiency (η) versus chilled water inlet temperature (T_{17}) at different mass flow rates

B.3.5   Effect of heat source temperature

Generally, different sources are available for heat of generation in the absorption cooling, e.g. fossil fuel, solar energy, and waste heat, which in turn provide different heat source temperatures. The heat source temperature variation affects its corresponding component, the generator. The specific outlet exergy of the generator is plotted in Figure B.13a. Again, closer temperatures to the dead state resulted in lower specific exergy. Therefore, the trend of the generator HTF outlet specific exergy variation was similar to that of the condenser and absorber. However, the values were much higher than other components, which is due to the high heat source temperatures. On the other hand, the effect of HTF mass flow rate was in contrast to those of other components. This is due to the fact that the lower HTF mass flow rates resulted in lower outlet enthalpy and entropy values, which in turn had lower outlet exergy values for the generator HTF. Yet, for other components the trend was the opposite. The reason is the opposite heat transfer direction in the generator and at the same time its higher temperature compared to the dead state. Nevertheless, Figure B.13b shows that heat source inlet temperature reduction resulted in about 0.06kW/°C decrease in generator exergy destruction. Besides, similar to all other components, the mass flow rate reduction of the heat source also resulted in lower exergy

190

destruction of the generator (Figure B.13b), slightly improving system exergetic efficiency (Figure B.14). Therefore, for this condition, heat source water mass flow rate change is not much recommended as long as the chilled water mass flow rate remains constant, since such an alteration does not provide significant exergetic performance enhancement.
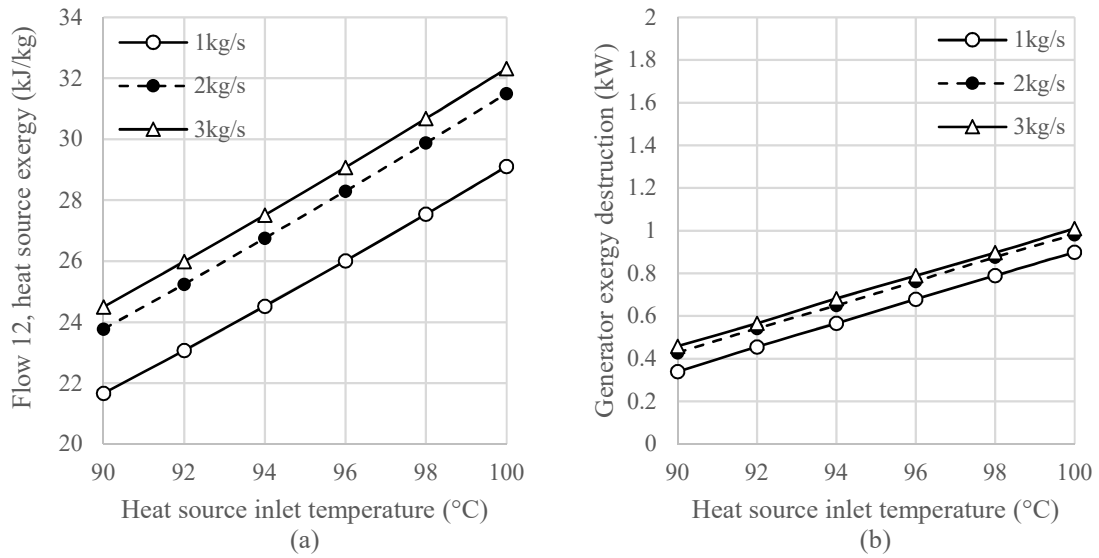

Figure B.13: Variation of (a) generator HTF outlet exergy, Ex_{12} and (b) generator exergy destruction versus heat source inlet temperature (T_{11}) at different mass flow rates
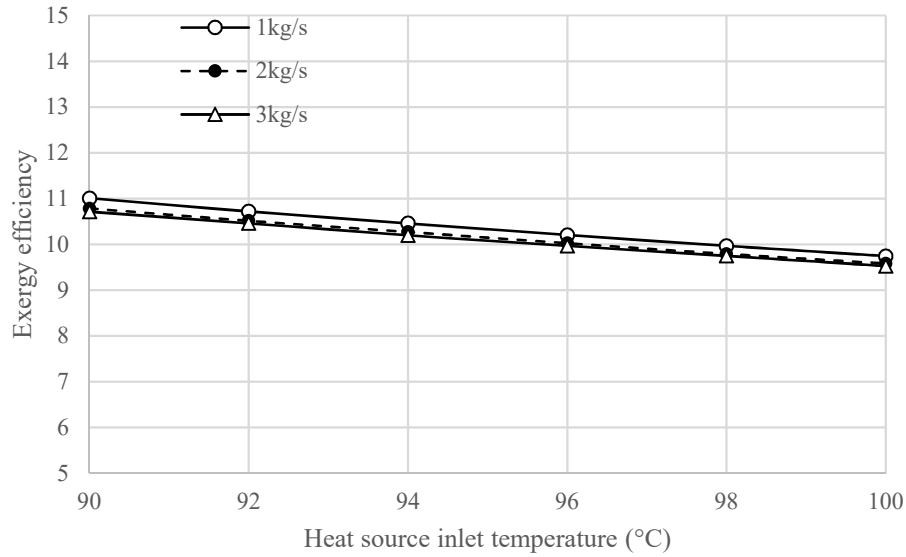
Figure B.14: Variation of exergetic efficiency (η) versus heat source water inlet temperature (T_{11}) at different mass flow rates

B.3.6 Effect of heat transfer rate

To this point, the results were limited to the base case system with given heat transfer rate values in Table B.7. In this section, the analysis is extended to systems with different heat transfer rates, which operate between the same heat source and chilled water temperatures as the base case in order to investigate the effect of HTF mass flow rate. It is important to point out that it is not possible to randomly pick heat transfer rate values in a cooling system due to the energy conservation (the first law of thermodynamics). According to the assumptions of this study, the following equation must be satisfied when selecting the heat transfer rate values [160]:

$$\dot{Q}_C + \dot{Q}_A = \dot{Q}_E + \dot{Q}_G \tag{B.7}$$

For the rest of the analysis it is assumed that the summation in Equation (B.7) is unchanged; e.g. if evaporator heat transfer rate is increased, generator heat transfer rate is decreased in a way that the total heat extracted from the system is constant. This means comparing systems with the same cooling tower load. Since in this step the analysis is generalized to systems different from the base case, instead of the exergy destruction rate,

the system exergetic efficiency, which depends on evaporator product exergy and generator fuel exergy, is presented.

It is interesting to point out an important difference between energy and exergy analyses. As Equation (B.2) shows, the first law efficiency of a system (COP) purely depends upon the heat transfer rates from the generator and evaporator. According to the values considered in this study (the last row in Table B.3), Figure B.15 shows the variation of system COP. To satisfy Equation (B.7), higher $\dot{Q}_E$ values (primary horizontal axis) are linked to lower $\dot{Q}_G$ ones (secondary horizontal axis). Obviously, higher COP is expected whenever higher amounts of heat is extracted at evaporator while providing lower amount of heat to generator side.
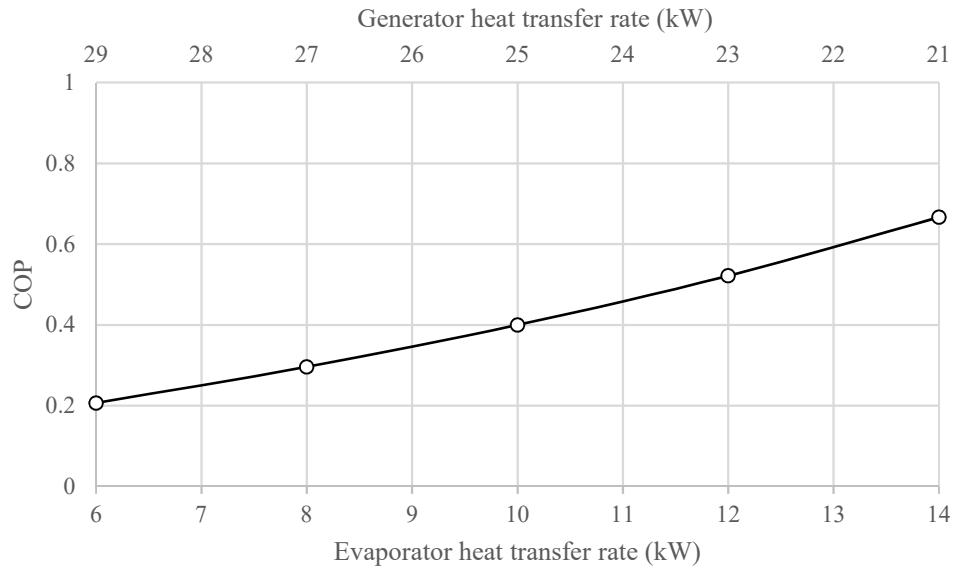
Figure B.15: COP variation versus evaporator and generator heat transfer rates ($\dot{Q}_E$ and $\dot{Q}_G$)

On the other hand, the scenario is completely different for the second law efficiency. Even for a given COP, depending upon the HTF mass flow rate and the inlet temperature for each of the chilled water and heat source streams, the system exergetic performance can vary. Therefore, to prevent complexity and to enable comparison of the

results, in this step, it is assumed that HTF mass flow rates for the chilled water and the heat source are equal ($\dot{m}_{11} = \dot{m}_{17}$). Considering the same heat source and chilled water inlet temperatures as the base case, Figure B.16 shows the variation of exergetic efficiency versus $\dot{Q}_E$ and $\dot{Q}_G$. Keep in mind that each vertically located set of data corresponds to a single COP value as shown in Figure B.15. Figure B.16 shows that for given heat source and chilled water inlet temperatures, among systems with equal COP, the system with lower HTF mass flow rate has higher exergetic efficiency. This shows how the exergy analysis can distinguish among systems, which were considered to be identical from the energy analysis point of view.
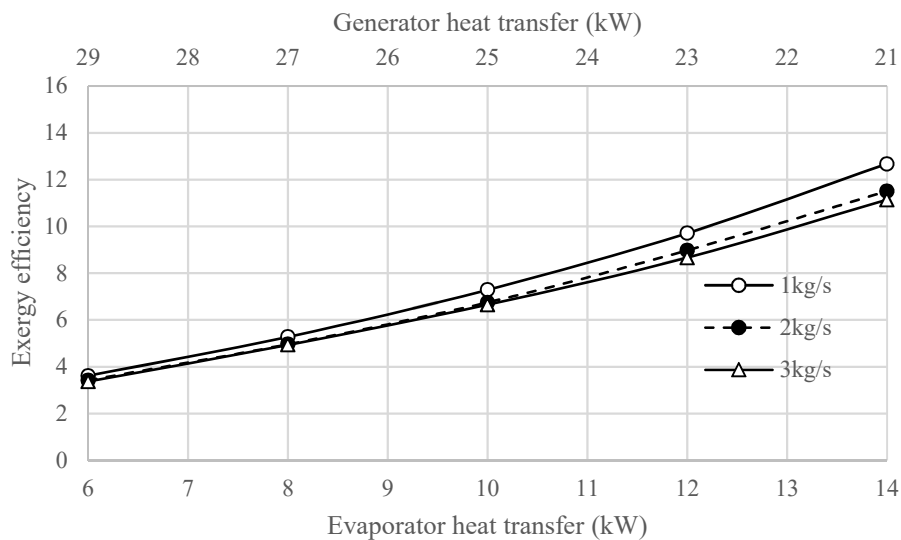
Figure B.16: Exergetic efficiency (η) variation versus evaporator and generator heat transfer rates ($\dot{Q}_E$ and $\dot{Q}_G$) at different HTF mass flow rates (assuming $\dot{m}_{11} = \dot{m}_{17}$)

So far the analysis was limited to cases with identical HTF mass flow rate at evaporator and generator ($\dot{m}_{11} = \dot{m}_{17}$). Figure B.17 extends the analysis to 1:2 and 2:1 ratios for the mass flow rates ($\dot{m}_{11}$ and $\dot{m}_{17}$). Again, each vertically located set of data corresponds to a single COP value as shown in Figure B.16. Figures B.16 and B.17

indicate that generally lower HTF mass flow rate is more desirable due to the exergetic efficiency enhancement. Nevertheless, for the same chilled water HTF mass flow rate of 1kg/s the highest exergetic efficiency was obtained for the case with heat source HTF mass flow rate of 0.5kg/s (Figure B.17b). This is due to the fact that in such a scenario the lowest exergy change occurs in the generator, while the evaporator delivers the highest exergy rate compared to the other cases. In summary, even for an identical COP value for different systems, lower HTF mass flow rates result in higher exergetic efficiency. This could be used as a guideline in early design stages i.e. for decision making about selecting heat exchanger size. For instance, among systems with similar economic conditions, the one with lower HTF mass flow rate, especially lower heat source HTF mass flow rate compared to the chilled water one, is more favored.
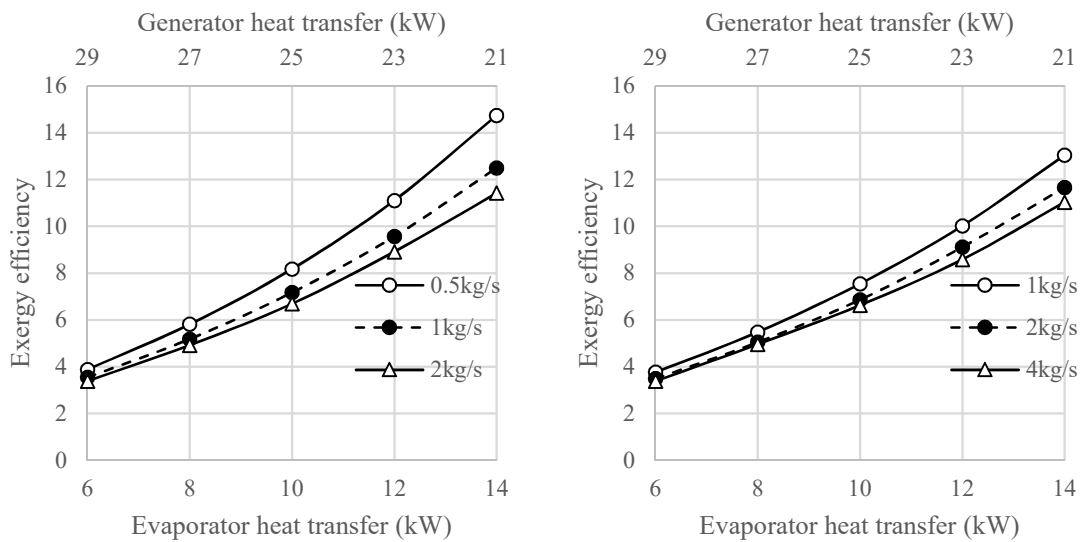
Figure B.17: Exergetic efficiency (η) variation versus evaporator and generator heat transfer rates ($\dot{Q}_E$ and $\dot{Q}_G$) at different HTF mass flow rates (a) assuming $\dot{m}_{11}=2\dot{m}_{17}$ and (b) assuming $\dot{m}_{17}=2\dot{m}_{11}$ (The values on the figure legends are chilled water mass flow rate, $\dot{m}_{17}$)

B.4　Conclusion

The results of this study revealed how HTF mass flow rate and temperature variation affected the performance of the four major components of an absorption system based on exergy analysis. HTF mass flow rate reduction reduced the exergy destruction of the components of the system while considering the same amount of heat transfer from/to the components. In other words, the changes did not affect the system COP. In summary, if the HTF mass flow rate is reduced (or even eliminated e.g. by application of phase change materials, which requires further analysis) the exergetic performance of the cycle is improved. More specifically, since the absorber and condenser accounted for about 62% of the total exergy destruction in the system, cooling water mass flow rate reduction in the cooling tower greatly improves the exergetic performance of the system. The major findings of this study include:

• Higher HTF mass flow rate resulted in higher exergy destruction of each component. However, for higher mass flow rates the influence was lower.

• Lower heat source and chilled water temperatures reduced the exergy destruction of the system, while the cooling water temperature needed to be increased to have the same outcome. This is due to the opposite heat transfer direction in these components.

• The influence of HTF mass flow rate change was the highest for the absorber, and

• For given heat source and chilled water inlet temperatures, among systems with identical COP, a system with lower HTF mass flow rate had higher exergetic efficiency.

Appendix C: Investigation of geometric and operating parameters on thermal behavior of vertical shell-and-tube latent systems

C.1   Introduction

Latent heat thermal energy storage (LHTES) technology has gained extensive attention in many solar energy applications by providing a reservoir of energy to solve the temporal mismatch between solar energy supply and demand [7, 10, 161-165]. Among all different types of LHTES units, the shell-and-tube system is the most intensely researched accounting for more than 70% of the systems studied due to its design simplicity and minimal heat loss from the system [166]. Much research has focused on investigating the effect of geometric and operating parameters on the storage system performance. Cao and Faghri [167] conducted a pioneering numerical investigation on the effect of geometric parameters such as shell radius and tube length. It was found that larger shell radius and longer tube length resulted in higher energy storage; however, this dropped the energy storage density. Lacroix [168] performed a numerical study on a shell-and-tube LHTES system using n-octadecane (melting temperature of 26 °C) at the shell side as the PCM and water as the HTF flowing inside the tubes. The results showed that the whole PCM melting time depended not only upon thermal and geometric parameters, but also on the PCM thermophysical properties. The same author evaluated the effect of shell radius, HTF mass flow rate and temperature for tubes with/without fins [169]. Three different shell radii were investigated while the inner tube radius was kept constant. It was observed that for higher shell radii, the PCM was either partially melted or undesirably stored sensible heat only. Bellecci and Conti [170, 171] conducted numerical studies for size optimization of a horizontal solar receiver unit considering different shell radii. It was reported that outer radius (R_o) played a crucial role in efficient performance of the thermal storage system. There was a certain R_o below which the PCM underwent sensible heat transfer (superheating or sub-cooling) and beyond that part of the PCM did not participate in the phase change process [171]. Furthermore, under the investigated conditions, it was found that a large portion of the PCM could not undergo phase change at all when the outer to inner tube radius ratio

(R_o/R_i) was larger than 4 [170]. Similar results were observed when a eutectic mixture (LiF-MgF$_2$) was used as the PCM [172]. Esen et al. [173] conducted a series of numerical simulations to investigate the effects of various PCMs, shell and tube radii, PCM volume, HTF mass flow rate and temperature on the charging time. The results indicated that the stored energy raised as the HTF inlet temperature increased. Further, Ismail and his collaborators [174, 175] developed a two-dimensional model to study the effect of the outer shell to inner tube radius ratio (R_o/R_i) on the thermal performance of a PCM in a vertical cylinder. The results indicated that the solidification mass fraction decreased and the time necessary for the complete fusion increased by increasing R_o/R_i. Trp et al. [176, 177] performed a numerical study to evaluate the influence of tube length, shell radius, as well as HTF inlet velocity and temperature on the amount of the stored and recovered energy during the charging and discharging processes. It was concluded that the selection of operating conditions and geometrical parameters depended on the required heat transfer rate and the time by which the energy was to be stored or delivered. Rathod and Banerjee [178, 179] experimentally investigated the effect of HTF mass flow rate and temperature on the thermal performance of a shell-and-tube heat exchanger with PCM at its shell side. The results showed that increasing the HTF mass flow rate and temperature decreased the melting time. Similar results were reported by Gong and Mujumdar [180], and Tao and He [181]. Moreover, considering constant cross sectional area ($R_o^2 - R_i^2 =$ constant), Tao et al. [182, 183] investigated the effect of shell radius variation on melting time. It was found that increasing the shell radius resulted in longer phase change process, which was attributed to the HTF velocity drop and its consequent heat transfer reduction.

Avci and Yazici [184] experimentally recorded the time histories of a paraffin (P56-58) PCM in a horizontal shell-and-tube heat exchanger LHTES. It was reported that increasing (for the charging process) and decreasing (for the discharging process) the HTF inlet temperature enhanced PCM melting and solidification, respectively. Hosseini et al. [185] experimentally and computationally investigated the heat transfer characteristics of a horizontal shell-and-tube heat exchanger LHTES system using RT50 as the PCM. It was revealed that as the inlet HTF temperature increased from 70 to 80 °C, the total melting time decreased by 37%, and the theoretical efficiency in charging

and discharging processes raised from 81.1% to 88.4% and from 79.7% to 81.4%, respectively. Seddegh et al. [3] compared heat transfer in horizontal and vertical shell-and-tube LHTES systems, and reported that the hot HTF inlet temperature had a great impact on the heat transfer in both horizontal and vertical systems. However, the HTF flow rate had negligible effect on charging and discharging processes in the LHTES units.

El-Sawi et al. [6] investigated the effect of HTF temperature, HTF flow rate and storage length on the thermal performance of a centralized LHTES using RT20 as the PCM. It was reported that longer storages could store higher amounts of energy; however, the effect of HTF flow rate was negligible. Furthermore, the highest energy recovery was found to be for cases having an HTF inlet temperature which was 10 °C above the mean PCM phase change temperature [186]. Wang et al. [187] numerically investigated the effects of HTF inlet temperature and mass flow rate on a horizontal shell-and-tube heat exchanger LHTES. The results showed that the HTF inlet temperature greatly affected the time required to complete the charging or discharging process. However, the HTF mass flow rate had little influence on the amount of stored energy, whereas the time needed to complete the charging or discharging process decreased nonlinearly as the HTF mass flow rate increased. They also found that a longer storage had lower energy efficiency ratio, but higher heat storage rate [188]. However, increasing the shell radius decreased both the energy efficiency ratio and the heat storage rate. Thus, further research is needed to investigate the impact of the shell radius on the system performance.

More recently, Tehrani et al. [189] reviewed low to medium temperature shell-and-tube LHTES systems and reported that the majority of the studies were numerical. Table C.1 detailed the current research on the shell-and-tube LHTES systems. The only experimental study (highlighted in the table) investigating the geometrical parameters in a vertical cylindrical shell-and-tube storage considered constant tube radius and variable shell radius [176]. In this study, the effect of geometric and operating parameters on a vertical shell-and-tube LHTES system is investigated. An experimental setup is developed for this purpose. Four LHTES units with the same shell radius but

variable HTF tube radius are investigated under different HTF temperature and flow rates. Maintaining the shell radius minimizes the effect of the PCM mass change on the storage performance. This has not been investigated in any literature. The temporal variations of experimental temperature in four LHTES units are measured. A new weighting mathematical method is developed to calculate the PCM average temperature, liquid fraction and stored/released energy fraction using the experimental PCM temperatures. These parameters are then used to determine the effect of geometric and operating parameters on the storage performance of the studied LHTES units. The optimal shell to tube radius ratio is investigated. Both the research method and finding have not been reported in other literature. The research provides useful information and guidance to researchers and engineers for design and optimization of vertical shell-and-tube LHTES systems.

Table C.1: Summary of the presented studies investigating shell-and-tube latent heat thermal energy storage systems

Ref.	Study type			Process		PCM	Phase change temperature	Orientation	Geometric parameters				
	Numerical	Experimental	Geometric analysis	Charging	Discharging				R_i	R_o	R_o/R_i	L	L/R_i
[167]	✓		✓	✓		-	-	Horizontal	-	-	2 ~ 4.2	0.1	20 ~ 48
[168]	✓	✓	✓	✓		n-octadecane	27.55	Horizontal	0.00635	0.011 ~ 0.0183	-	1	-
[169]	✓	✓	✓	✓		n-octadecane	27.55	Horizontal	0.00635	0.011 ~ 0.0183	-	1	-
[171]	✓		✓	✓	✓	Lithium fluoride	849	Horizontal	0.01	0.024 ~ 0.052	-	2.4	-
[170]	✓		✓	✓	✓	Lithium fluoride	849	Horizontal	-	-	3 ~ 5	-	110 ~ 350
[172]	✓		✓	✓	✓	LiF-MgF$_2$	735	Horizontal	-	-	2.4 ~ 4.6	-	50 ~ 120
[173]	✓		✓	✓		CaCl$_2$.6H$_2$O	29.7 ~ 29.85	Vertical	0.016 ~ 0.04	0.033 ~ 0.082	-	3.2	-
						Paraffin	32 ~ 32.1						
						Na$_2$SO$_4$.10H$_2$O	39 ~ 39.15						
						Paraffin was	46.7 ~ 46.85						
[175]	✓		✓	✓		n-eicosan	36.4	Vertical	Constant	-	2 ~ 4.4	-	4 ~ 7
[174]	✓		✓	✓		n-eicosan	36.4	Vertical	-	-	1 ~ 6	-	-
[176]	✓	✓	✓	✓	✓	RT30	27.55	Vertical	0.0165 (constant)	0.064	2.4 ~ 3.6	1	40 ~ 200
[177]	✓	✓		✓	✓	Technical grade paraffin	27.55	Vertical	0.0165	0.064	-	1	-
[178]		✓		✓		Paraffin wax	58 ~ 60	Vertical	0.0165	0.064	-	1	-
[179]		✓		✓	✓	Stearic acid	55.7 ~ 64.1	Vertical	0.0165	0.064	-	1	-
[180]	✓			✓	✓	LiF-CaF$_2$	767	Horizontal	0.0125	0.025	-	1.5	-
[181]	✓			✓	✓	n-octadecane	27.55	Horizontal	0.00635	0.01135	-	1	-
[182]	✓		✓	✓		LiF-CaF$_2$	767	Horizontal	0.0104 ~ 0.0178	0.024 ~ 0.028	-	1.5	-

[Ref]						Material	Temp	Orientation					
[183]	✓			✓		LiF-CaF$_2$	767	Horizontal	0.0125	0.025	-	1.5	-
[184]		✓		✓	✓	Paraffin (P56-P58)	56 ~ 58	Horizontal	0.028	0.103	-	0.5	-
[185]	✓	✓		✓	✓	RT50	44.05 ~ 54.15	Horizontal	0.022	0.085	-	1	-
[187]	✓			✓	✓	n-octadecane	27.55	Horizontal	0.00635	0.0079	-	1	-
[188]	✓		✓	✓	✓	n-octadecane	27.55	Horizontal	0.00635	-	1.3 ~ 5	-	50 ~ 300
						Paraffin C$_{18}$	25						
						Polyglycol E600	22						
						CaCl$_2$.6H$_2$O	29.9						
						Gallium	29.76						
						Methyl palmitate	29						
[189]	✓		✓	✓	✓	Lead	54	Vertical	-	-	1.3 ~ 3	1 ~ 5	20 ~ 200
						H425	152						
						Li$_2$CO$_3$-K$_2$CO$_3$	232						

C.2 Experimental setup

Figure C.1 shows the experimental setup which was used in this study. It consisted of a hot water tank, a cold water tank, PCM storage unit, hot and cold water pumps, a flow meter, a data acquisition module, thermocouples, valves and extensive piping systems. Water was used as both the hot and cold HTFs.

The PCM storage unit was made of a single pass shell-and-tube heat exchanger. Four cylinders of 0.5 m height and 0.05 m shell radius (R_o) with different HTF tube radii (R_i) of 0.00635 m, 0.00953 m, 0.01252 m, and 0.01905 m were constructed. The PCM was stored in the annulus, while the HTF passed through the inner tube (see Figure C.1). All cylinders were made of transparent polypropylene (with thermal conductivity k of 0.1 W/m·K) with a thickness of 0.006 m to allow observation of the melting process. The cylinders were insulated with Armaflex sheets with a thermal conductivity of 0.036 W/m·K. Table C.2 shows the specifications of each shell-and-tube unit.
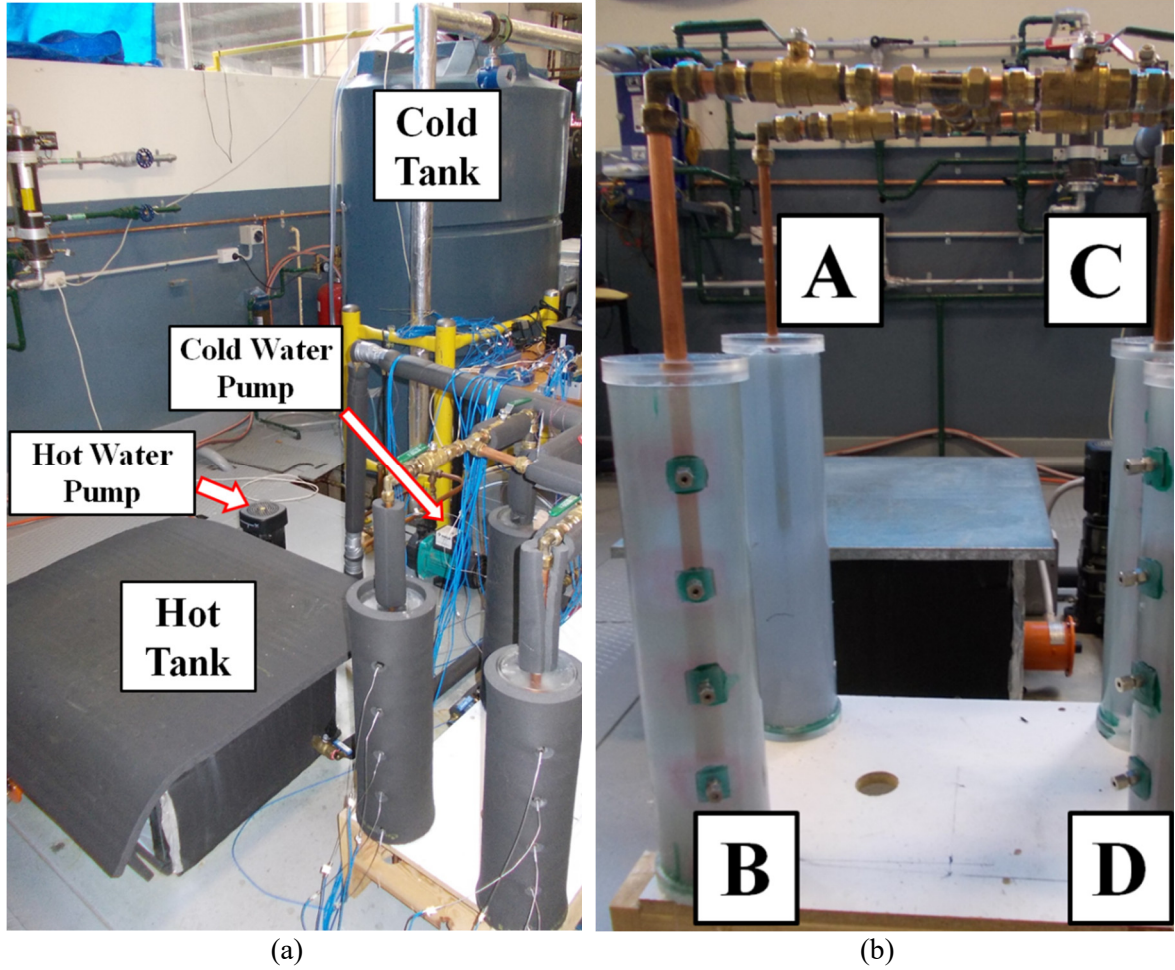
Figure C.1: Pictorial views of (a) the whole experimental rig (b) the four PCM storage cylinders

Table C.2: Specifications of the investigated shell and tube systems

LHTES unit	Length	Shell radius	Tube radius	Radius ratio	Mass
	L (m)	R_o (m)	R_i (m)	R_o/R_i	m (kg)
Cylinder A	0.5	0.0512	0.00635	8.1	2.98
Cylinder B	0.5	0.0512	0.00953	5.4	2.91
Cylinder C	0.5	0.0512	0.01270	4.0	2.83
Cylinder D	0.5	0.0512	0.01905	2.7	2.58

The PCM temperatures inside the four cylinders were measured by Type-T thermocouples with an accuracy of ±0.2 °C. Eight thermocouples were mounted inside each PCM cylinder as shown in Figure C.2 to monitor the temperature during the phase change process. In order to compare the PCM thermal behavior between these vertical

cylindrical containers, four thermocouples were located at four levels with the same radial position being 20 mm away from the outer surface of the HTF tube. Another four thermocouples were located at the same four levels in the same radial position but being 5 mm away from the inner surface of cylinder to study the PCM status.
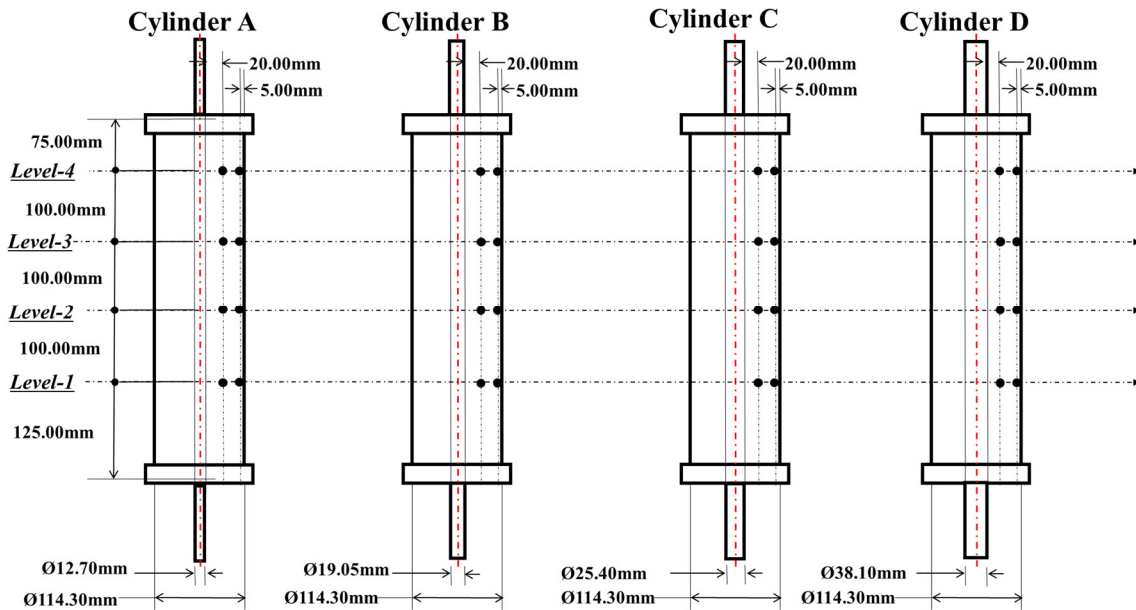

Figure C.2: Locations of thermocouples (bold points)

During the charging process, the hot HTF was heated up to a pre-set temperature in a hot water tank with a capacity of 108 L using two 2.4 kW thermal electric immersion heaters (model number: TWI50240) with externally adjustable thermostats. The hot water was circulated by a Grundfos vertical, multistage centrifugal pump (model number: CR 1-4 A-A-A-E-HQQE) through the tube in the PCM cylinder where PCM was packed between the tube and cylindrical shell. The hot water was then channeled back to the hot water tank from the storage outlet. During the discharging process, the cold water was maintained at the required temperature by a 20 kW chiller (model number: HWP020-3BB) in a 1,575 L capacity cold tank. The cold water was circulated by an Onga horizontal, centrifugal pump (model number: 413) through the tube in the PCM cylinder to cool the PCM. A Flomec oval gear positive-displacement flow meter with pulse output was placed in position between the cylinder outlets and hot/cold water tanks to monitor

the hot and cold water flow rates. Moreover, temperatures and water flow rates were recorded by a data acquisition system at 2.5 second time intervals (National Instruments NI9411). The PCM used in the study was RT60 paraffin wax from Rubitherm GmbH. The PCM thermophysical properties and testing conditions are listed in Table C.3.

Table C.3: Thermophysical properties and test conditions

PCM		HTF		Dimension
Liquidus temperature	61	Charging temperature	70 and 80	°C
Solidus temperature	55	Discharging temperature	10	°C
Specific heat	2	Specific heat	4.18	kJ/kg.K
Thermal conductivity	0.2	Thermal conductivity	0.58	W/m.K
Solid density	880 (at 15 °C)	Density	998	kg/m^3
Liquid density	770 (at 80 °C)			kg/m^3
Latent heat of fusion	123.5			kJ/kg
Volume expansion	12.5			%
Dynamic viscosity	3.705×10^{-5}			kg/m.s

C.3   Experimental data reduction

In order to compare the performance of the different storage units, three parameters (i.e. average PCM temperature, liquid fraction, and stored energy fraction) were introduced and utilized in the study. These three parameters were calculated using a newly developed weighting method as detailed below.
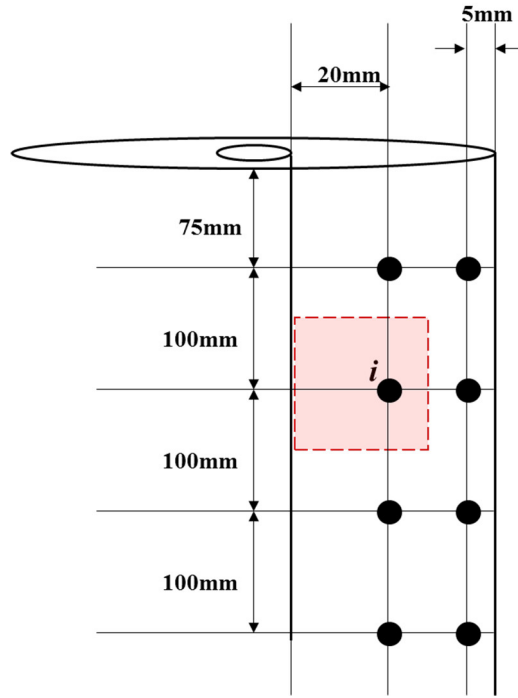
Figure C.3: Schematic representation of the experimental setup showing the location of thermocouples and the considered control volume

As presented earlier, the positions of the thermocouples were distributed at different locations which were altered based on the tube radius in each experimental setup. Therefore, the control volume around each node (see Figure C.3) had a different area (volume) due to the thermocouple location in each test. A weight factor (ω) is then defined to take into account the volume of the PCM, which is approximated by the corresponding node (thermocouple). Thus, for node i:

$$\omega_i = \frac{V_i}{V_t} \tag{C.1}$$

where V_i is the volume of the control volume surrounding node i as depicted in Figure C.3 and V_t is the total PCM storage volume. Thus, having the local measured temperature values (T_i), the average temperature of the storage is calculated by:

$$T = \sum_i \omega_i T_i \tag{C.2}$$

The liquid fraction at each thermocouple location is calculated where each location is accounted as a separate node with its actual available temperature value. Therefore, according to the measured temperature (T_i) at each node, three different options are possible based on which the liquid fraction at each node is calculated:

$$\gamma_i = \begin{cases} 0 & T_i < T_s \\ \dfrac{T_i - T_s}{T_l - T_s} & T_s < T_i < T_l \\ 1 & T_i > T_l \end{cases} \tag{C.3}$$

where T_s and T_l are the solidus and liquidus temperatures, respectively. Once the nodal liquid fraction values are calculated, the average liquid fraction would be:

$$\gamma = \sum_i \omega_i \gamma_i \tag{C.4}$$

To calculate the stored energy of the PCM, the same weighting approach was applied to the nodal temperatures. The stored energy by each node was calculated by:

$$Q_i = \begin{cases} mC_{p,s}\left(T_i - T_0\right) & T_i < T_s \\ mC_{p,s}\left(T_s - T_0\right) + m\gamma_i\lambda & T_s < T_i < T_l \\ mC_{p,s}\left(T_s - T_0\right) + m\lambda + mC_{p,l}\left(T_i - T_l\right) & T_i > T_l \end{cases} \tag{C.5}$$

where T_0 is the initial temperature of the PCM storage (15 °C), which is used for both charging and discharging processes. According to Table C.3, two different HTF temperatures of 70 and 80 °C are used in this study. Consequently, the final PCM temperature after the charging process would be different not only among the cylinders, but also according to the corresponding HTF temperature. In order to prevent ambiguity and enable solid comparison of the results, the initial PCM temperature (15 °C) is considered constant in Equation (5). In this way, under charging condition, the stored energy of the cylinders initiates from zero and reaches a maximum value (Q_{max}), while under discharging process, the stored energy declines from the maximum value back to zero. Then, the total stored energy of the PCM is calculated using the weight factor:

$$Q = \sum_i \omega_i Q_i \qquad (C.6)$$

Finally, the stored energy fraction would be:

$$Q_f = \frac{Q}{Q_{max}} \qquad (C.7)$$

In order to have smooth transition of the average temperature, liquid fraction and stored energy fraction values, curve fitting has been applied on the experimental data. As an example, Figure C.4 shows the fitted curve along with the experimental data for the liquid fraction values of Cylinder D.
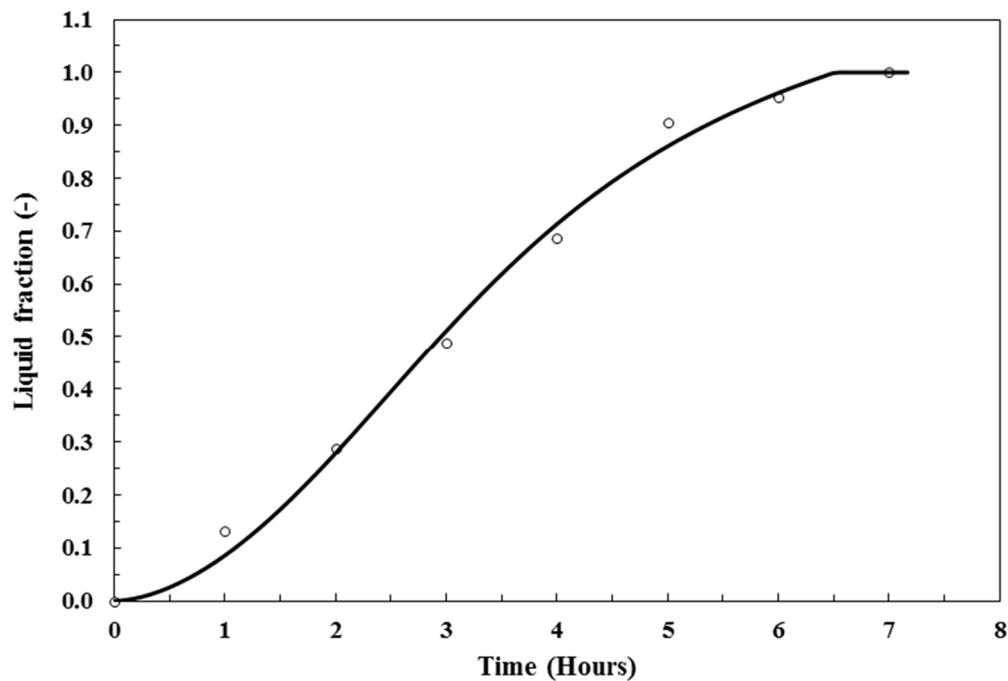

Figure C.4: Variation of liquid fraction for Cylinder D under charging showing the fitted curve against the experimental data

C.4   Results and discussion

The thermal behavior of the four different LHTES systems are investigated and compared under different operating conditions in the following sections.

C.4.1   Charging process

C.4.1.1   Charging process – 5 mm thermocouples

Figure C.5 (a-d) shows temperature variations in thermocouple probes located 5 mm away from the inner surface of the acrylic cylinder within each container under the charging HTF temperature of 80 °C and the flow rate of 10 L/min. It is seen that PCM temperatures at different levels reach the melting temperature at different times. The time needed for the PCM to melt for higher levels is shorter than that of the lower ones. This is due to the natural convection as reported in the literature [3]. It should be noted that the entire mass of PCM in each cylinder was completely melted once the thermocouple located 5 mm away from the inner surface of the acrylic cylinder at level 1 reached a stable temperature above the PCM melting temperature. Comparing the total melting time for different cylinders shows that increasing the HTF tube radius reduces the required charging time. This is due to the fact that the larger HTF tube radius provides larger heat transfer surface area; hence, larger heat transfer rate. Therefore, the charging time reduced by up to 38% as the shell to tube radius ratio decreased from 8.1 to 2.7 in Cylinders A to D.
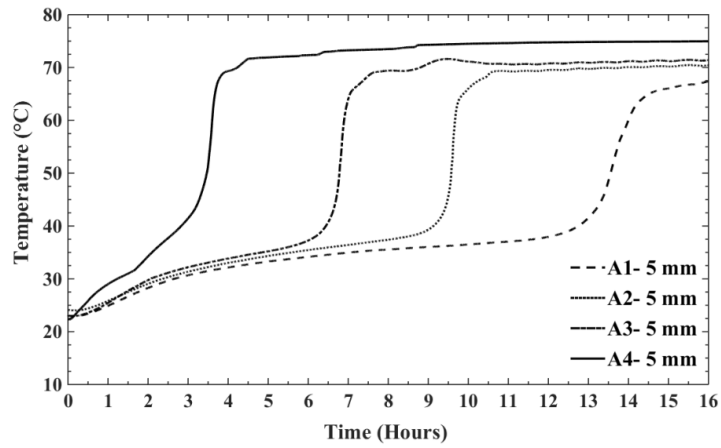
(a) Cylinder A   (b) Cylinder B
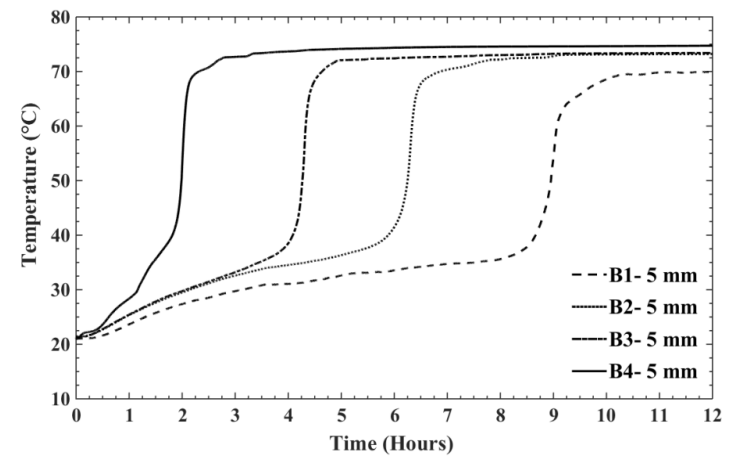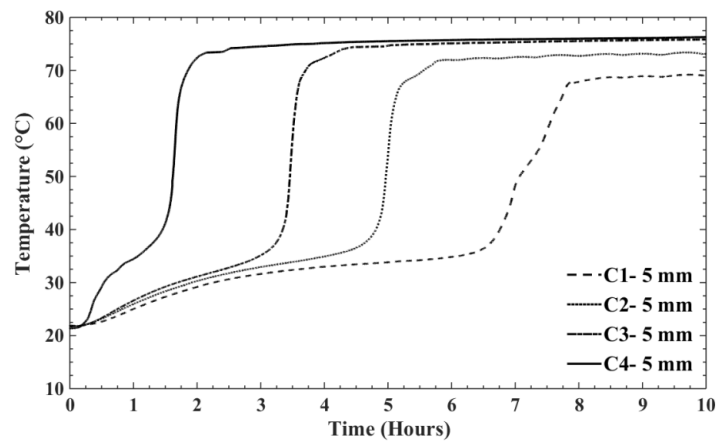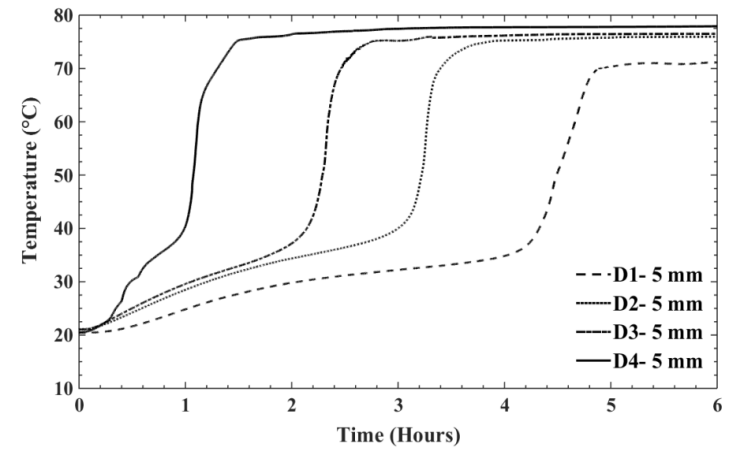
(c) Cylinder C   (d) Cylinder D

Figure C.5: Comparison of temperatures recorded by thermocouple probes located 5 mm away from the shells during the charging process

C.4.1.2 Charging process – 20 mm thermocouples

Figure C.6 (a-d) compares temperature variations of thermocouple probes located 20 mm away from the HTF tube at each level for the HTF charging temperature of 80 °C and flow rate of 10 L/min. As the tube radius increases from Cylinder A to D, the melting time decreases. This again demonstrates the significant effect of the HTF tube surface area on the heat transfer in the PCM. It also shows that the time difference to reach the melting point decreased from 7 hours at level 1 to 2.5 hours at level 4 as the radius increases from Cylinder A to D. This reveals that at higher levels, the influence of the radius ratio decreases as the time delay reduces, which is due to two reasons. First, natural convection enhances the heat transfer at the higher PCM levels. Second, the PCM mass in a cylinder with smaller tube radius is more than that of a cylinder with larger tube radius. The excess PCM requires more energy and consequently longer time to melt; thus, the time difference at the lower levels is longer.
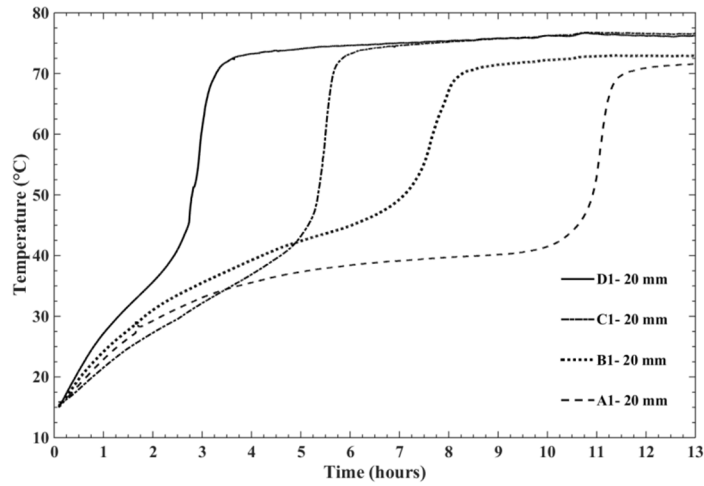
(a) Level 1   (b) Level 2
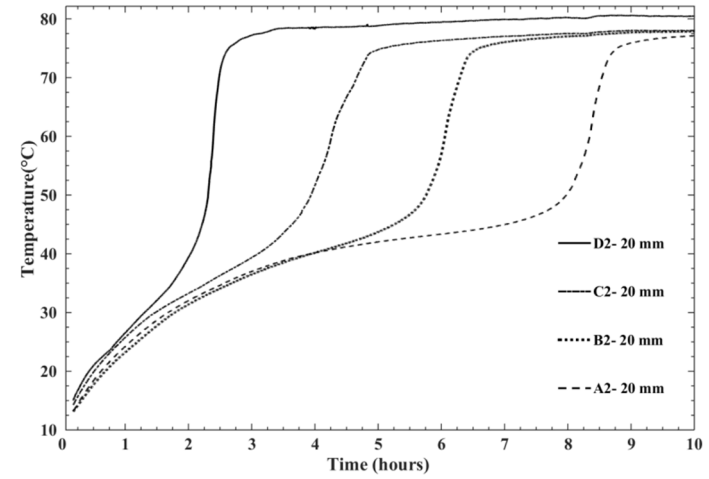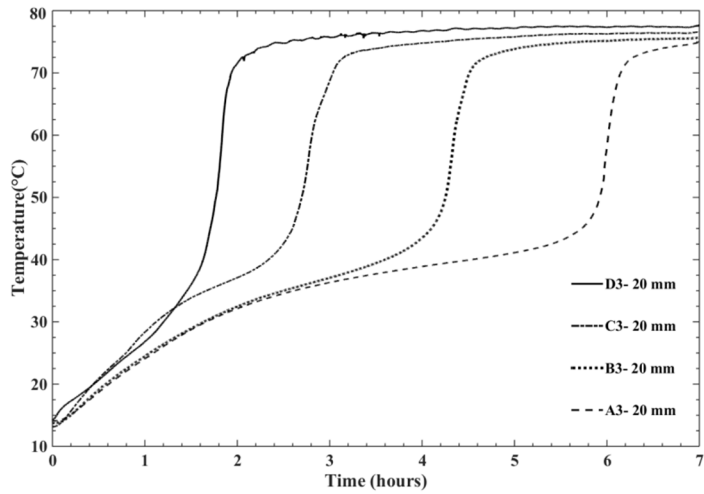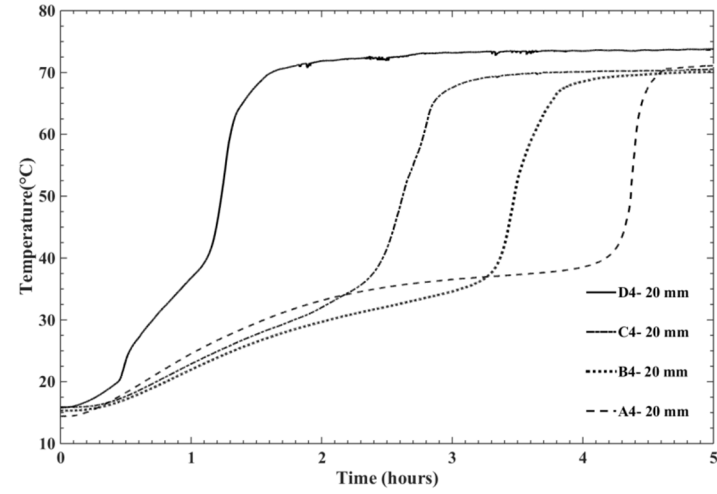
(c) Level 3   (d) Level 4

Figure C.6: Comparison of temperatures of thermocouples located 20 mm away from the HTF tubes during the charging process

C.4.1.3 Charging process – Comparison

Figure C.7 (a-c) compares the average PCM temperature, liquid fraction, and stored energy fraction of the LHTES systems during the charging process with the HTF temperature of 80 °C and the flow rate of 10 L/min. The results show that the trends in all cylinders are similar. However, among the cylinders, Cylinder A with the largest shell to tube radius ratio, has the slowest energy storage process and its average PCM temperature rise, liquid fraction rise and energy storage rate are much slower than others. On the other hand, Figure C.7c shows that the energy storage rate of Cylinders C is very close to that of Cylinder D although the shell to tube radius ratio is much different. These results indicate that an optimal shell to tube radius ratio exists. If the shell to tube radius ratio is too small, the energy storage rate is very low. On the other hand, if the ratio is too large, it wastes the initial cost and lowers the total stored energy since larger HTF tube reduces the amount of PCM in the system. The detailed discussion on the optimal ratio is presented in Section C.5.
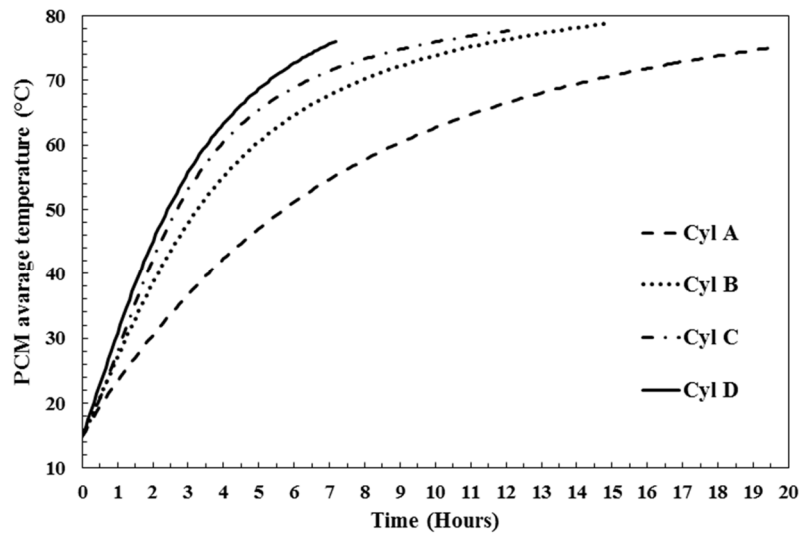
(a) Comparison of average PCM temperature
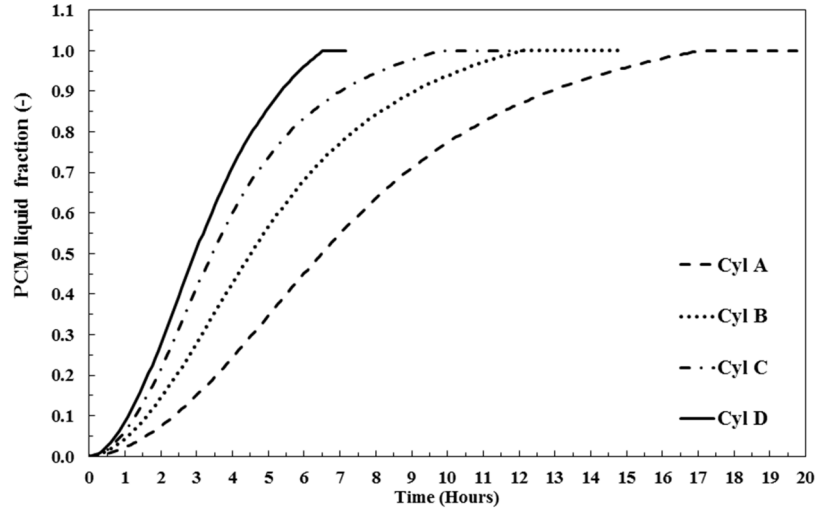
(b) Comparison of PCM liquid fraction
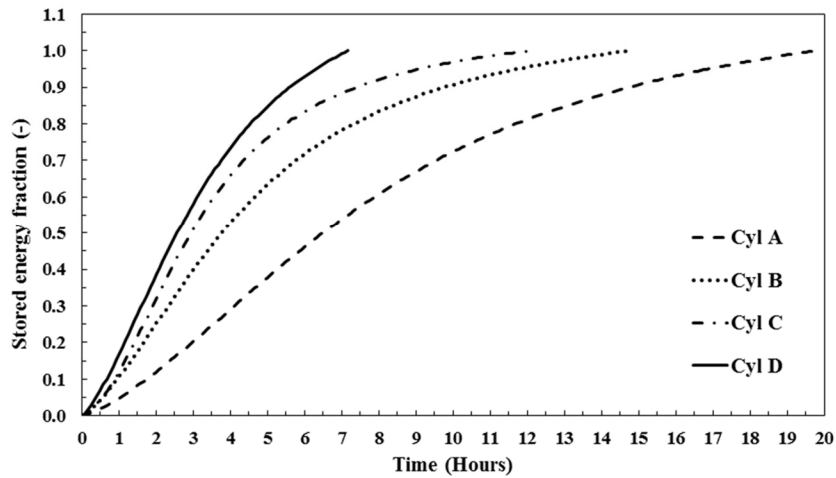
(c) Comparison of stored energy fraction

Figure C.7: Comparison of the PCM average temperature, liquid fraction, and stored energy fraction during the charging process

C.4.2   Discharging process

Upon completion of the charging process, the cylinders were immediately discharged by passing the cold HTF at a temperature of 10 °C and flow rate of 10 L/min.

C.4.2.1   Discharging process – 5 mm thermocouples

Figure C.8 (a-d) shows the temperature variation in thermocouple probes located 5 mm away from the inner surface of the acrylic cylinder within each cylinder during the

discharging process. The discharging process finishes when the temperatures at all four levels reach a stable temperature. This time is considered as the whole discharging time. The results show that the required discharging time is reduced by up to 44% as the shell to tube radius ratio decreases from 8.1 to 2.7. In addition, Figure C.8 also shows that the PCM at different thermocouple locations solidifies almost at the same time. This indicates that thermal conduction dominates the heat transfer in the discharging process.
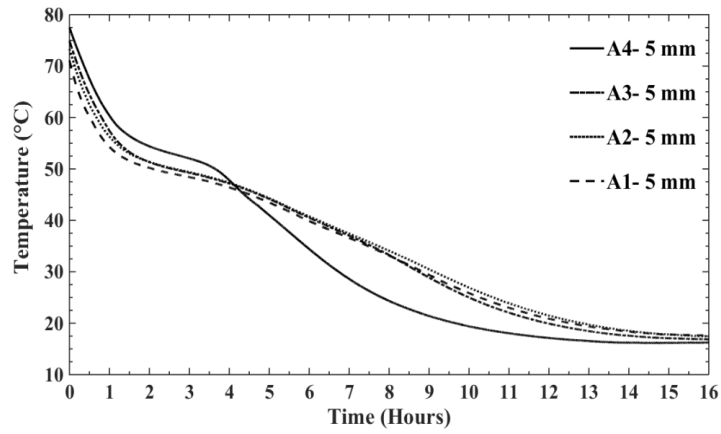
(a) Cylinder A
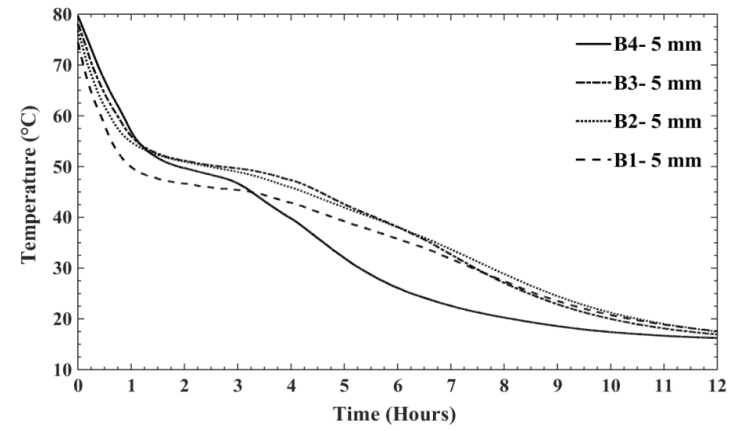
(b) Cylinder B
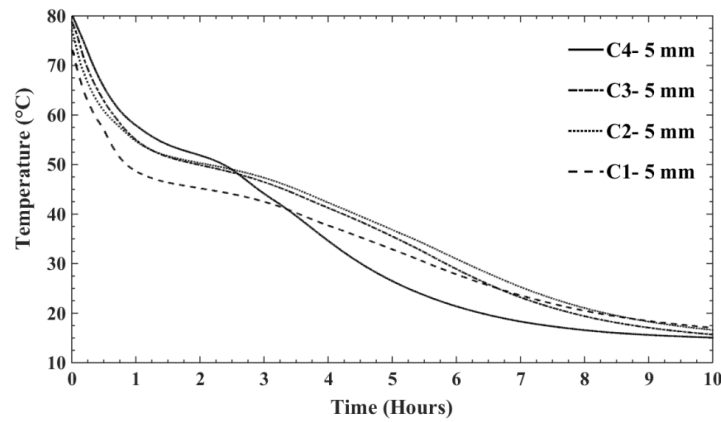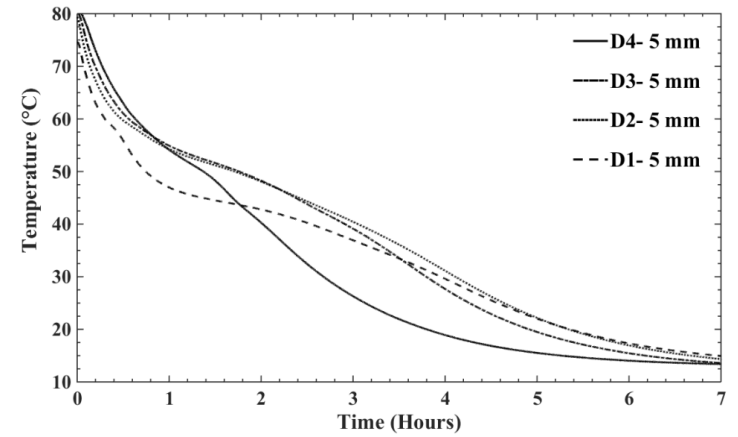
(c) Cylinder C

(d) Cylinder D

Figure C.8: Comparison of temperatures recorded by thermocouples located 5 mm away from the shells during the discharging process

C.4.2.2   Discharging process – 20 mm thermocouples

Figure C.9 (a-d) compares the temperature variation at each level for the thermocouple probes located 20 mm away from the HTF tube. It is obvious that the PCM temperature decreases much faster in a cylinder with larger tube radius. This is due to the larger heat transfer area, which increases the heat transfer rate. During discharging process, the solidified PCM surrounds the HTF tube; thus, the thermal energy exchange from the high temperature PCM to the cold HTF could only be transferred via thermal conduction. Therefore, the heat transfer surface area plays a very important role in the discharging process.
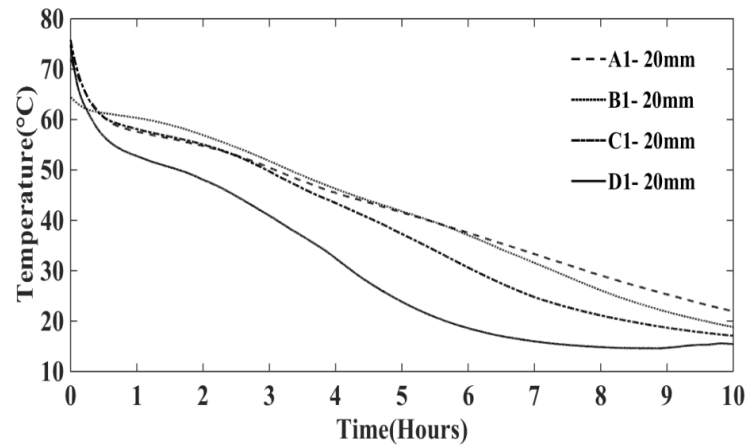
(a) Level 1
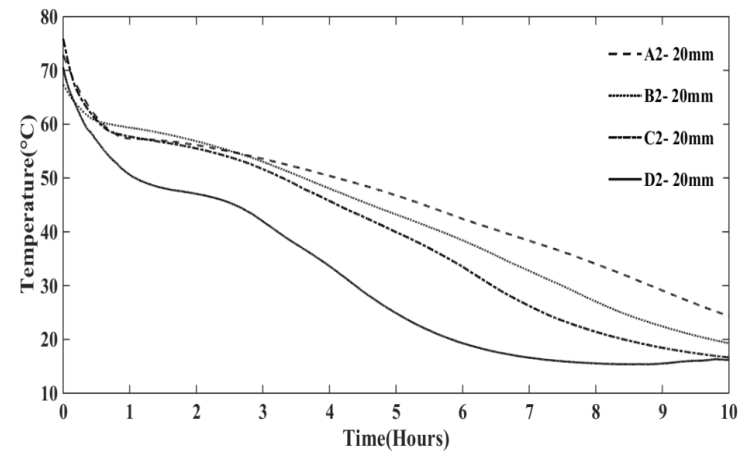
(b) Level 2
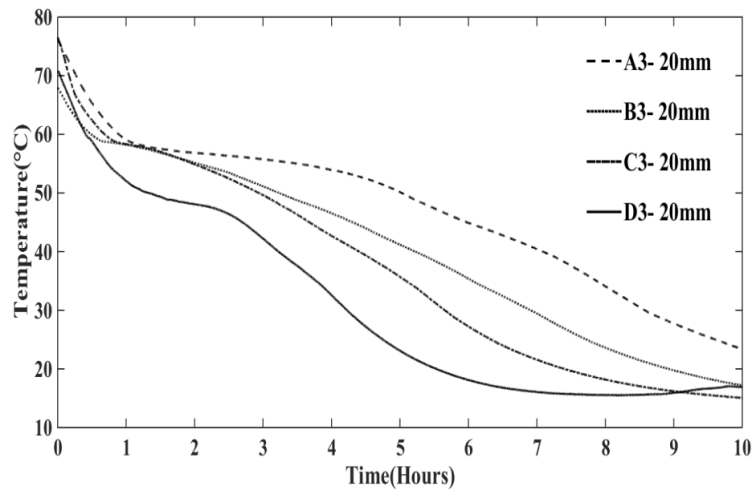
(c) Level 3
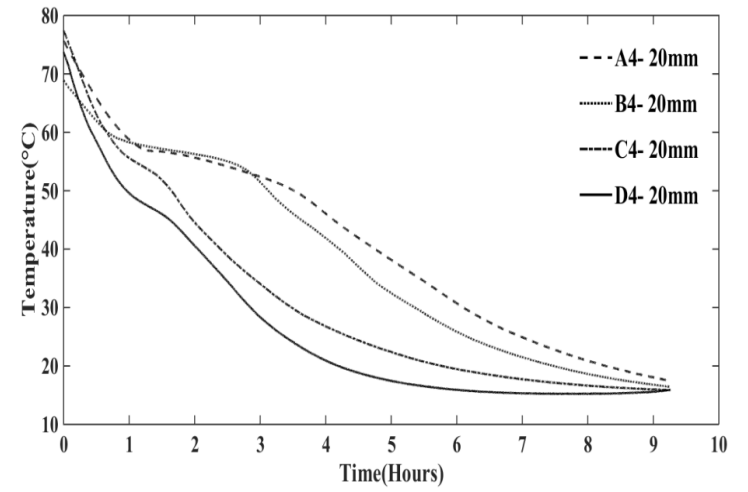
(d) Level 4

Figure C.9: Comparison of temperatures recorded by thermocouples located 20 mm away from the HTF tubes during the discharging process

C.4.2.3   Discharging process – Comparison

Figure C.10 (a-c) compares the average PCM temperature, liquid fraction, and stored energy fraction of the LHTES systems during the discharging process. As the shell to tube radius ratio decreases from 8.1 (Cylinder A) to 2.7 (Cylinder D), the rate of the average PCM temperature drop increases. This is mainly due to the large heat transfer rate caused by the large heat transfer area in the cylinder with the large tube radius. Figure C.10b shows that the solidification processes in all cylinders are much faster than the melting processes as shown in Figure C.7b. This is due to the fact that the temperature difference between the HTF and PCM phase change temperature was much higher for the discharging process as compared to the charging one. This also explains why the energy release in the discharging process is faster than the energy storage in the charging process as shown in Figure C.10c.
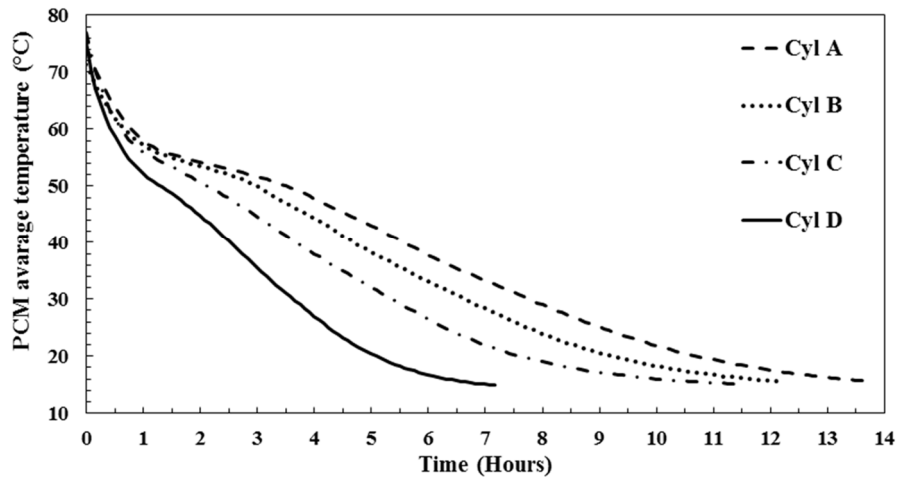
(a) Comparison of average PCM temperature
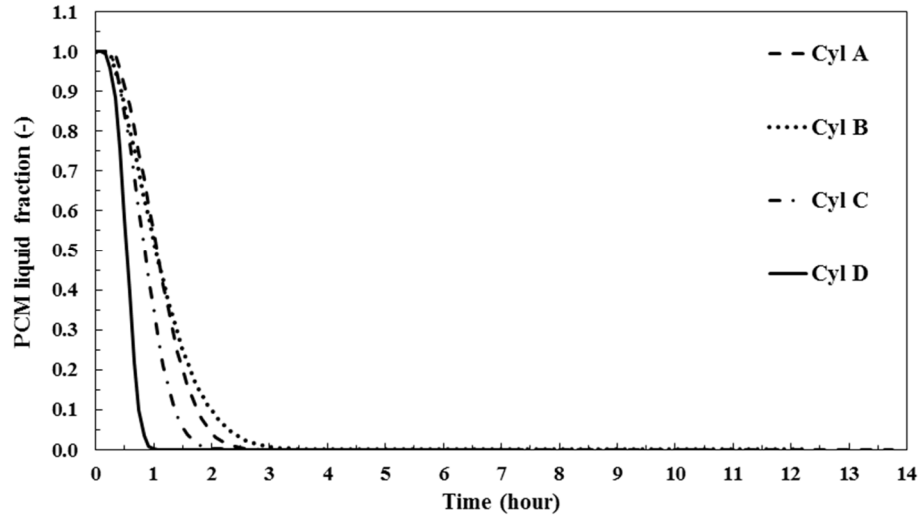
(b) Comparison of the PCM liquid fraction
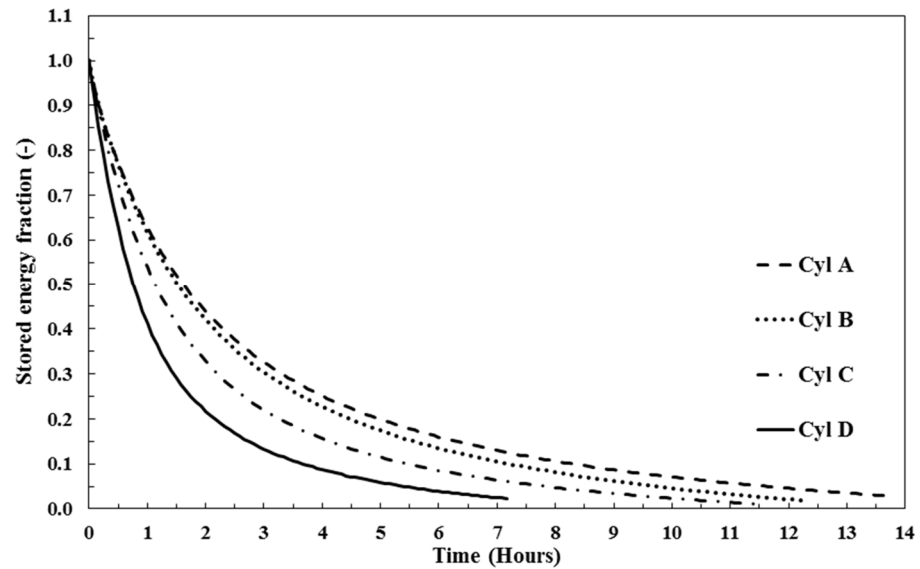
(c) Comparison of stored energy fraction

Figure C.10: Comparison of the PCM average temperature, liquid fraction, and stored energy fraction during the discharging process

C.4.3 Effect of operating parameters

C.4.3.1 HTF temperature

Figure C.11 (a-d) shows the variation of PCM temperature in a complete charging and discharging cycle for thermocouple probes located 5 mm from the inner surface of the acrylic shell for each cylinder. Two different HTF charging temperatures of 70 °C and 80 °C were considered with the same discharging temperature of 10 °C while the

HTF flow rate was kept at 10 L/min. It is observed that the overall charging-discharging time is highly dependent on the charging time, which is influenced by the HTF temperature. During the charging process, as the HTF temperature increased from 70 to 80 °C, the total charging time reduced by 68%, 63%, 60%, and 54% in Cylinders A, B, C, and D, respectively. However, during the discharging process with the HTF temperature of 10 °C after being charged with HTF at 70 °C and 80 °C, the PCM temperature drops rapidly and the HTF changing temperature has no significant effect on the discharging process. As the shell to tube radius ratio reduced from 8.1 to 2.7 between Cylinders A and D, the overall cycle time decreased by 34% and 40% for the HTF temperature of 70 to 80 °C, respectively.
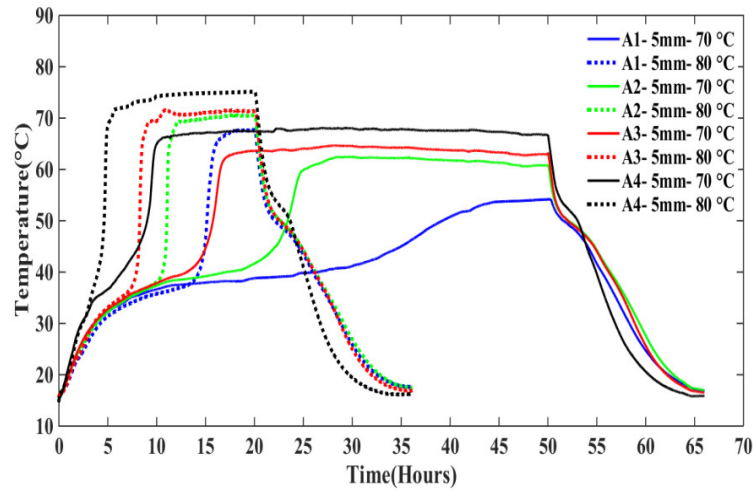
(a) Cylinder A
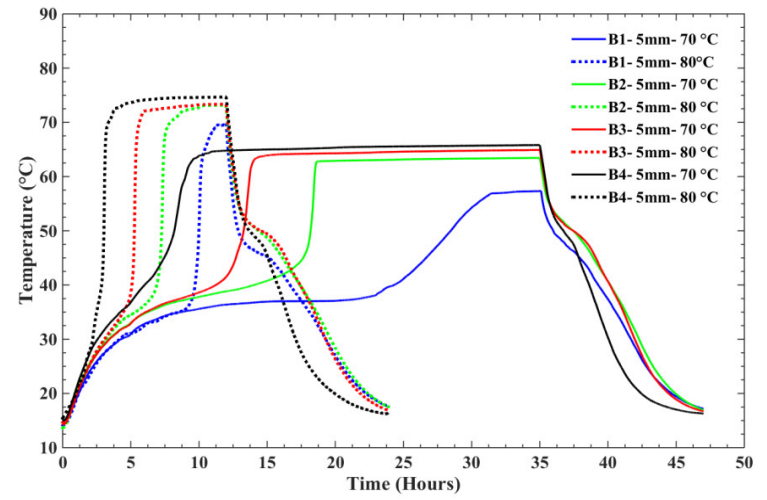
(b) Cylinder B
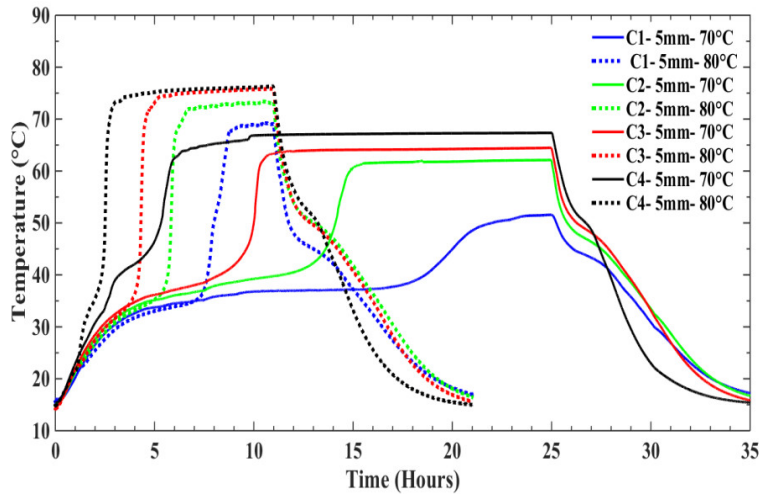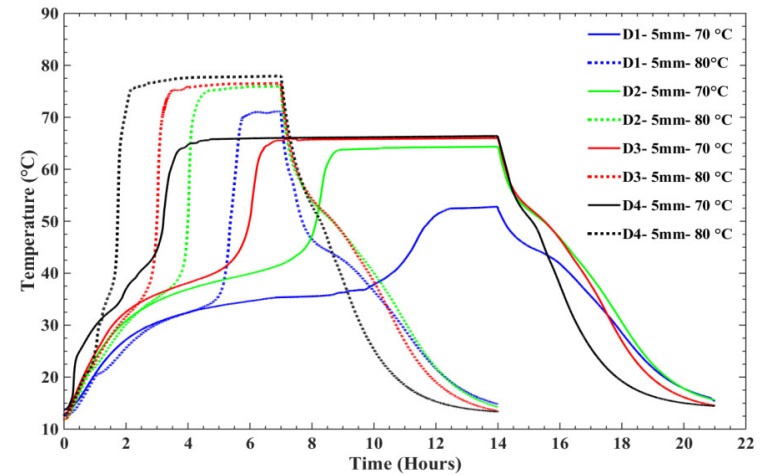
(c) Cylinder C

(d) Cylinder D

Figure C.11: Complete charging and discharging cycles for thermocouples located 5 mm away from the shells under different HTF temperatures

Figure C.12 (a-c) compares the average PCM temperature, liquid fraction, and stored energy fraction of the LHTES systems during the complete charging-discharging process with the HTF charging temperature of 70 and 80 °C. The results showed that the charging HTF temperature largely affected the charging time and total amount of energy storage. As the charging HTF temperature increased from 70 to 80 °C, the charging time reduced by more than 50% and the total stored energy increased by up to 20%. Furthermore, the results revealed that the effect on charging time in the system with the large shell to tube radius ratio was much larger than that in the system with the small radius ratio.
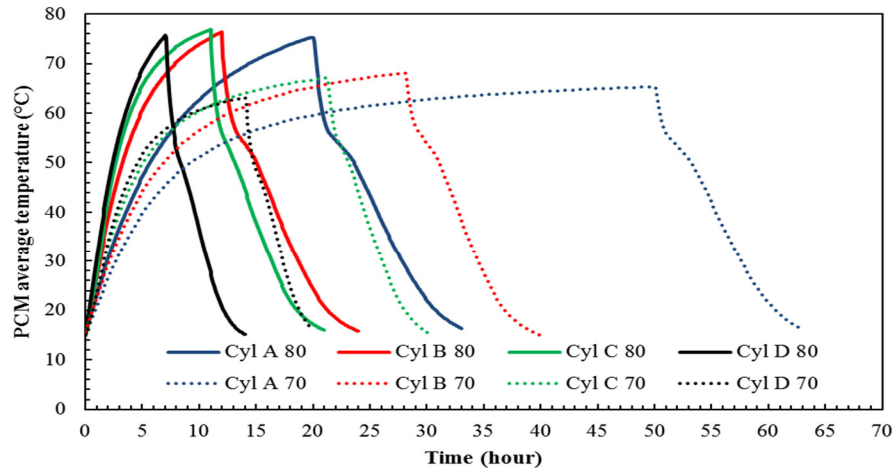
(a) Comparison of average PCM temperature
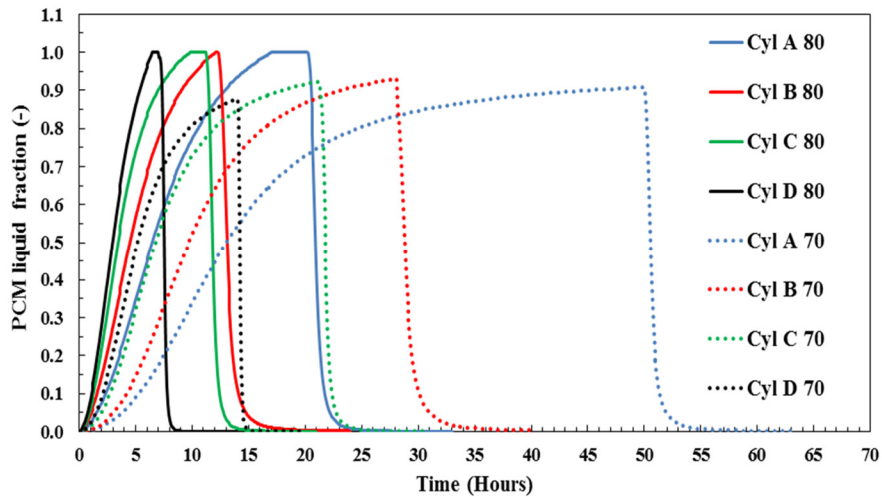
(b) Comparison of PCM liquid fraction
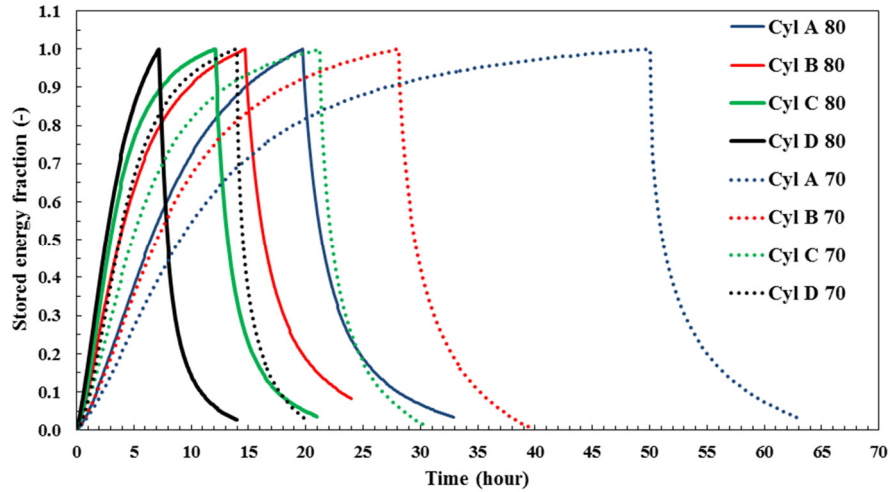
(c) Comparison of PCM liquid fraction

Figure C.12: Comparison of the PCM average temperature, liquid fraction, and stored energy fraction during the complete charging/discharging cycle

C.4.3.2   HTF flow rate

All previous presented experimental data were performed at the HTF flow rate of 10 L/min. This flow rate provides turbulent flow with the Reynolds number of 47225, 31400, 23612, and 15741 in Cylinders A, B, C, and D, respectively. In order to investigate the effect of HTF flow rate on the system energy storage performance, the experiments were also performed under different HTF mass flow rates with a constant HTF Reynolds number among cylinders. Table C.4 compares the charging and discharging times in different cylinders at the charging HTF temperature of 70 °C, and discharging HTF temperature of 10 °C under two scenarios: constant HTF Reynolds number with variable flow rates, and constant flow rate of 10 L/min with different Reynolds numbers. At the constant Reynolds number of 23612, the corresponding flow rates were 5, 7.5, 10, and 15 L/min in Cylinders A, B, C, and D, respectively. This approach produces the same Nusselt number in all tubes in the storage system. As the shell to tube radius ratio decreased from 8.1 to 2.7 between the Cylinder A and D, the charging, discharging and complete cycle times decreased by 28%, 44% and 34%, respectively at both scenarios. Furthermore, the charging and discharge times were almost the same in the same cylinder under different flow rates. These comparison results

indicated that the HTF flow rate has no significant effect on the charging and discharging processes. This can be explained by the heat transfer coefficient. In the storage systems, the heat transfer coefficient between the HTF and tube surface was much larger than that between the tube surface and PCM. The heat transfer rate was dominated by the heat transfer coefficient between the tube surface and PCM. Therefore, increasing heat transfer rate by varying the HTF flow rate did not change the overall heat transfer from the HTF flow to the PCM in the storage systems.

Table C.4: Effect of the HTF flow rate on the charging, discharging, and the complete cycle time

LHTES unit	Radius ratio	Same Re Number (23612), Different flow rates				Same flow rates (10 L/min), Different Re Number			
		HTF flow rate (L/min)	Charging Time (hrs)	Discharging Time (hrs)	Complete cycle Time (hrs)	Re number (-)	Charging Time (hrs)	Discharging Time (hrs)	Complete cycle Time (hrs)
Cylinder A	8.1	5	50.11	15.05	65.16	47,225	50	15	65
Cylinder B	5.4	7.5	35.15	12.52	47.67	31,400	35	12.5	47.5
Cylinder C	4.0	10	25	10	35	23,612	25	10	35
Cylinder D	2.7	15	13.90	6.95	20.85	15,741	14	7	21

C.5   Optimal shell to tube radius ratio

Figure C.13 shows the variation of the charging and discharging times, and stored energy under different HTF temperatures and shell to tube radius ratios at the HTF flow rate of 10 L/min. As the radius ratio increases, the charging as well as discharging time increases. As shown in Figure C.13a, the charging time increases drastically under both HTF temperatures when the radius ratio is larger than 5.4. This result indicated that the optimal shell to tube radius ratio should be less than 5.4 in the studied cylinders. Furthermore, as shown in Figure C.13b, as the radius ratio increased beyond 5.4, the increase in stored energy is insignificant. On the other hand, for the radius ratios below 5.4, the stored energy deceased sharply. By balancing the charging time and stored energy in Figure C.13, the optimal shell to tube radius ratio is around 5.4.
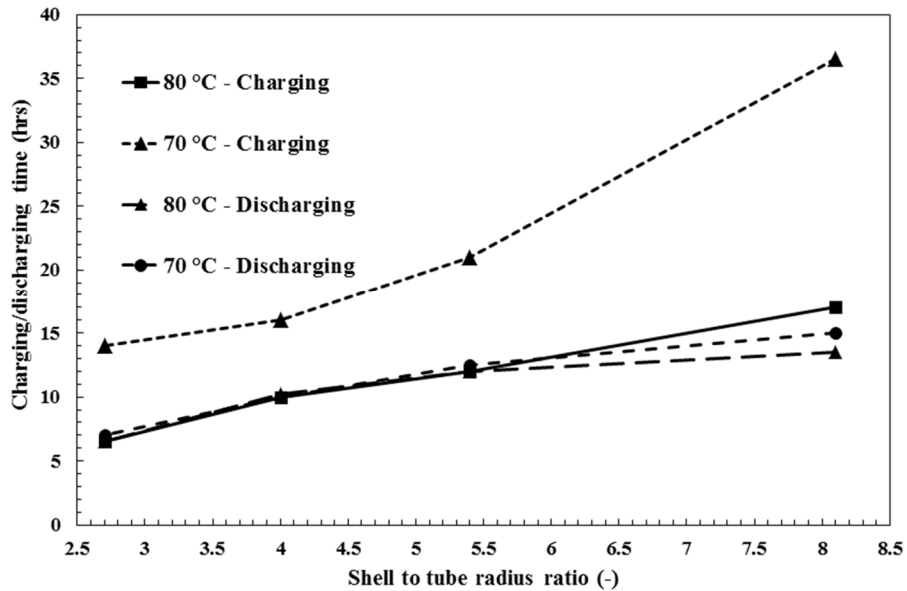
(a) Comparison of the charging and discharging time
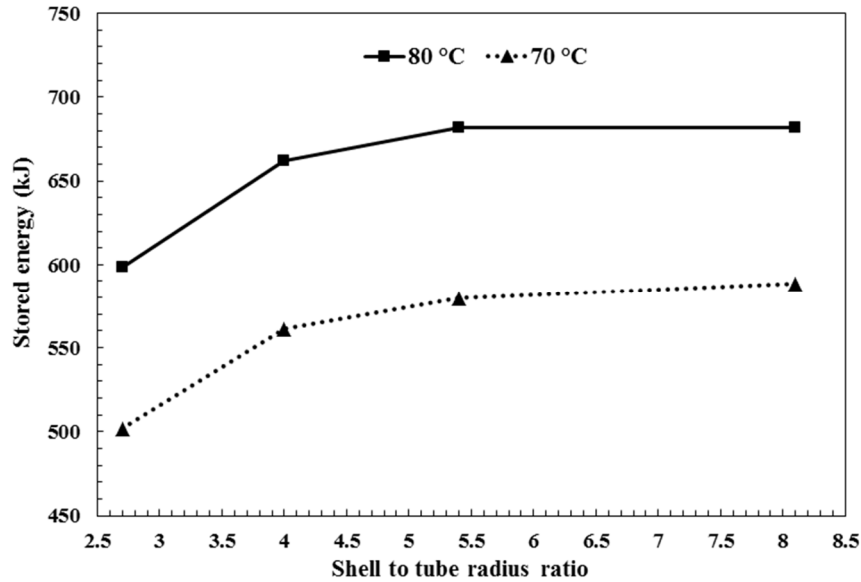
(b) Comparison based on stored energy

Figure C.13: The effect of the shell to tube radius ratio on the charging and discharging performance under different HTF temperatures

C.6 Conclusion

In this chapter, the effects of geometrical and operating parameters on the phase change performance of vertical cylindrical LHTES units were investigated. For this purpose, four different shell to tube radius ratios were considered with the PCM at the shell side and the HTF passing through the tube side. The storages had identical shell radii but different HTF tube radii to investigate the effect of heat transfer surface area on the system storage performance. The PCM temperature distributions were measured and compared experimentally among the considered cylinders. The experimental results and calculated PCM average temperature, liquid fraction, and stored energy fraction showed that complete charging and discharging is highly dependent on the shell to tube radius ratio as well as the HTF temperature while almost independent of the HTF flow rate. By balancing the discharging time and stored energy capacity, the optimal shell to tube radius ratio was found to be around 5.4 in the studied storage systems. This study provides engineers useful information for the design and optimization of vertical shell-and-tube LHTES systems.

Appendix D: Natural convection characterization in a vertical shell-and-tube system

D.1 Introduction

Latent heat thermal energy storage (LHTES) systems have received significant research attention in past decades [190, 191]. This is due to their high latent heat capacity, which is essentially required for management of time mismatch between energy supply and demand [5]. Therefore, PCMs have found several applications, e.g. in ventilation systems [6], refrigeration systems [7], net zero energy buildings [8], hot water tanks [9], etc. Besides, such systems offer high storage density and low energy loss through energy storage at a nearly constant temperature. However, the low thermal conductivity of PCMs used in LHTES systems has hindered their commercialization and widespread applications [165]. One solution to the problem of low thermal conductivity of PCMs is to enhance heat transfer by designing a proper heat exchanger system. This requires a deep understanding of the heat transfer mechanism in LHTES systems.

Some researchers believed that conduction played the dominant role during liquid/solid phase transformation processes [192-195]. Zivkovic and Fujii [194] and later Vyshak and Jilani [195] applied a pure conduction model and compared melting process of a PCM packed in three containers of different geometric configurations, i.e. rectangular, cylindrical and shell-and-tube. The shell-and-tube storage was found to require the shortest time for storing an equal amount of energy.

However, many researchers demonstrated that it is impossible to neglect the natural convection part of the heat transfer mechanism during the phase change process, especially for melting. Sporrow et al. [196] performed a pioneering study and concluded that natural convection could not be ignored in the analysis of a phase change process. Buddhi et al. [197] presented an explanation for the natural convection phenomenon: the density difference in the liquid PCM phase induced buoyancy, which caused convective motion within the liquid phase. Later, Lacroix and Duong [198] experimentally demonstrated that natural convection was the main heat transfer mechanism during the

melting process. This finding was further experimentally proven by Velraj et al. [199]. Hamdan and Al-Hinti [200] analytically investigated the melting process of a PCM contained in a rectangular enclosure heated from a vertical side at a constant heat flux. The model well predicted the liquid/solid interface propagation at the initial stages of the melting process and under-predicted it at the later stage of melting. Fan et al. [201] studied constrained melting heat transfer of a PCM in a circumferentially finned spherical capsule. Local natural convection was found to emerge from above and underneath the fin surface. Ezan et al. [202] investigated the natural convection and flow parametric effects on charging and discharging periods of water in a shell-and-tube LHTES unit. Experimental results indicated that natural convection was the dominant heat transfer mechanism after a short heat conduction dominated period for both solidification and melting processes. The heat transfer fluid (HTF) inlet temperature had considerable effect on the energy storage capacity during charging process as well as energy rejection during discharging period. Agyenim et al. [166] reviewed the development of LHTES systems and examined the effect of geometric and configurational design of PCM containers. It was concluded that the most intensely studied system was the shell-and-tube energy storage system.

A number of studies numerically and/or experimentally investigated the heat transfer in horizontal shell-and-tube LHTES systems [184, 185, 187, 203-205]. Agyenim et al. [203] performed a series of experimental studies on a horizontal shell-and-tube heat exchanger LHTES system. Convection heat transfer was found to play an important role during the melting process, while conduction heat transfer was significant during the solidification process. Hosseini et al. [185, 204] investigated heat transfer characteristics of a horizontal shell-and-tube heat exchanger LHTES system using RT50 (melting temperature of 50 ºC) as the PCM. It was found that recirculation was driven by convection within the liquid region during the melting process. Avci and Yazici [184] experimentally recorded the time histories of a paraffin (P56-58) as the PCM in a horizontal shell-and-tube heat exchanger LHTES system. It was concluded that the molten PCM ascended to the upper part of the storage unit and the melt region extended radially upward as a result of natural convection. Contrary to the melting process, during the solidification process natural convection has been observed to be initially effective

and then suppressed by conduction. Rösler and Brüggemann [205] performed a numerical and experimental study of convection dominated phase change around a single cylinder inside a horizontal shell-and-tube LHTES system. Industrial grade paraffin wax (RT42) and water were used as the PCM and the HTF, respectively. The calculated temperature, liquid fraction, and velocity field indicated that the phase boundary moved upward due to the natural convection induced motion during the melting of the paraffin wax. Wang et al. [187] numerically studied the charging and discharging characteristics of a horizontal shell-and-tube phase change heat storage unit. The results showed that charging and discharging processes have three stages for temporal temperature variation in PCM and temporal charging or discharging heat transfer rate; i.e. a rapidly changing period (dominated by convection), a slowly changing period (a mix of conduction and convection) and a more slowly changing period (conduction dominated).

Some researchers have focused on the study of heat transfer in vertical shell-and-tube LHTES systems [23, 177, 206-211]. Trp [177] investigated the heat transfer phenomenon during paraffin melting and solidification in a vertical shell-and-tube LHTES unit. Experimental results underlined that PCM melts non-isothermally within the melting zone but solidification occurs isothermally. Akgün et al. [206, 207] experimentally investigated a vertical shell-and-tube LHTES unit with a novel design in which the shell was inclined with an angle of 5 degrees. The effect of the HTF Reynolds number on the melting and solidification behaviors was analyzed. The studied design showed that the inclination of the shell surface could improve heat transfer during the melting process. Murray and Groulx [23] experimentally studied the heat transfer mechanism in a vertical cylindrical shell-and-tube LHTES system. The effect of natural convection in the melting process was found to be significant since more melted PCM was observed at the top of the container. Longeon et al. [208] experimentally and numerically investigated the heat transfer behavior of a shell-and-tube LHTES unit filled with paraffin RT35 as the PCM and water as the HTF. The study proved that the HTF flow direction coupled with free convection heat transfer mechanism influenced the evolution of the PCM melting front. In addition, it was recommended to use a downward HTF flow during the charging process and an upward one during the discharging process. Xiao and Zhang [209, 210] experimentally and numerically studied the heat transfer

characteristics of vertical PCM tubes during charging and discharging processes. It was found that the addition of expanded graphite to the paraffin substantially improved the heat transfer due to its high thermal conductivity. Recently, Wang et al. [211] experimentally studied the thermal behavior and heat transfer performance of a vertical shell-and-tube LHTES unit with erythritol (melting temperature of 120.39 ºC) as the PCM and air as the HTF. It was concluded that natural convection dominated heat transfer during the charging process as well as the initial stage of the discharging process. As the PCM solidified, the heat transfer was dominated by conduction during the discharging process. It was also found that higher HTF inlet temperature and mass flow rate during charging enhanced the heat transfer in the PCM and shortened the charging time.

Seddegh et al. [10] numerically compared thermal behavior and heat transfer characteristics of a vertical cylindrical shell-and-tube unit using a pure thermal conduction model and a combined conduction/convection heat transfer model. The results indicated that convection heat transfer dominated the melting process, while conduction dominated the solidification process. The same authors [3] further compared the heat transfer in horizontal and vertical shell-and-tube LHTES systems using the combined model. It was concluded that heat transfer mechanism in vertical shell-and-tube LHTES systems is significantly different from that in the horizontal units. In addition, Joybari and Haghighat [12] numerically analyzed the convective behavior during melting of a paraffin wax (RT31) in a horizontal shell-and-tube heat exchanger. It was found that the buoyancy-driven upward liquid PCM motion affected the upper half of the system. Recently, Joybari et al. [212] numerically investigated the heat transfer mechanism of a horizontal storage under simultaneous charging and discharging using the two models. It was concluded that for an initially solid storage the effect of natural convection could not be ignored, whereas for initially melted PCM pure conduction model could be applied with small error.

In this study, a vertical shell-and-tube heat exchanger is experimentally and numerically investigated to understand the effect of natural convection. The outcomes of this study clearly explain physics of the heat transfer during melting and solidification of

PCMs. It provides insights and guidance towards the design and optimization of vertical shell-and-tube LHTES systems.

D.2 Analysis procedure

According to the above literature, several studies investigated the heat transfer in vertical shell-and-tube LHTES systems. Most of the research concluded that natural convection played a very important role during the charging process and had insignificant effect during the discharging process. However, the question of how natural convection was initiated and affected the heat transfer during the charging process has rarely been investigated. Furthermore, some studies reported that the total charging time was almost similar to the discharging time. This implied whether convection affected discharging. In this chapter, a shell-and-tube LHTES system was developed to experimentally investigate how the natural convection is initiated and how the energy is transferred from the HTF to PCM through natural convection in the LHTES system. Visualized experiments were performed to observe the liquid/solid PCM interface evolution during melting and solidification in the vertical shell-and-tube LHTES system. In order to clearly visualize the natural convection and energy transfer mechanism during experiments, a large shell to tube radius ratio of 17.5 was considered. Since the nature of the transport phenomena in vertical shell-and-tube LHTES systems is the same regardless of shell diameter, the large shell to tube radius ratio does not affect the analysis.

The recorded temperatures in the storage system were then used to validate a combined conduction/convection mathematical model. Thereafter, the model was used to extract the temperature and liquid fraction contours during the charging and discharging processes. In addition, experimental images incorporating the theoretical velocity field inside PCM were further investigated to explain the heat transfer phenomena.

D.3 Experimental setup

Figure D.1 shows the investigated experimental setup, which consisted of a hot water tank, a cold water tank, a PCM storage unit, hot and cold water pumps, a flow

meter, a data acquisition module, thermocouples, valves and an extensive piping system. Water was used as both the hot and cold HTFs.

(a)
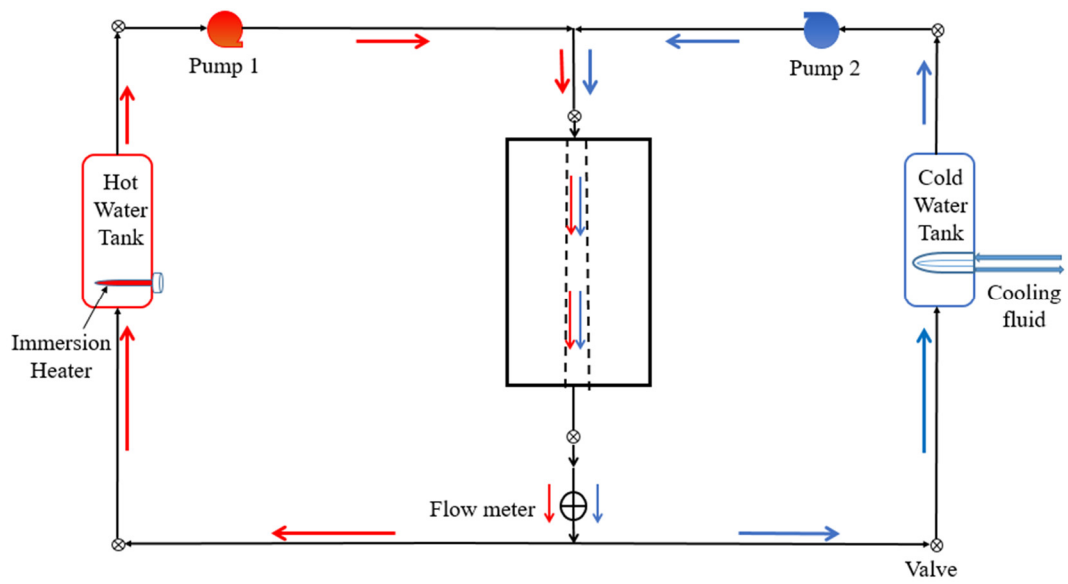
(b)

Figure D.1: a) The picture of the experimental system, and b) a schematic drawing of the test system

In order to clearly visualize the convection and its impact on the heat transfer, a vertical cylindrical container with a diameter of 0.35 m, a height of 0.5 m and a capacity of 48.11 L was used. The tank contained about 25 kg of PCM, and a DN20 copper pipe for the HTF was installed at the center of the container. The PCM used in the test was RT60 paraffin wax from Rubitherm GmbH. PCM thermophysical properties as well as testing conditions are listed in Table D.1. The container was made of transparent polypropylene (thermal conductivity k of 0.1 w/m·K) with a thickness of 6 mm for visual observation of the melting and solidification processes. The container was insulated by Armaflex sheets with a thermal conductivity of 0.036 W/m·K.

Table D.1: Thermophysical properties and test conditions

PCM	Melting temperature (°C)	Latent heat of fusion (kJ/kg)	Density (kg/m³)		Specific heat (J/kg.K)	Thermal conductivity (W/m.K)	Volume expansion (%)	Dynamic viscosity (kg/m.s)
			Solid (15 °C)	Liquid (80 °C)				
Paraffin wax (RT60)	55-61	123,506	880	770	2,000	0.2	12.5	3.705×10^{-5}

HTF	Charging temperature (°C)	Discharging temperature (°C)	Density (kg/m³)	Specific heat (J/kg.K)	Thermal conductivity (W/m.K)
Water	80	10	998	4,183	0.58

During the charging process, the hot HTF was heated up to a pre-set temperature using two 2.4 kW thermal electric immersion heaters (model number TWI50240) with externally adjustable thermostats in the hot water tank with a capacity of 108 L. The hot water was circulated through the inner pipe (in the container where the PCM was filled between the inner pipe and cylindrical shell) by a Grundfos vertical, multistage centrifugal pump (model number: CR 1-4 A-A-A-E-HQQE). Then the hot water was channeled back to the hot water tank. During the discharging process, the cold water was maintained at a required temperature using a 20 kW chiller (model number HWP020-3BB) in the cold tank with a capacity of 1575 L. The cold water was circulated through the same inner pipe in the container to cool the PCM using an Onga horizontal, centrifugal pump (model number: 413). A Flomec oval gear positive displacement flow meter with pulse output was placed between the container outlets and hot/cold water tanks to monitor the hot and cold water flow rates. The temperatures and water flow rates were recorded by a data acquisition system (National Instruments NI9411).

The PCM temperatures were measured by Type-T thermocouples with an accuracy of ±0.2 °C. Figure D.2 shows the position of the thermocouples. Four vertically aligned thermocouples were located at four levels in the same radial position (position A) being 115.5 mm away from the center of the HTF pipe. Another four vertically aligned thermocouples were located at the same four levels but in a different radial position (position B) being 5 mm away from the outer surface of the container. The inlet and outlet water temperatures of the container were measured by the same type of thermocouples.
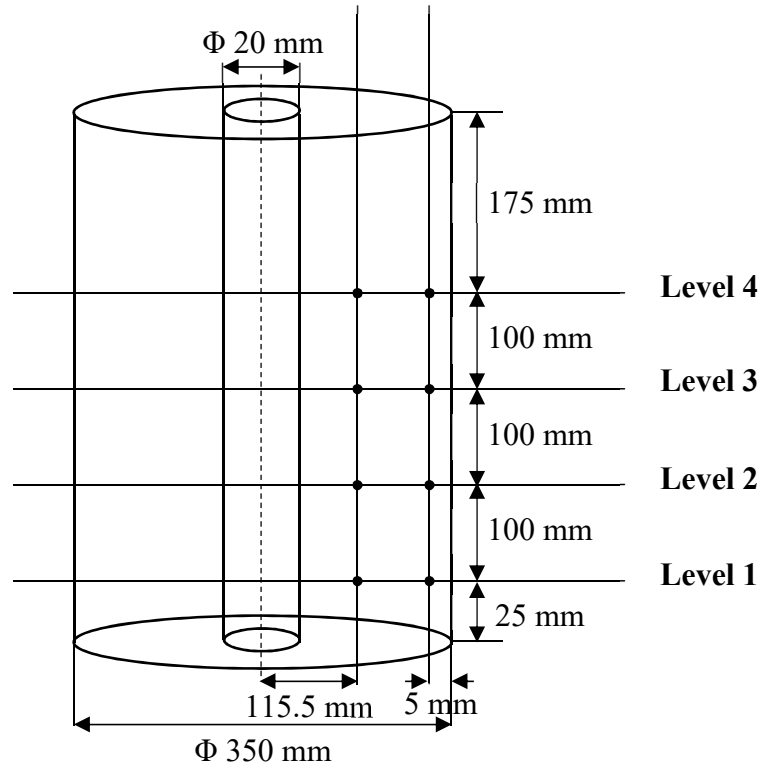
Figure D.2: Location of thermocouples (Bold points represent the thermocouple positions)

D.4 Numerical approach

In order to further investigate the experimental findings, the combined conduction/convection model was used to analyze natural convection within the PCM. The model is detailed in the literature [3, 10, 12, 212] and is summarized in this section. The energy conservation is expressed in terms of total volumetric enthalpy and temperature for thermophysical properties as:

$$\frac{\partial \rho H}{\partial t} + \nabla \cdot (\rho v H) = \nabla \cdot (k \nabla T) + S \tag{D.1}$$

The total volumetric enthalpy is calculated by:

$$H = h + fL \tag{D.2}$$

$$h = h_o + \int_{T_o}^{T} C_P dT \tag{D.3}$$

where h_o is the PCM sensible enthalpy at the reference temperature T_o. f refers to the liquid fraction that indicates the fraction of a cell volume in liquid form and is associated with each cell in the domain by Equation (D.4).

$$f = \begin{cases} 0 & T < T_{Solidus} \\ \dfrac{T - T_{Solidus}}{T_{Liquidus} - T_{Solidus}} & T_{Solidus} \leq T \leq T_{Liquidus} \\ 1 & T > T_{Liquidus} \end{cases} \qquad (D.4)$$

By combining Equations (D.2) to (D.4), the energy conservation equation can be simplified as:

$$\frac{\partial \rho h}{\partial t} + \nabla \cdot (\rho v h) = \nabla \cdot (k \nabla T) - \frac{\partial \rho f L}{\partial t} - \nabla \cdot (\rho v f L) + S \qquad (D.5)$$

The momentum equation is based on the Boussinesq approximation, which assumes a constant fluid density in all terms of the momentum equation except for the body force term, where it is modeled based on a reference density (ρ_0) and temperature (T_0), and the volumetric expansion coefficient (β).

Momentum equation:

$$\frac{\partial \rho_0 v}{\partial t} + \nabla \cdot (\rho_0 v v) = -\nabla P + \nabla \cdot (\mu \nabla v) + (\rho - \rho_0)g + \frac{(1-f)^2}{f^3 + \varepsilon} v A_{mush} \qquad (D.6)$$

Boussinesq approximation:

$$(\rho - \rho_0)g = -\rho_0 \beta (T - T_0) \qquad (D.7)$$

Continuity equation:

$$\frac{\partial \rho}{\partial t} + \nabla \cdot (\rho v) = 0 \qquad (D.8)$$

The computational study was conducted using ANSYS Fluent 17. The following parameters were used in this simulation [3, 10, 12, 212]: $A_{mush} = 10^5$ kg/m^3·s, $\varepsilon = 0.001$, and $T_o = 298.15$ K. Adiabatic boundary conditions were assumed on the outer wall surface as well as the top and bottom ends. The boundary condition for the HTF pipe wall was assumed as constant surface temperature. During the charging process, the PCM was

set to solid state with an initial temperature of 15 °C and the HTF pipe wall temperature was 80 °C. During the discharging process, the PCM temperature was initially set to liquid state with the temperature at the end of the charging process and the HTF pipe wall temperature was 10 °C.

Although this model has been validated for a small shell diameter LHTES system in previous studies [3, 10, 12, 212], it was further verified to check the dependency from time step and cell size for this large shell diameter system prior to the simulation. Therefore, three mesh sizes of 58000, 83000, and 128000 cells; and three time step sizes of 0.05 s, 0.1 s, and 0.2 s were examined. The model with 83000 cells and time step sizes of 0.05 s and 0.1 s produced a very similar variation for the PCM average temperature. The results did not show significant change as the number of cells increase to 128000. Therefore, in order to save the computational time, a mesh with 83000 cells and a time step size of 0.1 s was found to be sufficient to achieve the predetermined convergence level of the energy equation (10^{-6}). Figure D.3 shows the comparison of the PCM temperature between the experimental data and simulation results for the first 10 hours of charging process. The simulation results were found to agree well with the experimental data.
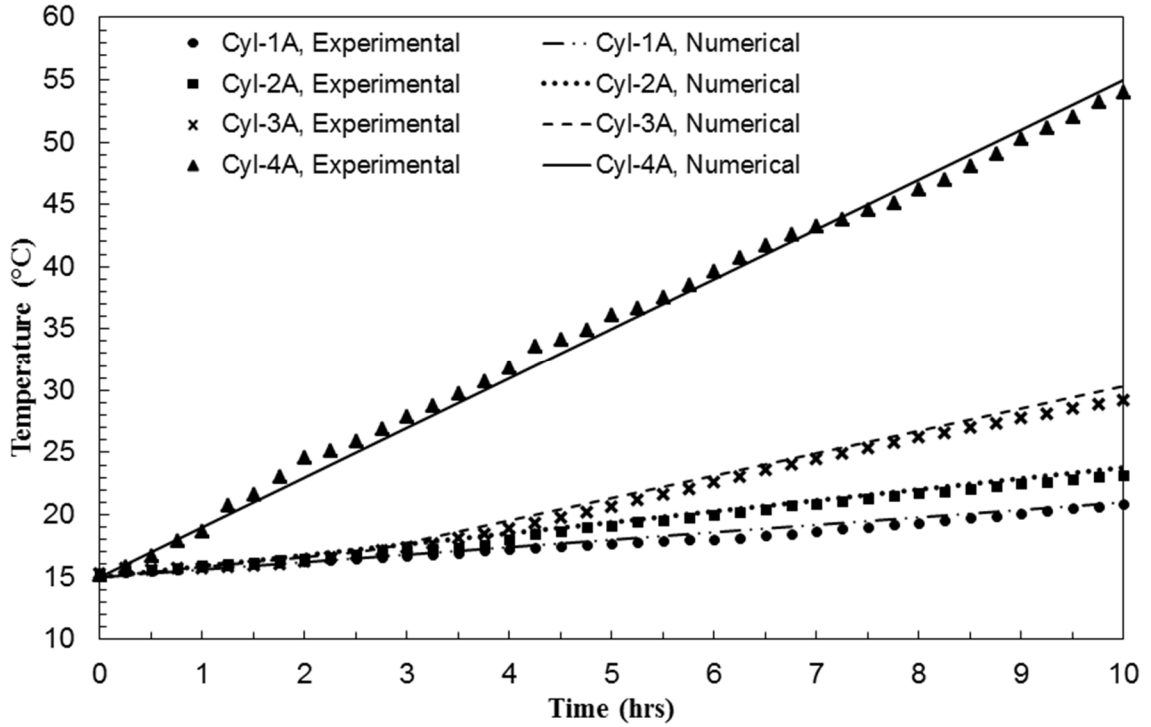
Figure D.3: Comparison between the simulated results and experimental data during the charging process

D.5   Results and discussion

The research focuses on both melting and solidification processes. Prior to experiments, cold water was first used to set the PCM temperature at 15 °C in the cylinder. Then the experiment was performed to investigate the heat transfer in the vertical cylindrical LHTES system during the melting process at a charging HTF temperature of 80 °C and a flow rate of 10 L/min. Once the PCM was completely melted, the discharging experiment was carried out to investigate the heat transfer mechanism of the LHTES system during solidification process at a discharging HTF temperature of 10 °C and a flow rate of 10 L/min. The temporal variation of the experimental temperature inside the PCM as well as experimental images are used to investigate the evolution of the liquid/solid PCM front and the heat transfer mechanism during the charging and discharging processes. Finally, the simulated velocity and temperature fields are used to explain the experimental findings.

D.5.1 Charging process

Figure D.4 shows the PCM temperature variations with time at positions A and B in the cylindrical storage unit during the charging process. The temperatures at the four levels are found to decrease from the top to the bottom of the storage unit at both positions A and B. This indicates that the thermal conduction cannot be the sole heat transfer mechanism within the PCM since conduction leads to an almost identical temperature along the vertical direction [12, 212]. Moreover, temperature recordings are affected by the height of the thermocouples, which indicates the effect of gravity. As a result, the temperatures at the upper levels always increases much faster than those of the lower levels. This can only be explained by natural convection, which brings high temperature melted PCM upward, and leads to stronger heat transfer at the upper levels. This can be evidenced by the experimental images as shown in Figure D.5. Therefore, experimental results proved the arguments as reported in the literature [23, 177, 206-208] that natural convection played an important role during the melting process of PCMs inside vertical storages.
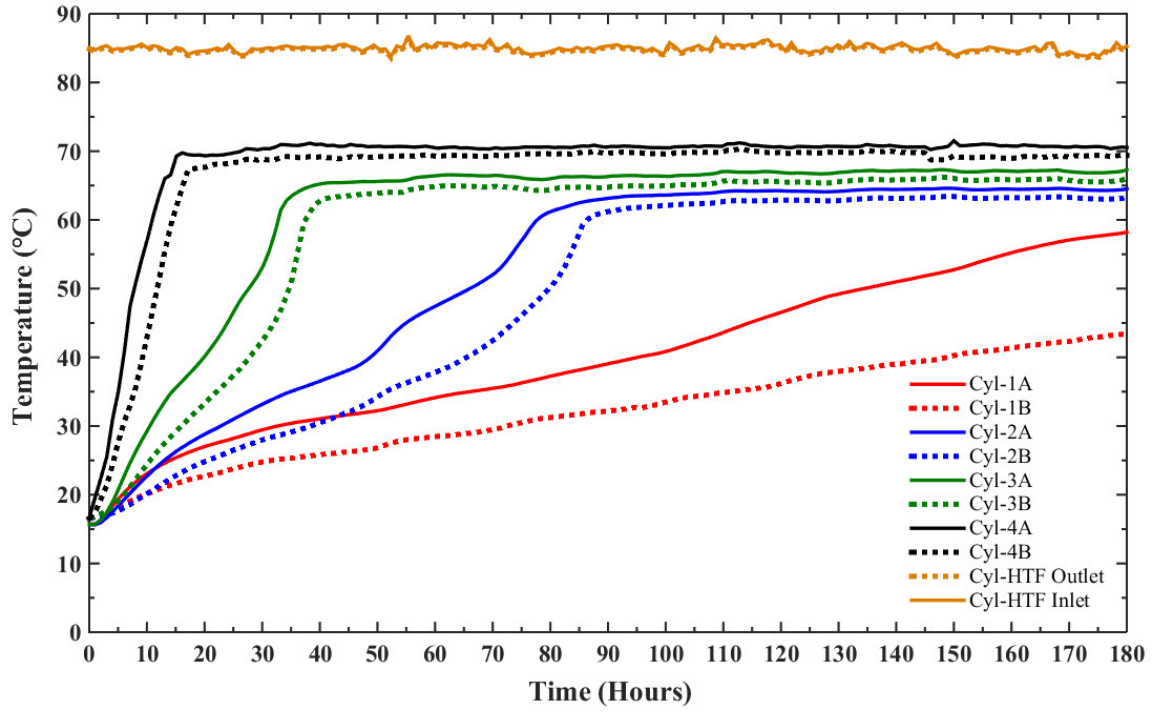
Figure D.4: Temperature variations in the cylindrical system during the charging process
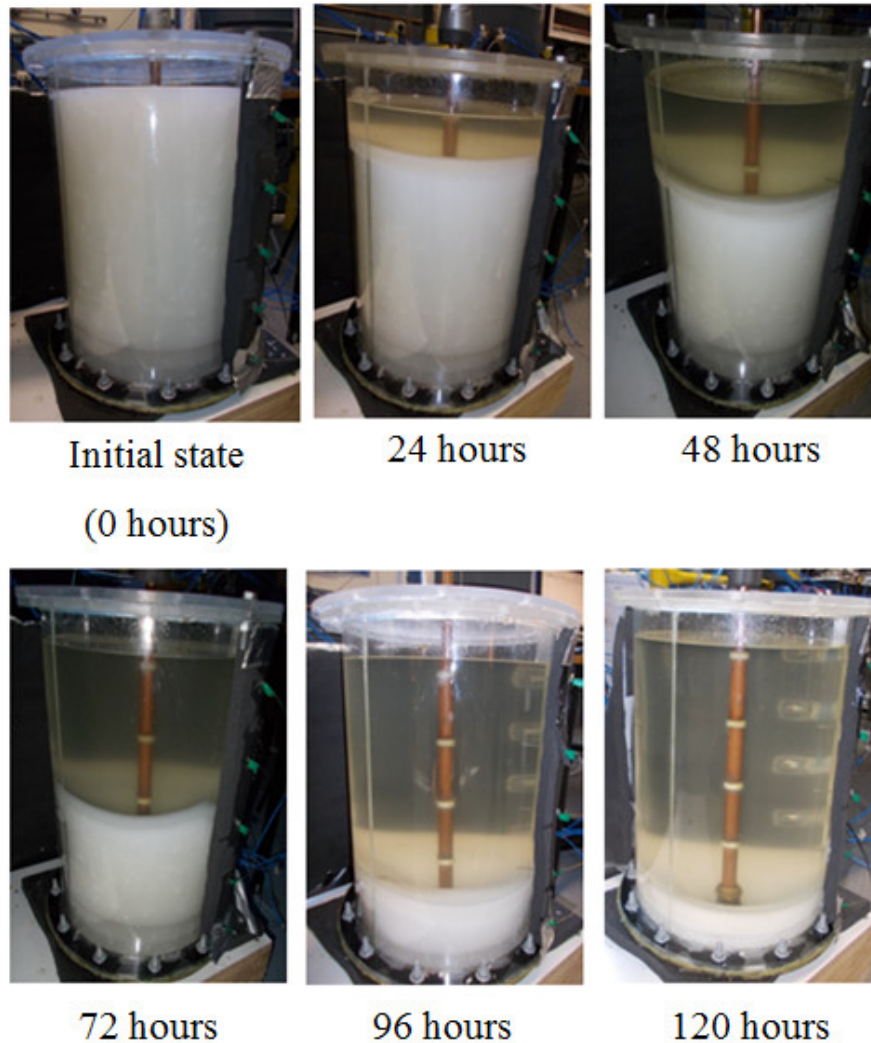
Figure D.5: Evolution of the liquid/solid PCM interface at different charging times

Figure D.5 shows the evolution of the liquid/solid PCM interface. The liquid PCM accumulates at the top of the storage unit and forms a cavity similar to an inverted cone (see Figure D.5). The conic liquid/solid interface surface gradually moves down and the liquid PCM region extends downward. This indicates that the PCM melts from the top to the bottom along the conic liquid/solid interface in the storage unit. This is in contrast to the previous understanding from thermal conduction that the PCM absorbs energy from the HTF pipe and melts from the center of the cylinder outwards to the edge of the shell (forming a cylindrical liquid/solid interface) [12, 212]. This finding clearly demonstrates that natural convection plays an important role in the heat transfer. Furthermore, it is

observed that a thin vertical annular liquid PCM layer exists around the HTF pipe. Little change in the width of the layer is found during the whole charging process as shown in Figure D.6. This is an interesting finding which has not been reported. In most studies, the ratio of the shell diameter to the HTF tube diameter was small; hence, the melting process happened very quickly due to the natural convection. In such cases, the layer might have been too small to be detected visually. In this study, however, the shell diameter is purposely enlarged to visualize the physics of heat transfer. Since the fundamentals of heat transfer phenomena in shell-and-tube LHTES systems is the same regardless of the diameter ratio, it helps to identify how the heat transfer initiates in the PCM. In order to better understand the phenomena, the numerical results are utilized.
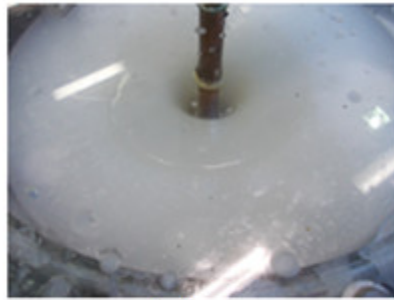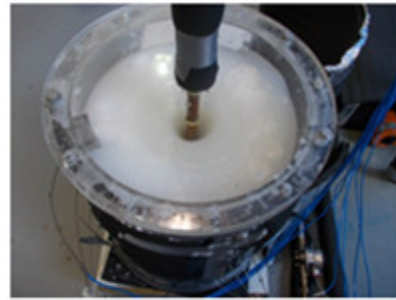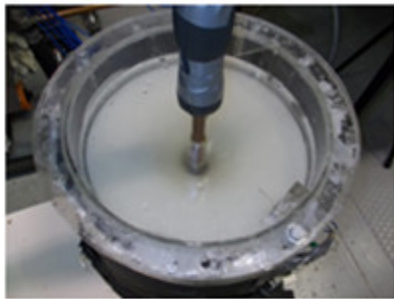
Figure D.6: Evolution of the vertical liquid PCM layer around the HTF pipe during the charging process

Figure D.7 shows simulated contours of the PCM liquid fraction (left side) and temperature field (right side) for the cylindrical storage unit. The liquid fraction contours show that a large portion of the molten PCM ascends to the upper part of the storage unit due to the natural convection. Only a small portion of the liquid PCM is found to exist in a vertical annular layer around the HTF pipe. The layer's width does not show a significant change over the charging process once it is formed. The reason is that at the beginning of melting, conduction is the dominant heat transfer mechanism resulting in an annular liquid layer around the HTF pipe. Later on, natural convection establishes and the thermal energy is transferred from the HTF to the liquid PCM, which then moves to the upper part of the storage system by the vertical convection in the liquid PCM layer around the HTF pipe. The motion induces horizontal convective circulation within the liquid PCM at the upper part of the system and is transferred outward towards the shell during the charging process. The temperature profile also shows that the temperature decreases along both vertical and radial directions. The liquid/solid interface is clearly not a straight line, which implies the domination of natural convection process. These findings are consistent with the experimental temperature profile presented in Figure D.4.
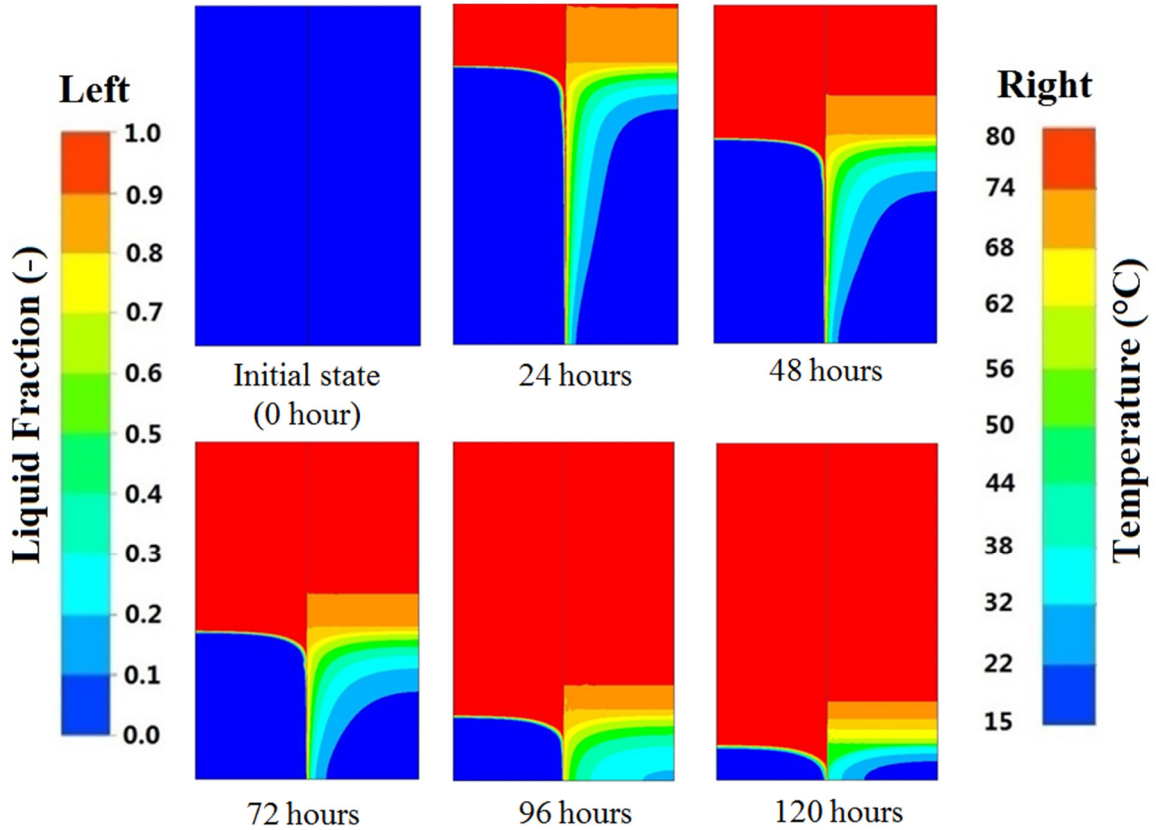
Figure D.7: The contour of the PCM liquid fraction (left) and temperature (right) during the charging process

Figure D.8 presents the simulated velocity field, which helps to understand the convection circulation within the liquid PCM. In Region 1, the liquid PCM is found to circulate vertically in the confined layer. The high temperature liquid PCM at the vicinity of the HTF pipe flows upward, whereas the low temperature liquid PCM flows downward along the liquid/solid interface from Region 2 to make up the PCM in the confined layer. This vertical convective circulation dominates the heat transfer between the HTF pipe surface and liquid PCM, transporting thermal energy to the upper part of the storage unit. According to the numerical results, the velocity of the liquid PCM flow is less than 0.02 m/s; hence, the flow in the layer is laminar. Therefore, laminar thermal boundary layers are established adjacent to the wall of the inner pipe as well as near the liquid/solid PCM interface. In this situation, it is difficult for thermal energy from the HTF to transfer across the boundary layer. It is virtually transported by the upward convective motion towards the top of the storage unit. As a consequence, the thermal

energy from the HTF is carried upward and less energy is transported to melt the PCM along the liquid/solid interface around the vertical PCM layer. This explains why the width of this confined liquid layer remains almost constant during the charging process as found experimentally.

In Region 2, the liquid PCM separates into two streams. One stream flows downward due to the pressure difference to make up the PCM in the confined layer, while the other stream is induced by the high temperature liquid PCM flowing upward. Along the liquid/solid interface, the convection enhances the heat transfer, melting the solid PCM. In Region 3, the liquid PCM above the liquid/solid interface forms a laminar flow circulation along the interface eroding the solid PCM. This flow circulation induces natural convection, which enhances heat transfer between the solid and liquid parts; hence, melting the solid PCM along the surface. In Region 4, the liquid PCM forms a flow circulation circuit, which enhances heat transfer in the liquid PCM and unifies its temperature due this circulation.
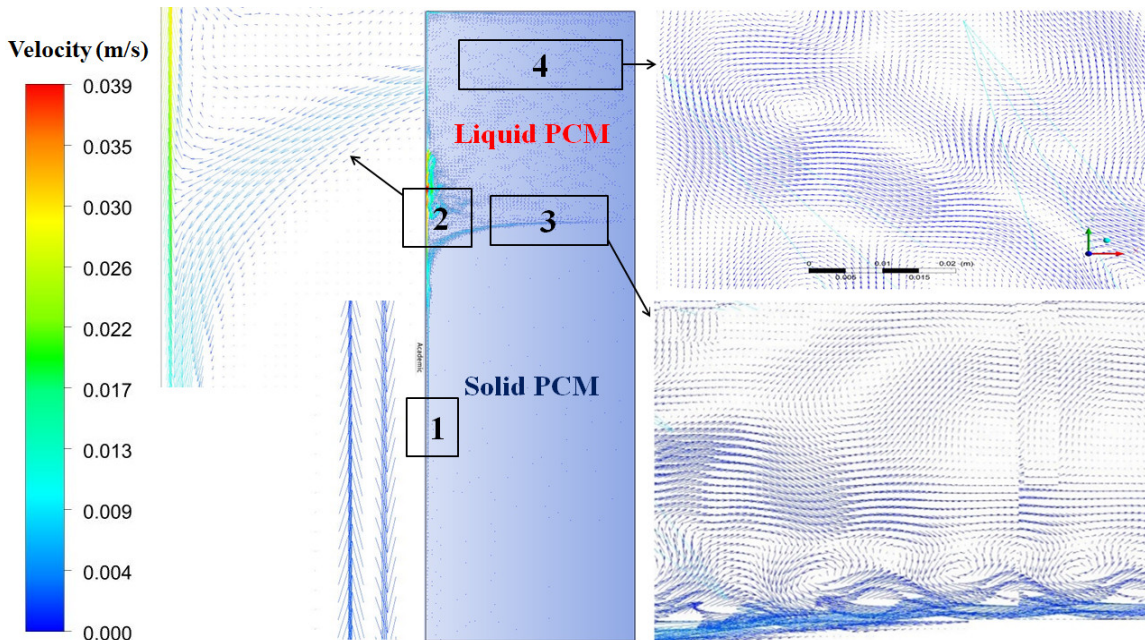

Figure D.8: The simulated liquid PCM velocity field during the charging process

D.5.2 Discharging process

Figure D.9 shows the PCM temperature variations over time at positions A and B in the cylindrical storage unit during the discharging process. It is seen that the temperatures decrease rapidly at the beginning of the solidification period due to the convective heat transfer within the liquid PCM, which quickly transfers the stored sensible energy to the cold HTF. No PCM is solidified prior to the temperature drop to the freezing point.
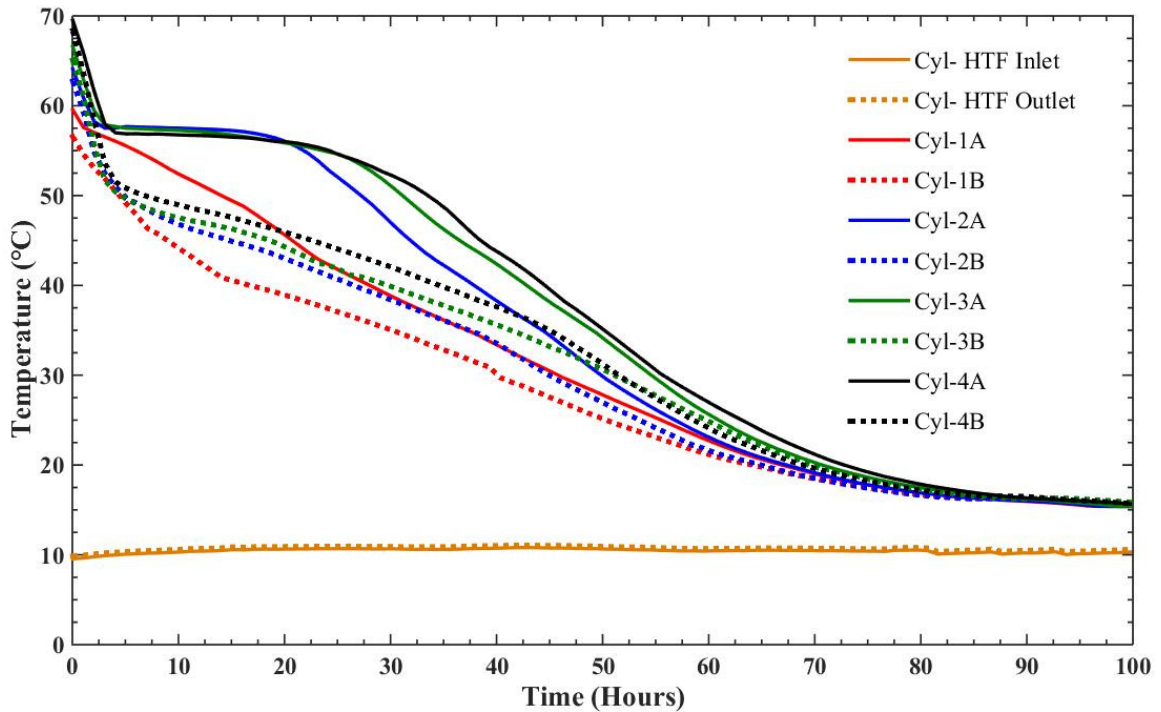

Figure D.9: Temperature variations during the discharging process

As shown in Figure D.9, the PCM temperature variation in the axial direction is not as significant as that of the charging process. The PCM temperature at lower levels decreases much faster than those at upper levels. This can be interpreted by the following reasoning. The PCM adjacent to the HTF pipe begins to solidify, forming a solid layer of PCM around the pipe, which increases the thermal resistance between the cold HTF and liquid PCM. The heat transfer rate decreases as the thickness of the solid PCM layer increases. Due to the lack of liquid PCM in the solid layer, conduction dominates the heat transfer from the HTF to the liquid PCM. Nevertheless, natural convection still exists

within the liquid PCM; hence, hot liquid PCM flows upward due to buoyancy forces. Therefore, the temperature at the lower part is lower than the upper part. Consequently, the PCM at the lower part solidifies first due to the lower temperature.

This phenomenon is clearly shown in Figure D.9 for positions A (2-4) where the PCM exists in liquid form for a quite long period as indicated by the flat lines due to the low heat transfer rate from the HTF to the liquid PCM. At position B, however, no flat line exists and the PCM temperature continues to drop. This might be due to the energy loss to the environment through the shell since position B is very close to the shell surface.

From the above analysis, it is clear that both conduction and convection heat transfer mechanisms exist during the solidification process. Although formation of the solid PCM around the HTF tube increases the thermal resistance, the natural convection within the liquid PCM increases the temperature difference between the PCM at the interface and the HTF. This in turn enhances heat transfer during the solidification process, which can be visually seen in Figure D.10.
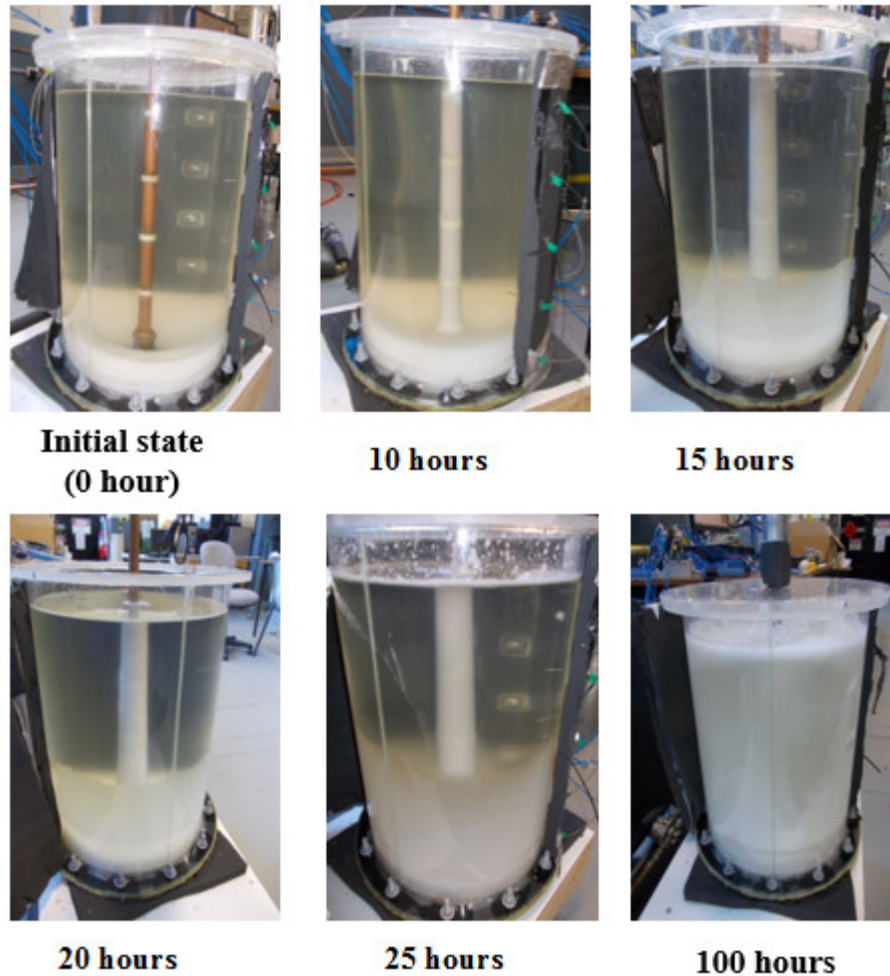
Figure D.10: Evolution of the liquid and solid PCM interface at different discharging times

Figure D.10 shows the evolution of the liquid/solid PCM front during the discharging process. The solidification front moves along both radial and axial directions simultaneously. When the cold HTF removes the heat from the PCM, it solidifies and thermal conduction dominates the heat transfer. The solidification front moves outwards along the radial direction. Meanwhile, the hot liquid PCM moves upward due to the buoyancy forces, whereas the solid PCM sinks at the bottom of the container due to the higher density of the mushy zone. Liquid PCM forms the natural convection process, which enhances the heat transfer within the mushy zone.

Figure D.11 shows the simulated contours of liquid fraction (left side) and temperature field (right side) for the cylindrical storage unit using the developed model.

The liquid fraction contours clearly show that the solidification front moves along both axial and radial directions, which is consistent with the experimental findings. The temperature contours show that the temperature along the axial direction is different as the PCM solidifies. The PCM temperature is found to remain at the freezing point prior to solidification. These phenomena can only be interpreted by presence of natural convection.
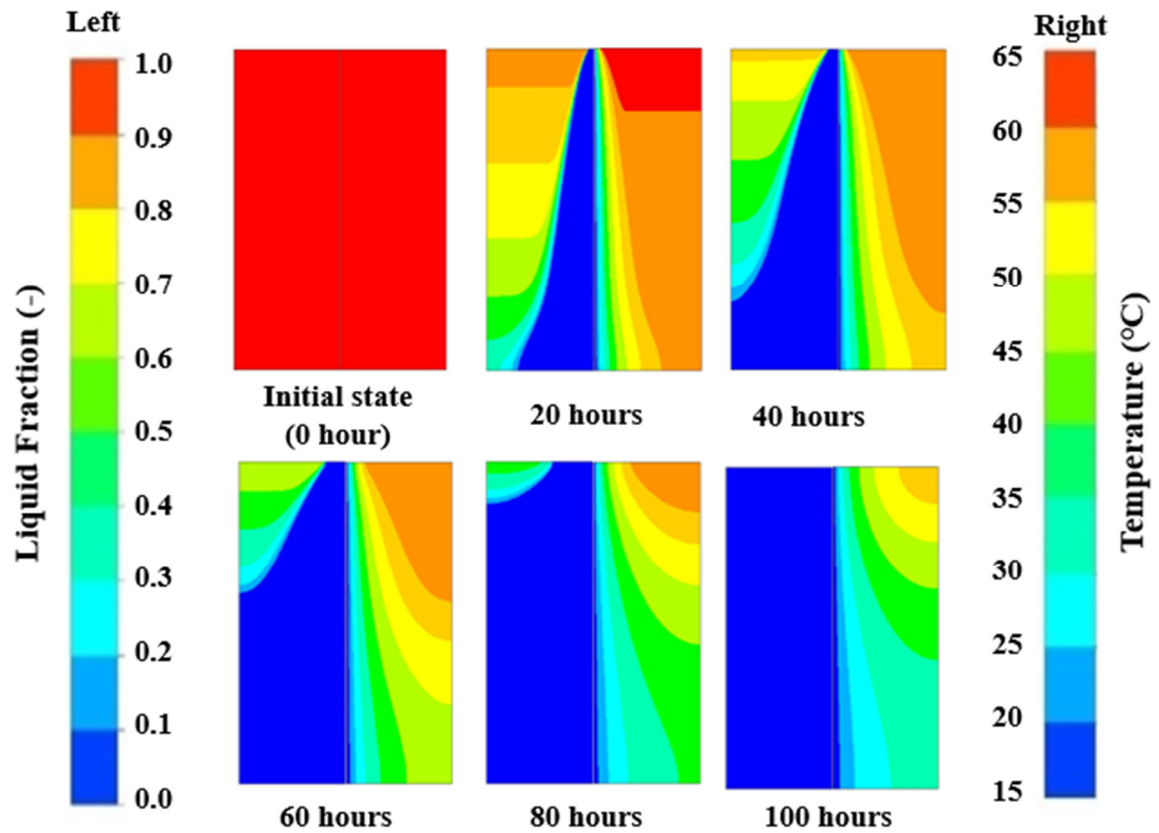

Figure D.11: The contour of the PCM liquid fraction (left) and temperature (right) during the discharging process

Figure D.12 presents the simulated velocity field. It clearly shows the presence of convective circulation within the liquid PCM in the mushy zone. It further explains that natural convection occurs during the discharging process as long as liquid PCM exists.
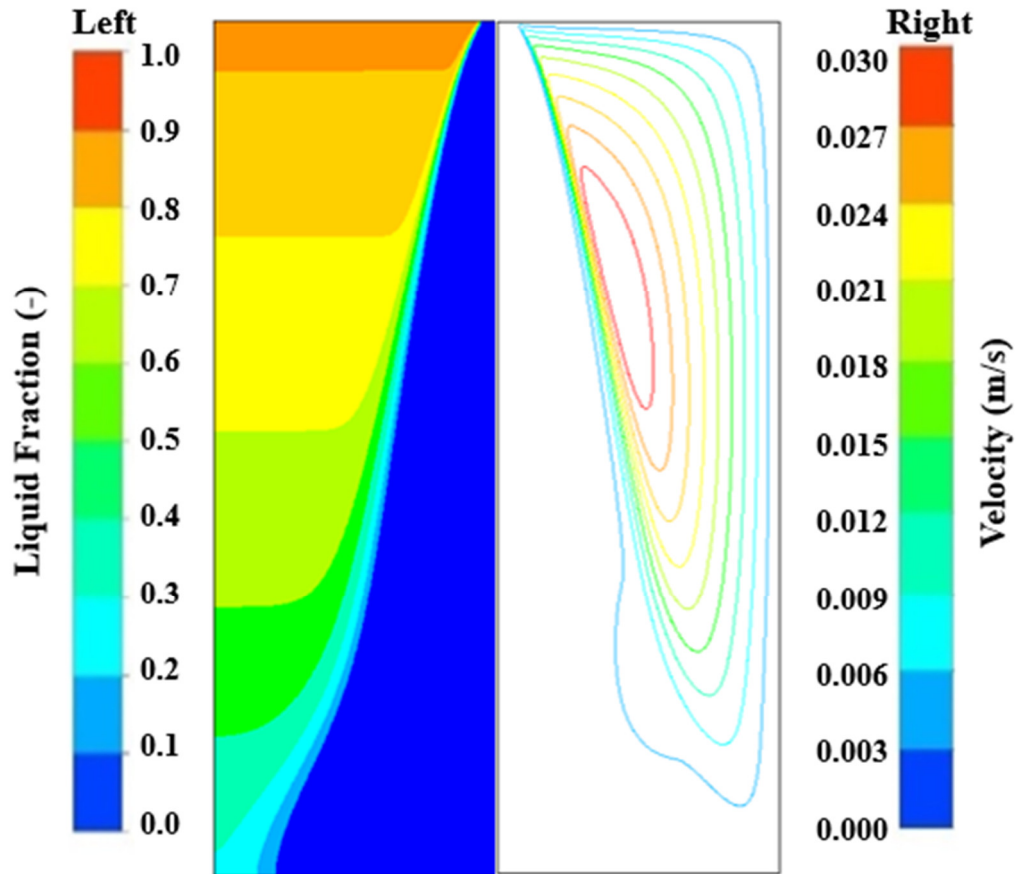
Figure D.12: The simulated liquid PCM velocity field during the discharging process

D.6　Conclusion

This chapter reported the outcomes of an experimental and numerical investigation on the thermal behavior and physics of energy transfer in a vertical cylindrical shell-and-tube LHTES unit during both charging and discharging processes. During the charging process, a confined vertical liquid PCM layer was formed around the HTF pipe once the melting started. In the layer, thermal energy was transferred from the HTF to the liquid PCM through the vertical convective circulation, which then carried it upward to the liquid PCM accumulated at the upper part of the storage system. This thermal energy was then spread through the liquid PCM at the upper part along the radial direction via a horizontal convective circulation, which enhanced heat transfer in the liquid PCM and liquid/solid interface above the solid PCM. The melting front moved downward from the top to the bottom of the storage system. During the discharging process, the results

demonstrated that the solidification front moved along both radial and axial directions at the same time. When the cold HTF removed the heat from the PCM, it was solidified and its temperature decreased. Then the solidification front moved outwards. Meanwhile, the liquid PCM moved upward due to the buoyancy forces and induced a convective circulation within the liquid PCM, which enhanced heat transfer during the discharging process.